MINISTRY OF EDUCATION AND TRAINING
HO CHI MINH CITY UNIVERSITY OF TECHNOLOGY AND EDUCATION

ACADEMIC PUBLICATION LIST
DANH MỤC BÀI BÁO KHOA HỌC

PHD CANDIDATE: XUAN BACH BUI
NGHIÊN CỨU SINH: BÙI XUÂN BÁCH

HO CHI MINH CITY, APRIL 2025

Stt	Tên bài báo	Tác giả	Tên tạp chí/kỷ yếu, số/tập, số ISSN/ISBN	Thời gian xuất bản	Link/Doi	Ghi chú
I.	Tạp chí khoa học trong danh mục WoS (SCIE, SSCI, AHCI, ESCI)					
1	*A general higher-order shear deformation theory for buckling and free vibration analysis of laminated thin-walled composite I-beams*	**Bui, X.-B.**, T.-K. Nguyen, N.-D. Nguyen, and T.P. Vo	Composite Structures ISSN: 0263-8223	2022	https://doi.org/10.1016/j.compstruct.2022.115775	
2	*Stochastic vibration and buckling analysis of functionally graded sandwich thin-walled beams*	**Bui, X.-B.**, T.-K. Nguyen, and P.T.T. Nguyen	Mechanics Based Design of Structures and Machines ISSN: 1539-7742	2023	https://doi.org/10.1080/15397734.2023.2165101	
3	*Deterministic and stochastic flexural behaviors of laminated composite thin-walled I-beams using a sinusoidal higher-order shear deformation theory*	**Bui, X.-B**. and T.-K. Nguyen	Mechanics Based Design of Structures and Machines ISSN: 1539-7742	2023	https://doi.org/10.1080/15397734.2023.2297840	
4	*Size-dependent behaviours of functionally graded sandwich thin-walled beams based on the modified couple stress theory*	**Bui, X.-B.**, T.-K. Nguyen, A. Karamanli, and T.P. Vo	Aerospace Science and Technology ISSN: 1270-9638	2023	https://doi.org/10.1016/j.ast.2023.108664	
5	*Spectral projection and linear regression approaches for stochastic flexural and vibration analysis of laminated composite beams*	**Bui, X.-B.**, P.T.T. Nguyen, and T.-K. Nguyen	Archive of Applied Mechanics ISSN: 0939-1533	2024	https://doi.org/10.1007/s00419-024-02565-x	
II	Kỷ yếu hội nghị khoa học quốc tế có phản biện và có ISBN					
1	*A novel two-variable model for bending analysis of laminated composite beams*	**Bui, X.B.**, T.K. Nguyen,	2020 5th International Conference on Green	2020	10.1109/GTSD50082.2020.9303157	

		Q.C. Le, and T.T.P. Nguyen	Technology and Sustainable Development (GTSD)			
2	*Stochastic Vibration Responses of Laminated Composite Beams Based on a Quasi-3D Theory*	**Bui, X.-B**., T.-K. Nguyen, T.T.-P. Nguyen, and V.-T. Nguyen	International Conference on Sustainable Civil Engineering and Architecture (ICSCEA 2021)	2021	https://www.springerprofessional.de/en/stochastic-vibration-responses-of-laminated-composite-beams-base/23517844	
III				**Tạp chí trong nước**		
1	*Buckling analysis of laminated composite thin-walled I-beam under mechanical and thermal loads*	**Bui, X.-B**., A.-C. Nguyen, N.-D. Nguyen, T.-T. Do, and T.-K. Nguyen	Vietnam Journal of Mechanics	2023	https://doi.org/10.15625/0866-7136/17956	

A general higher-order shear deformation theory for buckling and free vibration analysis of laminated thin-walled composite I-beams

Xuan-Bach Bui [a], Trung-Kien Nguyen [b,*], Ngoc-Duong Nguyen [a], Thuc P. Vo [c]

[a] *Faculty of Civil Engineering, Ho Chi Minh City University of Technology and Education, 1 Vo Van Ngan Street, Thu Duc City, Ho Chi Minh City, Viet Nam*
[b] *CIRTech Institute, HUTECH University, 475A Dien Bien Phu Street, Binh Thanh District, Ho Chi Minh City, Viet Nam*
[c] *School of Computing, Engineering and Mathematical Sciences, La Trobe University, Bundoora, VIC 3086, Australia*

ARTICLE INFO

ABSTRACT

A general higher-order shear deformation theory for buckling and free vibration analysis of laminated thin-walled composite I-beams is proposed in this paper. It is based on a unified nonlinear variation of shear strains in the wall thickness and then theoretical formulation is derived in the general form which can recover the previous conventional theories such as classical and first-order thin-walled beam theory. Series-type solutions with hybrid shape functions are developed for different boundary conditions. Numerical examples are performed on laminated thin-walled composite I-beams with arbitrary lay-ups. Effects of transverse shear strains, fiber angles and slenderness ratio on the critical buckling loads and natural frequencies of the beams are reported.

1. Introduction

Laminated composite (LC) thin-walled beams with many advantages in weight and strength have been used in many engineering fields such as mechanical engineering, aerospace [1], aircrafts [2,3], etc. Such structures have attracted a number of researchers with different methods and approaches to predict accurately their structural responses, only some representative references are herein cited, more details can be found in comprehensive review [4].

It is known that the classical thin-walled beam theory (CTWBT), which neglects shear effects, by Vlasov [5] is the simplest one to analyse LC thin-walled beams [6–9]. It underestimates the deflection and overestimates the natural frequencies/critical buckling loads. Latalski [10] developed a generalised beam theory for the semi-angular cross section based on Vlasov's work but added the effects of cross-section distortion. Yu and Hodges [11] developed a generalised Vlasov theory for composite beams using the finite element method. In order to account for effects of transverse shear strains, the first-order thin-walled beam theory (FTWBT) with the linear variation of the displacement in the wall thickness, which provides more accurate results than the CTWBT, has been employed [12–20]. However, this theory requires a shear correction factor to rectify the stress-free boundary conditions. To solve this problem, the higher-order thin-walled beam theory (HTWBT), in which the axial displacement is nonlinearly approximated in the wall

thickness, is proposed. It should be highlighted the work of Carrera and colleagues [21–35], who invented the Carrera Unified Formulation (CUF) by using Taylor expansion and Lagrange expansion in displacement fields to obtain any refined theories on the basis of known fundamental nuclei. This approach has been successfully employed for many problems such as plates [21,23,24,26,28,33,35], shells [22,25] and thin-walled composite beams sections such as C, box, I-section and wing structures [27,29–32,34]. It should be mentioned that the mathematic formulation from CUF is complicated with many variables in displacement fields. Chandiramani et al. [36] investigated free, forced and geometrically nonlinear vibration responses of LC composite box beams based on the assumption of a parabolic distribution of the transverse shear strains through the wall thickness. Literature review shows that the study on behaviour of thin-walled I-beams based on the general HTWBT, which can recover conventional theories such as CTWBT and FTWBT, is very limited. This intriguing topic therefore needs to be study further.

The objective of this paper is to develop a general higher-order shear deformation theory for buckling and free vibration analysis of LC thin-walled beams. The transverse shear strains are assumed to be non-linearly variation by a shear function, and the axial displacement is obtained with a higher-order variation in the wall thickness. A hybrid series solution is developed for solving equations of motion with different boundary conditions and various theories including CTWBT,
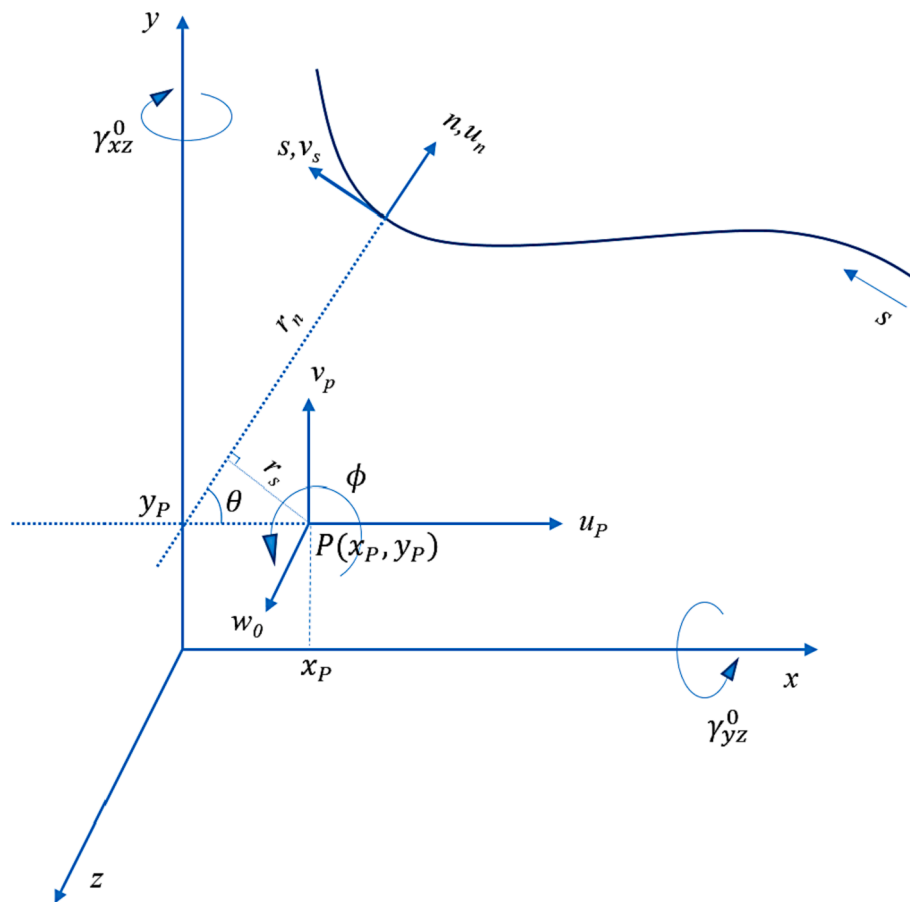

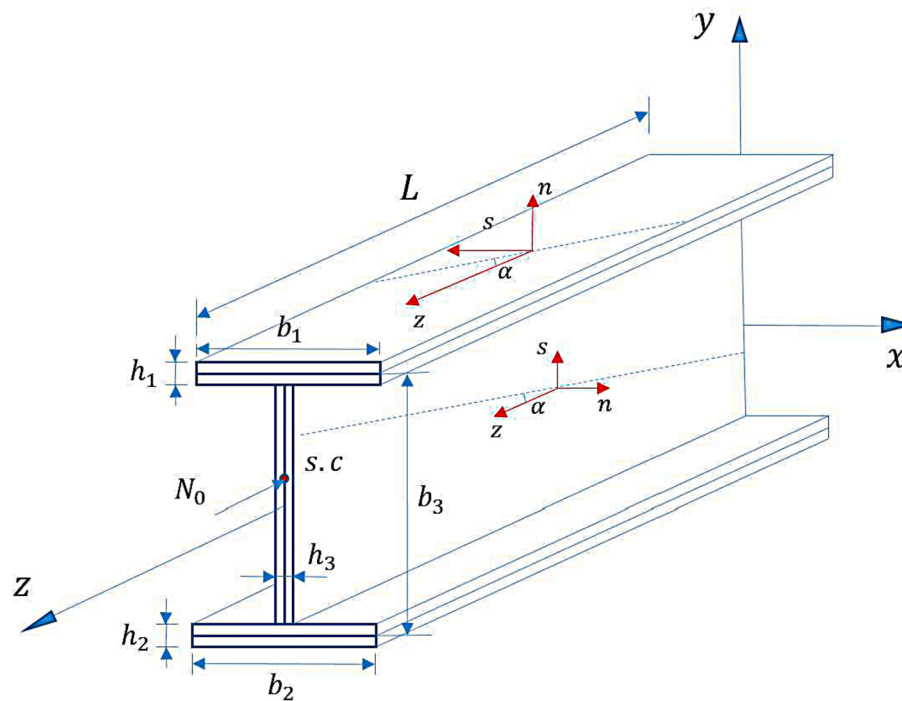**Fig. 1.** Thin-walled coordinate systems.

Fig. 2. Geometry of laminated composite thin-walled I-beams.

Table 1
Shape functions and essential BCs of LC thin-walled I-beams.

BC	$\varphi_j(z)$	$z = 0$	$z = L$
SS	$\frac{z}{L}\left(1 - \frac{z}{L}\right)e^{\frac{-jz}{L}}$	$u_P = v_P = \phi = 0$	$u_P = v_P = \phi = 0$
CF	$\left(\frac{z}{L}\right)^2 e^{\frac{-jz}{L}}$	$u_P = v_P = \phi = 0$ $u_{P,z} = v_{P,z} = \phi_{,z} = 0$ $w_0 = \gamma_{xz}^{(0)} = \gamma_{yz}^{(0)} = 0$	
CC	$\left(\frac{z}{L}\right)^2\left(1 - \frac{z}{L}\right)^2 e^{\frac{-jz}{L}}$	$u_P = v_P = \phi = 0$ $u_{P,z} = v_{P,z} = \phi_{,z} = 0$ $w_0 = \gamma_{xz}^{(0)} = \gamma_{yz}^{(0)} = 0$	$u_P = v_P = \phi = 0$ $u_{P,z} = v_{P,z} = \phi_{,z} = 0$ $w_0 = \gamma_{xz}^{(0)} = \gamma_{yz}^{(0)} = 0$

Table 2
Material properties of LC thin-walled I-beams.

Material properties	MAT I [39]	MAT II [42]	MAT III [43]	MAT IV [39]
$E_1(GPa)$	53.78	144	144	25
$E_2(GPa)$	17.93	9.65	9.68	1
$G_{12} = G_{13}(GPa)$	8.96	4.14	4.14	0.6
$G_{23}(GPa)$	3.45	3.45	3.45	0.6
ν	0.25	0.3	0.3	0.25
$\rho(kg/m^3)$	1968.90	1389	–	1

Table 3
Convergence of fundamental frequencies (Hz) and critical buckling loads (kN) for the LC thin-walled I-beam with different boundary conditions.

BC	m					
	2	4	6	8	10	12
Fundamental frequency (Hz)						
SS	16.7573	16.5382	16.4762	16.4753	16.4753	16.4753
CC	37.3798	37.2488	37.2435	37.2409	37.2374	37.2272
CF	5.9567	5.877	5.8723	5.8721	5.8721	5.8722
Critical buckling load (kN)						
SS	2.7505	2.6880	2.6691	2.6688	2.6688	2.6688
CC	10.7671	10.6489	10.6281	10.6281	10.6281	10.6281
CF	0.7060	0.6680	0.6679	0.6679	0.6679	0.6679

FTWBT and HTWBT. Numerical examples are performed to investigate the effects of lay-ups, fiber angle and and shear deformation on the natural frequencies and critical buckling loads of the LC thin-walled I-section beams.

2. Theoretical formulation

In order to investigate theoretical formulation, three coordinate systems, namely, Cartesian coordinate system (x, y, z), local plate coordinate system (n, s, z) and contour coordinate s along the profile of the section are considered and illustrated in Fig. 1. It is assumed that θ is an angle of orientation between (n, s, z) and (x, y, z) coordinate systems, the pole P with coordinates (x_P, y_P) is the shear center of the section. For simplicity purpose, the following assumptions are employed: the displacements are small so that the geometrically nonlinear behaviours are neglected, the section contour does not deform in its own plane and the transverse shear strains vary nonlinearly in the wall thickness. The geometry of the thin-walled I-beam is shown in Fig. 2 in which b_1, b_2, b_3 denote the widths and h_1, h_2, h_3 denote the thicknesses of top, bottom flange, and web, respectively.

2.1. Kinematics

The displacements $u(n, s, z, t)$ and $v(n, s, z, t)$ at any points of the beam cross-section under a small rotation $\phi(z, t)$ about the pole axis can be expressed in terms of those at the pole $u_P(z, t)$ and $v_P(z, t)$ in $x-$ and

$y-$directions, respectively, as follows ([37]):

$$u(n, s, z, t) = u_P(z, t) - (y - nx_{,s} - y_P)\phi(z, t) = u_P(z, t) - (Y - y_P)\phi(z, t) \tag{1a}$$

$$v(n, s, z, t) = v_P(z, t) + (x + ny_{,s} - x_P)\phi(z, t) = v_P(z, t) + (X - x_P)\phi(z, t) \tag{1b}$$

where the comma in the subscript is used to indicate the differentiation with respect to the variable that follows; $y_{,s}$ and $x_{,s}$ are the trigonometric functions $\cos\theta$ and $-\sin\theta$, respectively (see Fig. 1); X, Y are the coordinates of an arbitrary point along the n axis. It can be seen that the displacements in Eq. (1) satisfy the non-deformability conditions of cross-section. The displacements in the contour lines $u_n(n, s, z, t), v_s(n, s, z, t)$ can be hence derived from the displacements in Eq. (1) as follows:

$$u_n(n, s, z, t) = u_P(z, t)y_{,s} - v_P(z, t)x_{,s} - R_s(n, s)\phi(z, t) \tag{2a}$$

$$v_s(n, s, z, t) = u_P(z, t)x_{,s} + v_P(z, t)y_{,s} + R_n(n, s)\phi(z, t) \tag{2b}$$

where $R_s(n, s) = r_s(s)$, $R_n(n, s) = r_n(n, s) + n$ in which $r_s(s), r_n(s)$ are the lengths of the perpendiculars from P to the tangent and normal of the profile line center (see Fig. 1). Moreover, the shear strains $(\gamma_{sz}, \gamma_{nz})$ in the contour of thin-walled beams with open sections can be written in terms of the transverse shear strains $(\gamma_{xz}, \gamma_{yz})$ and a direct shear strain caused by the change rate of twist angle $\phi_{,z}$ ([2]) as follows:

$$\gamma_{sz}(n, s, z, t) = \gamma_{xz}(n, z, t)X_{,s} + \gamma_{yz}(n, z, t)Y_{,s} + 2n\phi_{,z}(z, t) = v_{s,z} + w_{,s} \tag{3a}$$

$$\gamma_{nz}(n, s, z, t) = \gamma_{xz}(n, z, t)Y_{,s} - \gamma_{yz}(n, z, t)X_{,s} = u_{n,z} + w_{,n} \tag{3b}$$

where w is the axial displacement at any point of the beam cross-section. It is assumed that the transverse shear strains $(\gamma_{xz}, \gamma_{yz})$ vary nonlinearly through the wall thickness as follows:

$$\gamma_{xz}(n, z, t) = g(n)\gamma_{xz}^{(0)}(z, t) \tag{4a}$$

$$\gamma_{yz}(n, z, t) = g(n)\gamma_{yz}^{(0)}(z, t) \tag{4b}$$

where $\gamma_{xz}^{(0)}, \gamma_{yz}^{(0)}$ are mid-surface transverse shear strains; $g(n)$ is a general higher-order shear function which satisfies the stress-free boundary conditions, i.e. $g(n = \pm h/2) = 0$ where h is the wall thickness.

$$\gamma_{xz}^{(0)} = \psi_y + u_{P,z} \tag{5a}$$

$$\gamma_{yz}^{(0)} = \psi_x + v_{P,z} \tag{5b}$$

where ψ_x, ψ_y are the rotations of the cross-section with respect to x and y, respectively.

Substituting Eqs. (2) and (4) into Eq. (3) and then integrating the subsequent results with respect to s and n lead to the expression of the axial displacement as follows:

$$w(n, s, z, t) = w_0(z, t) + \gamma_{xz}^{(0)}(z, t)(g_0x + fy_{,s}) + \gamma_{yz}^{(0)}(z, t)(g_0y - fx_{,s}) - u_{P,z}(z, t)(x + ny_{,s}) - v_{P,z}(z, t)(y - nx_{,s}) - \phi_{,z}(z, t)(\overline{F}_\omega - nr_s) \tag{6}$$

where $g_0 = g(n = 0)$, $g = f_{,n}$; $\overline{F}_\omega(s)$ is a warping function which is defined by:

$$\overline{F}_\omega(s) = \int_{s_0}^s r_n(s)ds \tag{7}$$

A general higher-order shear deformation kinematics at any points of the LC thin-walled beam can be expressed as follows:

$$u(n, s, z, t) = u_P(z, t) - (y - nx_{,s} - y_P)\phi(z, t) \tag{8a}$$

Table 4

Fundamental frequency (*Hz*) of LC thin-walled I-beams with different boundary conditions and span-to-height ratios.

BC	Reference	Lay-up						
		$[0]_{4s}$	$[15/-15]_{4s}$	$[30/-30]_{4s}$	$[45/-45]_{4s}$	$[60/-60]_{4s}$	$[75/-75]_{4s}$	$[90/-90]_{4s}$
$L/b_3 = 40$								
SS	Present (HTWBT)	24.135	22.954	19.794	16.475	14.657	14.068	13.538
	Present (FTWBT)	24.163	22.974	19.805	16.481	14.661	14.072	13.965
	Nguyen et al. [39] (FTWBT)	24.169	22.977	19.806	16.481	14.660	14.071	13.964
	Nguyen et al. [39] (CTWBT)	24.198	23.001	19.820	16.490	14.668	14.079	13.972
	Vo and Lee [16] (FTWBT)	24.150	22.955	19.776	16.446	14.627	14.042	13.937
	Kim et al. [40] (CTWBT)	24.194	22.997	19.816	16.487	14.666	14.077	13.970
$L/b_3 = 20$								
CF	Present (HTWBT)	26.436	25.143	21.685	18.050	16.058	15.413	15.296
	Present (FTWBT)	26.470	25.168	21.698	18.057	16.063	15.418	15.301
	Kim and Lee [41] (FTWBT)	26.460	25.160	21.700	18.060	16.060	15.420	15.300
	Nguyen et al. [39] (FTWBT)	26.479	25.174	21.699	18.057	16.063	15.417	15.299
	Nguyen et al. [39] (CTWBT)	26.514	25.202	21.717	18.069	16.072	15.427	15.309
$L/b_3 = 40$								
CC	Present (HTWBT)	54.198	51.655	44.677	37.237	33.142	31.811	31.568
	Present (FTWBT)	54.499	51.876	44.790	37.302	33.1897	31.856	31.613
$L/b_3 = 10$								
SS	Present (HTWBT)	372.076	356.585	310.809	260.096	231.742	222.431	220.705
	Present (FTWBT)	378.427	361.331	313.311	261.494	232.810	223.457	221.739
CF	Present (HTWBT)	104.813	99.874	86.359	71.977	64.058	61.487	61.018
	Present (FTWBT)	105.351	100.271	86.564	72.090	64.143	61.567	61.099
CC	Present (HTWBT)	745.489	731.822	661.601	564.603	506.049	485.710	481.698
	Present (FTWBT)	798.300	773.783	685.611	578.677	516.922	496.144	492.167
$L/b_3 = 5$								
SS	Present (HTWBT)	1344.158	1312.736	1176.720	999.590	894.553	858.598	851.566
	Present (FTWBT)	1422.882	1374.247	1211.303	1019.590	909.980	873.414	866.491
CF	Present (HTWBT)	405.333	388.894	339.562	284.438	253.531	243.382	241.503
	Present (FTWBT)	413.280	394.858	342.708	286.182	254.845	244.626	242.751
CC	Present (HTWBT)	2200.409	2252.548	2193.488	1964.319	1787.989	1715.788	1698.878
	Present (FTWBT)	2594.384	2600.996	2434.795	2123.285	1915.436	1838.472	1822.071

$$v(n, s, z, t) = v_p(z, t) + \left(x + ny_{,s} - x_P\right)\phi(z, t) \tag{8b}$$

$$\begin{aligned}w(n, s, z, t) &= w_0(z, t) + \gamma_{xz}^{(0)}(z, t)\left(g_0 x + f y_{,s}\right) + \gamma_{yz}^{(0)}(z, t)\left(g_0 y - f x_{,s}\right)\\&\quad - u_{P,z}(z, t)\left(x + ny_{,s}\right) - v_{P,z}(z, t)\left(y - nx_{,s}\right) - \phi_{,z}(z, t)\left(\overline{F}_\omega - nr_{,s}\right)\end{aligned} \tag{8c}$$

In this paper, $f = n - \frac{4n^3}{3h^2}$ and $g = 1 - \frac{4n^2}{h^2}$ will be selected. It is worth noticing that the CTWBT can be found by setting $\gamma_{xz}^{(0)} = 0, \gamma_{yz}^{(0)} = 0$, while the FTWBT is recovered by putting $g = g_0 = 1, f = n$.

2.2. Strains

The linear non-zero strains related to the displacement in Eq. (8) are given by:

$$\varepsilon_z(n, s, z, t) = \varepsilon_z^{(0)} + n\varepsilon_z^{(1)} + f\varepsilon_z^{(2)} \tag{9a}$$

$$\gamma_{sz}(n, s, z, t) = n\gamma_{sz}^{(1)} + g\gamma_{sz}^{(2)} \tag{9b}$$

$$\gamma_{nz}(n, s, z, t) = g\gamma_{nz}^{(0)} \tag{9c}$$

where

$$\varepsilon_z^{(0)}(s, z, t) = w_{0,z} + \left(g_0\gamma_{xz}^{(0)} - u_{P,zz}\right)x + \left(g_0\gamma_{yz}^{(0)} - v_{P,zz}\right)y - \phi_{,zz}\overline{F}_\omega \tag{10a}$$

$$\varepsilon_z^{(1)}(s, z, t) = v_{P,zz}x_{,s} - u_{P,zz}y_{,s} + \phi_{,zz}r_{,s} \tag{10b}$$

$$\varepsilon_z^{(2)}(s, z, t) = \gamma_{xz,z}^{(0)}y_{,s} - \gamma_{yz,z}^{(0)}x_{,s} \tag{10c}$$

$$\gamma_{sz}^{(1)}(s, z, t) = 2\phi_{,z} \tag{10d}$$

$$\gamma_{sz}^{(2)}(s, z, t) = \gamma_{xz}^{(0)}x_{,s} + \gamma_{yz}^{(0)}y_{,s} \tag{10e}$$

$$\gamma_{nz}^{(0)}(s, z, t) = \gamma_{xz}^{(0)}y_{,s} - \gamma_{yz}^{(0)}x_{,s} \tag{10f}$$

2.3. Stresses

For LC thin-walled beams, it is supposed to be constituted by a number of orthotropic material layers with the same thickness. The reduced constitutive equations at the kth − layer is given by:

$$\begin{Bmatrix} \sigma_z \\ \sigma_{sz} \\ \sigma_{nz} \end{Bmatrix} = \begin{pmatrix} P_{11} & P_{16} & 0 \\ P_{16} & P_{66} & 0 \\ 0 & 0 & P_{55} \end{pmatrix} \begin{Bmatrix} \varepsilon_z \\ \gamma_{sz} \\ \gamma_{nz} \end{Bmatrix} \tag{11}$$

where $P_{11} = \overline{Q}_{11} - \frac{\overline{Q}_{11}^2}{\overline{Q}_{22}}$, $P_{16} = \overline{Q}_{16} - \frac{\overline{Q}_{12}\overline{Q}_{26}}{\overline{Q}_{22}}$, $P_{66} = \overline{Q}_{66} - \frac{\overline{Q}_{26}^2}{\overline{Q}_{22}}$, $P_{55} = \overline{Q}_{55}$; $\overline{Q}_{ij}$ are the reduced stiffness components of materials (see [38] for more details).

2.4. Variational formulation

The characteristic equations of the LC thin-walled beams can be derived by Hamilton's equations in which the total energy of the system Π is composed of the strain energy Π_S, work done by external force Π_W and kinetic energy Π_K as follows:

Table 5
Critical buckling load (*N*) of LC thin-walled I-beams with different boundary conditions and span-to-height ratios.

BC	Reference	Lay-up						
		$[0]_{4s}$	$[15/-15]_{4s}$	$[30/-30]_{4s}$	$[45/-45]_{4s}$	$[60/-60]_{4s}$	$[75/-75]_{4s}$	$[90/-90]_{4s}$
$L/b_3 = 80$								
SS	Present (HTWBT)	1437.0	1298.7	964.7	667.9	528.5	486.9	958.6
	Present (FTWBT)	1438.0	1299.4	965.1	668.1	528.7	487.0	959.0
	Nguyen et al. [39] (FTWBT)	1438.1	1299.4	965.0	668.1	528.6	487.0	959.0
	Nguyen et al. [39] (CTWBT)	1438.8	1300.0	965.2	668.2	528.7	487.1	959.3
	Kim et al. [44] (CTWBT)	1438.8	1300.0	965.2	668.2	528.7	487.1	964.4
$L/b_3 = 20$								
CF	Present (HTWBT)	5727.4	5180.3	3852.4	2668.8	2112.1	1945.8	3826.0
	Present (FTWBT)	5740.3	5189.3	3856.4	2670.6	2113.3	1946.9	3831.1
	Nguyen et al. [39] (FTWBT)	5743.3	5191.0	3856.8	2670.6	2113.2	1946.7	3831.4
	Nguyen et al. [39] (CTWBT)	5755.2	5199.7	3861.0	2672.7	2114.7	1948.3	3837.3
	Kim et al. [44] (CTWBT)	5755.2	5199.8	3861.0	2672.7	2114.7	1948.3	3837.8
	Vo and Lee [16] (FTWBT)	5741.5	5189.0	3854.5	2668.4	2111.3	1945.1	3829.8
$L/b_3 = 80$								
CC	Present (HTWBT)	5727.4	5180.3	3852.4	2668.8	2112.1	1945.8	3826.0
	Present (FTWBT)	5740.3	5189.3	3856.4	2670.6	2113.3	1946.9	3831.1
$L/b_3 = 10$								
SS	Present (HTWBT)	85.45	78.50	59.65	41.78	33.17	30.56	58.70
	Present (FTWBT)	88.43	80.63	60.63	42.24	33.48	30.84	59.93
CF	Present (HTWBT)	22.58	20.49	15.31	10.63	8.42	7.75	15.17
	Present (FTWBT)	22.78	20.63	15.37	10.66	8.44	7.77	15.25
CC	Present (HTWBT)	281.03	268.44	216.23	156.26	125.21	115.34	207.48
	Present (FTWBT)	315.97	295.06	229.62	162.83	129.74	119.52	223.67
$L/b_3 = 5$								
SS	Present (HTWBT)	281.05	268.47	216.25	156.28	125.22	115.35	207.49
	Present (FTWBT)	316.00	295.08	229.64	162.85	129.75	119.54	223.69
CF	Present (HTWBT)	85.45	78.49	59.65	41.77	33.16	30.55	58.69
	Present (FTWBT)	88.42	80.62	60.62	42.23	33.47	30.84	59.93
CC	Present (HTWBT)	657.01	679.58	629.11	496.32	408.95	376.70	566.53
	Present (FTWBT)	885.99	880.70	757.62	569.25	461.62	425.24	705.90

$$\int_{t_1}^{t_2} (\delta\Pi_S + \delta\Pi_W - \delta\Pi_K)dt = 0 \tag{12}$$

The variation of strain energy Π_S is defined by:

$$\delta\Pi_S = \int_\Omega (\sigma_z\delta\varepsilon_z + \sigma_{sz}\delta\gamma_{sz} + \sigma_{nz}\delta\gamma_{nz})d\Omega \tag{13}$$

Substituting Eqs. (9) and (11) into Eq. (13) leads to:

$$\delta\Pi_S = \int_0^L \Big[T_z\delta w_{0,z} + M_y\delta\gamma_{xz,z}^{(0)} + M_x\delta\gamma_{yz}^{(0)} + M_{ya}\delta u_{P,zz} + M_{xa}\delta v_{P,zz} + M_\omega\delta\phi_{,zz} + Q_x\delta\delta\gamma_{xz}^{(0)} + Q_y\delta\delta\gamma_{yz}^{(0)} + M_z\delta\phi_{,z} \Big]dz \tag{14}$$

where the stress resultants $(T_z, M_y, M_x, M_{ya}, M_{xa}, M_\omega, Q_x, Q_y, M_z)$ are defined as follows:

$$(T_z, M_y, M_x) = \int_A \sigma_z(1, g_0 x + fy_{,s}, g_0 y - fx_{,s})dsdn \tag{15a}$$

$$(M_{ya}, M_{xa}, M_\omega) = \int_A \sigma_z\big[-(x + ny_{,s}), -y + nx_{,s}, -\overline{F}_\omega + nr_{,s} \big]dsdn \tag{15b}$$

$$Q_x = \int_A g(\sigma_{sz}x_{,s} + \sigma_{nz}y_{,s})dsdn \tag{15c}$$

$$Q_y = \int_A g(\sigma_{sz}y_{,s} - \sigma_{nz}x_{,s})dsdn \tag{15d}$$

$$M_z = \int_A 2n\sigma_{sz}dsdn \tag{15e}$$

These stress resultants are related to the displacement gradients as follows:

$$
\begin{Bmatrix} T_z \\ M_y \\ M_x \\ Q_x \\ Q_y \\ M_{ya} \\ M_{xa} \\ M_\omega \\ M_z \end{Bmatrix} =
\begin{bmatrix}
L_{11} & L_{12} & L_{13} & L_{14} & L_{15} & L_{16} & L_{17} & L_{18} & L_{19} \\
L_{12} & L_{22} & L_{23} & L_{24} & L_{25} & L_{26} & L_{27} & L_{28} & L_{29} \\
L_{13} & L_{23} & L_{33} & L_{34} & L_{35} & L_{36} & L_{37} & L_{38} & L_{39} \\
L_{14} & L_{24} & L_{34} & L_{44} & L_{45} & L_{46} & L_{47} & L_{48} & L_{49} \\
L_{15} & L_{25} & L_{35} & L_{45} & L_{55} & L_{56} & L_{57} & L_{58} & L_{59} \\
L_{16} & L_{26} & L_{36} & L_{46} & L_{56} & L_{66} & L_{67} & L_{68} & L_{69} \\
L_{17} & L_{27} & L_{37} & L_{47} & L_{57} & L_{67} & L_{77} & L_{78} & L_{79} \\
L_{18} & L_{28} & L_{38} & L_{48} & L_{58} & L_{68} & L_{78} & L_{88} & L_{89} \\
L_{19} & L_{29} & L_{39} & L_{49} & L_{59} & L_{69} & L_{79} & L_{89} & L_{99}
\end{bmatrix}
\begin{Bmatrix} w_{0,z} \\ \gamma_{xz,z}^{(0)} \\ \gamma_{yz,z}^{(0)} \\ \gamma_{xz}^{(0)} \\ \gamma_{yz}^{(0)} \\ u_{P,zz} \\ v_{P,zz} \\ \phi_{,zz} \\ \phi_{,z} \end{Bmatrix}
\tag{16}
$$

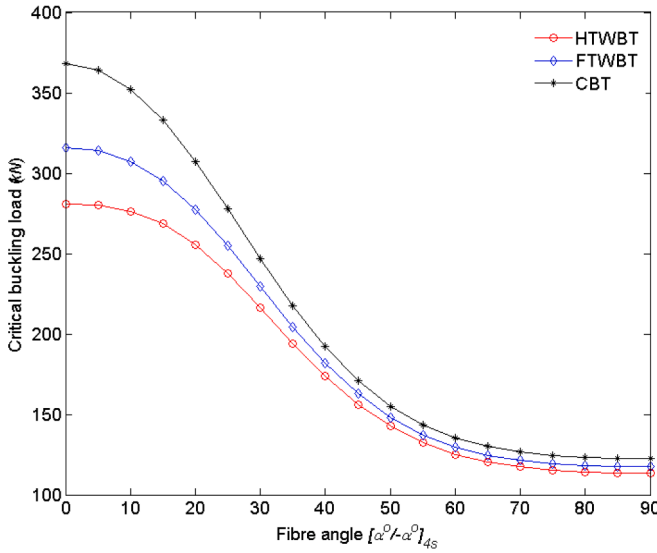where the stiffness components of the LC thin-walled beams L_{ij} $(i, j = 1, ..., 9)$ are defined by:

$$L_{11} = \int_s A_{11}ds, \quad L_{12} = \int_s (A_{11}g_0 x + E_{11}y_{,s})ds, \quad L_{13} = \int_s (A_{11}g_0 y - E_{11}x_{,s})ds$$

$$L_{14} = \int_s A_{s16}x_{,s}ds, \quad L_{15} = \int_s A_{s16}y_{,s}ds, \quad L_{16} = -\int_s (A_{11}x + B_{11}y_{,s})ds$$

$$L_{17} = \int_s (-A_{11}y + B_{11}x_{,s})ds \quad L_{18} = \int_s (-A_{11}\overline{F}_\omega + B_{11}r_{,s})ds \quad L_{19} = \int_s 2B_{16}ds$$
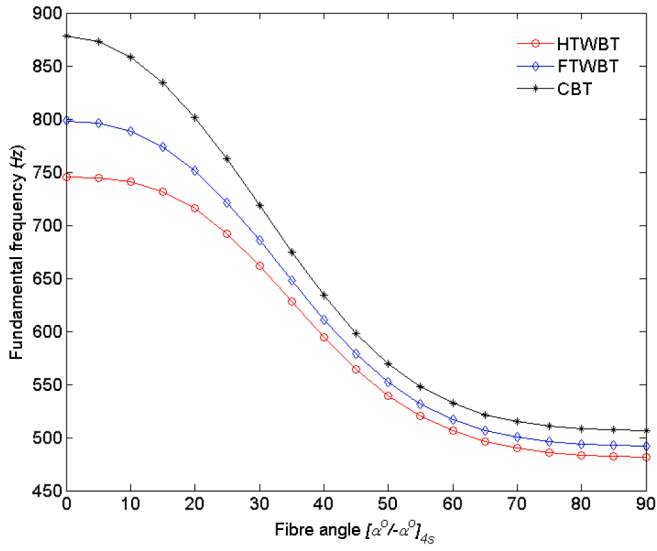
a) Fundamental frequencies

b) Critical buckling loads

Fig. 3. Variation of the fundamental frequencies (Hz) and critical buckling loads of LC thin-walled I-beam with respect to fiber angle change $[\alpha^0/-\alpha^0]_{4s}$ (CC boundary condition, $L/b_3 = 10$).

$$L_{22} = \int_s \left[g_0 x \left(A_{11} g_0 x + 2E_{11} y_{,s} \right) + H_{11} y_{,s}^2 \right] ds$$

$$L_{23} = \int_s \left[g_0 x \left(A_{11} g_0 y - E_{11} x_{,s} \right) + y_{,s} \left(E_{11} g_0 y - H_{11} x_{,s} \right) \right] ds$$

$$L_{24} = \int_s \left(A_{s16} x g_0 + D_{s16} y_{,s} \right) x_{,s} ds, L_{25} = \int_s \left(A_{s16} x g_0 + D_{s16} y_{,s} \right) y_{,s} ds$$

$$L_{26} = -\int_s \left[g_0 x \left(A_{11} x + B_{11} y_{,s} \right) + y_{,s} \left(E_{11} x + F_{11} y_{,s} \right) \right] ds$$

$$L_{27} = \int_s \left[g_0 x \left(-A_{11} y + B_{11} x_{,s} \right) + y_{,s} \left(-E_{11} y + F_{11} x_{,s} \right) \right] ds$$

$$L_{28} = \int_s g_0 x \left(-A_{11} \overline{F}_\omega + B_{11} r_s \right) + y_{,s} \left(-E_{11} \overline{F}_\omega + F_{11} r_s \right) ds$$

$$L_{29} = \int_s 2 \left(B_{16} x g_0 + F_{16} y_{,s} \right) ds$$

$$L_{33} = \int_s \left[g_0 y \left(A_{11} g_0 y - E_{11} x_{,s} \right) - x_{,s} \left(E_{11} g_0 y - H_{11} x_{,s} \right) \right] ds$$

$$L_{34} = \int_s \left(A_{s16} y g_0 - D_{s16} x_{,s} \right) x_{,s} ds, \ L_{35} = \int_s \left(A_{s16} y g_0 - D_{s16} x_{,s} \right) y_{,s} ds$$

$$L_{36} = -\int_s \left[x \left(A_{11} g_0 y - E_{11} x_{,s} \right) + y_{,s} \left(B_{11} g_0 y - F_{11} x_{,s} \right) \right] ds$$

$$L_{37} = \int_s \left[-y \left(A_{11} g_0 y - E_{11} x_{,s} \right) + x_{,s} \left(B_{11} g_0 y - F_{11} x_{,s} \right) \right] ds$$

$$L_{38} = \int_s \left[-\overline{F}_\omega \left(A_{11} g_0 y - E_{11} x_{,s} \right) + r_s \left(B_{11} g_0 y - F_{11} x_{,s} \right) \right] ds$$

$$L_{39} = \int_s 2 \left(B_{16} y g_0 - F_{16} x_{,s} \right) ds$$

$$L_{44} = \int_s \left(H_{s66} x_{,s}^2 + H_{s44} y_{,s}^2 \right) ds \ L_{45} = \int_s x_{,s} y_{,s} \left(H_{s66} - H_{s44} \right) ds$$

$$L_{46} = -\int_s \left(A_{s16} x + B_{s16} y_{,s} \right) x_{,s} ds, \ L_{47} = \int_s \left(-A_{s16} y + B_{s16} x_{,s} \right) x_{,s} ds$$

$$L_{48} = \int_s \left(-A_{s16} \overline{F}_\omega + B_{s16} r_s \right) x_{,s} ds, \ L_{49} = \int_s 2 x_{,s} B_{s66} ds$$

$$L_{55} = \int_s \left(H_{s66} y_{,s}^2 + H_{s44} x_{,s}^2 \right) ds, \ L_{56} = -\int_s \left(A_{s16} x + B_{s16} y_{,s} \right) y_{,s} ds$$

$$L_{57} = \int_s \left(-A_{s16} y + B_{s16} x_{,s} \right) y_{,s} ds, \ L_{58} = \int_s \left(-A_{s16} \overline{F}_\omega + B_{s16} r_s \right) y_{,s} ds$$

$$L_{59} = \int_s 2 y_{,s} B_{s66} ds, \ L_{66} = -\int_s \left[x \left(A_{11} x + B_{11} y_{,s} \right) + y_{,s} \left(B_{11} x + D_{11} y_{,s} \right) \right] ds$$

$$L_{67} = \int_s \left[-y \left(A_{11} x + B_{11} y_{,s} \right) + x_{,s} \left(B_{11} x + D_{11} y_{,s} \right) \right] ds$$

$$L_{68} = \int_s \left[-\overline{F}_\omega \left(A_{11} x + B_{11} y_{,s} \right) + r_s \left(B_{11} x + D_{11} y_{,s} \right) \right] ds$$

$$L_{69} = \int_s 2 \left(B_{16} x + D_{16} y_{,s} \right) ds, \ L_{77}$$
$$= \int_s \left[y \left(A_{11} y - B_{11} x_{,s} \right) + x_{,s} \left(-B_{11} y + D_{11} x_{,s} \right) \right] ds$$

$$L_{78} = \int_s \left[\overline{F}_\omega \left(A_{11} y - B_{11} x_{,s} \right) + r_s \left(-B_{11} y + D_{11} x_{,s} \right) \right] ds$$

$$L_{79} = \int_s 2 \left(-B_{16} y + D_{16} x_{,s} \right) ds$$

$$L_{88} = \int_s \left[-\overline{F}_\omega \left(-\overline{F}_\omega A_{11} + B_{11} r_s \right) + r_s \left(-B_{11} \overline{F}_\omega + D_{11} r_s \right) \right] ds$$

$$L_{89} = \int_s 2 \left(-B_{16} \overline{F}_\omega + D_{16} r_s \right) ds, \ L_{99} = \int_s 4 D_{66} ds$$

$$\left(A_{ij}, B_{ij}, D_{ij}, E_{ij}, F_{ij}, H_{ij}, B_{sij}, H_{sij} \right) = \sum_{k=1}^{nl} \left(\int_{n_k}^{n_{k+1}} \left(1, n, n^2, f, nf, f^2, ng, g^2 \right) Q_{ij} dn \right)$$

(17)

where nl is the number of layers and k is the layer index.

The variation of potential energy Π_W of the LC thin-walled beams subjected to axial compressive load N_0 can be expressed as:

Table 6

Torsional frequencies (*Hz*) of LC thin-walled I-beams with various fibre lay-up and slenderness span-to-height ratios.

Lay-up	b_3/L	Theory	ω_1	ω_2	ω_3	ω_4
$[0^o/0^o/0^o/0^o]$	0.05	Present (FTWBT)	16.24	63.22	141.08	249.51
		Present (HTWBT)	16.24	63.22	141.09	249.56
		Cortinez and Piovan (CTWBT) [42]	16.24	63.35	141.86	251.76
		Cortinez and Piovan (FTWBT) [42]	15.64	55.00	107.55	165.41
	0.10	Present (FTWBT)	63.22	249.20	552.69	966.04
		Present (HTWBT)	63.22	249.20	552.69	966.01
		Cortinez and Piovan (CTWBT) [42]	63.35	251.76	565.78	1005.4
		Cortinez and Piovan (FTWBT) [42]	55.00	165.41	284.29	401.86
	0.15	Present (FTWBT)	141.08	552.65	1207.87	2070.50
		Present (HTWBT)	141.07	552.65	1207.81	2069.76
		Cortinez and Piovan (CTWBT) [42]	141.86	565.78	1272.31	2261.46
		Cortinez and Piovan (FTWBT) [42]	107.55	284.29	459.86	631.49
$[0^o/90^o/90^o/0^o]$	0.05	Present (FTWBT)	12.20	46.54	103.44	182.69
		Present (HTWBT)	12.20	46.54	103.44	182.72
		Cortinez and Piovan (CTWBT) [42]	12.19	46.61	103.95	184.21
		Cortinez and Piovan (FTWBT) [42]	11.96	43.02	87.94	140.98
	0.10	Present (FTWBT)	46.54	182.44	404.19	706.08
		Present (HTWBT)	46.54	182.44	404.18	705.98
		Cortinez and Piovan (CTWBT) [42]	46.61	184.21	413.54	734.59
		Cortinez and Piovan (FTWBT) [42]	43.02	140.98	257.02	375.94
	0.15	Present (FTWBT)	103.43	404.18	882.88	1511.93
		Present (HTWBT)	103.43	404.17	882.91	1512.98
		Cortinez and Piovan (CTWBT) [42]	103.95	413.54	929.52	1651.89
		Cortinez and Piovan (FTWBT) [42]	87.94	257.02	435.12	610.43
$[45^o/-45^o$ $/-45^o/45^o]$	0.05	Present (FTWBT)	8.54	24.45	49.80	84.88
		Present (HTWBT)	8.54	24.45	49.80	84.82
		Cortinez and Piovan (CTWBT) [42]	10.98	28.11	54.18	89.99
		Cortinez and Piovan (FTWBT) [42]	10.96	27.98	53.61	88.35
	0.10	Present (FTWBT)	24.45	84.78	182.77	316.11
		Present (HTWBT)	24.45	84.78	182.77	316.10
		Cortinez and Piovan (CTWBT) [42]	28.11	89.99	191.65	333.74
		Cortinez and Piovan (FTWBT) [42]	27.98	88.34	184.14	311.75
	0.15	Present (FTWBT)	49.80	182.76	394.21	672.39
		Present (HTWBT)	49.80	182.76	394.20	672.38
		Cortinez and Piovan (CTWBT) [42]	54.18	191.65	419.94	739.46
		Cortinez and Piovan (FTWBT) [42]	53.61	184.14	386.03	644.07

Table 7

Critical buckling load (N) of LC cantilever I-beam with various lay-ups and span-to-height ratios.

Lay-up		$L/b_3 = 20$	$L/b_3 = 10$
$[0^o/0^o/0^o/0^o]$	Present (HTWBT)	19,144	75,403
	Present (FTWBT)	19,179	75,951
	Piovan and Cortinez (FTWBT) [43]	19,175	75,559
	COSMOS/M [43]	19,058	73,564
$[0^o/90^o/90^o/0^o]$	Present (HTWBT)	10,495	41,591
	Present (FTWBT)	10,501	41,683
	Piovan and Cortinez (FTWBT) [43]	10,561	41,861
	COSMOS/M [43]	10,350	40,698
$[45^o/-45^o/-45^o/45^o]$	Present (HTWBT)	1935	7846
	Present (FTWBT)	1935	7848
	Piovan and Cortinez (FTWBT) [43]	2003	8012
	COSMOS/M [43]	2033	7958

$$\delta\Pi_W = \int_\Omega \sigma_z^0 \left(u_{,z}\delta u_{,z} + v_{,z}\delta v_{,z}\right)d\Omega$$
$$= \int_0^L N_0\left[\delta u_{P,z}\left(u_{P,z} - J_P\phi_{,z}\right) + \delta v_{P,z}\left(v_{P,z} + I_P\phi_{,z}\right) + \delta\phi_{,z}\left(I_P v_{P,z} + K_P\phi_{,z} - J_P u_{P,z}\right)\right]dz$$

$$(18)$$

where $\sigma_z^0 = N^0/A$ is averaged axial stress; A is the cross-sectional area; (I_P, J_P, K_P) are moments of inertia of the cross-section about the centroid defined by:

$$\{I_P, J_P, K_P\} = \frac{1}{A}\int_{-h/2}^{h/2}\int_s \left\{X - x_P, Y - y_P, (Y - y_P)^2 + (X - x_P)^2\right\}dsdn$$

$$(19)$$

The variation of kinetic energy Π_K of the LC thin-walled beams is given by:

Table 8
Non-dimensional fundamental frequency of LC thin-walled I-beams with different boundary conditions and span-to-height ratios.

BC	Reference	Frequency	Lay-up						
			[0]	[15/-15]	[30/-30]	[45/-45]	[60/-60]	[75/-75]	[90/-90]
SS	Present (HTWBT)	ω_1	7.042	6.305	3.751	2.150	1.627	1.492	1.468
		ω_2	8.300	7.737	5.356	3.663	2.975	2.715	2.647
		ω_3	17.967	16.676	12.574	8.567	6.485	5.949	5.851
	Present (FTWBT)	ω_1	7.107	6.326	3.755	2.150	1.625	1.490	1.465
		ω_2	8.300	7.737	5.357	3.665	2.979	2.720	2.652
		ω_3	19.140	17.583	12.943	8.569	6.469	5.925	5.824
	Nguyen et al. [39] (FTWBT)	ω_1	7.107	6.327	3.755	2.151	1.627	1.493	1.468
		ω_2	8.189	7.528	5.137	3.610	2.967	2.713	2.645
		ω_3	19.140	17.594	12.904	8.538	6.495	5.985	5.860
CF	Present (HTWBT)	ω_1	2.536	2.255	1.338	0.767	0.580	0.532	0.523
		ω_2	3.197	3.247	2.612	1.915	1.577	1.439	1.401
		ω_3	6.886	6.327	4.642	3.778	3.565	3.323	3.268
	Present (FTWBT)	ω_1	2.547	2.259	1.339	0.766	0.580	0.532	0.523
		ω_2	3.197	3.247	2.612	1.915	1.578	1.440	1.402
		ω_3	7.123	6.502	4.708	3.814	3.596	3.318	3.263
	Nguyen et al. [39] (FTWBT)	ω_1	2.547	2.259	1.339	0.767	0.580	0.532	0.523
		ω_2	3.174	3.057	2.423	1.877	1.572	1.438	1.400
		ω_3	7.123	6.538	4.746	3.821	3.597	3.327	3.272
CC	Present (HTWBT)	ω_1	14.867	13.907	8.432	4.854	3.675	3.373	3.316
		ω_2	18.354	16.434	10.190	6.233	4.853	4.436	4.344
		ω_3	28.752	27.689	23.010	13.310	10.088	9.261	9.099
	Present (FTWBT)	ω_1	15.481	14.129	8.472	4.857	3.667	3.358	3.301
		ω_2	18.354	16.434	10.192	6.243	4.873	4.462	4.372
		ω_3	34.230	32.473	23.215	13.337	10.060	9.205	9.046
	Nguyen et al. [39] (FTWBT)	ω_1	15.480	14.129	8.474	4.865	3.682	3.378	3.322
		ω_2	17.239	16.086	10.104	6.206	4.839	4.423	4.332
		ω_3	34.221	32.379	23.221	13.368	10.121	9.285	9.131
	Vo and Lee [16] (FTWBT)	ω_1	15.460	14.122	8.471	4.862	3.678	3.374	3.319
		ω_2	17.211	16.064	10.092	6.202	4.836	4.421	4.330
		ω_3	33.996	32.174	23.209	13.392	10.147	9.308	9.152

$$\delta\Pi_K = \int_\Omega \rho(n)(\dot{u}\delta\dot{u} + \dot{v}\delta\dot{v} + \dot{w}\delta\dot{w})d\Omega$$

$$
\begin{aligned}
= \int_0^L \Bigg\{ &\delta\dot{u}_P\left(m_1\dot{u}_P - m_2\dot{\phi}\right) + \delta\dot{v}_P\left(m_1\dot{v}_P - m_3\dot{\phi}\right) + \delta\dot{\phi}\left[-m_2\dot{u}_P + (m_4 + m_5)\dot{\phi} - m_3\dot{v}_P\right] \\
&+ \delta\dot{w}_0\left(m_1\dot{w}_0 + m_{17}\dot{\gamma}_{xz}^{(0)} + m_{21}\dot{\gamma}_{yz}^{(0)} - m_6\dot{u}_{P,z} - m_{13}\dot{v}_{P,z} - m_{24}\dot{\phi}_{,z}\right) \\
&+ \delta\dot{\gamma}_{xz}^{(0)}\left(m_{17}\dot{w}_0 + m_{18}\dot{\gamma}_{xz}^{(0)} + m_{19}\dot{\gamma}_{yz}^{(0)} - m_9\dot{u}_{P,z} - m_{14}\dot{v}_{P,z} - m_{20}\dot{\phi}_{,z}\right) \\
&+ \delta\dot{\gamma}_{yz}^{(0)}\left(m_{21}\dot{w}_0 + m_{19}\dot{\gamma}_{xz}^{(0)} + m_{22}\dot{\gamma}_{yz}^{(0)} - m_{10}\dot{u}_{P,z} - m_{15}\dot{v}_{P,z} - m_{23}\dot{\phi}_{,z}\right) \\
&- \delta\dot{u}_{P,z}\left(m_6\dot{w}_0 + m_9\dot{\gamma}_{xz}^{(0)} + m_{10}\dot{\gamma}_{yz}^{(0)} - m_7\dot{u}_{P,z} - m_8\dot{v}_{P,z} - m_{11}\dot{\phi}_{,z}\right) \\
&- \delta\dot{v}_{P,z}\left(m_{12}\dot{w}_0 + m_{14}\dot{\gamma}_{xz}^{(0)} + m_{15}\dot{\gamma}_{yz}^{(0)} - m_8\dot{u}_{P,z} - m_{13}\dot{v}_{P,z} - m_{16}\dot{\phi}_{,z}\right) \\
&- \delta\dot{\phi}_{,z}\left(m_{24}\dot{w}_0 + m_{20}\dot{\gamma}_{xz}^{(0)} + m_{23}\dot{\gamma}_{yz}^{(0)} - m_{11}\dot{u}_{P,z} - m_{16}\dot{v}_{P,z} - m_{25}\dot{\phi}_{,z}\right) \Bigg\}dz
\end{aligned}
\tag{20}
$$

where the following relations have been used: $X_1 = g_0 x + f y_{,s}$, $Y_1 = g_0 y - f x_{,s}$; $F = \bar{F}_\omega - n r_s$; the dot-superscript is used to denote the differentiation with respect to the time t; $\rho(n)$ is the mass density and the inertia coefficients are given as follows:

$$\{m_1, m_2, m_3, m_4, m_5\} = \int_{-h/2}^{h/2}\int_s \rho\{1, Y - y_P, X - x_P, (Y - y_P)^2, (X - x_P)^2\}dsdn \tag{21a}$$

$$\{m_6, m_7, m_8, m_9, m_{10}, m_{11}\} = \int_{-h/2}^{h/2}\int_s \rho X\{1, X, Y, X_1, Y_1, F\}dsdn \tag{21b}$$

$$\{m_{12}, m_{13}, m_{14}, m_{15}, m_{16}\} = \int_{-h/2}^{h/2}\int_s \rho Y\{1, Y, X_1, Y_1, F\}dsdn \tag{21c}$$

$$\{m_{17}, m_{18}, m_{19}, m_{20}\} = \int_{-h/2}^{h/2}\int_s \rho X_1\{1, X_1, Y_1, F\}dsdn \tag{21d}$$

Table 9

Non-dimensional fundamental frequency of LC thin-walled I-beams with different boundary conditions and span-to-height ratios.

BC	Reference	Frequency	Lay-up						
			[0]	[15/-15]	[30/-30]	[45/-45]	[60/-60]	[75/-75]	[90/-90]
$L/b_3 = 10$									
SS	Present (HTWBT)	ω_1	6.657	6.168	3.724	2.140	1.617	1.482	1.457
		ω_2	8.091	7.257	4.510	2.764	2.157	1.974	1.934
		ω_3	13.506	12.932	10.697	8.424	6.373	5.834	5.733
	Present (FTWBT)	ω_1	6.886	6.250	3.739	2.146	1.624	1.490	1.465
		ω_2	8.091	7.257	4.510	2.762	2.152	1.967	1.926
		ω_3	15.790	14.874	11.714	8.501	6.442	5.909	5.810
CF	Present (HTWBT)	ω_1	2.466	2.232	1.333	0.765	0.578	0.530	0.521
		ω_2	2.949	2.730	1.863	1.251	1.007	0.920	0.898
		ω_3	5.756	5.418	4.244	3.552	3.373	3.274	3.218
	Present (FTWBT)	ω_1	2.508	2.246	1.336	0.766	0.579	0.531	0.523
		ω_2	2.949	2.729	1.863	1.251	1.006	0.919	0.897
		ω_3	6.382	5.923	4.470	3.681	3.483	3.305	3.250
CC	Present (HTWBT)	ω_1	12.121	12.681	8.170	4.770	3.612	3.306	3.249
		ω_2	16.777	16.158	9.676	5.638	4.302	3.944	3.874
		ω_3	18.220	16.651	15.560	12.891	9.797	8.959	8.801
	Present (FTWBT)	ω_1	13.621	13.395	8.325	4.822	3.655	3.353	3.297
		ω_2	18.220	16.158	9.674	5.628	4.280	3.916	3.845
		ω_3	21.931	21.449	19.233	13.125	9.969	9.144	8.990
$L/b_3 = 5$									
SS	Present (HTWBT)	ω_1	5.580	5.701	3.621	2.106	1.593	1.459	1.433
		ω_2	8.009	7.106	4.258	2.482	1.894	1.736	1.705
		ω_3	8.169	8.033	7.393	6.833	6.086	5.570	5.469
	Present (FTWBT)	ω_1	6.173	5.969	3.678	2.125	1.610	1.477	1.453
		ω_2	8.009	7.106	4.257	2.477	1.884	1.724	1.693
		ω_3	10.486	10.201	8.960	8.006	6.245	5.727	5.628
CF	Present (HTWBT)	ω_1	2.234	2.144	1.316	0.759	0.574	0.526	0.517
		ω_2	2.877	2.576	1.594	0.972	0.756	0.692	0.678
		ω_3	3.858	3.749	3.289	2.928	2.828	3.143	2.808
	Present (FTWBT)	ω_1	2.369	2.196	1.326	0.762	0.577	0.529	0.521
		ω_2	2.877	2.576	1.594	0.971	0.754	0.690	0.676
		ω_3	4.756	4.554	3.778	3.261	3.119	3.085	3.081
CC	Present (HTWBT)	ω_1	7.913	8.858	7.327	4.504	3.447	3.155	3.097
		ω_2	8.875	9.778	8.660	5.449	4.125	3.782	3.718
		ω_3	16.826	16.016	9.499	8.616	8.411	8.232	8.046
	Present (FTWBT)	ω_1	9.860	11.306	7.802	4.647	3.525	3.221	3.163
		ω_2	12.082	11.912	9.500	5.456	4.141	3.802	3.739
		ω_3	18.104	16.016	11.369	11.006	9.371	8.559	8.401

$$\{m_{21}, m_{22}, m_{23}, m_{24}, m_{25}\} = \int_{-h/2}^{h/2} \int_s \rho \{Y_1, Y_1^2, Y_1 F, F, F^2\} ds \, dn \tag{21e}$$

2.5. Hybrid series solution

The displacement field is approximated as follows:

$$\{u_P, v_P, \phi\}(z, t) = \sum_{j=1}^{m} \varphi_j(z) \{u_{Pj}, v_{Pj}, \phi_j\}(t) \tag{22a}$$

$$\left\{w_0, \gamma_{xz}^{(0)}, \gamma_{yz}^{(0)}\right\}(z, t) = \sum_{j=1}^{m} \varphi_{j,z}(z) \{w_j, \xi_j, \eta_j\}(t) \tag{22b}$$

where $w_j(t), u_{Pj}(t), v_{Pj}(t), \xi_j(t), \eta_j(t)$ and $\phi_j(t)$ are six unknowns to be determined; $\varphi_j(z)$ are shape functions. It is noted that the approximations in Eq. (22) are known as Ritz-type series ones whose functions of approximation should be constructed to satisfy the specified essential boundary conditions (BCs). For the present paper, shape functions are proposed in Table 1 and these functions must satisfy various BCs such as simply-supported (SS), clamped-free (CF) and clamped-clamped (CC).

Substituting Eq. (22) into Eq. (12) accounting for Eqs. (14), (18), (20), and then using Lagrange's equations lead to the characteristic equations for vibration and buckling analysis of LC thin-walled beams as follows:

$$\mathbf{K}d + \mathbf{M}\ddot{d} = \mathbf{0} \tag{23}$$

where $\mathbf{K}, \mathbf{M}$ are the stiffness and mass matrix, respectively; $d = \begin{bmatrix} \mathbf{w} & \mathbf{u} & \mathbf{v} & \boldsymbol{\xi} & \boldsymbol{\eta} & \boldsymbol{\Phi} \end{bmatrix}^T$ is the displacement vector. The components of the stiffness matrix $\mathbf{K}$ are expressed by:

$$\mathbf{K} = \begin{bmatrix} \mathbf{K}^{11} & \mathbf{K}^{12} & \mathbf{K}^{13} & \mathbf{K}^{14} & \mathbf{K}^{15} & \mathbf{K}^{16} \\ {}^T\mathbf{K}^{12} & \mathbf{K}^{22} & \mathbf{K}^{23} & \mathbf{K}^{24} & \mathbf{K}^{25} & \mathbf{K}^{26} \\ {}^T\mathbf{K}^{13} & {}^T\mathbf{K}^{23} & \mathbf{K}^{33} & \mathbf{K}^{34} & \mathbf{K}^{35} & \mathbf{K}^{36} \\ {}^T\mathbf{K}^{14} & {}^T\mathbf{K}^{24} & {}^T\mathbf{K}^{34} & \mathbf{K}^{44} & \mathbf{K}^{45} & \mathbf{K}^{46} \\ {}^T\mathbf{K}^{15} & {}^T\mathbf{K}^{25} & {}^T\mathbf{K}^{35} & {}^T\mathbf{K}^{45} & \mathbf{K}^{55} & \mathbf{K}^{56} \\ {}^T\mathbf{K}^{16} & {}^T\mathbf{K}^{26} & {}^T\mathbf{K}^{36} & {}^T\mathbf{K}^{46} & {}^T\mathbf{K}^{56} & \mathbf{K}^{66} \end{bmatrix} \tag{24}$$

where

$$K_{ij}^{11} = L_{11} S_{ij}^{22}, \quad K_{ij}^{12} = L_{16} S_{ij}^{22}, \quad K_{ij}^{13} = L_{17} S_{ij}^{22}, \quad K_{ij}^{14} = L_{12} S_{ij}^{22} + L_{14} S_{ij}^{12}$$

$$K_{ij}^{15} = L_{13} S_{ij}^{22} + L_{15} S_{ij}^{12}, \quad K_{ij}^{16} = L_{18} S_{ij}^{22} + L_{19} S_{ij}^{12}, \quad K_{ij}^{22} = L_{66} S_{ij}^{22} + N_0 S_{ij}^{11}, \quad K_{ij}^{23} = L_{67} S_{ij}^{22}$$

Table 10

Non-dimensional critical buckling load of LC thin-walled I-beams with different boundary conditions and span-to-height ratios.

BC	Reference	Lay-up						
		[0]	[15/-15]	[30/-30]	[45/-45]	[60/-60]	[75/-75]	[90/-90]
$L/b_3 = 20$								
SS	Present (HTWBT)	11.730	9.405	3.329	1.094	0.626	0.527	0.509
	Present (FTWBT)	11.948	9.469	3.336	1.095	0.626	0.527	0.510
	Nguyen et al. [39]	11.947	9.468	3.336	1.094	0.626	0.527	0.510
CF	Present (HTWBT)	3.021	2.377	0.835	0.274	0.157	0.132	0.128
	Present (FTWBT)	3.035	2.381	0.835	0.274	0.157	0.132	0.128
	Nguyen et al. [39]	3.035	2.381	0.835	0.274	0.157	0.132	0.128
CC	Present (HTWBT)	41.973	36.051	13.143	4.347	2.491	2.096	2.027
	Present (FTWBT)	44.914	37.007	13.249	4.363	2.498	2.103	2.034
	Nguyen et al. [39]	44.914	37.007	13.249	4.363	2.498	2.102	2.034
$L/b_3 = 10$								
SS	Present (HTWBT)	10.494	9.014	3.286	1.087	0.623	0.524	0.507
	Present (FTWBT)	11.230	9.253	3.313	1.091	0.625	0.526	0.508
CF	Present (HTWBT)	2.932	2.351	0.832	0.273	0.156	0.132	0.127
	Present (FTWBT)	2.987	2.367	0.834	0.274	0.157	0.132	0.127
CC	Present (HTWBT)	29.532	30.909	12.494	4.242	2.444	2.056	1.988
	Present (FTWBT)	36.203	33.915	12.889	4.306	2.473	2.080	2.012
$L/b_3 = 5$								
SS	Present (HTWBT)	7.384	7.728	3.124	1.061	0.611	0.514	0.497
	Present (FTWBT)	9.052	8.480	3.223	1.077	0.618	0.520	0.503
CF	Present (HTWBT)	2.623	2.253	0.821	0.272	0.156	0.131	0.127
	Present (FTWBT)	2.807	2.313	0.828	0.273	0.156	0.131	0.127
CC	Present (HTWBT)	13.514	17.699	10.435	3.870	2.272	1.910	1.843
	Present (FTWBT)	20.387	25.420	11.623	4.091	2.374	1.997	1.929

$$K_{ij}^{24} = L_{26}S_{ij}^{22} + L_{46}S_{ij}^{12}, \quad K_{ij}^{25} = L_{36}S_{ij}^{22} + L_{56}S_{ij}^{12}, \quad K_{ij}^{26}$$
$$= L_{68}S_{ij}^{22} + L_{69}S_{ij}^{12} - N_0 J_P S_{ij}^{11}$$

$$K_{ij}^{33} = L_{77}S_{ij}^{22} + N_0 S_{ij}^{11}, \quad K_{ij}^{34} = L_{27}S_{ij}^{22} + L_{47}S_{ij}^{12}, \quad K_{ij}^{35} = L_{37}S_{ij}^{22} + L_{57}S_{ij}^{12}$$

$$K_{ij}^{36} = L_{78}S_{ij}^{22} + L_{79}S_{ij}^{12} + N_0 I_P S_{ij}^{11}, \quad K_{ij}^{44} = L_{22}S_{ij}^{22} + L_{24}\left(S_{ij}^{12} + S_{ij}^{21}\right) + L_{44}S_{ij}^{11}$$

$$K_{ij}^{45} = L_{23}S_{ij}^{22} + L_{25}S_{ij}^{12} + L_{34}S_{ij}^{21} + L_{45}S_{ij}^{11}, \quad K_{ij}^{46}$$
$$= L_{28}S_{ij}^{22} + L_{29}S_{ij}^{12} + L_{48}S_{ij}^{21} + L_{49}S_{ij}^{11}$$

$$K_{ij}^{55} = L_{33}S_{ij}^{22} + L_{35}\left(S_{ij}^{12} + S_{ij}^{21}\right) + L_{55}S_{ij}^{11}, \quad K_{ij}^{56}$$
$$= L_{38}S_{ij}^{22} + L_{39}S_{ij}^{12} + L_{58}S_{ij}^{21} + L_{59}S_{ij}^{11}$$

$$K_{ij}^{66} = L_{88}S_{ij}^{22} + L_{89}\left(S_{ij}^{12} + S_{ij}^{21}\right) + L_{99}S_{ij}^{11} + N_0 K_P S_{ij}^{11}$$

$$S_{ij}^{rs} = \int_0^L \frac{\partial^r \varphi_i}{\partial z^r} \frac{\partial^s \varphi_j}{\partial z^s} dz \tag{25}$$

The components of mass matrix M are given by:

$$M = \begin{bmatrix} M^{11} & M^{12} & M^{13} & M^{14} & M^{15} & M^{16} \\ {}^T M^{12} & M^{22} & M^{23} & M^{24} & M^{25} & M^{26} \\ {}^T M^{13} & {}^T M^{23} & M^{33} & M^{34} & M^{35} & M^{36} \\ {}^T M^{14} & {}^T M^{24} & {}^T M^{34} & M^{44} & M^{45} & M^{46} \\ {}^T M^{15} & {}^T M^{25} & {}^T M^{35} & {}^T M^{45} & M^{55} & M^{56} \\ {}^T M^{16} & {}^T M^{26} & {}^T M^{36} & {}^T M^{46} & {}^T M^{56} & M^{66} \end{bmatrix} \tag{26}$$

where

$$M_{ij}^{11} = m_1 S_{ij}^{11}, \quad M_{ij}^{12} = -m_6 S_{ij}^{11}, \quad M_{ij}^{13} = -m_{12} S_{ij}^{11}, \quad M_{ij}^{14} = m_{17} S_{ij}^{11}, \quad M_{ij}^{15}$$
$$= m_{21} S_{ij}^{11}$$

$$M_{ij}^{16} = -m_{24} S_{ij}^{11}, \quad M_{ij}^{22} = m_7 S_{ij}^{11} + m_1 S_{ij}^{00}, \quad M_{ij}^{23} = m_8 S_{ij}^{11}, \quad M_{ij}^{24} = -m_9 S_{ij}^{11}$$

$$M_{ij}^{25} = -m_{10} S_{ij}^{11}, \quad M_{ij}^{26} = m_{11} S_{ij}^{11} - m_2 S_{ij}^{00}, \quad M_{ij}^{33} = m_{13} S_{ij}^{11} + m_1 S_{ij}^{00}$$

$$M_{ij}^{34} = -m_{14} S_{ij}^{11}, \quad M_{ij}^{35} = -m_{15} S_{ij}^{11}, \quad M_{ij}^{36} = m_{16} S_{ij}^{11} + m_3 S_{ij}^{00}, \quad M_{ij}^{44}$$
$$= m_{18} S_{ij}^{11}, \quad M_{ij}^{45} = m_{19} S_{ij}^{11}$$

$$M_{ij}^{46} = -m_{20} S_{ij}^{11}, \quad M_{ij}^{55} = m_{22} S_{ij}^{11}, \quad M_{ij}^{56} = -m_{23} S_{ij}^{11}, \quad M_{ij}^{66}$$
$$= m_{25} S_{ij}^{11} + (m_4 + m_5) S_{ij}^{00} \tag{27}$$

It is noted that the buckling responses of the LC thin-walled beams can be derived from Eq. (23) by solving $\det(\boldsymbol{K}) = \boldsymbol{0}$, whereas the free vibration behaviours are obtained by setting $\boldsymbol{d}(t) = \boldsymbol{d}e^{i\omega t}$ where ω is the natural frequency, $i^2 = -1$ the imaginary unit, and then solving the subsequent result $(\boldsymbol{K} - \omega^2 \boldsymbol{M})\boldsymbol{d} = \boldsymbol{0}$.

3. Numerical results

The vibration frequencies and critical buckling loads of the laminated thin-walled composite I-beams are presented in the following sub-sections in which the material properties of the beams are given in Table 2.

3.1. Convergence study

This section conducts convergence study of the present solution for vibration and buckling analysis of composite I-beams (MAT I, $b_1 = b_2 =$
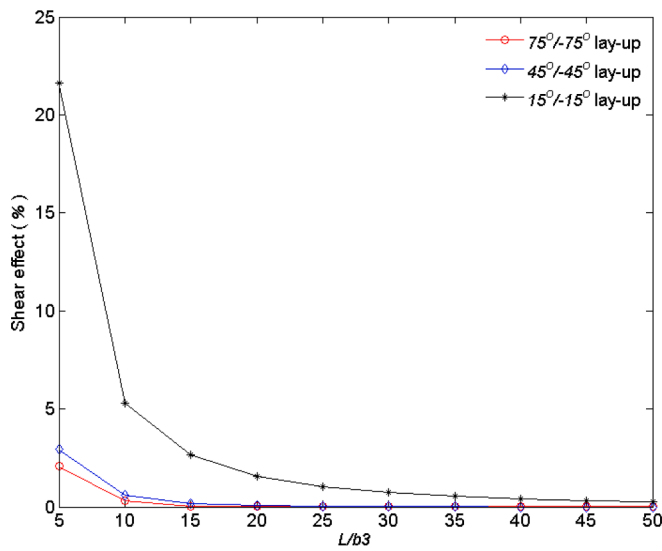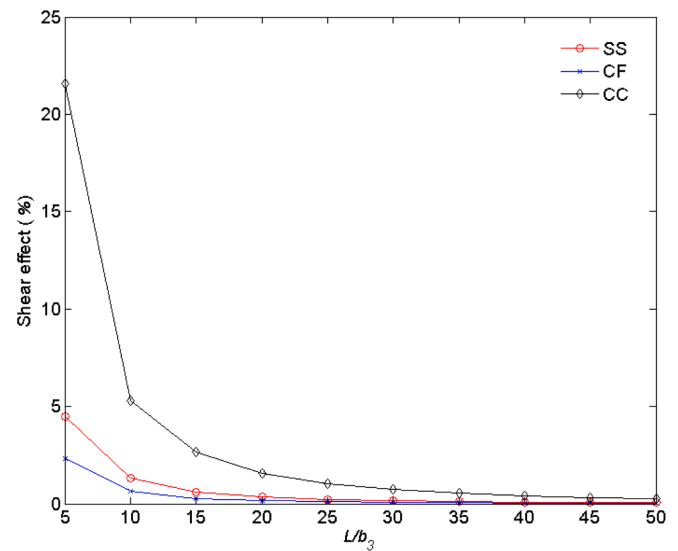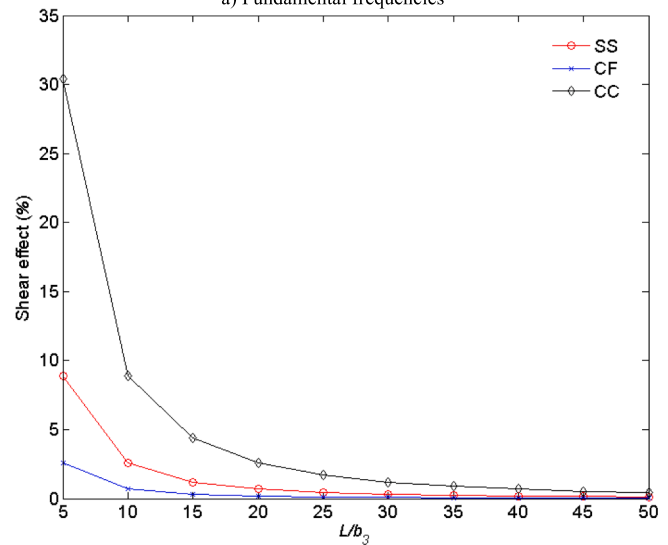
a) Fundamental frequencies
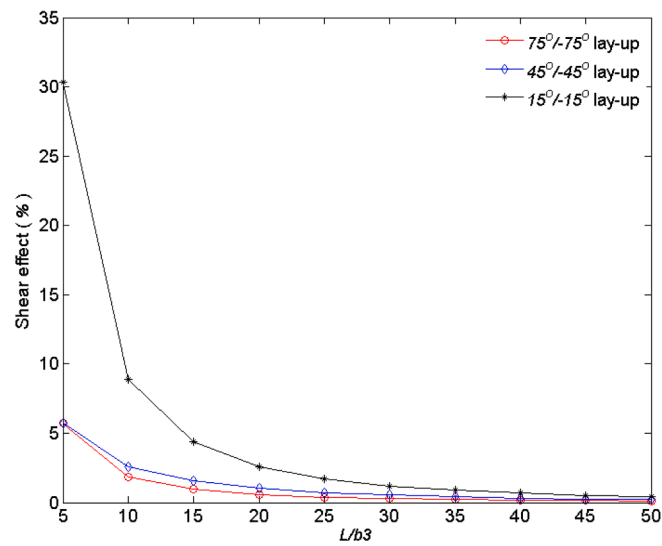
b) Critical buckling loads

Fig. 4. Shear effect (%) on the fundamental frequencies and critical buckling loads of LC thin-walled I-beam for various span-to-height ratios with lay-ups $[15^o/{-}15^o]_{4s}$, $[45^o/{-}45^o]_{4s}$ and $[75^o/{-}75^o]_{4s}$.

a) Fundamental frequencies

b) Critical buckling loads

Fig. 5. Shear effect (%) on the fundamental frequencies and critical buckling loads for various span-to-height ratios with lay-up $[15^o/{-}15^o]_{4s}$ (SS, CC, CF boundary conditions).

3.2. Verification and parametric study

Example 1: For verification purpose, composite I-beams (MAT I, $b_1 = b_2 = b_3 = 0.05$m, $h_1 = h_2 = h_3 = h = 0.00208$m) and symmetrical lay-up $[\alpha^o/-\alpha^o]_{4s}$ in both flanges and web are studied. Tables 4 and 5 show the fundamental frequencies and critical buckling loads with various BCs. It is clear that the present solutions for FTWBT are in excellent agreement with those from previous studies [16,39–41]. Due to the additional shear effect, the results from HTWBT are slightly different. These tables also present some new results for thicker beams ($L/b_3 = 5$ and 10), which can be useful for future references. Fig. 3 displays the variation of the fundamental frequencies and critical buckling loads with respect to fiber angle change for various theories. It can be observed that the results from HTWBT are slightly lower than those from FTWBT and those from CBWBT are noticeably higher than the HTWBT

$b_3 = 5 \times 10^{-2}$m, $h_1 = h_2 = h_3 = 2.08 \times 10^{-3}$m and $L = 2$ m) with various boundary conditions, namely, SS, CF and CC. For lay-up, all the flanges and web are angle-ply $[45^o/-45^o]_{4s}$ with 16 plies and uniform thickness. Their fundamental frequencies (*Hz*) and critical buckling loads (*kN*) are given in Table 3. It can be observed that the convergence speed of the buckling analysis is quicker than the vibration one. The proposed solutions converge with series number $m = 10$ for natural frequencies and $m = 6$ for buckling loads. These series numbers are therefore applied in the subsequent analyses.

a) Fundamental frequencies

b) Critical buckling loads

Fig. 6. Variation of shear effect (%) on the fundamental frequencies and critical buckling loads with respect to fiber angle change and boundary conditions ($L/b_3 = 10$).

and FTWBT in all fiber angles.

Example 2: Two composite I-beams with three different lay-ups $[0^o/0^o/0^o/0^o]$, $[0^o/90^o/90^o/0^o]$, $[45^o/-45^o/-45^o/45^o]$ in both flanges and web are considered, the first one for torsional frequencies (MAT II, $h_1 = h_2 = h_3 = h = 0.03$m, $b_1 = b_2 = b_3 = 0.6$m) and the second one for critical buckling loads (MAT III, $h_1 = h_2 = h_3 = h = 0.01$m, $b_1 = b_2 = 0.05$m, $b_3 = 0.1m$). The present solutions of torsional frequencies in Table 6 for both FTWBT and HTWBT, match with those without shear effect [42] but differ from the results accounting for the shear effect. The discrepancy in transverse shear effect in the FTWBT and HTWBT model does not have much impact on the torsional

frequencies. On the other hand, the critical buckling loads in Table 7 show good agreement with those from Piovan and Cortinez [43]. It is worth noting that the critical buckling loads from HTWBT model are slightly less than those from FTWBT in the cases of $[0^o/0^o/0^o/0^o]$ and $[0^o/90^o/90^o/0^o]$ lay-ups but are almost the same for $[45^o/-45^o/-45^o/45^o]$.

Example 3: This example further confirms the accuracy of the present solution and investigates the effects of additional shear deformation with respect to fiber angle change. Tables 8-10 present the first three natural frequencies and critical buckling loads of composite I-beams (MAT IV, $h_1 = h_2 = h_3 = h = 0.01$m, $b_1 = b_2 = 0.2$m, $b_3 = 0.3$m) with angle-ply lay-up $[\alpha^o/-\alpha^o]$ in both flanges and unidirectional in the web. The following non-dimensional terms are used: $\overline{\omega} = \frac{\omega L^2}{b_3}\sqrt{\frac{\rho}{E_2}}$ and $\overline{N}_{cr} = N_{cr}\frac{L^2}{E_2 h b_3^3}$. Again, the present results for both HTWBT and FTWBT are in excellent match with those from Nguyen et al. [39] and Vo and Lee [16]. Some new results for thick beams $L/b_3 = 5$ and 10 are also given for future benchmark.

The additional shear effect of HTWBT when compared to FTWBT for fundamental frequencies and buckling loads is investigated. The shear effect percentage is defined as $S.E(\%) = \frac{\overline{\omega}_{FTWBT} - \overline{\omega}_{HTWBT}}{\overline{\omega}_{FTWBT}} \times 100\%$ or $S.E(\%) = \frac{\overline{N}_{cr-FTWBT} - \overline{N}_{cr-HTWBT}}{\overline{N}_{cr-FTWBT}} \times 100\%$. As expected, the shear effect is particularly significant for thick beam where L/b_3 is small in Figs. 4 and 5. For lay-up $[15^o/-15^o]$ and $L/b_3 = 5$, the maximum shear effect on the critical buckling load of CC beams is 30%, which is higher than that of fundamental frequency (21%). The increase in the fiber angle drastically reduces the shear effect from more than 18% for unidirectional lay-up $[0^o/0^o]$ to 2% one with lay-up with fiber angle greater than 60^o(Fig. 6b). The shear effect of CC beams is much higher than that of SS and CF ones even though these differences become lower as the L/b_3 ratio and the fiber angle increases (Figs. 5 and 6).

Figs. 7-9 present the first three vibration mode shapes, which are plotted from the FTWBT and HTWBT, of CC beam with lay-up $[45^o/-45^o]$. There is no visible difference in Fig. 8 between two models as expected since the beam is in torsion mode and the transverse shear strain γ_{xz}^0 and γ_{yz}^0 are zero along the beam length. This explains the torsional frequencies of two models in Table 6 are almost identical. Nonetheless, the transverse shear strains γ_{xz}^0 and γ_{yz}^0 in Figs. 7 and 9 are different and more apparent at the beam ends.

4. Conclusions

A general higher-order shear deformation theory for thin-walled composite I-beams is proposed in this paper. Theoretical formulation is derived in the general form which can recover the previous conventional theories. A hybrid series solution is developed to solve equations of motion for various theories including CTWBT, FTWBT and HTWBT of thin-walled composite I-beams with different boundary conditions. Numerical examples are performed to investigate the effects of lay-ups, fiber angle and shear deformation on the natural frequencies and critical buckling loads of the thin-walled I-section beams. Some new results for thick-beams are provided for future reference. Due to the additional shear effects, the results from the HTWBT are slightly lower than those from the CTWBT and FTWBT. They become particularly significant for low span-to-high ratio and small fiber angle of angle-ply lay-up. The present model has proved to be reliable in analysing laminated composite thin-walled beams.
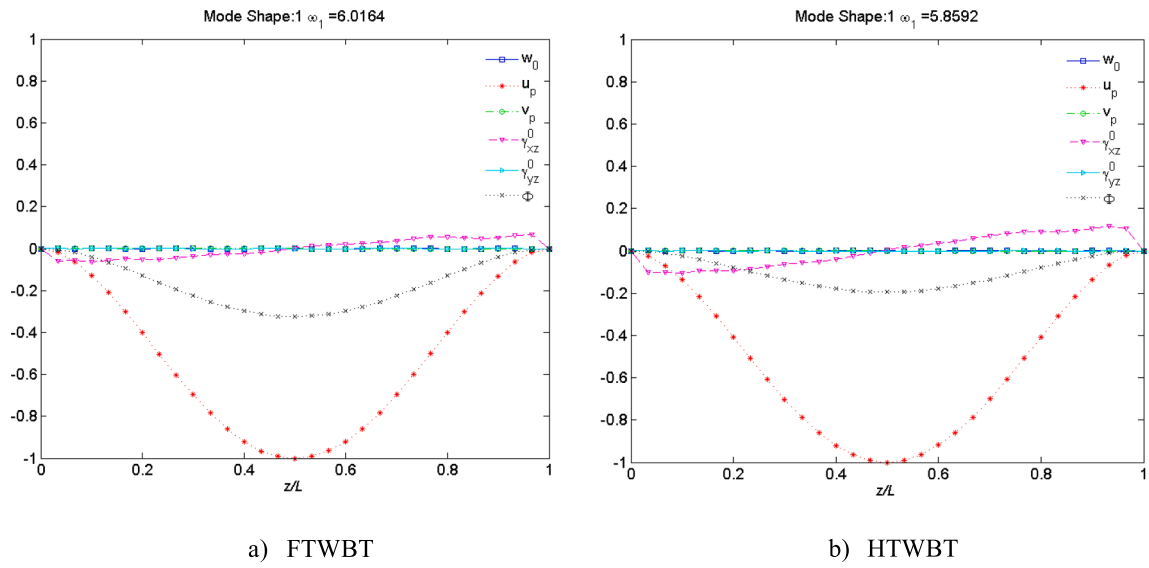
a) FTWBT

b) HTWBT

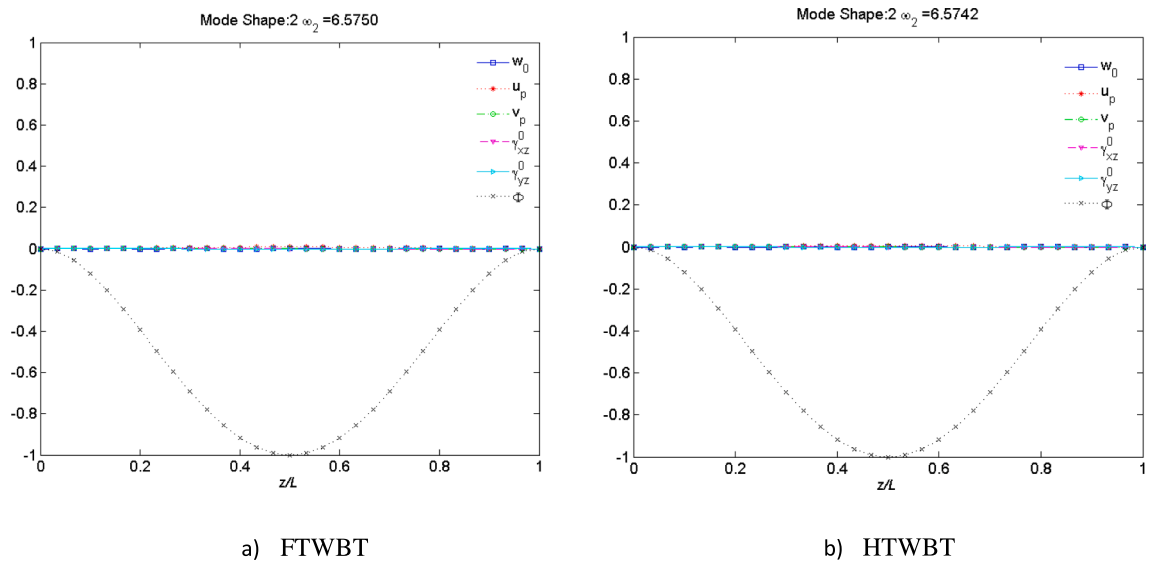**Fig. 7.** The first mode shape of LC thin-walled I-beams with lay-up $[45^0/\!-\!45^0]$.

a) FTWBT

b) HTWBT

Fig. 8. Second mode shape of LC thin-walled I-beams with lay-up $[45^0/\!-\!45^0]$.
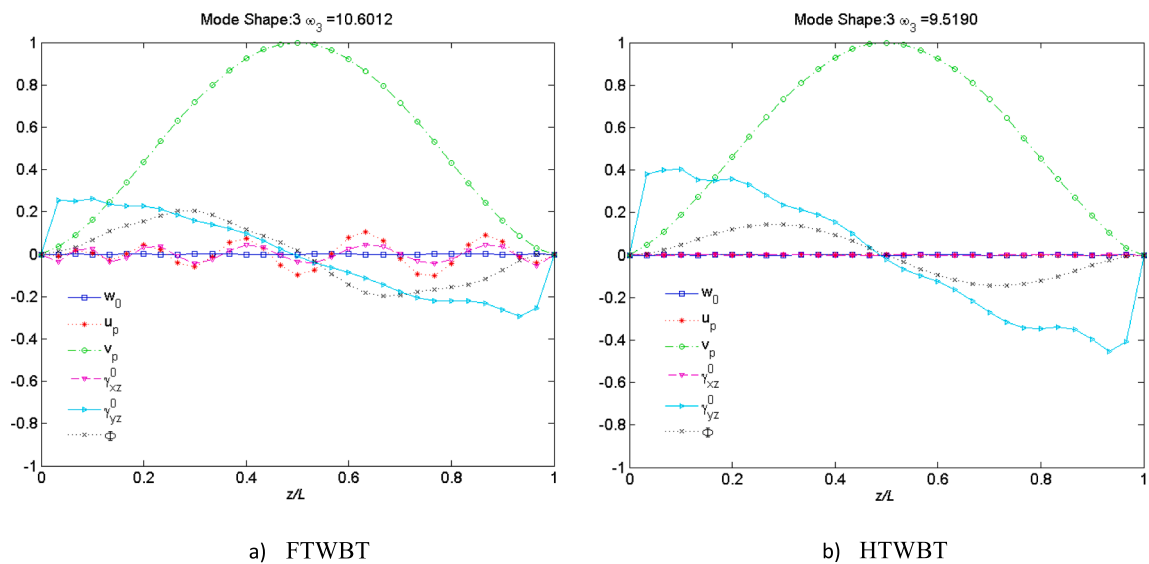

a) FTWBT

b) HTWBT

Fig. 9. Third mode shape of LC thin-walled I-beams with lay-up $[45^0/\!-\!45^0]$.

CRediT authorship contribution statement

Xuan-Bach Bui: Methodology, Software, Validation. **Trung-Kien Nguyen:** Conceptualization, Methodology, Writing – review & editing. **Ngoc-Duong Nguyen:** Writing – review & editing. **Thuc P. Vo:** Writing – review & editing.

Declaration of Competing Interest

The authors declare that they have no known competing financial interests or personal relationships that could have appeared to influence the work reported in this paper.

References

[1] Bauchau OA, Craig JI. Structural Analysis: With Applications to Aerospace Structures. Netherlands: Springer; 2009.

[2] Megson THG. Aircraft Structures for Engineering Students. Seventh Edition ed. 2021, United Kingdom: Butterworth-Heinemann. 649.

[3] Eken S. Free vibration analysis of composite aircraft wings modeled as thin-walled beams with NACA airfoil sections. Thin-Walled Structures 2019;139:362–71. https://doi.org/10.1016/j.tws.2019.01.042.

[4] Mittelstedt C. Buckling and Post-Buckling of Thin-Walled Composite Laminated Beams—A Review of Engineering Analysis Methods. Appl Mech Rev 2019;72. https://doi.org/10.1115/1.4045680.

[5] Piovan MT, Ramirez JM, Sampaio R. Dynamics of thin-walled composite beams: Analysis of parametric uncertainties. Compos Struct 2013;105:14–28. https://doi.org/10.1016/j.compstruct.2013.04.039.

[6] Bauld NR, Lih-Shyng T. A Vlasov theory for fiber-reinforced beams with thin-walled open cross sections. Int J Solids Struct 1984;20(3):277–97. https://doi.org/10.1016/0020-7683(84)90039-8.

[7] Pandey MD, Kabir MZ, Sherbourne AN. Flexural-torsional stability of thin-walled composite I-section beams. Compos Eng 1995;5(3):321–42. https://doi.org/10.1016/0961-9526(94)00101-E.

[8] Lee J, Kim S-E. Free vibration of thin-walled composite beams with I-shaped cross-sections. Compos Struct 2002;55(2):205–15. https://doi.org/10.1016/S0263-8223(01)00150-7.

[9] Lee J, Kim S-E. Flexural–torsional buckling of thin-walled I-section composites. Comput Struct 2001;79(10):987–95. https://doi.org/10.1016/S0045-7949(00)00195-4.

[10] Latalski J, Zulli D. Generalized Beam Theory for Thin-Walled Beams with Curvilinear Open Cross-Sections. Appl Sci 2020;10(21):7802. https://doi.org/10.3390/app10217802.

[11] Yu W, Hodges D, Volovoi V, Fuchs E. A generalized Vlasov theory of composite beams. Thin-Walled Structures 2005;43:1493–511. https://doi.org/10.1016/j.tws.2005.02.003.

[12] Maddur SS, Chaturvedi SK. Laminated composite open profile sections: non-uniform torsion of I-sections. Compos Struct 2000;50(2):159–69. https://doi.org/10.1016/S0263-8223(00)00093-3.

[13] Maddur SS, Chaturvedi SK. Laminated composite open profile sections: first order shear deformation theory. Compos Struct 1999;45(2):105–14. https://doi.org/10.1016/S0263-8223(99)00005-7.

[14] Lee J. Flexural analysis of thin-walled composite beams using shear-deformable beam theory. Compos Struct 2005;70(2):212–22. https://doi.org/10.1016/j.compstruct.2004.08.023.

[15] Qin Z, Librescu L. On a shear-deformable theory of anisotropic thin-walled beams: further contribution and validations. Compos Struct 2002;56(4):345–58. https://doi.org/10.1016/S0263-8223(02)00019-3.

[16] Vo TP, Lee J. Flexural–torsional coupled vibration and buckling of thin-walled open section composite beams using shear-deformable beam theory. Int J Mech Sci 2009;51(9–10):631–41. https://doi.org/10.1016/j.ijmecsci.2009.05.001.

[17] Lee J. Center of gravity and shear center of thin-walled open-section composite beams. Compos Struct 2001;52(2):255–60. https://doi.org/10.1016/S0263-8223(00)00177-X.

[18] Jung SN, Lee J-Y. Closed-form analysis of thin-walled composite I-beams considering non-classical effects. Compos Struct 2003;60(1):9–17. https://doi.org/10.1016/S0263-8223(02)00318-5.

[19] Kim N-I, Shin DK. Coupled deflection analysis of thin-walled Timoshenko laminated composite beams. Comput Mech 2009;43(4):493–514. https://doi.org/10.1007/s00466-008-0324-9.

[20] Wu L, Mohareb M. Finite element formulation for shear deformable thin-walled beams. Can J Civ Eng 2011;38(4):383–92. https://doi.org/10.1139/l11-007.

[21] Carrera E, Miglioretti F, Petrolo M. Accuracy of refined finite elements for laminated plate analysis. Compos Struct 2011;93(5):1311–27. https://doi.org/10.1016/j.compstruct.2010.11.007.

[22] Fazzolari FA, Carrera E. Refined hierarchical kinematics quasi-3D Ritz models for free vibration analysis of doubly curved FGM shells and sandwich shells with FGM core. J Sound Vib 2014;333(5):1485–508. https://doi.org/10.1016/j.jsv.2013.10.030.

[23] Carrera E. Transverse Normal Stress Effects in Multilayered Plates. J Appl Mech 1999;66(4):1004–12. https://doi.org/10.1115/1.2791769.

[24] Robaldo A, Carrera E, Benjeddou A. A Unified Formulation for finite element analysis of piezoelectric plates. Computers & Structures - COMPUT STRUCT 2006;84:1494–505. https://doi.org/10.1016/j.compstruc.2006.01.029.

[25] Cinefra M, Carrera E, Brischetto S, Belouettar S. ThermoMechanical Analysis Of Functionally Graded Shells. Journal of Thermal Stresses - J THERMAL STRESSES 2010;33(10):942–63. https://doi.org/10.1080/01495739.2010.482379.

[26] Fazzolari FA, Carrera E. Thermal Stability of FGM Sandwich Plates Under Various Through-the-Thickness Temperature Distributions. J Therm Stresses 2014;37(12):1449–81. https://doi.org/10.1080/01495739.2014.937251.

[27] Pagani A, Carrera E, Boscolo M, Banerjee JR. Refined dynamic stiffness elements applied to free vibration analysis of generally laminated composite beams with arbitrary boundary conditions. Compos Struct 2014;110:305–16. https://doi.org/10.1016/j.compstruct.2013.12.010.

[28] Carrera E, Kröplin B. ZIGZAG AND INTERLAMINAR EQUILIBRIA EFFECTS IN LARGE-DEFLECTION AND POSTBUCKLING ANALYSIS OF MULTILAYERED PLATES. Mech Compos Mater Struct 1997;4(1):69–94.

[29] Khalili SMR, Botshekanan Dehkordi M, Carrera E, Shariyat M. Non-linear dynamic analysis of a sandwich beam with pseudoelastic SMA hybrid composite faces based on higher order finite element theory. Compos Struct 2013;96:243–55. https://doi.org/10.1016/j.compstruct.2012.08.020.

[30] Carrera E, Filippi M, Zappino E. Free vibration analysis of rotating composite blades via Carrera Unified Formulation. Compos Struct 2013;106:317–25. https://doi.org/10.1016/j.compstruct.2013.05.055.

[31] Pagani A, de Miguel AG, Petrolo M, Carrera E. Analysis of laminated beams via Unified Formulation and Legendre polynomial expansions. Compos Struct 2016;156:78–92. https://doi.org/10.1016/j.compstruct.2016.01.095.

[32] Carrera E, Petrolo M, Zappino E. Performance of CUF Approach to Analyze the Structural Behavior of Slender Bodies. J Struct Eng 2012;138(2):285–97. https://doi.org/10.1061/(ASCE)ST.1943-541X.0000402.

[33] Carrera E, Boscolo M, Robaldo A. Hierarchic Multilayered Plate Elements for Coupled Multifield Problems of Piezoelectric Adaptive Structures: Formulation and Numerical Assessment. Arch Comput Methods Eng 2007;14(4):383–430. https://doi.org/10.1007/s11831-007-9012-8.

[34] Carrera E, Pagani A, Petrolo M. Classical, Refined, and Component-Wise Analysis of Reinforced-Shell Wing Structures. AIAA Journal 2013;51(5):1255–68. https://doi.org/10.2514/1.J052331.

[35] Carrera E. Temperature Profile Influence on Layered Plates Response Considering Classical and Advanced Theories. Aiaa Journal - AIAA J 2002;40(9):1885–96. https://doi.org/10.2514/2.1868.

[36] Chandiramani NK, Librescu L, Shete CD. On the free-vibration of rotating composite beams using a higher-order shear formulation. Aerosp Sci Technol 2002;6(8):545–61. https://doi.org/10.1016/S1270-9638(02)01195-1.

[37] Bhaskar K, Librescu L. A geometrically non-linear theory for laminated anisotropic thin-walled beams. Int J Eng Sci 1995;33(9):1331–44. https://doi.org/10.1016/0020-7225(94)00118-4.

[38] Reddy JN. Mechanics of Laminated Composite Plates and Shells. 2nd ed. Boca Raton: CRC Press; 2003.

[39] Nguyen N-D, Nguyen T-K, Vo TP, Nguyen T-N, Lee S. Vibration and buckling behaviours of thin-walled composite and functionally graded sandwich I-beams. Compos B Eng 2019;166:414–27. https://doi.org/10.1016/j.compositesb.2019.02.033.

[40] Kim N-I, Shin DK, Park Y-S. Dynamic stiffness matrix of thin-walled composite I-beam with symmetric and arbitrary laminations. J Sound Vib 2008;318(1–2):364–88. https://doi.org/10.1016/j.jsv.2008.04.006.

[41] Kim N-I, Lee J. Exact solutions for stability and free vibration of thin-walled Timoshenko laminated beams under variable forces. Arch Appl Mech 2014;84(12):1785–809. https://doi.org/10.1007/s00419-014-0886-2.

[42] Cortínez VH, Piovan MT. VIBRATION AND BUCKLING OF COMPOSITE THIN-WALLED BEAMS WITH SHEAR DEFORMABILITY. J Sound Vib 2002;258(4):701–23. https://doi.org/10.1006/jsvi.2002.5146.

[43] Piovan MT, Cortínez VH. Mechanics of shear deformable thin-walled beams made of composite materials. Thin-Walled Structures 2007;45(1):37–62. https://doi.org/10.1016/j.tws.2006.12.001.

[44] Kim N-I, Shin DK, Kim M-Y. Flexural–torsional buckling loads for spatially coupled stability analysis of thin-walled composite columns. Adv Eng Softw 2008;39(12):949–61. https://doi.org/10.1016/j.advengsoft.2008.03.001.

Taylor & Francis
Taylor & Francis Group

Stochastic vibration and buckling analysis of functionally graded sandwich thin-walled beams

Xuan-Bach Bui, Trung-Kien Nguyen & Phong T. T. Nguyen

Published online: 12 Jan 2023.

Submit your article to this journal

View related articles

View Crossmark data

Taylor & Francis
Taylor & Francis Group

Check for updates

Stochastic vibration and buckling analysis of functionally graded sandwich thin-walled beams

Xuan-Bach Bui[a], Trung-Kien Nguyen[b], and Phong T. T. Nguyen[c]

aFaculty of Civil Engineering, Ho Chi Minh City University of Technology and Education, Ho Chi Minh City, Viet Nam; bCIRTech Institute, HUTECH University, Ho Chi Minh City, Viet Nam; cFaculty of International Education, Ho Chi Minh City University of Technology and Education, Ho Chi Minh City, Viet Nam

ABSTRACT

Stochastic vibration and buckling analysis of functionally graded sandwich thin-walled beams with I-section based on the first-order shear deformation theory is for the first time proposed in this paper. The material properties of beams in both web and two flanges are assumed to be continuously varied in its thickness. Additionally, the constituent material properties are randomly changed according to the lognormal distributions. These stochastic variabilities are then propagated to the stochastic responses of the thin-walled beam through a beam solver with hybrid series-type approximation functions. To achieve efficient evaluations for stochastic responses including natural frequencies and critical buckling loads, polynomial chaos expansion (PCE) based surrogate model is developed. The efficiency and accuracy of PCE's results are assessed by comparing with those of crude Monte Carlo simulation. Sensitivity analysis is carried out to compare the importance of the uncertainty in material properties to stochastic responses. New results reported in this paper can be interesting benchmarks for scientific and engineering community in the future.

1. Introduction

Owing to the continuous variation of material constituents, functionally graded materials (FGMs) present many advantages in comparison with multi-layered laminated composite materials. Many researches have been performed in predicting static and dynamic responses of functionally graded (FG) beams and plates with different theories and computational methods, only some representative references are herein cited (Jalaei, Thai, and Civalek 2022, Chaikittiratana and Wattanasakulpong 2022, Madrahalli Chidanandamurthy et al. 2021, Civalek and Kiracioglu 2010, Ebrahimi, Barati, and Civalek 2020, Demir et al. 2018). Moreover, it is known that the thin-walled beam is a slender structural element whose thickness is small compared with the cross-sectional dimensions, while its length greatly exceeds the dimensions of its cross-section. Thanks to its high efficiency in strength-to-weight ratio, the thin-walled beams with open and closed sections have been widely applied in aerospace, helicopter and turbomachinery rotor blades, civil, mechanical and naval engineerings, etc (Librescu and Song 2006). The application of the FGMs for thin-walled beams will hence promise important uses in different engineering fields. In order to study behaviors of the thin-walled beams, Vlasov's classical thin-walled beam theory (CTWBT), first-order shear deformation thin-walled beam theory (FTWBT) and higher-order shear deformation thin-walled beam theory (HTWBT)

CONTACT Trung-Kien Nguyen ✉ ntkien@hutech.edu.vn 🏢 CIRTech Institute, HUTECH University, 475A Dien Bien Phu Street, Binh Thanh District, Ho Chi Minh City, Viet Nam.
Communicated by Babak Safaei.

have been considered. The CTWBT initiated by Vlasov (1961) is mostly used thanks to its simplicity. Based on this approach and the finite element method (FEM), Nguyen and Lee (2018) investigated effects of bi-directional FGM distribution in web and flanges of I- and channel-sections on deflections of FG thin-walled beams. Moreover, the effects of continuous variations of FGMs on vibration, nonlinear buckling responses, center of gravity and shear center of FG thin-walled beams with I- and channel-sections have been studied by Lanc et al. (2016), Nguyen, Kim, and Lee (2016a) and (Nguyen, Kim, and Lee 2016b) respectively. Although the CTWBT is commonly applied for the analysis of FG thin-walled beams, this theory neglects the effects of transverse shear strains and therefore, it underestimates the deflection and overestimates the frequencies as well as the critical buckling loads. In order to overcome the disadvantages of the CTWBT, the FTWBT with linear variation of the displacement in the section accounts for the effects of transverse shear strains and thus predicts more accurate than the CTWBT. Based on the FTWBT and FEM, Kim and Lee (2018, 2017) studied static, buckling and vibration behaviors of FG sandwich thin-walled beams with I-section. Based on the FTWBT and Ritz method, several authors (Nguyen et al. 2019, Nguyen, Vo, et al. 2020, Nguyen, Vo, et al. 2020) examined static, vibration and buckling behaviors of thin-walled FG sandwich beams with channel- and I-section, respectively. Oh, Librescu, and Song (2003) studied vibration behaviors of FG thin-walled box beams in a thermal environment. Although the FTWBT provides more accurate results than the CTWBT, it requires a shear factor to correct the traction-free boundary conditions. In order to overcome this problem, the HTWBT (Bui et al. 2022, Chandiramani, Librescu, and Shete 2002) can be used by supposing a nonlinear variation of the transverse shear strains in the wall thickness. However practically, this approach appears to be complicated for implementation.

Furthermore, the component materials' properties can inadvertently vary due to their manufacturing process or other unforeseen factors. This leads to the change in static and dynamic behaviors of the structures, and therefore calls for the field of uncertainty quantification or stochastic analysis. In order to investigate stochastic static and dynamic behaviors of structures with uncertainties in material properties, the most straightforward and intuitive method is the Monte Carlo Simulation method (MCS) which simply runs the computational model as many times as the accuracy required. Nonetheless, when the physical model is complicated, the MCS demands too much computing time and is infeasible to obtain desired sample outputs. The MCS has been used with different level of success for analysis of laminated composite structures (Nguyen et al. 2017, Grover et al. 2017, Li et al. 2016, Naskar et al. 2017, Sasikumar, Suresh, and Gupta 2014, Mishra, Kumar, and Topal 2020). However, as the studied system becomes more computationally exhausting, the MCS fail to deliver a quick result for a high number of simulations. To overcome this drawback, stochastic numerical methods based on polynomial chaos expansion (PCE) that requires the fewer input samples but still produces accurate outputs have attracted considerable attention (Stefanou 2009). Various numerical methods have been proposed to address this issue, among which the polynomial chaos expansion (PCE) has attracted considerable attention for composite plates (Peng et al. 2019, Carvalho et al. 2017, Umesh and Ganguli 2013, Chandra et al. 2019, Chakraborty et al. 2016, Parviz and Fakoor 2021) and beam structures (Mukherjee, Gopalakrishnan, and Ganguli 2019, Sharma, Mukherjee, and Ganguli 2022) lately. The key idea of this approach is to approximate the stochastic outputs as an orthogonal series including the basis functions and their corresponding coefficients. A small number of simulation runs is needed to compute these PCE coefficients and the substitution of the random input variables into the series is computationally inexpensive. Therefore, the stochastic output can be computed easily as many times as needed. Importantly, the PCE method reduces the computational cost significantly while maintaining the accuracy of the stochastic model output. A brief literature review shows that although a numer of researches have been performed to examine behaviors of FG thin-walled beams, stochastic responses of these structures with the uncertainty of material properties are extremely limited, this gap needs to be studied further.

The objective of this paper is to develop a stochastic model for free vibration and buckling analysis of FG sandwich thin-walled I-beams by using the PCE with spectral projection approach. The governing equations of motion are derived by using Hamilton's principle and then a new hybrid series solution is developed for FG sandwich thin-walled beams with different boundary conditions. The Monte Carlo simulation method with one hundred thousand samples is considered as the exact results and used to investigate the performance of the proposed model. The outputs for the deterministic system with mean material properties are also computed and verified with the earlier FG thin-walled models. A parametric study is performed to investigate the effects of material distribution and material uncertainty parameters on natural frequencies and critical buckling loads of the FG sandwich thin-walled beams.

2. Theoretical formulation

Consider a FG sandwich thin-walled beam with length L and section I. Three sets of coordinate systems are introduced in Figure 1. They are the Cartesian coordinate system (x_1, x_2, x_3), the local plate coordinate system (n, s, x_3) and the contour coordinate s along the profile of the section. θ is an angle of orientation between (n, s, x_3) and (x_1, x_2, x_3) coordinate systems. The pole P with coordinates (x_1^P, x_2^P) is considered as the shear center of the section. For simplicity purpose, the following assumptions are made: the strains are small and the section contour does not deform in its own plane, the shear and warping shear strains are uniform over the section, local buckling and pre-buckling deformation are negligible.

2.1. Kinematics, strains and stresses

The mid-surface displacements $u_0(s, x_3)$ and $v_0(s, x_3)$ at any points in the contour coordinate system under a rotation ϕ about the pole axis can be expressed in terms of those at the pole $\xi(x_3)$ and $\eta(x_3)$ in x_1- and x_2- directions, respectively, as follows:
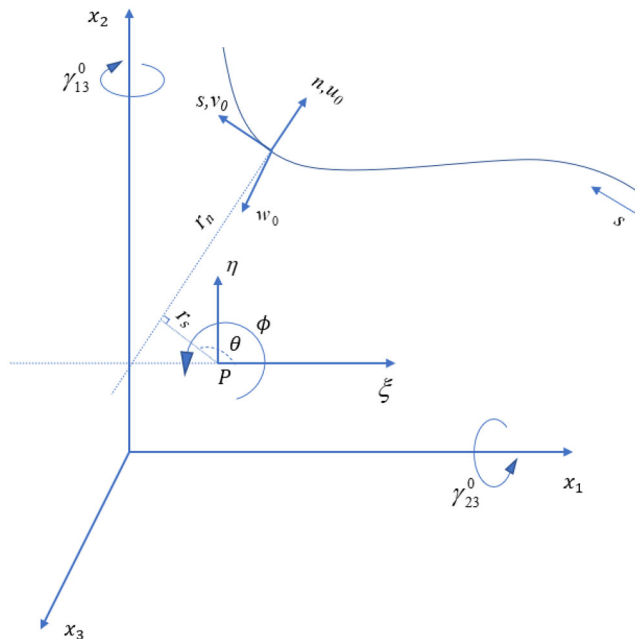

Figure 1. Thin-walled coordinate systems.

$$u_0(s, x_3) = \xi(x_3) \sin \theta(s) - \eta(x_3) \cos \theta(s) - \phi(x_3) r_s(s) \tag{1a}$$

$$v_0(s, x_3) = \xi(x_3) \cos \theta(s) + \eta(x_3) \sin \theta(s) + \phi(x_3) r_n(s) \tag{1b}$$

where $r_s(x_3), r_n(x_3)$ are the lengths of the perpendiculars from P to the tangent and normal of the profile line at the considered point. It is observed from Eq. (1) that the displacements at any points of the contour depend on those of the pole point and its length to the pole point.

Moreover, the mid-surface shear strains in the contour can be written in terms of the transverse strains $\gamma_{13}^0, \gamma_{23}^0$ and warping one γ_ϖ^0 as follows:

$$\gamma_{n3}^0(s, x_3) = u_{0,3} + w_{0,n}$$
$$= \gamma_{13}^0(x_3) \sin \theta(s) - \gamma_{23}^0(x_3) \cos \theta(s) - \gamma_\varpi^0(x_3) r_s(s) \tag{2a}$$

$$\gamma_{s3}^0(s, x_3) = \gamma_{13}^0(x_3) \cos \theta(s) + \gamma_{23}^0(v) \sin \theta(s) + \gamma_\varpi^0(x_3) r_n(s)$$
$$= v_{0,3} + w_{0,s} \tag{2b}$$

where the comma in the subscript is used to indicate the differentiation with respect to the variable that follows. Moreover, substituting Eq. (1b) into Eq. (2b) and then integrating the subsequent result with respect to s lead to:

$$w_0(s, x_3) = \zeta(x_3) + \psi_2(x_3) x_1(s) + \psi_1(x_3) x_2(s) + \psi_\varpi(x_3) \varpi(s) \tag{3}$$

where $\zeta(x_3)$ is the displacement of P in the x_3- direction; ψ_1, ψ_2 and ψ_ϖ represent rotations of the cross-section with respect to x_1, x_2; ϖ is warping function.

$$\psi_2 = \gamma_{13}^0 - \xi_{,3} \tag{4a}$$

$$\psi_1 = \gamma_{23}^0 - \eta_{,3} \tag{4b}$$

$$\psi_\varpi = \gamma_\varpi^0 - \phi_{,3} \tag{4c}$$

$$\varpi(s) = \int_{s_0}^s r_n(s) ds \tag{4d}$$

It is worth noticing that the Vlasov's classical thin-walled beam can be found by setting $\gamma_{13}^0 = 0, \gamma_{23}^0 = 0, \gamma_\varpi^0 = 0$. For the present beam based on the first-order shear deformation theory, the displacements (u, v, w) at any points on the section can be expressed linearly in terms of the mid-surface displacements (u_0, v_0, w_0) as follows:

$$u(n, s, x_3) = u_0(s, x_3) \tag{5a}$$

$$v(n, s, x_3) = v_0(s, x_3) + n\psi_s^0(s, x_3) \tag{5b}$$

$$w(n, s, x_3) = w_0(s, x_3) + n\psi_3^0(s, x_3) \tag{5c}$$

where ψ_s^0 and ψ_3^0 are rotations of a transverse normal about x_3- and $s-$ axis, respectively; ψ_3^0 can be derived from the balance of the shear strain γ_{n3}^0 from Eq. (2a) and Eqs. (5) as follows:

$$\psi_3^0 = \psi_2 \sin \theta - \psi_1 \cos \theta - \psi_\varpi r_s \tag{6}$$

whereas ψ_s^0 can be determined from the restraint $\gamma_{sn} = 0$:

$$\psi_s^0(s, x_3) = -u_{,s}^0 \tag{7}$$

The non-zero strains related to the displacements in Eq. (5) are given by:

$$\varepsilon_{33} = w_{,3} = \zeta_{,3} + (x_1 + n \sin \theta)\psi_{2,3} + (x_2 - n \cos \theta)\psi_{1,3} + (\varpi - n r_s)\psi_{\varpi,3} \tag{8a}$$

$$\gamma_{s3} = v_{,3} + w_{,s} = (\xi_{,3} + \psi_2) \cos\theta + (\eta_{,3} + \psi_1) \sin\theta + (\phi_{,3} + \psi_\varpi) r_n + n(\phi_{,3} - \psi_\varpi) \tag{8b}$$

$$\gamma_{n3} = u_{,3} + w_{,n} = (\xi_{,3} + \psi_2) \sin\theta - (\eta_{,3} + \psi_1) \cos\theta - (\phi_{,3} + \psi_\varpi) r_s \tag{8c}$$

where the following assumptions have been included: $\varepsilon_s = v_{,s} = 0$. Moreover, it is supposed that the web and flanges are maded of FGMs whose properties vary continuously in its thickness. The constitutive relation of the FG sandwich thin-walled beams can be written as follows:

$$\begin{Bmatrix} \sigma_{33} \\ \sigma_{s3} \\ \sigma_{n3} \end{Bmatrix} = \begin{pmatrix} Q_{11} & 0 & 0 \\ 0 & Q_{66} & 0 \\ 0 & 0 & Q_{55} \end{pmatrix} \begin{Bmatrix} \varepsilon_{33} \\ \gamma_{s3} \\ \gamma_{n3} \end{Bmatrix} \tag{9}$$

where $Q_{11} = E(n)$, $Q_{66} = Q_{55} = \frac{E(n)}{2(1+\nu)}$; $E(n)$ is Young's modulus; ν is Poisson's coefficient which is supposed to be constant. The effective mass density ρ and Young's modulus E of the FG sandwich thin-walled beam are approximated by (Kim and Lee 2018, Nguyen et al. 2019):

$$\rho = \rho_c V_c + \rho_m(1 - V_c) \tag{10a}$$

$$E = E_c V_c + E_m(1 - V_c) \tag{10b}$$

where the subscripts c and m are used to indicate the ceramic and metal constituents, respectively; V_c is the volume fraction of ceramic material. It is noted that the implicit assumption within Eq. (10) is known as the Voigt's model, many more approximations of the effective elastic properties of FGMs can be found in Gasik (1998). The distribution of materials of FG sandwich thin-walled beams is presented in Figure 2 in which the volume fraction of the ceramic material is given by:

- For the flanges:

$$V_c = \left[\frac{n + 0.5h}{(1 - \alpha)h} \right]^p, \quad -0.5h \leq n \leq (0.5 - \alpha)h \tag{11a}$$

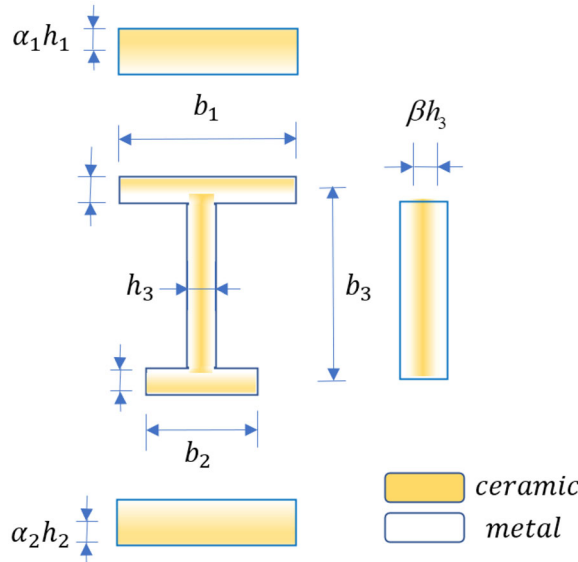$$V_c = 1, \quad (0.5 - \alpha)h \leq n \leq 0.5h \tag{11b}$$

Figure 2. Geometry of FG sandwich thin-walled I-beams.

where h (h_1, h_2) are the thickness of the top and bottom flanges; p is material parameter $(p \geq 0)$; α (α_1, α_2) are thickness ratio of ceramic material of the top and bottom flanges.

- For the web:

$$V_c = \left[\frac{-|n| + 0.5h}{0.5(1-\beta)h}\right]^p, \quad -0.5h \leq n \leq -0.5\beta h \ \ or \ \ 0.5\beta h \leq n \leq 0.5h \tag{12a}$$

$$V_c = 1, \ -0.5\beta h \leq n \leq 0.5\beta h \tag{12b}$$

where $h = h_3$ is the thickness of the web; β is thickness ratio of the ceramic material of the web.

2.2. Variational formulation

The characteristic equations of the FG sandwich thin-walled beams can be derived by Hamilton's equations in which the total energy of the system Π is composed of the strain energy Π_U, work done by external force Π_V and kinetic energy Π_K as follows:

$$\int_{t_1}^{t_2} (\delta\Pi_U + \delta\Pi_V - \delta\Pi_K)dt = 0 \tag{13}$$

The variation of strain energy Π_U of the FG sandwich thin-walled beams is defined by:

$$\delta\Pi_U = \int_\Omega (\sigma_{33}\delta\varepsilon_{33} + \sigma_{s3}\delta\gamma_{s3} + \sigma_{n3}\delta\gamma_{n3})d\Omega \tag{14}$$

where a shear correction coefficient has been supposed to unity in Eq. (14). Substituting Eqs. (8) and (9) into Eq. (14) leads to:

$$\delta\Pi_U = \int_0^L \Big[N_{33}\delta\zeta_{,3} + M_{22}\delta\psi_{2,3} + M_{11}\delta\psi_{1,3} + M_{\varpi}\delta\psi_{\varpi,3} \tag{15}$$
$$+ V_{11}\delta(\xi_{,3} + \psi_2) + V_{22}\delta(\eta_{,3} + \psi_1) + T\delta(\phi_{,3} + \psi_{\varpi}) + M_t\delta(\phi_{,3} - \psi_{\varpi})\Big]dx_3$$

where the stress resultants $(N_{33}, M_{22}, M_{11}, M_{\varpi}, V_{11}, V_{22}, T, M_t)$ are defined as follows:

$$(N_{33}, M_{22}, M_{11}, M_{\varpi}) = \int_A (1, x_1 + n\sin\theta, x_2 - n\cos\theta, \varpi - nr_s)\sigma_{33}dsdn \tag{16a}$$

$$V_{11} = \int_A (\sigma_{s3}\cos\theta + \sigma_{n3}\sin\theta)dsdn \tag{16b}$$

$$V_{22} = \int_A (\sigma_{s3}\sin\theta - \sigma_{n3}\cos\theta)dsdn \tag{16c}$$

$$T = \int_A (\sigma_{s3}r_n - \sigma_{n3}r_s)dsdn \tag{16d}$$

$$M_t = \int_A n\sigma_{s3}dsdn \tag{16e}$$

These stress resultants are related to the displacement gradients as follows:

$$
\begin{Bmatrix}
N_{33} \\
M_{22} \\
M_{11} \\
M_{\varpi} \\
V_{11} \\
V_{22} \\
T \\
M_t
\end{Bmatrix}
=
\begin{bmatrix}
\bar{H}_{11} & \bar{H}_{12} & \bar{H}_{13} & \bar{H}_{14} & 0 & 0 & 0 & 0 \\
\bar{H}_{12} & \bar{H}_{22} & \bar{H}_{23} & \bar{H}_{24} & 0 & 0 & 0 & 0 \\
\bar{H}_{13} & \bar{H}_{23} & \bar{H}_{33} & \bar{H}_{34} & 0 & 0 & 0 & 0 \\
\bar{H}_{14} & \bar{H}_{24} & \bar{H}_{34} & \bar{H}_{44} & 0 & 0 & 0 & 0 \\
0 & 0 & 0 & 0 & \bar{H}_{55} & \bar{H}_{56} & \bar{H}_{57} & \bar{H}_{58} \\
0 & 0 & 0 & 0 & \bar{H}_{56} & \bar{H}_{66} & \bar{H}_{67} & \bar{H}_{68} \\
0 & 0 & 0 & 0 & \bar{H}_{57} & \bar{H}_{67} & \bar{H}_{77} & \bar{H}_{78} \\
0 & 0 & 0 & 0 & \bar{H}_{58} & \bar{H}_{68} & \bar{H}_{78} & \bar{H}_{88}
\end{bmatrix}
\begin{Bmatrix}
\zeta_{,3} \\
\psi_{2,3} \\
\psi_{1,3} \\
\psi_{\varpi,3} \\
\phi_{,3} - \psi_{\varpi} \\
\xi_{,3} + \psi_2 \\
\eta_{,3} + \psi_1 \\
\phi_{,3} + \psi_{\varpi}
\end{Bmatrix}
\tag{17}
$$

where the stiffness components of the FG sandwich thin-walled beams $\bar{H}_{ij}(i,j=1,...,8)$ are defined by:

$$
\bar{H}_{11} = \int_s A_{11}ds, \bar{H}_{12} = \int_s (A_{11}x_1 + B_{11}\sin\theta)ds, \bar{H}_{13} = \int_s (A_{11}x_2 - B_{11}\cos\theta)ds
$$

$$
\bar{H}_{14} = \int_s (A_{11}\varpi - B_{11}r_s)ds, \bar{H}_{22} = \int_s \left(A_{11}x_1^2 + 2B_{11}x_1\sin\theta + D_{11}\sin^2\theta\right)ds
$$

$$
\bar{H}_{23} = \int_s (A_{11}x_1x_2 + B_{11}x_2\sin\theta - B_{11}x_1\cos\theta - D_{11}\sin\theta\cos\theta)ds
$$

$$
\bar{H}_{24} = \int_s (A_{11}x_1\varpi + B_{11}\varpi\sin\theta - B_{11}x_1r_s - D_{11}r_s\sin\theta)ds
$$

$$
\bar{H}_{33} = \int_s \left(A_{11}x_2^2 - 2B_{11}x_2\cos\theta + D_{11}\cos^2\theta\right)ds
$$

$$
\bar{H}_{34} = \int_s (A_{11}x_2\varpi - B_{11}\varpi\cos\theta - B_{11}x_2r_s + D_{11}r_s\cos\theta)ds
\tag{18}
$$

$$
\bar{H}_{44} = \int_s \left(A_{11}\varpi^2 - 2B_{11}\varpi r_s + D_{11}r_s^2\right)ds, \bar{H}_{55} = \int_s D_{66}ds, \bar{H}_{56} = \int_s B_{66}\cos\theta ds
$$

$$
\bar{H}_{57} = \int_s B_{66}\sin\theta ds, \bar{H}_{58} = \int_s B_{66}r_n ds, \bar{H}_{66} = \int_s \left(A_{66}\cos^2\theta + A_{55}\sin^2\theta\right)ds
$$

$$
\bar{H}_{67} = \int_s (A_{66}\sin\theta\cos\theta - A_{55}\sin\theta\cos\theta)ds, \bar{H}_{68} = \int_s (A_{66}r_n\cos\theta - A_{55}r_s\sin\theta)ds
$$

$$
\bar{H}_{77} = \int_s \left(A_{66}\sin^2\theta + A_{55}\cos^2\theta\right)ds, \bar{H}_{78} = \int_s (A_{66}r_n\sin\theta + A_{55}r_s\cos\theta)ds
$$

$$
\bar{H}_{88} = \int_s \left(A_{66}r_n^2 + A_{55}r_s^2\right)ds, (A_{ij}, B_{ij}, D_{ij}) = \int_s (1, n, n^2)Q_{ij}ds
$$

The variation of potential energy Π_W of the FG sandwich thin-walled beams subjected to axial compressive load N_0 can be expressed as:

$$
\delta\Pi_W = \int_\Omega \frac{N_0}{A}(u_{,3}\delta u_{,3} + v_{,3}\delta v_{,3})d\Omega
$$

$$
= \int_0^L N_0 \left[\xi_{,3}\delta\xi_{,3} + \eta_{,3}\delta\eta_{,3} + x_2^P(\xi_{,3}\delta\phi_{,3} + \phi_{,3}\delta\xi_{,3}) - x_1^P(\eta_{,3}\delta\phi_{,3} + \phi_{,3}\delta\eta_{,3}) + \frac{I_P}{A}\phi_{,3}\delta\phi_{,3}\right]dx_3
$$

$$
\tag{19}
$$

where A is the cross-sectional area; I_P is polar moment of inertia of the cross-section about the centroid defined by:

$$I_P = I_{x_1} + I_{x_2} \tag{20}$$

where I_{x_1} and I_{x_2} are second moment of inertia with respect to x_1- and x_2- axis, respectively, defined by:

$$I_{x_1} = \int_A x_2^2 dA, \ I_{x_2} = \int_A x_1^2 dA \tag{21}$$

The variation of kinetic energy Π_K of the FG sandwich thin-walled beams is given by:

$$
\begin{aligned}
\delta \Pi_K &= \int_\Omega \rho(n)(\dot{u}\delta\dot{u} + \dot{v}\delta\dot{v} + \dot{w}\delta\dot{w})d\Omega \\
&= \int_0^L \left\{ \delta\dot{\zeta}\left[J_0\dot{\zeta} - J_c\dot{\psi}_1 + J_s\dot{\psi}_2 + (J_\varpi - J_{r_s})\dot{\psi}_\varpi \right] + \delta\dot{\xi}\left[J_0\dot{\xi} + (J_c + x_2^P J_0)\dot{\phi} \right] \right. \\
&\quad + \delta\dot{\eta}\left[J_0\dot{\eta} + (J_s - x_1^P J_0)\dot{\phi} \right] + \delta\dot{\phi}\left[(J_c + x_2^P J_0)\dot{\xi} + (J_s - x_1^P J_0)\dot{\eta} + (J_{rs} + J_2 + 2J_{r_n})\dot{\phi} \right] \\
&\quad + \delta\dot{\psi}_1\left[-J_c\dot{\zeta} + (J_{22} - 2J_{2c} + J_{c2})\dot{\psi}_1 + (J_{12cs} - J_{cs})\dot{\psi}_2 + (J_{2\varpi} - J_{2\varpi r_s c} + J_{r_s c})\dot{\psi}_\varpi \right] \\
&\quad + \delta\dot{\psi}_2\left[J_s\dot{\zeta} + (J_{12cs} - J_{cs})\dot{\psi}_1 + (J_{12} + 2J_{1s} + J_{s2})\dot{\psi}_2 + (J_{1\varpi} + J_{1\varpi r_s s} - J_{r_s s})\dot{\psi}_\varpi \right] \\
&\quad + \delta\dot{\psi}_\varpi\left[(J_\varpi - J_{r_s})\delta\dot{\zeta} + (J_{2\varpi} - J_{2\varpi r_s c} + J_{r_s c})\dot{\psi}_1 + (J_{1\varpi} + J_{1\varpi r_s s} - J_{r_s s})\dot{\psi}_2 \right. \\
&\quad \left. \left. + (J_{\varpi 2} - 2J_{r_s \varpi} + J_{r_s 2})\dot{\psi}_\varpi \right] \right\} dx_3
\end{aligned}
\tag{22}
$$

where the following relations have been used: $x_1 - x_1^P = r_s \cos\theta + r_n \sin\theta$, $x_2 - x_2^P = r_s \sin\theta - r_n \cos\theta$; the dot-superscript is used to denote the differentiation with respect to the time t; $\rho(n)$ is the mass density and the inertia coefficients are given as follows:

$$(J_{sn}, J_\varpi, J_{12}, J_{22}, J_{\varpi 2}, J_{1\varpi}, J_{2\varpi}) = I_0 \int_s \left(r_s^2 + r_n^2, \varpi, x_1^2, x_2^2, \varpi^2, x_1\varpi, x_2\varpi \right)ds \tag{23a}$$

$$(J_{c2}, J_{s2}, J_{r_s2}, J_{cs}, J_{r_sc}, J_{r_ss}) = I_2 \int_s \left(\cos^2\theta, \ \sin^2\theta, r_s^2, \ \sin\theta\cos\theta, r_s\cos\theta, r_s\sin\theta \right)ds \tag{23b}$$

$$(J_0, J_2) = (I_0, I_2) \int_s ds, \ (J_c, J_{r_n}, J_{r_s}, J_s) = I_1 \int_s (\cos\theta, r_n, r_s, \ \sin\theta)ds \tag{23c}$$

$$(J_{1s}, J_{2c}, J_{r_s\varpi}, J_{\varpi c}, J_{\varpi s}) = I_1 \int_s (x_1 \sin\theta, x_2 \cos\theta, r_s\varpi, \varpi\cos\theta, \varpi\sin\theta)ds \tag{23d}$$

$$(J_{12cs}, J_{1\varpi r_s s}, J_{2\varpi r_s c}) = I_1 \int_s (-x_1\cos\theta + x_2\sin\theta, \ -r_s x_1 + \varpi\sin\theta, r_s x_2 + \varpi\cos\theta)ds \tag{23e}$$

$$(I_0, I_1, I_2) = \int_n (1, n, n^2)\rho \, dn \tag{23f}$$

2.4. Hybrid series solution

The displacement field is approximated as follows:

$$\{\zeta, \psi_2, \psi_1, \psi_\varpi\}(x_3, t) = \sum_{j=1}^{N} \varphi_{j,3}(x_3)\{\zeta_j, \psi_{2j}, \psi_{1j}, \psi_{\varpi j}\}(t) \tag{24a}$$

$$\{\xi, \eta, \phi\}(x_3, t) = \sum_{j=1}^{N} \varphi_j(x_3)\{\xi_j, \eta_j, \phi_j\}(t) \tag{24b}$$

where $\zeta_j(t)$, $\xi_j(t)$, $\eta_j(t)$, $\phi_j(t)$, $\psi_{2j}(t)$, $\psi_{1j}(t)$ and $\psi_{\varpi j}(t)$ are unknowns to be determined; $\varphi_j(x_3)$ are shape functions. It is noted that the approximations in Eq. (24) are known as Ritz-type series ones whose functions of approximation should be constructed to satisfy the specified essential boundary conditions (BCs) (Reddy 1997). For the present paper, new hybrid shape functions are proposed in Table 1 by a combination of exponential and admissible trigonometric functions to satisfy various BCs such as simply-supported (S-S), clamped-free (C-F) and clamped-clamped (C-C).

Substituting Eq. (24) into Eq. (13) accounting for Eqs. (15)(19) and (22) leads to the characteristic equations for vibration and buckling analysis of FG sandwich thin-walled beams as follows:

$$\mathbf{K}\mathbf{d} + \mathbf{M}''\mathbf{d} = \mathbf{0} \tag{25}$$

where $\mathbf{K}, \mathbf{M}$ are the stiffness and mass matrix, respectively; $\mathbf{d} = \begin{bmatrix} \mathbf{w} & \mathbf{u} & \mathbf{v} & \mathbf{\Phi} & \mathbf{\psi}_2 & \mathbf{\psi}_1 & \mathbf{\psi}_\varpi \end{bmatrix}^T$ is the displacement vector. The components of the stiffness matrix $\mathbf{K}$ are expressed by:

$$\mathbf{K} = \begin{bmatrix} \mathbf{K}^{11} & \mathbf{0} & \mathbf{0} & \mathbf{0} & \mathbf{K}^{15} & \mathbf{K}^{16} & \mathbf{K}^{17} \\ \mathbf{0} & \mathbf{K}^{22} & \mathbf{K}^{23} & \mathbf{K}^{24} & \mathbf{K}^{25} & \mathbf{K}^{26} & \mathbf{K}^{27} \\ \mathbf{0} & {}^T\mathbf{K}^{23} & \mathbf{K}^{33} & \mathbf{K}^{34} & \mathbf{K}^{35} & \mathbf{K}^{36} & \mathbf{K}^{37} \\ \mathbf{0} & {}^T\mathbf{K}^{24} & {}^T\mathbf{K}^{34} & \mathbf{K}^{44} & \mathbf{K}^{45} & \mathbf{K}^{46} & \mathbf{K}^{47} \\ {}^T\mathbf{K}^{15} & {}^T\mathbf{K}^{25} & {}^T\mathbf{K}^{35} & {}^T\mathbf{K}^{45} & \mathbf{K}^{55} & \mathbf{K}^{56} & \mathbf{K}^{57} \\ {}^T\mathbf{K}^{16} & {}^T\mathbf{K}^{26} & {}^T\mathbf{K}^{36} & {}^T\mathbf{K}^{46} & {}^T\mathbf{K}^{56} & \mathbf{K}^{66} & \mathbf{K}^{67} \\ {}^T\mathbf{K}^{17} & {}^T\mathbf{K}^{27} & {}^T\mathbf{K}^{37} & {}^T\mathbf{K}^{47} & {}^T\mathbf{K}^{57} & {}^T\mathbf{K}^{67} & \mathbf{K}^{77} \end{bmatrix} \tag{26}$$

where

Table 1. Shape functions and essential BCs of FG sandwich thin-walled I-beams.

BC	$\varphi_j(x_3)$	$x_3 = 0$	$x_3 = L$
S-S	$\sin\left(\frac{\pi x_3}{L}\right)e^{\frac{-jx_3}{L}}$	$\xi = \eta = \phi = 0$	$\xi = \eta = \phi = 0$
C-F	$\sin^2\left(\frac{\pi x_3}{2L}\right)e^{\frac{-jx_3}{L}}$	$\xi = \eta = \phi = 0$ $\xi_{,3} = \eta_{,3} = \phi_{,3} = 0$ $\zeta = \psi_2 = \psi_1 = \psi_\varpi = 0$	
C-C	$\sin^2\left(\frac{\pi x_3}{L}\right)e^{\frac{-jx_3}{L}}$	$\xi = \eta = \phi = 0$ $\xi_{,3} = \eta_{,3} = \phi_{,3} = 0$ $\zeta = \psi_2 = \psi_1 = \psi_\varpi = 0$	$\xi = \eta = \phi = 0$ $\xi_{,3} = \eta_{,3} = \phi_{,3} = 0$ $\zeta = \psi_2 = \psi_1 = \psi_\varpi = 0$

$$K_{ij}^{11} = \bar{H}_{11}S_{ij}^{22}, \; K_{ij}^{15} = \bar{H}_{12}S_{ij}^{22}, \; K_{ij}^{16} = \bar{H}_{13}S_{ij}^{22}, \; K_{ij}^{17} = \bar{H}_{14}S_{ij}^{22}, \; K_{ij}^{22} = (\bar{H}_{66} + N_0)S_{ij}^{11}$$

$$K_{ij}^{23} = \bar{H}_{67}S_{ij}^{11}, \; K_{ij}^{24} = (\bar{H}_{56} + \bar{H}_{68} + N_0 x_2^P)S_{ij}^{11}, \; K_{ij}^{25} = \bar{H}_{66}S_{ij}^{11}, \; K_{ij}^{26} = \bar{H}_{67}S_{ij}^{11}$$

$$K_{ij}^{27} = (\bar{H}_{68} - \bar{H}_{56})S_{ij}^{11}, \; K_{ij}^{33} = (\bar{H}_{77} + N_0)S_{ij}^{11}, \; K_{ij}^{34} = (\bar{H}_{57} + \bar{H}_{78} - N_0 x_1^P)S_{ij}^{11}$$

$$K_{ij}^{35} = \bar{H}_{67}S_{ij}^{11}, \; K_{ij}^{36} = \bar{H}_{77}S_{ij}^{11}, \; K_{ij}^{37} = (\bar{H}_{78} - \bar{H}_{57})S_{ij}^{11}, \; K_{ij}^{45} = (\bar{H}_{56} + \bar{H}_{68})S_{ij}^{11}$$

$$K_{ij}^{44} = \left(\bar{H}_{55} + 2\bar{H}_{58} + \bar{H}_{88} + \frac{N_0 I_p}{A}\right)S_{ij}^{11}, \; K_{ij}^{46}(\bar{H}_{57} + \bar{H}_{78})S_{ij}^{11}$$

$$K_{ij}^{47} = (\bar{H}_{88} - \bar{H}_{55})S_{ij}^{11}, \; K_{ij}^{55} = \bar{H}_{22}S_{ij}^{22} + \bar{H}_{66}S_{ij}^{11}, \; K_{ij}^{56} = \bar{H}_{23}S_{ij}^{22} + \bar{H}_{67}S_{ij}^{11}$$ (27)

$$K_{ij}^{57} = \bar{H}_{24}S_{ij}^{22} + (\bar{H}_{68} - \bar{H}_{56})S_{ij}^{11}, \; K_{ij}^{66} = \bar{H}_{33}S_{ij}^{22} + \bar{H}_{77}S_{ij}^{11}$$

$$K_{ij}^{67} = \bar{H}_{34}S_{ij}^{22} + (\bar{H}_{78} - \bar{H}_{57})S_{ij}^{11}, \; K_{ij}^{77} = \bar{H}_{44}S_{ij}^{22} + (\bar{H}_{88} - 2\bar{H}_{58} + \bar{H}_{55})S_{ij}^{11}$$

$$S_{ij}^{rs} = \int_0^L \frac{\partial^r \varphi_i}{\partial x_3^r} \frac{\partial^s \varphi_j}{\partial x_3^s} dx_3$$

The components of mass matrix **M** are given by:

$$\mathbf{M} = \begin{bmatrix} \mathbf{M}^{11} & 0 & 0 & 0 & \mathbf{M}^{15} & \mathbf{M}^{16} & \mathbf{M}^{17} \\ 0 & \mathbf{M}^{22} & 0 & \mathbf{M}^{24} & 0 & 0 & 0 \\ 0 & 0 & \mathbf{M}^{33} & \mathbf{M}^{34} & 0 & 0 & 0 \\ 0 & {}^T\mathbf{M}^{24} & {}^T\mathbf{M}^{34} & \mathbf{M}^{44} & 0 & 0 & 0 \\ {}^T\mathbf{M}^{15} & 0 & 0 & 0 & \mathbf{M}^{55} & \mathbf{M}^{56} & \mathbf{M}^{57} \\ {}^T\mathbf{M}^{16} & 0 & 0 & 0 & {}^T\mathbf{M}^{56} & \mathbf{M}^{66} & \mathbf{M}^{67} \\ {}^T\mathbf{M}^{17} & 0 & 0 & 0 & {}^T\mathbf{M}^{57} & {}^T\mathbf{M}^{67} & \mathbf{M}^{77} \end{bmatrix}$$ (28)

where

$$M_{ij}^{11} = J_0 S_{ij}^{11}, \; M_{ij}^{15} = J_s S_{ij}^{11}, \; M_{ij}^{16} = -J_c S_{ij}^{11}, \; M_{ij}^{17} = (J_\varpi - J_{r_s})S_{ij}^{11}, \; M_{ij}^{22} = J_0 S_{ij}^{00}$$

$$M_{ij}^{24} = (J_c + J_0 x_2^P)S_{ij}^{00}, \; M_{ij}^{33} = J_0 S_{ij}^{00}, \; M_{ij}^{34} = (J_s - J_0 x_1^P)S_{ij}^{00}, \; M_{ij}^{44} = (J_p + J_2 + 2J_{r_n})S_{ij}^{00}$$

$$M_{ij}^{55} = (J_{x2} + 2J_{xs} + J_{s2})S_{ij}^{11}, \; M_{ij}^{56} = (J_{12cs} - J_{cs})S_{ij}^{11}, \; M_{ij}^{57} = (J_{1\varpi} + J_{1\varpi r_s} - J_{r_s s})S_{ij}^{11}$$

$$M_{ij}^{66} = (J_{22} - 2J_{2c} + J_{c2})S_{ij}^{11}, \; M_{ij}^{67} = (J_{2\varpi} - J_{2\varpi r_s c} + J_{r_s c})S_{ij}^{11}, \; M_{ij}^{77} = (J_{\varpi 2} - 2J_{r_s \varpi} + J_{r_s 2})S_{ij}^{11}$$ (29)

It is noted that the buckling responses of the FG sandwich thin-walled beams can be derived from Eq. (25) by solving $\det(\mathbf{Kd}) = \mathbf{0}$, whereas the free vibration behaviors are obtained by setting $\mathbf{d}(t) = \mathbf{d}e^{i\omega t}$ where ω is the natural frequency, $i^2 = -1$ the imaginary unit, and then solving the subsequent result $(\mathbf{K} - \omega^2 \mathbf{M})\mathbf{d} = \mathbf{0}$.

2.5. Polynomial chaos expansion

Constituent material properties of the FG sandwich thin-walled beam such as Young's modulus (E_c, E_m) and mass densities (ρ_c, ρ_m) are supposed to be randomly changed according to lognormal distributions. In order to efficiently propagate the variability in material properties to that in the responses of FG sandwich thin-walled beams, a surrogate model based on the PCE is constructed in which the framework for probabilistically assessing the responses of FG sandwich thin walled beams is described in Figure 3 for both PCE and MCS methods. It is noted that though two quantities of interests (QoIs) of the present study are natural frequencies and critical buckling loads, this approach can be applied to other responses of interest. For the MCS method, it is known that the implementation of MCS is straightforward in which material properties are generated with a large number of
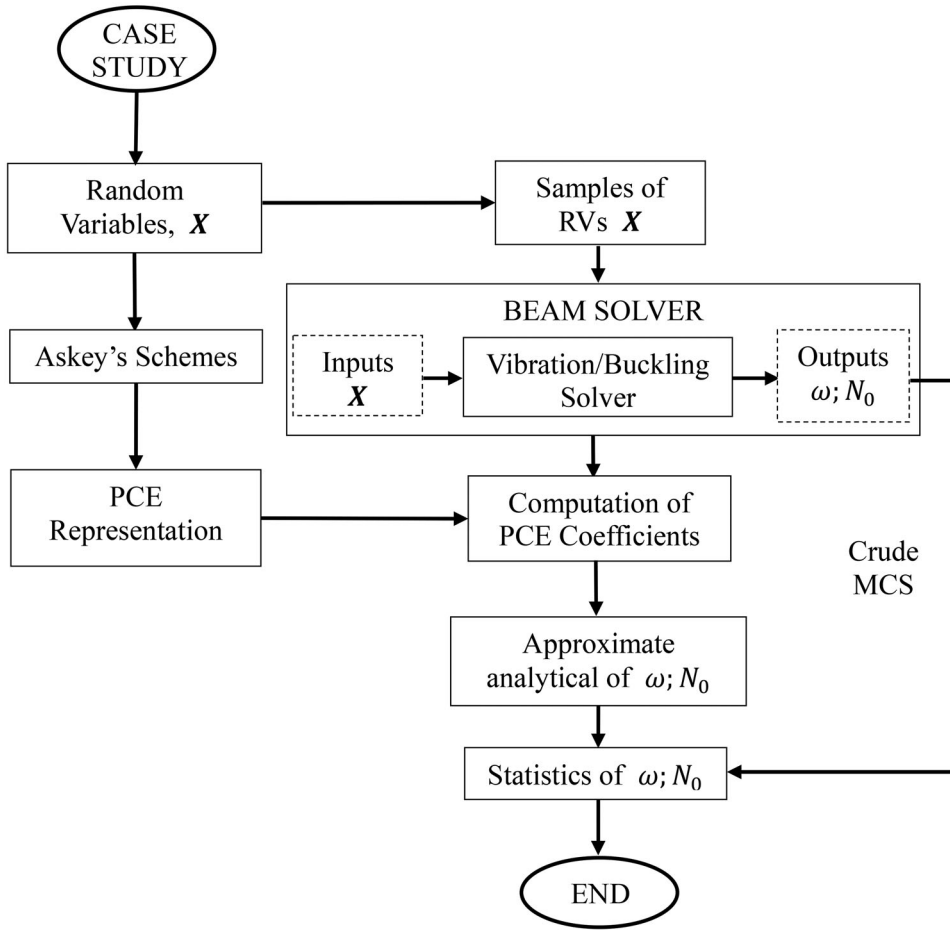
Figure 3. Flowchart of stochastic free vibration and buckling analysis of thin-walled I-beam using PCE and MCS.

samples, and then natural frequencies and critical buckling loads of the FG sandwich thin-walled beams are computed for each simulation by solving Eq. (25). The outputs obtained from the MCS method will be considered as benchmarks for the comparison purpose. Otherwise, the PCE model is considered as an alternative method with less computational costs for a required accuracy.

For the PCE method, the first step of this approach is to approximate the responses $\hat{u}$ of FG sandwich thin-walled beams in terms of a truncated orthogonal series as follows:

$$\hat{u} \simeq \hat{u}_{PCE}(\mathbf{x}) = \sum_{i=0}^{P-1} c_i He_i(\mathbf{q}) + \varepsilon \qquad (30)$$

where $\hat{u}_{PCE}$ are the responses of interest obtained from PCE; $\mathbf{q}$ is a vector of independent random variables in the PCE space mapped to physical random parameters $\mathbf{x}$; He_i are multivariate orthogonal basis functions; c_i are coefficients to be determined so that the residual ε is minimized; P is the permutation of the qualified order of polynomial p and the number of random variable d which is given by: $P = \frac{(d+p)!}{d!p!}$. It is noted that based on Askey's scheme (Xiu and Karniadakis 2002), the Hermite polynomials, He_i, is chosen for input variables with lognormal distribution.

The second step is to estimate all associated coefficients. This task can be easily obtained by forcing the residual minimum resulting in the inner product of the residual and each basis function He_i becomes zero. Taking the inner product of both sides of Eq. (30), with respect to He_j:

$$\langle \hat{u}, He_j \rangle = \sum_{i=0}^{P-1} c_i \langle He_i, He_j \rangle \tag{31}$$

then enforcing the orthogonality of He_j, Eq. (31) becomes:

$$c_i = \frac{\langle \hat{u}, He_i \rangle}{\langle He_i, He_i \rangle} = \frac{1}{\langle He_i, He_i \rangle} \int \hat{u} He_i \rho_Q(\mathbf{q}) d\mathbf{q} \tag{32}$$

Note that He_i is Hermite polynomial, so the normalization factor $\langle He_i, He_i \rangle$ in Eq. (32) can be analytically evaluated. It is noted that all coefficients can be theoretically obtained by solving the integral term in Eq. (32), however the random response $\hat{u}$ is unknown. In the present paper, therefore, the coefficient c_i will be numerically computed using the simple tensor product Gauss-Hermite quadrature:

$$\langle \hat{u}, He_i \rangle = \sum_{j_1=1}^{N_{gp}^1} \cdots \sum_{j_d=1}^{N_{gp}^d} \left(w_{j_1}^1 \otimes \cdots \otimes w_{j_d}^d \right) \hat{u} \left(q_{j_1}^1, ..., q_{j_d}^d \right) He_i \left(q_{j_1}^1, ..., q_{j_d}^d \right) \tag{33}$$

where N_{gp}^i is the number of quadrature point; q_j^i and w_j^i are the set of quadrature points and their weights, respectively for the random variable i^{th}. For convenience, the number of quadrature points for each variable is chosen equally such that $N_{gp}^1 = N_{gp}^2 = \cdots = N_{gp}^d = N_{gp}$. It is worth noticing that if the order of the model output $\hat{u}$ is p, the highest order of the integrands in Eq. (32) is at least $2p$, so the minimum number of quadrature points for each dimension is $N_{gp} = p + 1$ and the total number of Gauss points is at least $(p+1)^d$. Therefore, $(p+1)^d$ problems shown in Eq. (25) need to be solved for the model response $\hat{u}(q_{j_1}^1...q_{j_d}^d)$.

Once the PCE model is developed, the uncertainty is explicitly propagated from the random inputs to the stochastic response via the polynomial function in Eq. (30) which takes a fraction of a second. The predominant computational cost required to predict the stochastic responses using the PCE model is therefore associated with obtaining $\hat{u}(q_{j_1}^1...q_{j_d}^d)$ for coefficients estimations shown in Eq. (33). This computational cost is much less than those of applying the crude MCS. Another advantage of the PCE is that the mean and the variance of the response can be analytically estimated from the PCE coefficients as follows:

$$\mu_{\hat{u}} = E[\hat{u}] = c_0 \tag{34a}$$

$$\bar{\sigma}_{\hat{u}}^2 = E\left[(\hat{u} - \mu_{\hat{u}})^2\right] = \sum_{i=1}^{P-1} c_i^2 \langle He_i, He_i \rangle \tag{34b}$$

Furthermore, Sobol' sensitivity indices can be also estimated directly from the PCE coefficients (Sudret 2008). In particular, the first-order main effect S_k and the total sensitivity index S_k^T of a random variable X_k are estimated as follows:

$$S_k = \frac{D_k}{\sigma_{\hat{u}}^2} \tag{35a}$$

$$S_k^T = \frac{D_k^T}{\sigma_{\hat{u}}^2} \tag{35b}$$

where $D_k = \sum_{j \in \Gamma_k} c_j^2 \langle He_j(\mathbf{q}), He_j(\mathbf{q}) \rangle$ and $D_k^T = \sum_{j \in \Gamma_k^T} c_j^2 \langle He_j(\mathbf{q}), He_j(\mathbf{q}) \rangle$; Γ_k includes all j such that the multivariate function $He_j(\mathbf{q})$ only include the variable q_k (i.e., $He_j(\mathbf{q}) = He_j(q_k)$), while

Γ_k^T includes all j such that $He_j(\mathbf{q})$ must include the variable q_k (i.e., $He_j(\mathbf{q}) = He_j(q_1, ..., q_k, ..., q_d)$).

3. Numerical results

This section investigates natural frequencies and critical buckling loads of FG sandwich thin-walled I-beams with various configurations of material parameters, boundary conditions and thickness ratios of the ceramic material. Two types of material of the FG sandwich thin-walled beams are introduced in Table 2 including the means and coefficients of variation (COV) in which the material MAT I is used for vibration analysis and MAT II for buckling problems. The material properties are supposed to be randomly changed according to lognormal distributions. Unless stated otherwise, the following geometries of the FG sandwich thin-walled beams is used in numerical examples: $b_1 = b_2 = 15$cm, $b_3 = 20$cm, $h = h_1 = h_2 = h_3 = 0.5$cm and $L = 10b_3$).

3.1. Convergence and verification study

For the convergence study of hybrid series solutions in predicting buckling and vibration behaviors, Tables 3 and 4 give the fundamental frequency and critical buckling load for the FG sandwich thin-walled I-beams with the increase in the number of series N. The material properties of the FG sandwich thin-walled beams for Table 3 are MAT I and for Tables 4 and 5 are MAT II. The thickness ratios of ceramic material are $\alpha_1 = \alpha_2 = \beta = 0.1$ for Table 3 and $\alpha_1 = \alpha_2 = 0.7, \beta = 0.4$ for Tables 4 and 5. Three boundary conditions of simply-supported (S-S), clamped-clamped (C-C) and clamped-free (CF) are considered with different values of the power index p. It is seen in Table 3 that for vibration analysis, the output is numerically converged at $N = 10$ under C-C boundary condition and is converged at $N = 6$ and $N = 8$ under S-S and C-F boundary conditions, respectively. Meanwhile, the output of buckling analysis shown in Table 4 shows faster convergence at $N = 6$ in most cases. In the subsequent analysis, $N = 8$ is hence chosen for numerical computations.

Table 2. Material properties of FG sandwich thin-walled I-beams.

Material properties	Mean		COV	Distribution
	MAT I	MAT II		
E_c (GPa)	380	320.7	0.1	Lognormal
E_m (GPa)	70	101.69	0.1	Lognormal
$\nu = \nu_c = \nu_m$	0.3	0.3	–	–
ρ_c (kg/m³)	3960	–	0.1	Lognormal
ρ_m (kg/m³)	2702	–	0.1	Lognormal
α_1	0.1	0.7	–	–
α_2	0.1	0.7	–	–
β	0.1	0.4	–	–

Table 3. Convergence of fundamental frequencies (*Hz*) of the FG sandwich thin-walled beams without any variation in input variables (MAT I, $\alpha_1 = \alpha_2 = \beta = 0.1$).

BCs	Reference	N					
		2	4	6	8	10	12
S-S	Present (Shear)	96.18	91.33	91.18	91.18	91.18	91.18
	Nguyen et al. (2019; Shear)	92.72	91.52	91.18	91.18	91.18	91.18
C-C	Present (Shear)	209.49	201.24	200.25	200.02	199.91	199.92
	Nguyen et al. (2019; Shear)	201.80	200.43	200.13	199.97	199.89	199.88
C-F	Present (Shear)	63.60	46.64	34.25	32.73	32.66	32.65
	Nguyen et al. (2019; Shear)	33.14	32.69	32.66	32.66	32.66	32.66

Table 4. Convergence of critical buckling loads (x10^6 N) of the FG sandwich thin-walled beam without any variation in input variables (MAT II, $\alpha_1 = \alpha_2 = 0.7, \beta = 0.4$).

BCs	p	N					
		2	4	6	8	10	12
S-S	0.5	2.02	1.97	1.96	1.96	1.96	1.96
	1	1.69	1.65	1.64	1.64	1.64	1.64
	2	1.36	1.33	1.32	1.32	1.32	1.32
	5	1.04	1.01	1.01	1.01	1.01	1.01
	10	0.89	0.87	0.86	0.86	0.86	0.86
C-C	0.5	7.53	7.45	7.43	7.43	7.43	7.43
	1	6.31	6.24	6.23	6.23	6.23	6.23
	2	5.09	5.03	5.02	5.02	5.02	5.02
	5	3.87	3.83	3.82	3.82	3.82	3.82
	10	3.31	3.28	3.27	3.27	3.27	3.27
C-F	0.5	0.52	0.50	0.50	0.50	0.50	0.50
	1	0.44	0.42	0.42	0.42	0.42	0.42
	2	0.35	0.34	0.34	0.34	0.34	0.34
	5	0.27	0.25	0.25	0.25	0.25	0.25
	10	0.23	0.22	0.22	0.22	0.22	0.22

Table 5. Critical buckling load (kN) of the FG sandwich thin-walled I-beams without any variation in input variables (MAT II, $\alpha_1 = \alpha_2 = 0.7, \beta = 0.4$).

| BCs	Reference	$p=0$	0.25	0.5	1	2	5	10	20
S-S	Present (Shear)	421.633	404.155	392.508	377.958	363.420	348.899	342.305	338.539
	Kim and Lee (2018; No shear)	423.083	405.933	394.515	380.286	366.056	351.825	345.333	341.605
	Kim and Lee (2018; Shear)	422.359	405.208	393.783	379.533	365.280	351.058	344.601	340.906
	Lanc et al. (2016; No shear)	423.296	406.130	394.692	380.412	366.150	351.914	345.451	341.762
C-C	Present (Shear)	1669.413	1599.491	1552.860	1494.550	1436.212	1377.838	1351.288	1336.110
	Kim and Lee (2018; No shear)	1692.352	1623.751	1578.078	1521.156	1464.229	1407.293	1381.317	1366.399
	Kim and Lee (2018; Shear)	1680.840	1612.410	1566.830	1509.950	1453.060	1396.270	1370.490	1355.730
	Lanc et al. (2016; No shear)	1705.050	1635.900	1589.830	1532.310	1474.860	1417.520	1391.480	1376.630
C-F	Present (Shear)	106.144	101.755	98.832	95.180	91.533	87.892	86.239	85.295
	Kim and Lee (2018; No shear)	105.771	101.483	98.629	95.072	91.514	87.957	86.334	85.403
	Kim and Lee (2018; Shear)	105.725	101.435	98.577	95.013	91.448	87.891	86.277	85.353
	Lanc et al. (2016; No shear)	105.773	101.484	98.626	95.057	91.494	87.936	86.321	85.400
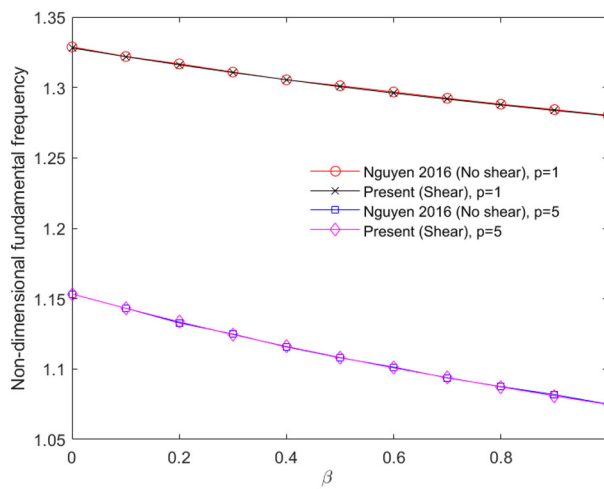
Figure 4. Non-dimensional fundamental frequency of thin-walled FG sandwich thin-walled I-beams without any variation in input variables.

Table 6. Comparative study between MCS (100.000 samples) and PCE (625 samples) for the mean, standard deviation (SD), kurtosis and skewness of the fundamental frequency outputs (*Hz*, MAT I: $\alpha_1 = \alpha_2 = \beta = 0.1$).

BCs	p	MCS ($N_s = 100,000$)					PCE ($N_s = 625$)					Deterministic
		Mean	SD	Kurtosis	Skewness	Time (s)	Mean	SD	Kurtosis	Skewness	Time (s)	
S-S	0	128.05	9.04	3.10	0.21	344.64	128.11	9.05	3.11	0.21	13.65	127.75
	0.5	116.84	7.21	3.06	0.20	311.88	116.89	7.19	3.08	0.18	10.21	116.72
	1	109.89	6.27	3.06	0.17	310.84	109.89	6.28	3.09	0.19	10.90	109.77
	2	101.55	5.48	3.04	0.18	310.97	101.52	5.47	3.07	0.17	10.72	101.45
	5	91.30	4.79	3.05	0.15	312.93	91.28	4.77	3.05	0.15	10.73	91.18
	10	85.74	4.55	3.03	0.15	323.72	85.74	4.56	3.03	0.15	10.70	85.62
C-C	0	281.01	19.81	3.05	0.21	360.44	280.95	19.87	3.08	0.22	12.17	280.25
	0.5	256.36	15.70	3.05	0.17	329.66	256.32	15.79	3.05	0.18	10.58	256.04
	1	241.01	13.86	3.03	0.17	326.74	241.05	13.80	3.05	0.18	10.53	240.80
	2	222.75	11.98	3.03	0.18	317.96	222.76	12.03	3.03	0.16	10.53	222.54
	5	200.29	10.46	3.05	0.17	312.41	200.27	10.48	3.05	0.16	10.56	200.02
	10	188.20	10.02	3.04	0.15	313.17	188.15	9.98	3.03	0.15	10.51	187.82
C-F	0	46.00	3.25	3.08	0.20	398.56	45.98	3.24	3.06	0.21	14.83	45.86
	0.5	41.97	2.58	3.11	0.20	363.63	41.96	2.57	3.07	0.19	12.84	41.90
	1	39.45	2.26	3.06	0.17	366.03	39.45	2.26	3.09	0.19	12.69	39.41
	2	36.45	1.96	3.03	0.18	365.92	36.45	1.96	3.06	0.18	13.12	36.42
	5	32.78	1.72	3.01	0.15	357.95	32.79	1.72	3.07	0.17	13.54	32.73
	10	30.78	1.64	3.03	0.15	362.76	30.80	1.64	3.04	0.14	13.09	30.74

Table 7. Comparative study between MCS (100.000 samples) and PCE (64 samples) for the mean, standard deviation (SD), kurtosis and skewness of the critical buckling load outputs (*kN*, MAT II: $\alpha_1 = \alpha_2 = 0.7$, $\beta = 0.4$).

BCs	P	MCS ($N_s = 100,000$)					PCE ($N_s = 64$)					Deterministic 421.633
		Mean	SD	Kurtosis	Skewness	Time (s)	Mean	SD	Kurtosis	Skewness	Time (s)	
S-S	0	421.46	42.11	3.17	0.29	105.19	421.48	42.12	3.17	0.31	1.59	421.63
	0.5	392.24	37.83	3.14	0.29	101.15	392.23	37.89	3.15	0.30	1.43	392.51
	1	377.91	35.85	3.12	0.28	101.45	377.99	35.77	3.15	0.30	1.44	377.96
	2	363.50	33.76	3.13	0.28	102.03	363.49	33.74	3.20	0.32	1.47	363.42
	5	348.91	31.77	3.16	0.30	101.13	348.91	31.73	3.17	0.30	1.44	348.90
	10	342.38	30.86	3.15	0.29	101.98	342.25	30.74	3.14	0.30	1.51	342.31
C-C	0	1669.40	166.82	3.18	0.29	116.18	1668.24	166.97	3.14	0.30	1.53	1669.41
	0.5	1553.10	150.19	3.17	0.30	110.69	1552.98	149.89	3.15	0.30	1.59	1552.86
	1	1494.50	141.46	3.16	0.29	111.43	1495.30	141.02	3.16	0.29	1.54	1494.55
	2	1436.70	133.88	3.17	0.31	118.93	1435.96	133.53	3.16	0.30	1.56	1436.21
	5	1377.60	124.80	3.20	0.31	109.34	1378.50	125.30	3.14	0.30	1.53	1377.84
	10	1351.50	121.42	3.13	0.29	110.25	1351.27	121.11	3.13	0.28	1.55	1351.29
C-F	0	105.67	10.53	3.14	0.29	107.87	105.70	10.58	3.20	0.32	1.49	105.68
	0.5	98.35	9.50	3.12	0.29	110.89	98.41	9.51	3.16	0.31	1.60	98.40
	1	94.70	8.98	3.16	0.30	110.20	94.73	9.02	3.19	0.30	1.55	94.76
	2	91.10	8.47	3.15	0.30	110.11	91.12	8.47	3.19	0.30	1.53	91.13
	5	87.50	7.97	3.18	0.30	109.60	87.50	7.95	3.14	0.29	1.50	87.51
	10	85.90	7.73	3.14	0.29	111.91	85.86	7.71	3.15	0.30	1.55	85.86

In order to verify the accuracy of present theory, the deterministic vibration and buckling responses of the FG sandwich thin-walled I-beam are compared with results of Nguyen et al. (2019), Nguyen, Kim, and Lee (2016b), Lanc et al. (2016), and Kim and Lee (2018). It is noted that the term "deterministic" indicates that the results are calculated with mean material properties (see Table 2). It can be seen from Table 3 that the fundamental frequencies computed from the present model concur with those of Nguyen et al. (2019). Moreover, Figure 4 also shows that the non-dimensional frequencies for the FG sandwich thin-walled beam (MAT I, $h = h_1 = h_2 = h_3 = 0.5cm$, $b_1 = 20h$, $b_2 = 10h$, $b_3 = 40h$, $L = 40b_3$ $\alpha_1 = 0.1, \alpha_2 = 0.9$) of the present solution are in excellent agreements with those of Nguyen, Kim, and Lee (2016b). Additionally, the critical buckling loads for the FG sandwich thin-walled beam (MAT II, $h = h_1 = h_2 = h_3 = 0.5cm$, $b_1 = b_2 = 20h$, $b_3 = 40h$, $L = 12.5b_3$) presented in Table 5 are comparable to the results of Kim and

Lee (2018) and Lanc et al. (2016). Thus, the present FG sandwich thin-walled beam model is valid for the subsequent stochastic analysis.
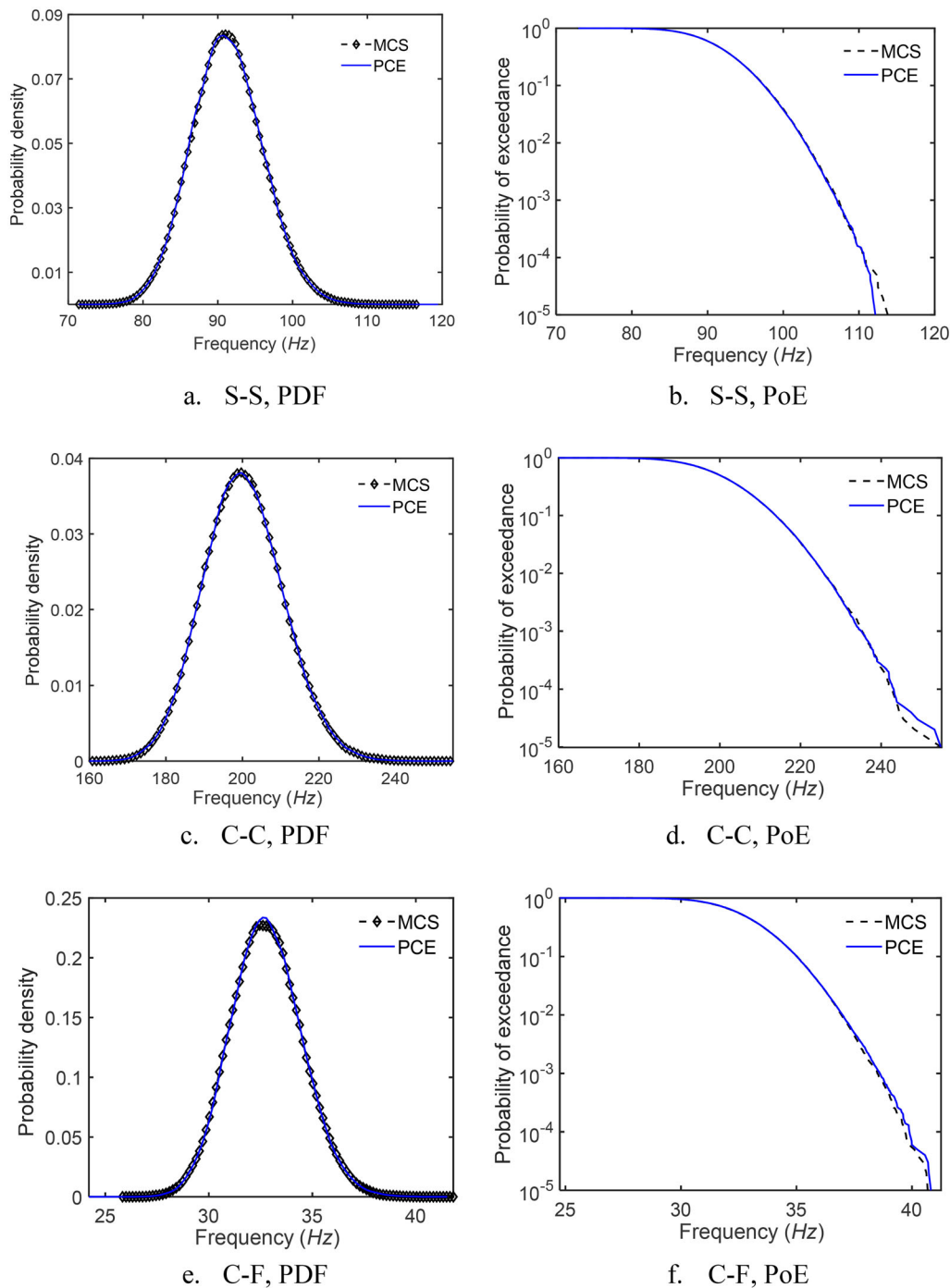

a. S-S, PDF b. S-S, PoE c. C-C, PDF d. C-C, PoE e. C-F, PDF f. C-F, PoE

Figure 5. Probability density function (PDF) and Probability of exceedance (PoE) of MCS and PCE methods of the fundamental frequency (Hz) for FG sandwich thin-walled beams with S-S, C-C and C-F boundary condition, $p = 5, \alpha_1 = \alpha_2 = \beta = 0.1$.

3.3. Stochastic analysis

For stochastic analysis, the MCS with $N_s = 100,000$ samples is carried out to verify the accuracy and efficiency of PCE surrogate model. Four first statistical moments of the fundamental frequencies and critical buckling loads, namely the mean, standard deviation (SD), skewness and kurtosis

a. S-S, PDF   b. S-S, PoE

c. C-C, PDF   d. C-C, PoE

e. C-F, PDF   f. C-F, PoE
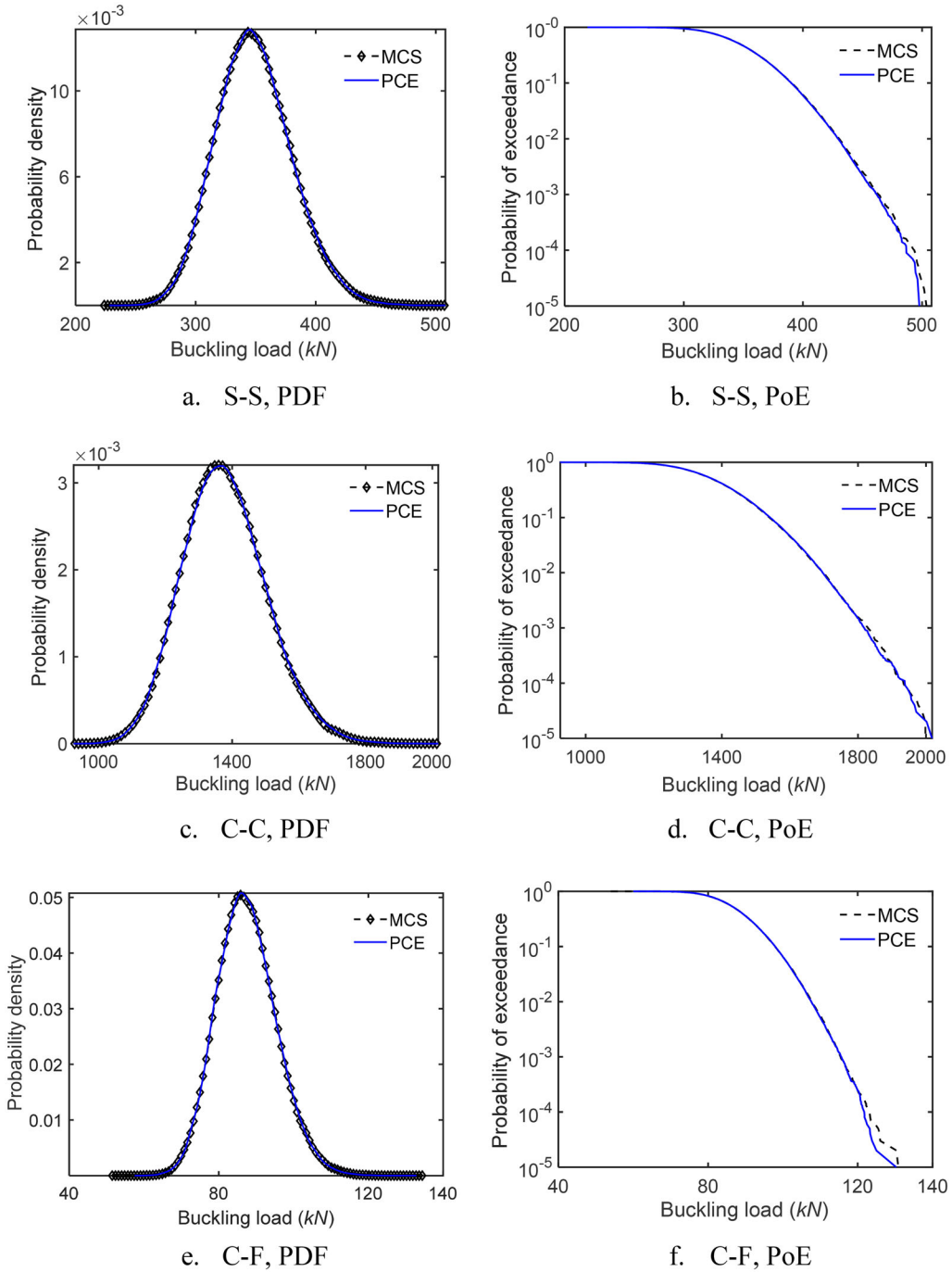
Figure 6. Probability density function (PDF) and Probability of exceedance (PoE) of MCS and PCE methods of critical buckling load (kN) for FG sandwich thin-walled beams with S-S, C-C and C-F boundary conditions, $p = 5, \alpha_1 = \alpha_2 = 0.7, \beta = 0.4$.

obtained from the MCS and PCE models are compared in Tables 6 and 7. The running time and deterministic values of each case are also reported for three different boundary conditions and five different values of the power index p. It is noted that for deterministic analysis, all random variables are set to equal the mean values. It can be seen from Tables 6 and 7 that the deterministic responses are in excellent agreement with those from Nguyen et al. (2019). These results demonstrate the accuracy of the beam model with the proposed hybrid shape functions in predicting vibration and buckling responses of the FG sandwich thin-walled I-section beams.

Besides the MCS approach, the fourth-order PCE model is used for FG I-beam vibration analysis and the third-order PCE model is for buckling analysis of the same beam. Consequently, 625 and 64 output samples obtained from the beam solver are required to construct the PCE model for fundamental frequencies and critical buckling loads, respectively. It is observed that the mean and standard deviation of the fundamental frequencies obtained from the MCS and PCE show good agreement in all cases. Meanwhile, most of the skewness and kurtosis are closely matched with the exception of some cases where these two higher-order statistical moments are different by at most 10%. A similar trend can be seen in the results of critical buckling loads in Table 7. The skewness and kurtosis are two statistical moments measuring the tails of the distributions and might vary due to the lack of samples. From Figures 5 and 6, the probability density function (PDF) plots produced from MCS and PCE methods for both QoIs show no discrepancy

a. S-S Boundary Condition

b. C-C Boundary Condition

c. C-F Boundary Condition
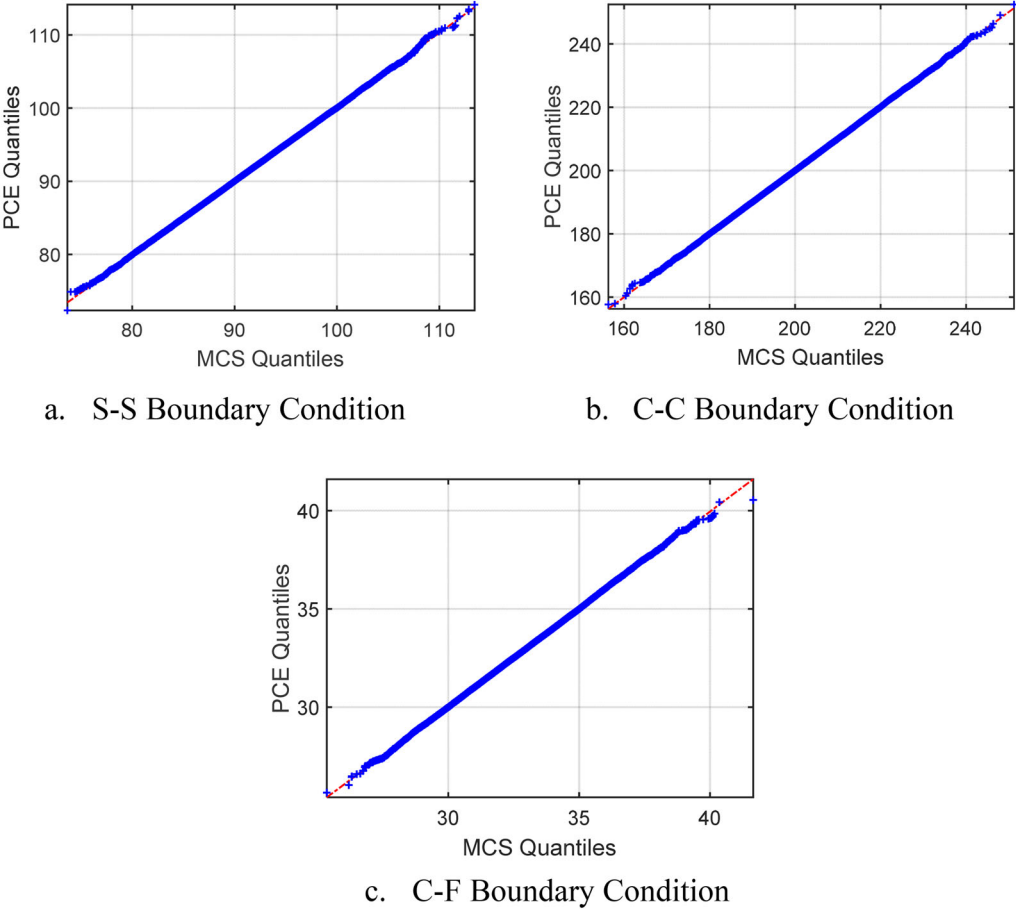
Figure 7. Quantile-quantile plot of the PCE method with respect to the MCS method for the fundamental frequency of FG thin-walled I-beam with S-S, C-C and C-F boundary conditions ($p = 5, \alpha_1 = \alpha_2 = \beta = 0.1$).

but the probability of exceedance (PoE) graph can represent the difference in skewness and kurtosis. As the probability of exceedance, $P(X > x)$, becomes smaller, there are fewer samples in both methods to represent the randomness in model outputs and this leads to the difference mentioned above. It is worth noting that with 100,000 samples, the PoE obtained from MCS and PCE only agrees well up to the point of $P(X > x) = 10^{-4}$.

Regarding the computational cost, PCE requires only 625 and 64 'truth' samples (i.e., generated from the beam model) to develop surrogate models for the fundamental frequency and buckling load, respectively compared with 100,000 samples of the MCS. Considering the whole process for assessing the probabilistic characteristics of stochastic outputs (as illustrated in Figure 3), the running time of the PCE method is also significantly lower than the running time of the MCS method. This running time can vary between computing processor power and for efficiency comparison; the ratio between the running time of both methods is a better index. It is observed that the required computational time of the present PCE method with respect to the direct MCS method is 1/50 for vibration analysis and 1/72 for buckling analysis.

In Figure 7, the 45-degree linear quantile-quantile plot further confirms the matching statistical distribution of the fundamental frequency computed from the MCS and PCE. Thus, the PCE method gives an affordable alternative solution to numerically simulate the uncertainties in multiple material properties and predict the fundamental frequency responses.

a. S-S Boundary Condition

b. C-C Boundary Condition

c. C-F Boundary Condition
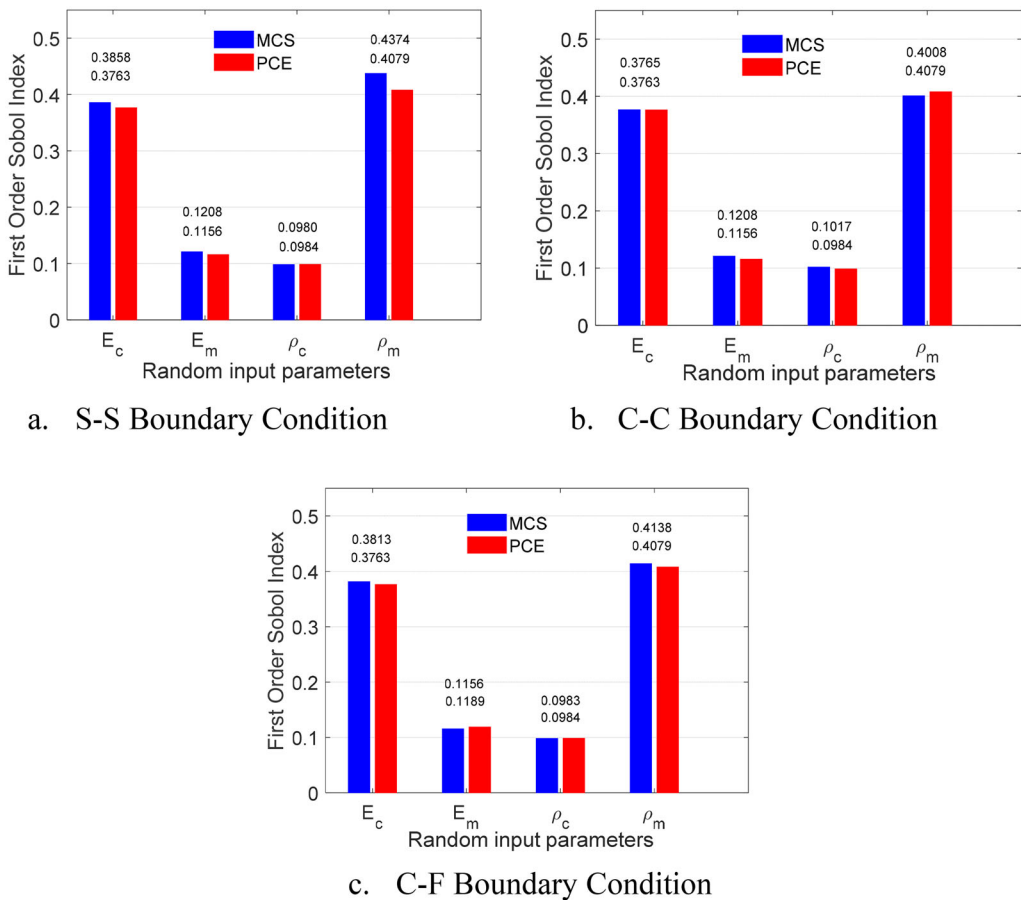
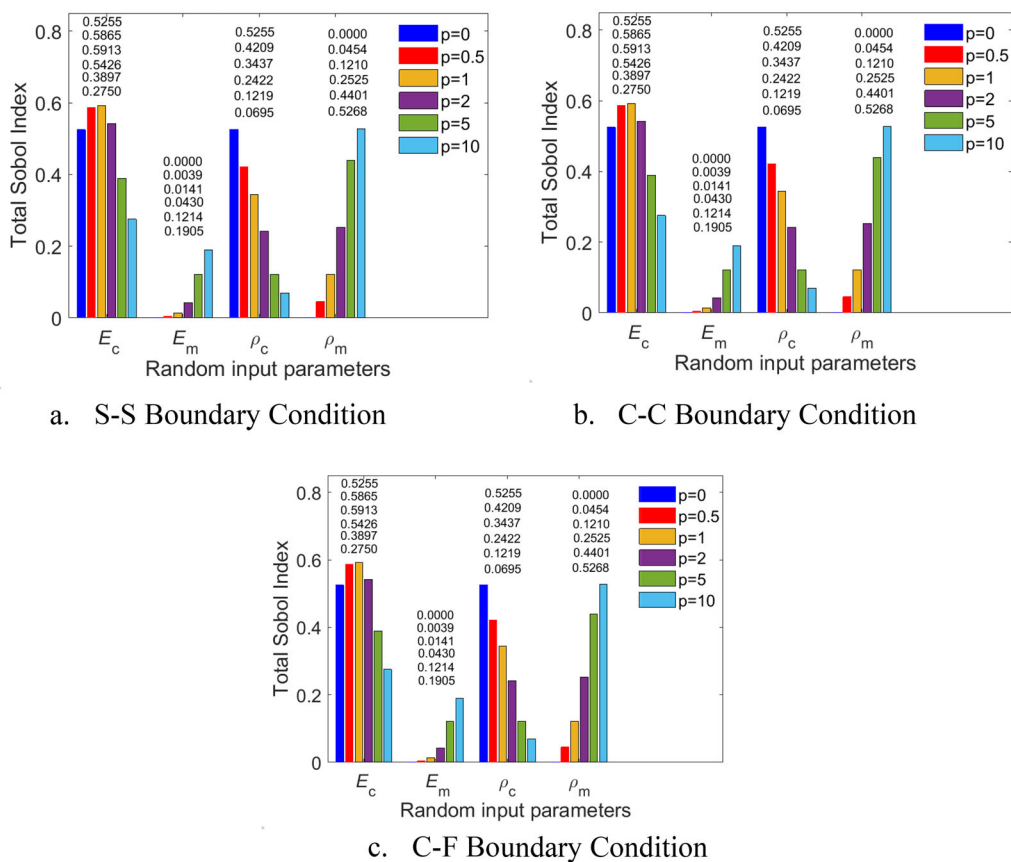**Figure 8.** First order Sobol index of the random input variables with respect to the fundamental frequency of the FG thin-walled beam models obtained from both MCS and PCE; three boundary conditions (S-S, C-C, C-F); $p = 5$; $\alpha_1 = \alpha_2 = \beta = 0.1$.

3.4. Sensitivity analysis

In addition to the probabilistic characteristics of the outputs, the influence of each random input on the variability of model responses is also a topic of interest in this study. Figure 8 compares the sensitivity indices based on the first-order Sobol indices for the vibration analysis using MCS and PCE methods for the power index . It is seen that the Sobol indices computed from the polynomial expansion coefficients are closely matched with those calculated from MCS. In this sensitivity study, the PCE method is far more efficient than the MCS. Note that a random input parameter with a greater first-order Sobol index has higher influence on the variance of the model output without accounting for the interaction between different input parameters. Therefore, the effects of E_c and ρ_m on the fundamental frequency of this stochastic model (with $p = 5$) are about four-fold compared to E_m and ρ_c. As expected, the first Sobol indices are independent with the beam boundary conditions.

The total Sobol indices obtained from the PCE method of each random variable corresponding to fundamental frequency for different p values are presented in Figure 9. It is observed that the sensitivity index for each parameter is the same for three boundary conditions. Moreover, the power-law index p has a significant impact on the sensitivity results. In particular, as p increases, the importance of metal constituent increases; in contrast, the influence of ceramic material properties decreases except for E_c as its influence increases when $p \leq 1$. Subjected to different cases, the total Sobol indices can help filter out unimportant input variables and therefore, improve the computing time. To further investigate the effect of values of p on the outputs'

a. S-S Boundary Condition

b. C-C Boundary Condition

c. C-F Boundary Condition

Figure 9. Total Sobol index of the random input variables with respect to the fundamental frequency of the FG thin-walled beam models obtained from PCE; three boundary conditions (S-S, C-C, C-F); $\alpha_1 = \alpha_2 = \beta = 0.1$.
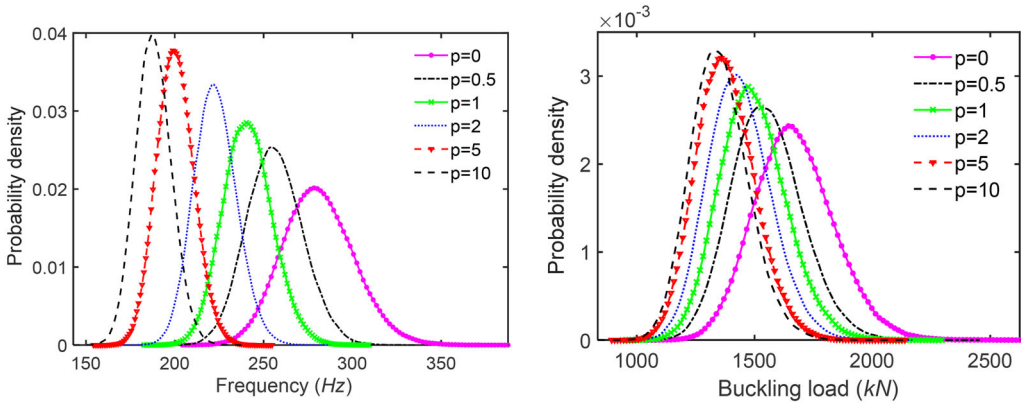
Figure 10. Probability density function (PDF) of the natural frequency (*Hz*, MAT I, fourth-order-PCE) and critical buckling load (*kN*, MAT II, third-order-PCE) for FG I-beams with various power index *p* (C-C boundary condition).

uncertainty, the probability density functions of fundamental frequency and buckling load of C-C beam for different values of *p* are compared in Figure 10. Interestingly, the uncertainty in both frequency and buckling load appears larger with the decrease in the values of *p* where the distributions of two outputs are spread wider.

4. Conclusions

A stochastic model for buckling and vibration analysis of FG sandwich thin-walled beam with I-section based on the first-order shear deformation theory is proposed in this paper. The FGM properties are supposed to be randomly varied according to lognormal distributions. These variabilities are propagated to the stochastic responses of FG sandwich thin-walled beams through a beam solver with novel hybrid series-type approximation functions. Polynomial chaos expansion (PCE) based surrogate model is developed for evaluations of stochastic responses. The efficiency and accuracy of PCE's results are assessed by comparing them with those of crude Monte Carlo simulation (MCS). Sensitivity analysis is investigated to compare the importance of the uncertainty in material properties to stochastic responses. Numerical results showed that the efficiency of the proposed PCE based model is far more superior than the conventional MCS while ensuring accuracy. In addition, the PCE method is also faster than MCS in determining Sobol sensitivity indices, which successively helps reduce the number of random input variables. The present theory and model is found to be efficient in predicting stochastic buckling and vibration behaviors of the FG sandwich thin-walled beams.

References

Bui, X.-B., T.-K. Nguyen, N.-D. Nguyen, and T. P. Vo. 2022. A general higher-order shear deformation theory for buckling and free vibration analysis of laminated thin-walled composite I-beams. *Composite Structures* 295: 115775. doi:10.1016/j.compstruct.2022.115775.

Carvalho, A., T. Silva, M. A. R. Loja, and F. R. Damásio. 2017. Assessing the influence of material and geometrical uncertainty on the mechanical behavior of functionally graded material plates. *Mechanics of Advanced Materials and Structures* 24 (5):417–26. doi:10.1080/15376494.2016.1191100.

Chaikittiratana, A., and N. Wattanasakulpong. 2022. Gram-Schmidt-Ritz method for dynamic response of FG-GPLRC beams under multiple moving loads. *Mechanics Based Design of Structures and Machines* 50 (7):2427–48. doi:10.1080/15397734.2020.1778488.

Chakraborty, S., B. Mandal, R. Chowdhury, and A. Chakrabarti. 2016. Stochastic free vibration analysis of laminated composite plates using polynomial correlated function expansion. *Composite Structures* 135:236–49. doi:10.1016/j.compstruct.2015.09.044.

Chandiramani, N. K., L. Librescu, and C. D. Shete. 2002. On the free-vibration of rotating composite beams using a higher-order shear formulation. *Aerospace Science and Technology* 6 (8):545–61. doi:10.1016/S1270-9638(02)01195-1.

Chandra, S., K. Sepahvand, V. A. Matsagar, and S. Marburg. 2019. Stochastic dynamic analysis of composite plate with random temperature increment. *Composite Structures* 226:111159. doi:10.1016/j.compstruct.2019.111159.

Civalek, Ö., and O. Kiracioglu. 2010. Free vibration analysis of Timoshenko beams by DSC method. *International Journal for Numerical Methods in Biomedical Engineering* 26 (12):1890–8. doi:10.1002/cnm.1279.

Demir, C., K. Mercan, H. M. Numanoglu, and O. Civalek. 2018. Bending response of nanobeams resting on elastic foundation. *Journal of Applied and Computational Mechanics* 4 (2):105–14. doi:10.22055/jacm.2017.22594.1137.

Ebrahimi, F., M. R. Barati, and Ö. Civalek. 2020. Application of Chebyshev–Ritz method for static stability and vibration analysis of nonlocal microstructure-dependent nanostructures. *Engineering with Computers* 36 (3):953–64. doi:10.1007/s00366-019-00742-z.

Gasik, M. M. 1998. Micromechanical modelling of functionally graded materials. *Computational Materials Science* 13 (1–3):42–55. doi:10.1016/S0927-0256(98)00044-5.

Grover, N., R. Sahoo, B. N. Singh, and D. K. Maiti. 2017. Influence of parametric uncertainties on the deflection statistics of general laminated composite and sandwich plates. *Composite Structures* 171:158–69. doi:10.1016/j.compstruct.2017.03.036.

Jalaei, M. H., H. T. Thai, and Ö. Civalek. 2022. On viscoelastic transient response of magnetically imperfect functionally graded nanobeams. *International Journal of Engineering Science* 172:103629. doi:10.1016/j.ijengsci.2022.103629.

Kim, N.-I., and J. Lee. 2017. Coupled vibration characteristics of shear flexible thin-walled functionally graded sandwich I-beams. *Composites Part B: Engineering* 110:229–47. doi:10.1016/j.compositesb.2016.11.025.

Kim, N.-I., and J. Lee. 2018. Investigation of coupled instability for shear flexible FG sandwich I-beams subjected to variable axial force. *Acta Mechanica* 229 (1):47–70. doi:10.1007/s00707-017-1949-6.

Lanc, D., G. Turkalj, T. P. Vo, and J. Brnić. 2016. Nonlinear buckling behaviours of thin-walled functionally graded open section beams. *Composite Structures* 152:829–39. doi:10.1016/j.compstruct.2016.06.023.

Li, J., X. Tian, Z. Han, and Y. Narita. 2016. Stochastic thermal buckling analysis of laminated plates using perturbation technique. *Composite Structures* 139:1–12. doi:10.1016/j.compstruct.2015.11.076.

Librescu, L., and O. Song. 2006. Thin-walled composite beams: Theory and application. Dordrecht: Springer Press.

Madrahalli Chidanandamurthy, K., W. Wang, C. Fang, and S. Kattimani. 2021. Static, buckling, and free vibration characteristics of porous skew partially functionally graded magneto-electro-elastic plate. *Mechanics Based Design of Structures and Machines*:1–36. doi:10.1080/15397734.2021.2008257.

Mishra, B. B., A. Kumar, and U. Topal. 2020. Stochastic normal mode frequency analysis of hybrid angle ply laminated composite skew plate with opening using a novel approach. *Mechanics Based Design of Structures and Machines*:1–35. doi:10.1080/15397734.2020.1840393.

Mukherjee, S., S. Gopalakrishnan, and R. Ganguli. 2019. Stochastic time domain spectral element analysis of beam structures. *Acta Mechanica* 230 (5):1487–512. doi:10.1007/s00707-018-2272-6.

Naskar, S., T. Mukhopadhyay, S. Sriramula, and S. Adhikari. 2017. Stochastic natural frequency analysis of damaged thin-walled laminated composite beams with uncertainty in micromechanical properties. *Composite Structures* 160:312–34. doi:10.1016/j.compstruct.2016.10.035.

Nguyen, H. X., T. Duy Hien, J. Lee, and H. Nguyen-Xuan. 2017. Stochastic buckling behaviour of laminated composite structures with uncertain material properties. *Aerospace Science and Technology* 66:274–83. doi:10.1016/j.ast.2017.01.028.

Nguyen, N.-D., T. P. Vo, and T.-K. Nguyen. 2020. An improved shear deformable theory for bending and buckling response of thin-walled FG sandwich I-beams resting on the elastic foundation. *Composite Structures* 254:112823. doi:10.1016/j.compstruct.2020.112823.

Nguyen, N.-D., T.-K. Nguyen, T. P. Vo, and L. B. Nguyen. 2020. Bending, buckling and free vibration behaviors of thin-walled functionally graded sandwich and composite channel-section beams. *Mechanics Based Design of Structures and Machines*:1–29. doi:10.1080/15397734.2020.1859385.

Nguyen, N.-D., T.-K. Nguyen, T. P. Vo, T.-N. Nguyen, and S. Lee. 2019. Vibration and buckling behaviours of thin-walled composite and functionally graded sandwich I-beams. *Composites Part B: Engineering* 166:414–27. doi:10.1016/j.compositesb.2019.02.033.

Nguyen, T.-T., and J. Lee. 2018. Interactive geometric interpretation and static analysis of thin-walled bi-directional functionally graded beams. *Composite Structures* 191:1–11. doi:10.1016/j.compstruct.2018.01.064.

Nguyen, T.-T., N.-I. Kim, and J. Lee. 2016a. Analysis of thin-walled open-section beams with functionally graded materials. *Composite Structures* 138:75–83. doi:10.1016/j.compstruct.2015.11.052.

Nguyen, T.-T., N.-I. Kim, and J. Lee. 2016b. Free vibration of thin-walled functionally graded open-section beams. *Composites Part B: Engineering* 95:105–16. doi:10.1016/j.compositesb.2016.03.057.

Oh, S. Y., L. Librescu, and O. Song. 2003. Vibration of turbomachinery rotating blades made-up of functionally graded materials and operating in a high temperature field. *Acta Mechanica* 166 (1–4):69–87. doi:10.1007/s00707-003-0049-y.

Parviz, H., and M. Fakoor. 2021. Stochastic free vibration of composite plates with temperature-dependent properties under spatially varying stochastic high thermal gradient. *Mechanics Based Design of Structures and Machines*:1–24. doi:10.1080/15397734.2021.2014863.

Peng, X., D. Li, H. Wu, Z. Liu, J. Li, S. Jiang, and J. Tan. 2019. Uncertainty analysis of composite laminated plate with data-driven polynomial chaos expansion method under insufficient input data of uncertain parameters. *Composite Structures* 209:625–33. doi:10.1016/j.compstruct.2018.11.015.

Reddy, J. N. 1997. *Mechanics of laminated composite plates: Theory and analysis*. Boca Raton, FL: CRC press.

Sasikumar, P., R. Suresh, and S. Gupta. 2014. Stochastic finite element analysis of layered composite beams with spatially varying non-Gaussian inhomogeneities. *Acta Mechanica* 225 (6):1503–22. doi:10.1007/s00707-013-1009-9.

Sharma, H., S. Mukherjee, and R. Ganguli. 2022. Stochastic strain and stress computation of a higher-order sandwich beam using hybrid stochastic time domain spectral element method. *Mechanics of Advanced Materials and Structures* 29 (4):525–38. doi:10.1080/15376494.2020.1778144.

Stefanou, G. 2009. The stochastic finite element method: Past, present and future. *Computer Methods in Applied Mechanics and Engineering* 198 (9–12):1031–51. doi:10.1016/j.cma.2008.11.007.

Sudret, B. 2008. Global sensitivity analysis using polynomial chaos expansion. *Reliability Engineering & System Safety* 93 (7):964–79. doi:10.1016/j.ress.2007.04.002.

Umesh, K., and R. Ganguli. 2013. Material uncertainty effect on vibration control of smart composite plate using polynomial chaos expansion. *Mechanics of Advanced Materials and Structures* 20 (7):580–91. doi:10.1080/15376494.2011.643279.

Vlasov, V. 1961. *Thin-walled elastic beams. Israel program for scientific translations, Jerusalem*. London: Oldbourne Press.

Xiu, D., and G. E. Karniadakis. 2002. The Wiener–Askey polynomial chaos for stochastic differential equations. *SIAM Journal on Scientific Computing* 24 (2):619–44. doi:10.1137/S1064827501387826.

Deterministic and stochastic flexural behaviors of laminated composite thin-walled I-beams using a sinusoidal higher-order shear deformation theory

Xuan-Bach Bui & Trung-Kien Nguyen

Published online: 28 Dec 2023.

Submit your article to this journal ⤷

View related articles ⤷

View Crossmark data ⤷

Taylor & Francis
Taylor & Francis Group

Check for updates

Deterministic and stochastic flexural behaviors of laminated composite thin-walled I-beams using a sinusoidal higher-order shear deformation theory

Xuan-Bach Bui[a] and Trung-Kien Nguyen[b]

aFaculty of Civil Engineering, Ho Chi Minh City University of Technology and Education, Ho Chi Minh City, Viet Nam; bCIRTech Institute, HUTECH University, Ho Chi Minh City, Viet Nam

ABSTRACT

In this study, a novel sinusoidal higher-order shear deformation thin-walled beam theory is presented to examine the effects of material properties and external load uncertainty on static responses of laminated composite thin-walled beams with open sections. The solution for the deterministic flexural analysis is based on Hamilton's principle and Ritz-type exponential shape function series. Several mechanical parameters of laminated composite materials are randomized and plugged into the beam solver to investigate the thin-walled beam's stochastic flexural behaviors. The computational cost and accuracy of the polynomial chaos expansion (PCE) method with both projection and linear regression approaches are presented and evaluated by comparing its results with crude Monte Carlo simulation (MCS). This comparison allows for a thorough assessment of the PCE method's performance. Additionally, a sensitivity analysis is conducted to compare the relative significance of the uncertainty in material properties and loads on the stochastic responses. The supervised training of the artificial neural network based on the MCS beam data is also conducted and compared to the PCE and MCS methods. The findings about the stochastic outputs are introduced in various statistical metrics and illustrations to demonstrate the influences of material properties' randomness on different laminated composite thin-walled beam configurations.

1. Introduction

Laminated composite thin-walled beams are an essential structural element that has been extensively used in engineering applications, particularly in aerospace, aircraft, and mechanical engineering. These thin-walled beams are made of multilayered materials in web and flanges with enhanced material properties compared to their constituent materials in weight-to-strength ratio. However, the design and analysis of laminated composite thin-walled beams have been challenging due to their complex geometry, anisotropic material behaviors, uncertainty in external loads, and material properties. This interesting topic has, therefore, attracted numerous researchers.

Based on the transverse shear deformation, the beam theories can be divided into three groups: classical beam theory, first-order shear deformation beam theory, and higher-order shear deformation beam theory (HSDT). The order of the shear function can be as high as the accuracy required to accurately simulate the transverse shear effect (Abdelmalek et al. 2019). Even though the HSDT has been well-studied for solid beams, it has rarely been implemented for thin-walled

---

beams. Further investigation of HSDT-based thin-walled beams is therefore needed to predict the thin-walled beams' responses more accurately. Various analytical and numerical techniques have been developed to predict behaviors of the laminated composite thin-walled beams in which most of the research focused on its deterministic responses. By the simplicity in theoretical formulation, Vlasov's thin-walled beam theory (CTWT) (Piovan, Ramirez, and Sampaio 2013) has been commonly used for analysis of laminated composite thin-walled beams (Bauld and Lih-Shyng 1984; Pandey, Kabir, and Sherbourne 1995; Lee and Kim 2002, 2001; Latalski and Zulli 2020; Yu et al. 2005). However, the CTWT does not accurately predict static and dynamic responses due to the lack of transverse shear strains. To overcome this adverse, the first-order thin-walled beam theory (FTWT) accounted for the shear strain effects has become a surrogate model by introducing constant shear strains in the wall thickness. This approach enabled to predict the deflection, buckling loads and natural frequencies more accurately than the CTWT (Maddur and Chaturvedi 2000, 1999; Lee 2005; Qin and Librescu 2002; Vo and Lee 2009; Lee 2001; Jung and Lee 2003; Kim and Shin 2008; Wu and Mohareb 2011; Kim and Jeon 2013; Ramaprasad, Dattaguru, and Singh 2022; Nguyen et al. 2023). In practice, the FTWT violated the free-stress boundary conditions, which required a shear correction factor in calculation of the shear strain energy. An alternative way to solve this problem is to use the higher-order shear deformation thin-walled beams (HTWT) in which a nonlinear variation of the transverse shear strains is supposed in the wall thickness. Based on this approach, several works have been developed for deterministic analysis of laminated composite thin-walled beams. Chandiramani, Librescu, and Shete (2002) investigated free, forced and geometrically nonlinear vibration responses of laminated composite thin-walled beams with closed sections by introducing a parabolic distribution of the transverse shear strains in the wall thickness. Bui et al. (2022) recently presented a HTWT for vibration and buckling analysis of laminated composite I-beams in which the authors showed that the higher-order transverse shear strain effects impacted importantly on the behaviors of thin-walled beams. In this context, this study proposes a novel HTWT using a higher-order sinusoidal shear function to analyze the static behaviors of laminated composite I-beams.

Besides the beam models, the computational methods have also had an important influence on behaviors of the beam. There exist many numerical methods to solve for the beam models' responses such as Cottrell, Hughes, and Bazilevs (2009), Oñate (2013), and Carrera, Giunta, and Petrolo (2011). Among those, the Ritz method proves to be simple and accurate in investigating the static and dynamic responses of beams and plates with different boundary conditions (Reddy 2003b), this approach has been successfully applied for analysis of laminated composite plates (Abdelmalek et al. 2019), laminated composite nanoplates (Tayeb Tayeb et al. 2020; Boulal et al. 2020; Guessas et al. 2018), laminated composite beams (Bouazza et al. 2015), and laminated composite nanobeams (Zerrouki, Karas, and Zidour 2020). It is worth to noticing that the performance of the Ritz method relies on the construction of approximate functions for the entire beam's length. A substantial number of researchers (Moreno-García, dos Santos, and Lopes 2018; Nguyen et al. 2018) have focused on proposing these functions so that the solution has a quick convergence rate and optimal computational cost (Chaikittiratana and Wattanasakulpong 2022). Based on the Ritz method, in order to compute deterministic responses of the HTWT-based laminated composite thin-walled beams, this article will develop hybrid functions which are a combination of exponential functions and admissible ones satisfying the boundary conditions.

The deterministic models mentioned above do not involve the randomness of the beam model's inputs. Nonetheless, in practice, it is known that the material properties and loads could be uncertain due to unexpected factors, which probably lead to change of behaviors of the thin-walled beams. Hence, it is essential to study various efficient probabilistic methods for the stochastic beam models. A literature survey reveals that though many researches have been performed in examining stochastic responses of laminated composite plates with different approaches (Nguyen et al. 2017; Jagtap, Lal, and Singh 2012; Trinh et al. 2021; Borges et al. 2021; Kumar

et al. 2019; Peng et al. 2019; Umesh and Ganguli 2013; Chakraborty et al. 2016; Sasikumar et al. 2015; Shaker et al. 2008; Parhi and Singh 2014), the number of studies on stochastic behaviors of laminated composite thin-walled beams is extremely limited. In general, in order to compute the stochastic responses of the beam, the crude Monte Carlo Simulation (MCS) method is the simplest one. However, when the beam's outcome of interest takes minutes or hours to compute, the surrogate model is preferred. This surrogate model can save computational costs by learning patterns from much fewer data points and provide the highly similar outputs of MCS with a higher number of simulations. In recent years, the artificial neural network (ANN) and deep feedforward neural network (DNN) based surrogate modeling have seen a growing trend and have been applied to many engineering problems involving uncertainties. Guo, Zhuang, and Rabczuk (2019) proposed a deep collocation method that is based on the DNN to study the bending of Kirchhoff's plates. Samaniego et al. (2020) opted for the DNN to approximate the solution of the partial differential equations of a mechanical system. Zhuang et al. (2021) used an improved DNN method based on a deep autoencoder to minimize the total potential energy and thus, compute the bending, vibration and buckling behaviors of Kirchhoff's plates. Tran et al. (2023) made use of the ANN and balancing composite motion optimization algorithm to study vibration and buckling responses of the functionally graded porous plates with uncertainties in material properties. Despite its ease of implementation, the ANN-based surrogate model requires further steps to compute sensitivity indices of the input variables. This drawback is not the case with the polynomial chaos expansion (PCE) method (Tsokanas et al. 2022). Besides, when the size of the random input vector is reasonably small, the PCE method is more efficient in providing the stochastic responses of a mechanical system (Jakeman, Perego, and Severa 2018). Recently, Bui, Nguyen, and Nguyen (2023) investigated stochastic buckling and free vibration behaviors of functionally graded sandwich thin-walled beams based on the FTWT and PCE with spectral projection approach. A literature review shows that according to the authors' knowledge, the effects of transverse shear strains and uncertainty of mechanical loads and materials properties on flexural behaviors of laminated composite thin-walled beams using the sinusoidal HTWT have not been carried out, this gap needs to be considered further.

This article proposes a deterministic and stochastic model for flexural behaviors of laminated composite thin-walled I-beams with uncertainty in material properties and loads. The theory is based on a novel sinusoidal higher-order shear deformation thin-walled beam theory (STWT) with a sinusoidal variation of the transverse shear strains in the wall thickness. A hybrid series solution is developed for solving characteristic equations with different boundary conditions and various theories, including FTWT and STWT. Numerical results are presented to investigate the effects of the stochasticity, fiber angle, span-to-thickness ratio, and boundary conditions on the probabilistic deflections of laminated composite thin-walled beams with I-sections. Both the polynomial chaos expansion method and artificial neural network method are used to learn a small amount of data and produce the stochastic static behaviors of laminated composite thin-walled I-beams. The accuracy and efficiency of both methods are determined by comparing them to the MCS. Additionally, Sobol's sensitivity indices are computed to quantify the significance of random input variables on the bending responses of laminated composite thin-walled beams. These probabilistic aspects of the STWT-based laminated composite thin-walled beams have not been studied in depth by past researches, and are presented in this article. The workflow of the stochastic analysis is introduced to significantly reduce computational cost for the MCS.

2. Theoretical formulation

Consider a laminated composite thin-walled I-section beam with widths (b_1, b_2, b_3) and thicknesses (h_1, h_2, h_3) as in Figure 1 in which Cartesian coordinate system (x_1, x_2, x_3), local coordinate system (n, s, x_3) and contour coordinate s along the profile of the section are used for the

Figure 1. Thin-walled coordinate systems.

theoretical formulation. The angle of orientation between (n, s, x_3) and (x_1, x_2, x_3) coordinate systems is namely α, the pole point P with coordinates (x_1^P, x_2^P) is considered as the shear center of the section. Moreover, it is assumed that the displacements are small, the section contour does not deform in its own plane, and the transverse shear strains vary nonlinearly under a sinusoidal function in the wall thickness.

2.1. Displacements

At any points of the thin-walled beam cross-section under a small rotation $\phi(x_3)$ about the pole axis, the displacements $u_1(n, s, x_3)$ and $u_2(n, s, x_3)$ in x_1- and x_2- directions can be derived from those at the shear center P with $u_1^P(x_3)$ and $u_2^P(x_3)$ as follows:

$$u_1(n, s, x_3) = u_1^P(x_3) - \left(x_2 - nx_{1,s} - x_2^P\right)\phi(x_3) = u_1^P(x_3) - \left(X_2 - x_2^P\right)\phi(x_3) \tag{1a}$$

$$u_2(n, s, x_3) = u_2^P(x_3) + \left(x_1 + nx_{2,s} - x_1^P\right)\phi(x_3) = u_2^P(x_3) + \left(X_1 - x_1^P\right)\phi(x_3) \tag{1b}$$

where $x_{2,s} = \cos\alpha$ and $x_{1,s} = -\sin\alpha$; $X_1 = x_1 + nx_{2,s}$, $X_2 = x_2 - nx_{1,s}$; the comma in the subscript is used to indicate the differentiation with respect to the variable that follows. Obviously, as expected the kinematics in (x_1, x_2) defined in Eq. (1) meet the non-deformability conditions of cross-section. Moreover, in order to derive the axial displacement in x_3- direction $u_3(n, s, x_3)$, the shear strains in the contour of thin-walled open-section beams $(\gamma_{s3}, \gamma_{n3})$ can be expressed in terms of the transverse shear strains $(\gamma_{13}, \gamma_{23})$ and a direct shear strain caused by the change rate of twist angle $\phi_{,3}$ (Megson 2021) as follows:

$$\gamma_{s3}(n, s, x_3) = \gamma_{13}(n, x_3)X_{1,s} + \gamma_{23}(n, x_3)X_{2,s} + 2n\phi_{,3}(x_3) = u_{s,3} + u_{3,s} \tag{2a}$$

$$\gamma_{n3}(n, s, x_3) = \gamma_{13}(n, x_3)X_{2,s} - \gamma_{23}(n, x_3)X_{1,s} = u_{n,3} + u_{3,n} \tag{2b}$$

where $u_n(n, s, x_3)$ and $u_s(n, s, x_3)$ are the displacements in the contour lines given by:

$$u_n(n, s, x_3) = u_1^P(x_3)x_{2,s} - u_2^P(x_3)x_{1,s} - R_s(n, s)\phi(x_3) \tag{3a}$$

$$u_s(n, s, x_3) = u_1^P(x_3)x_{1,s} + u_2^P(x_3)x_{2,s} + R_n(n, s)\phi(x_3) \tag{3b}$$

with $R_s(n, s) = r_s(s)$, $R_n(n, s) = r_n(s) + n$; $r_s(s)$ and $r_n(s)$ are the lengths of the perpendiculars from P to the tangent and normal of the profile line center. Furthermore, the transverse shear strains $(\gamma_{13}, \gamma_{23})$ are supposed to vary nonlinearly through the wall thickness under sinusoidal function as follows:

$$\gamma_{13}(n, x_3) = \cos\frac{\pi n}{h}\gamma_{13}^{(0)}(x_3) = \Psi(n)\gamma_{13}^{(0)}(x_3) \tag{4a}$$

$$\gamma_{23}(n, x_3) = \cos\frac{\pi n}{h}\gamma_{23}^{(0)}(x_3) = \Psi(n)\gamma_{23}^{(0)}(x_3) \tag{4b}$$

where h is the wall thickness; $\Psi(n)$ is the first derivative of the shear function $\Upsilon(n)$, $\gamma_{13}^{(0)}, \gamma_{23}^{(0)}$ are mid-surface transverse shear strains given by:

$$\gamma_{13}^{(0)}(x_3) = \varphi_2(x_3) + u_{1,3}^P \tag{5a}$$

$$\gamma_{23}^{(0)}(x_3) = \varphi_1(x_3) + u_{2,3}^P \tag{5b}$$

where φ_1 and φ_2 are the rotations of the cross-section with respect to x_1 and x_3, respectively. By accounting for Eqs. (2)–(5) and mathematical manipulations, the axial displacement of the present thin-walled beams can be obtained as follows:

$$u_3(n, s, x_3) = u_3^{(0)}(x_3) + \gamma_{13}^{(0)}(x_3)\bar{X}_1(n, s) + \gamma_{23}^{(0)}(x_3)\bar{X}_2(n, s) - u_{1,3}^P(x_3)X_1(n, s)$$
$$- u_{2,3}^P(x_3)X_2(n, s) - \phi_{,z}(x_3)\bar{\varpi}(n, s) \tag{6}$$

where $\bar{X}_1(n, s) = x_1 + \Upsilon(n)x_{2,s}$, $\bar{X}_2 = x_2 - \Upsilon(n)x_{1,s}$ $\Upsilon(n) = \frac{h}{\pi}\sin\frac{\pi n}{h}$; $\bar{\varpi}(n, s) = \varpi(s) - nr_s(s)$; $\varpi(s)$ is a primary warping function defined by:

$$\varpi(s) = \int_{s_0}^{s} r_n(s)ds \tag{7}$$

The displacement field based on the STWT for thin-walled beams with open sections is finally obtained as follows:

$$u_1(n, s, x_3) = u_1^P(x_3) - \left[X_2(n, s) - x_2^P\right]\phi(x_3) \tag{8a}$$

$$u_2(n, s, x_3) = u_2^P(x_3) + \left[X_1(n, s) - x_1^P\right]\phi(x_3) \tag{8b}$$

$$u_3(n, s, x_3) = u_3^{(0)}(x_3) + \gamma_{13}^{(0)}(x_3)\bar{X}_1(n, s) + \gamma_{23}^{(0)}(x_3)\bar{X}_2(n, s) - u_{1,3}^P(x_3)X_1(n, s)$$
$$- u_{2,3}^P(x_3)X_2(n, s) - \phi_{,z}(x_3)\bar{\varpi}(n, s) \tag{8c}$$

2.2. Strains and stresses

The web and flanges of present laminated composite thin-walled beams are assumed to be composed of n_l orthotropic material layers with the same thickness. The stresses $(\sigma_{33}, \sigma_{s3}, \sigma_{n3})$ at the $k^{th}-$ layer are expressed in terms of the strains $(\varepsilon_{33}, \gamma_{s3}, \gamma_{n3})$ as follows:

$$
\begin{Bmatrix} \sigma_{33} \\ \sigma_{s3} \\ \sigma_{n3} \end{Bmatrix} = \begin{pmatrix} \bar{P}_{11} & \bar{P}_{16} & 0 \\ \bar{P}_{16} & \bar{P}_{66} & 0 \\ 0 & 0 & \bar{P}_{55} \end{pmatrix} \begin{Bmatrix} \varepsilon_{33} \\ \gamma_{s3} \\ \gamma_{n3} \end{Bmatrix} \tag{9}
$$

where $\bar{P}_{11} = \bar{Q}_{11} - \frac{\bar{Q}_{11}^2}{\bar{Q}_{22}}$, $\bar{P}_{16} = \bar{Q}_{16} - \frac{\bar{Q}_{12}\bar{Q}_{26}}{\bar{Q}_{22}}$, $\bar{P}_{66} = \bar{Q}_{66} - \frac{\bar{Q}_{26}^2}{\bar{Q}_{22}}$, $\bar{P}_{55} = \bar{Q}_{55}$; $\bar{Q}_{ij}$ are the reduced stiffness components of materials (see Reddy (2003a) for more details); the non-zero strains can be written under a compact form as follows:

$$
\varepsilon_{33}(n, s, x_3) = \varepsilon_{33}^{(0)} + n\varepsilon_{33}^{(1)} + \Upsilon(n)\varepsilon_{33}^{(2)} \tag{10a}
$$

$$
\gamma_{s3}(n, s, x_3) = n\gamma_{s3}^{(1)} + \Psi(n)\gamma_{s3}^{(2)} \tag{10b}
$$

$$
\gamma_{n3}(n, s, x_3) = \Psi(n)\gamma_{n3}^{(0)} \tag{10c}
$$

where

$$
\varepsilon_{33}^{(0)}(s, x_3) = u_{3,3}^{(0)} + \left(\gamma_{13,3}^{(0)} - u_{1,33}^P\right)x_1 + \left(\gamma_{23,3}^{(0)} - u_{2,33}^P\right)x_2 - \phi_{,33}\varpi(s) \tag{11a}
$$

$$
\varepsilon_{33}^{(1)}(s, x_3) = u_{2,33}^P x_{1,s} - u_{1,33}^P x_{2,s} + \phi_{,33}r_s \tag{11b}
$$

$$
\varepsilon_{33}^{(2)}(s, x_3) = \gamma_{13,3}^{(0)}x_{2,s} - \gamma_{23,3}^{(0)}x_{1,s} \tag{11c}
$$

$$
\gamma_{s3}^{(1)}(s, x_3) = 2\phi_{,3} \tag{11d}
$$

$$
\gamma_{s3}^{(2)}(s, x_3) = \gamma_{13}^{(0)}x_{1,s} + \gamma_{23}^{(0)}x_{2,s} \tag{11e}
$$

$$
\gamma_{n3}^{(0)}(s, x_3) = \gamma_{13}^{(0)}x_{2,s} - \gamma_{23}^{(0)}x_{1,s} \tag{11f}
$$

2.3. Hamilton's principle for laminated composite thin-walled beams

Hamilton's principle is used to derive the characteristic equations of the laminated composite thin-walled beams as follows:

$$
\int_{t_1}^{t_2} (\delta\Pi_S + \delta\Pi_W)dt = 0 \tag{12}
$$

where $\delta\Pi_S$ is the variation of strain energy of the thin-walled beam; $\delta\Pi_W$ is the variation of work done by external force. The variation of strain energy $\delta\Pi_S$ is given by:

$$
\delta\Pi_S = \int_\Omega (\sigma_{33}\delta\varepsilon_{33} + \sigma_{s3}\delta\gamma_{s3} + \sigma_{n3}\delta\gamma_{n3})d\Omega \tag{13}
$$

Substituting Eqs. (9) and (11) into Eq. (13) leads to:

$$\delta\Pi_S = \int_0^L [T_{33}\delta w_{0,3} + M_{22}\delta\gamma_{13,3}^{(0)} + M_{11}\delta\gamma_{23}^{(0)} + M_{2a}\delta u_{P,33} + M_{1a}\delta v_{P,33}$$
$$+ M_\omega\delta\phi_{,33} + Q_1\delta\delta\gamma_{13}^{(0)} + Q_2\delta\delta\gamma_{23}^{(0)} + M_{33}\delta\phi_{,3}]dx_3 \tag{14}$$

where the stress resultants $(T_{33}, M_{22}, M_{11}, M_{2a}, M_{1a}, M_\omega, Q_1, Q_2, M_{33})$ are defined as follows:

$$(T_{33}, M_{22}, M_{11}) = \int_A \sigma_{33}(1, \bar{X}_1, \bar{X}_2)dsdn \tag{15a}$$

$$(M_{2a}, M_{1a}, M_\omega) = \int_A \sigma_{33}(-X_1, -X_2, -\bar{\omega})dsdn \tag{15b}$$

$$Q_1 = \int_A \Psi(\sigma_{s3}x_{1,s} + \sigma_{n3}x_{2,s})dsdn \tag{15c}$$

$$Q_2 = \int_A \Psi(\sigma_{s3}x_{2,s} - \sigma_{n3}x_{1,s})dsdn \tag{15d}$$

$$M_{33} = \int_A 2n\sigma_{s3}dsdn \tag{15e}$$

The stress resultants and displacement gradients are associated by:

$$\begin{Bmatrix} T_{33} \\ M_{22} \\ M_{11} \\ Q_1 \\ Q_2 \\ M_{2a} \\ M_{1a} \\ M_\omega \\ M_{33} \end{Bmatrix} = \begin{bmatrix} \bar{L}_{11} & \bar{L}_{12} & \bar{L}_{13} & \bar{L}_{14} & \bar{L}_{15} & \bar{L}_{16} & \bar{L}_{17} & \bar{L}_{18} & \bar{L}_{19} \\ \bar{L}_{12} & \bar{L}_{22} & \bar{L}_{23} & \bar{L}_{24} & \bar{L}_{25} & \bar{L}_{26} & \bar{L}_{27} & \bar{L}_{28} & \bar{L}_{29} \\ \bar{L}_{13} & \bar{L}_{23} & \bar{L}_{33} & \bar{L}_{34} & \bar{L}_{35} & \bar{L}_{36} & \bar{L}_{37} & \bar{L}_{38} & \bar{L}_{39} \\ \bar{L}_{14} & \bar{L}_{24} & \bar{L}_{34} & \bar{L}_{44} & \bar{L}_{45} & \bar{L}_{46} & \bar{L}_{47} & \bar{L}_{48} & \bar{L}_{49} \\ \bar{L}_{15} & \bar{L}_{25} & \bar{L}_{35} & \bar{L}_{45} & \bar{L}_{55} & \bar{L}_{56} & \bar{L}_{57} & \bar{L}_{58} & \bar{L}_{59} \\ \bar{L}_{16} & \bar{L}_{26} & \bar{L}_{36} & \bar{L}_{46} & \bar{L}_{56} & \bar{L}_{66} & \bar{L}_{67} & \bar{L}_{68} & \bar{L}_{69} \\ \bar{L}_{17} & \bar{L}_{27} & \bar{L}_{37} & \bar{L}_{47} & \bar{L}_{57} & \bar{L}_{67} & \bar{L}_{77} & \bar{L}_{78} & \bar{L}_{79} \\ \bar{L}_{18} & \bar{L}_{28} & \bar{L}_{38} & \bar{L}_{48} & \bar{L}_{58} & \bar{L}_{68} & \bar{L}_{78} & \bar{L}_{88} & \bar{L}_{89} \\ \bar{L}_{19} & \bar{L}_{29} & \bar{L}_{39} & \bar{L}_{49} & \bar{L}_{59} & \bar{L}_{69} & \bar{L}_{79} & \bar{L}_{89} & \bar{L}_{99} \end{bmatrix} \begin{Bmatrix} u_{3,3}^{(0)} \\ \gamma_{13,3}^{(0)} \\ \gamma_{23,3}^{(0)} \\ \gamma_{13}^{(0)} \\ \gamma_{23}^{(0)} \\ u_{1,33}^P \\ u_{2,33}^P \\ \phi_{,33} \\ \phi_{,3} \end{Bmatrix} \tag{16}$$

where $\bar{L}_{ij}$ $(i, j = 1, ..., 9)$ are the stiffness components of the laminated composite thin-walled beams, which are given by:

$$\bar{L}_{11} = \int_s A_{11}ds, \quad \bar{L}_{12} = \int_s (A_{11}x_1 + E_{11}x_{2,s})ds, \quad \bar{L}_{13} = \int_s (A_{11}x_2 - E_{11}x_{1,s})ds$$

$$\bar{L}_{14} = \int_s A_{s16}x_{1,s}ds, \quad \bar{L}_{15} = \int_s A_{s16}x_{2,s}ds, \quad \bar{L}_{16} = -\int_s (A_{11}x_1 + B_{11}x_{2,s})ds$$

$$\bar{L}_{17} = \int_s (-A_{11}x_2 + B_{11}x_{1,s})ds, \quad \bar{L}_{18} = \int_s (-A_{11}\varpi + B_{11}r_s)ds, \quad \bar{L}_{19} = \int_s 2B_{16}ds$$

$$\bar{L}_{22} = \int_s \left[x_1(A_{11}x_1 + 2E_{11}x_{2,s}) + H_{11}x_{2,s}^2 \right] ds$$

$$\bar{L}_{23} = \int_s \left[x_1(A_{11}x_2 - E_{11}x_{1,s}) + x_{2,s}(E_{11}x_2 - H_{11}x_{1,s}) \right] ds$$

$$\bar{L}_{24} = \int_s (A_{s16}x_1 + D_{s16}x_{2,s})x_{1,s}ds, \quad \bar{L}_{25} = \int_s (A_{s16}x_1 + D_{s16}x_{2,s})x_{2,s}ds$$

$$\bar{L}_{26} = -\int_s \left[x_1(A_{11}x_1 + B_{11}x_{2,s}) + x_{2,s}(E_{11}x_1 + F_{11}x_{2,s}) \right] ds$$

$$\bar{L}_{27} = \int_s \left[x_1(-A_{11}x_2 + B_{11}x_{1,s}) + x_{2,s}(-E_{11}x_2 + F_{11}x_{1,s}) \right] ds$$

$$\bar{L}_{28} = \int_s x_1(-A_{11}\varpi + B_{11}r_s) + x_{2,s}(-E_{11}\varpi + F_{11}r_s)ds$$

$$\bar{L}_{29} = \int_s 2(B_{16}x_1 + F_{16}x_{2,s})ds$$

$$\bar{L}_{33} = \int_s \left[x_2(A_{11}x_2 - E_{11}x_{1,s}) - x_{1,s}(E_{11}x_2 - H_{11}x_{1,s}) \right] ds$$

$$\bar{L}_{34} = \int_s (A_{s16}x_2 - D_{s16}x_{1,s})x_{1,s}ds, \quad \bar{L}_{35} = \int_s (A_{s16}x_2 - D_{s16}x_{1,s})x_{2,s}ds$$

$$\bar{L}_{36} = -\int_s \left[x_1(A_{11}x_2 - E_{11}x_{1,s}) + x_{2,s}(B_{11}x_2 - F_{11}x_{1,s}) \right] ds$$

$$\bar{L}_{37} = \int_s \left[-x_2(A_{11}x_2 - E_{11}x_{1,s}) + x_{1,s}(B_{11}x_2 - F_{11}x_{1,s}) \right] ds$$

$$\bar{L}_{38} = \int_s \left[-\varpi(A_{11}x_2 - E_{11}x_{1,s}) + r_s(B_{11}x_2 - F_{11}x_{1,s}) \right] ds$$

$$\bar{L}_{39} = \int_s 2(B_{16}x_2 - F_{16}x_{1,s})ds$$

$$\bar{L}_{44} = \int_s \left(H_{s66} x_{1,s}^2 + H_{s44} x_{2,s}^2 \right) ds, \ \ \bar{L}_{45} = \int_s x_{1,s} x_{2,s} (H_{s66} - H_{s44}) ds,$$

$$\bar{L}_{46} = -\int_s (A_{s16} x_1 + B_{s16} x_{2,s}) x_{1,s} ds, \ \ \bar{L}_{47} = \int_s (-A_{s16} x_2 + B_{s16} x_{1,s}) x_{1,s} ds$$

$$\bar{L}_{48} = \int_s (-A_{s16} \varpi + B_{s16} r_s) x_{1,s} ds, \ \ \bar{L}_{49} = \int_s 2 x_{1,s} B_{s66} ds$$

$$\bar{L}_{55} = \int_s \left(H_{s66} x_{2,s}^2 + H_{s44} x_{1,s}^2 \right) ds, \ \ \bar{L}_{56} = -\int_s (A_{s16} x_1 + B_{s16} x_{2,s}) x_{2,s} ds$$

$$\bar{L}_{57} = \int_s (-A_{s16} x_2 + B_{s16} x_{1,s}) x_{2,s} ds, \ \ \bar{L}_{58} = \int_s (-A_{s16} \varpi + B_{s16} r_s) x_{2,s} ds$$

$$\bar{L}_{59} = \int_s 2 x_{2,s} B_{s66} ds, \ \ \bar{L}_{66} = -\int_s \left[x_1 (A_{11} x_1 + B_{11} x_{2,s}) + x_{2,s} (B_{11} x_1 + D_{11} x_{2,s}) \right] ds$$

$$\bar{L}_{67} = \int_s \left[-x_2 (A_{11} x_1 + B_{11} x_{2,s}) + x_{1,s} (B_{11} x_1 + D_{11} x_{2,s}) \right] ds$$

$$\bar{L}_{68} = \int_s \left[-\varpi (A_{11} x_1 + B_{11} x_{2,s}) + r_s (B_{11} x_1 + D_{11} x_{2,s}) \right] ds$$

$$\bar{L}_{69} = \int_s 2 (B_{16} x_1 + D_{16} x_{2,s}) ds, \ \ \bar{L}_{77} = \int_s \left[x_2 (A_{11} x_2 - B_{11} x_{1,s}) + x_{1,s} (-B_{11} x_2 + D_{11} x_{1,s}) \right] ds$$

$$\bar{L}_{78} = \int_s \left[\varpi (A_{11} x_2 - B_{11} x_{1,s}) + r_s (-B_{11} x_2 + D_{11} x_{1,s}) \right] ds$$

$$\bar{L}_{79} = \int_s 2 (-B_{16} x_2 + D_{16} x_{1,s}) ds$$

$$\bar{L}_{88} = \int_s \left[-\varpi (-\varpi A_{11} + B_{11} r_s) + r_s (-B_{11} \varpi + D_{11} r_s) \right] ds$$

$$\bar{L}_{89} = \int_s 2 (-B_{16} \varpi + D_{16} r_s) ds, \ \ \bar{L}_{99} = \int_s 4 D_{66} ds$$

$$(A_{ij}, B_{ij}, D_{ij}, E_{ij}, F_{ij}, H_{ij}, B_{sij}, H_{sij}) = \sum_{k=1}^{n_l} \left(\int_{n_k}^{n_{k+1}} \left(1, n, n^2, \Upsilon, n\Upsilon, \Upsilon^2, n\Psi, \Psi^2 \right) \bar{P}_{ij} dn \right) \tag{17}$$

The variation of potential energy $\delta\Pi_W$ of the laminated composite thin-walled beams subjected to transverse load $\bar{f}$ can be expressed as:

$$\delta\Pi_W = -\int_0^L \bar{f}\,\delta u_2^P\,dx_3 \tag{18}$$

2.4. Ritz-type series solution

By noticing that $u_3^{(0)}(x_3)$, $u_1^P(x_3)$, $u_2^P(x_3)$, $\gamma_{13}^{(0)}(x_3)$, $\gamma_{23}^{(0)}(x_3)$ and $\phi(x_3)$ are considered as variables to be determined, based on the Ritz method, these components can be approximated as follows:

$$\left\{u_1^P, u_2^P, \phi\right\}(x_3) = \sum_{j=1}^m \chi_j(x_3)\left\{u_{1j}^P, u_{2j}^P, \phi_j\right\} \tag{19a}$$

$$\left\{u_3^{(0)}, \gamma_{13}^{(0)}, \gamma_{23}^{(0)}\right\}(x_3) = \sum_{j=1}^m \chi_{j,3}(x_3)\left\{u_{3j}, \xi_j, \eta_j\right\} \tag{19b}$$

where u_{3j}, u_{1j}^P, u_{2j}^P, ξ_j, η_j and ϕ_j are the six unknowns to be solved; $\chi_j(x_3)$ are shape functions. These shape functions in Eq. (19) should be constructed to satisfy the specified essential boundary conditions (BCs). For the present article, the shape functions are proposed under hybrid functions which are composed of admissible functions and exponential ones. It is observed that these functions satisfy various BCs such as simply-supported (S-S), clamped-free (C-F) and clamped-clamped (C-C).

- S-S: $\chi(x_3) = \frac{x_3}{L}\left(1 - \frac{x_3}{L}\right)e^{\frac{-jx_3}{L}}$
- C-F: $\chi(x_3) = \left(\frac{x_3}{L}\right)^2 e^{\frac{-jx_3}{L}}$
- C-C: $\chi(x_3) = \left(\frac{x_3}{L}\right)^2\left(1 - \frac{x_3}{L}\right)^2 e^{\frac{-jx_3}{L}}$

Substituting Eq. (19) into Eq. (12) accounting for Eqs. (13) and (18) leads to the characteristic equations for bending analysis of laminated composite thin-walled beams as follows:

$$\mathbf{Kd} = \mathbf{F} \tag{20}$$

where $\mathbf{K}, \mathbf{F}$ are the stiffness matrix and force vector, respectively; $\mathbf{d} = \begin{bmatrix}\mathbf{u}_3 & \mathbf{u}_1^P & \mathbf{u}_2^P & \boldsymbol{\xi} & \boldsymbol{\eta} & \boldsymbol{\Phi}\end{bmatrix}^T$ is the displacement vector. The components of the stiffness matrix $\mathbf{K}$ are expressed by:

$$\mathbf{K} = \begin{bmatrix} \mathbf{K}^{11} & \mathbf{K}^{12} & \mathbf{K}^{13} & \mathbf{K}^{14} & \mathbf{K}^{15} & \mathbf{K}^{16} \\ \mathbf{K}^{12} & \mathbf{K}^{22} & \mathbf{K}^{23} & \mathbf{K}^{24} & \mathbf{K}^{25} & \mathbf{K}^{26} \\ \mathbf{K}^{13} & \mathbf{K}^{23} & \mathbf{K}^{33} & \mathbf{K}^{34} & \mathbf{K}^{35} & \mathbf{K}^{36} \\ \mathbf{K}^{14} & \mathbf{K}^{24} & \mathbf{K}^{34} & \mathbf{K}^{44} & \mathbf{K}^{45} & \mathbf{K}^{46} \\ \mathbf{K}^{15} & \mathbf{K}^{25} & \mathbf{K}^{35} & \mathbf{K}^{45} & \mathbf{K}^{55} & \mathbf{K}^{56} \\ \mathbf{K}^{16} & \mathbf{K}^{26} & \mathbf{K}^{36} & \mathbf{K}^{46} & \mathbf{K}^{56} & \mathbf{K}^{66} \end{bmatrix} \tag{21}$$

where

$$K_{ij}^{11} = \bar{L}_{11}S_{ij}^{22}, \quad K_{ij}^{12} = \bar{L}_{16}S_{ij}^{22}, \quad K_{ij}^{13} = \bar{L}_{17}S_{ij}^{22}, \quad K_{ij}^{14} = \bar{L}_{12}S_{ij}^{22} + \bar{L}_{14}S_{ij}^{12}$$

$$K_{ij}^{15} = \bar{L}_{13}S_{ij}^{22} + \bar{L}_{15}S_{ij}^{12}, \ K_{ij}^{16} = \bar{L}_{18}S_{ij}^{22} + \bar{L}_{19}S_{ij}^{12}, \ K_{ij}^{22} = \bar{L}_{66}S_{ij}^{22}, \ K_{ij}^{23} = \bar{L}_{67}S_{ij}^{22}$$

$$K_{ij}^{24} = \bar{L}_{26}S_{ij}^{22} + \bar{L}_{46}S_{ij}^{12}, \ K_{ij}^{25} = \bar{L}_{36}S_{ij}^{22} + \bar{L}_{56}S_{ij}^{12}, \ K_{ij}^{26} = \bar{L}_{68}S_{ij}^{22} + \bar{L}_{69}S_{ij}^{12}$$

$$K_{ij}^{33} = \bar{L}_{77}S_{ij}^{22}, \ K_{ij}^{34} = \bar{L}_{27}S_{ij}^{22} + \bar{L}_{47}S_{ij}^{12}, \ K_{ij}^{35} = \bar{L}_{37}S_{ij}^{22} + \bar{L}_{57}S_{ij}^{12}$$

$$K_{ij}^{36} = \bar{L}_{78}S_{ij}^{22} + \bar{L}_{79}S_{ij}^{12}, \ K_{ij}^{44} = \bar{L}_{22}S_{ij}^{22} + \bar{L}_{24}\left(S_{ij}^{12} + S_{ij}^{21}\right) + \bar{L}_{44}S_{ij}^{11}$$

$$K_{ij}^{45} = \bar{L}_{23}S_{ij}^{22} + \bar{L}_{25}S_{ij}^{12} + \bar{L}_{34}S_{ij}^{21} + \bar{L}_{45}S_{ij}^{11}, \ K_{ij}^{46} = \bar{L}_{28}S_{ij}^{22} + \bar{L}_{29}S_{ij}^{12} + \bar{L}_{48}S_{ij}^{21} + \bar{L}_{49}S_{ij}^{11}$$

$$K_{ij}^{55} = \bar{L}_{33}S_{ij}^{22} + \bar{L}_{35}\left(S_{ij}^{12} + S_{ij}^{21}\right) + \bar{L}_{55}S_{ij}^{11}, \ K_{ij}^{56} = \bar{L}_{38}S_{ij}^{22} + \bar{L}_{39}S_{ij}^{12} + \bar{L}_{58}S_{ij}^{21} + \bar{L}_{59}S_{ij}^{11}$$

$$K_{ij}^{66} = \bar{L}_{88}S_{ij}^{22} + \bar{L}_{89}\left(S_{ij}^{12} + S_{ij}^{21}\right) + \bar{L}_{99}S_{ij}^{11}$$

$$S_{ij}^{rs} = \int_{0}^{L} \frac{\partial^r \varphi_i}{\partial x_3^r} \frac{\partial^s \varphi_j}{\partial x_3^s} dx_3 \tag{22}$$

2.5. Polynomial chaos expansion

The responses for computational models with input uncertainties can be approximated by using a series of orthogonal functions as follows:

$$\bar{r}(\mathbf{q}) = \sum_{i=0}^{\infty} \beta_i \Omega_i(\mathbf{q}) \tag{23}$$

where $\mathbf{q}$ is a vector of d independent random variables mapped to physical random parameters; Ω_i are multivariate orthogonal basis functions; β_i are the unknown coefficients. In order to determine these coefficients β_i, two main following approaches could be considered: polynomial chaos expansion (PCE) and stochastic collocation. In the PCE approach, the coefficients are estimated by fitting a suitable set of basis functions using either a projection approach or least-square regression. Meanwhile, the stochastic collocation approach constructs interpolation polynomials for known coefficients at specific collocation points (Dalbey et al. 2020). In this manuscript, the PCE method is developed using multivariate Hermite polynomials as basis functions and standard normal variables $\mathbf{q}$ as inputs (Xiu and Karniadakis 2002).

In practice, the number of series terms in Eq. (23) is reduced to a carefully chosen finite number, so that the model responses are sufficiently accurate while using a minimal computing resource. Given N_{rv} random variables and polynomial order p, the number of polynomial terms N is the permutation of p and N_{rv}, which can be expressed as: $N = \frac{(N_{rv}+p)!}{N_{rv}!p!}$, Eq. (23) therefore becomes:

$$\bar{r}(\mathbf{q}) = \sum_{i=0}^{N-1} \beta_i \Omega_i(\mathbf{q}) + \varepsilon \tag{24}$$

where the basis functions Ω_i are multivariate Hermite polynomials and the associated coefficients β_i need to be determined to minimize the residual term.

2.5.1. Spectral projection approach

In the spectral projection approach, the residual term must be orthogonal to the projection of the response in the selected space. Therefore, the inner product of the residual and each basis function is zero. By taking the inner product of both sides of Eq. (24) with Ω_j and enforcing orthogonality:

$$\langle \bar{r}, \Omega_j \rangle = \sum_{i=0}^{N} \beta_i \langle \Omega_i, \Omega_j \rangle \tag{25}$$

Because Ω_j are mutually orthogonal, Eq. (25) becomes:

$$\beta_i = \frac{\langle \bar{r}, \Omega_i \rangle}{\langle \Omega_i, \Omega_i \rangle} = \frac{1}{\langle \Omega_i, \Omega_i \rangle} \int \bar{r} \Omega_i \rho_Q(\mathbf{q}) d\mathbf{q} \tag{26}$$

In order to solve for β_i in Eq. (26), a number of sampling responses $\bar{r}$ is required. The multidimensional integral representing the inner product of beam responses $\bar{r}$ and the basis function Ω are calculated using the Gaussian quadrature numerical method. The order p of the basis function and the number or quadrature points n_s are chosen based on the stochastic model precision requirement. For a beam model with N_{rv} random input variables and p^{th} order Hermite basis functions, the number of quadrature points are given as $n_s = (p+1)^{N_{rv}}$. This also means n_s samples of beam model need to be generated and solved. On the account of this n_s formula, the computational cost of this spectral projection approach does not scale up well with a high order basis function and large number of random input parameters.

2.5.2. Least-square regression approach

Let $\mathfrak{R} = \left\{ \mathbf{q}^1, ..., \mathbf{q}^{N_s} \right\}$ be a set of $N_s(N_s > N)$ realizations of input random vector, and $\mathbf{R} = \left\{ \bar{r}^1, ..., \bar{r}^{N_s} \right\}$ be corresponding output evaluations $(\bar{r}^i = \bar{r}(\mathbf{q}^i), i = 1, ..., N_s)$. The vector of residuals can be estimated from Eq. (24) in the compact form:

$$\Upsilon = \mathbf{R} - \beta^T \mathbf{\Omega} \tag{27}$$

where $\mathbf{\Omega}$ is the matrix whose elements are given by $\Omega_{ij} = \Omega_j(\mathbf{q}^i), i = 1, ..., N_s; \ j = 1, ..., N$. The coefficients β are estimated by minimizing the L_2- norm (least-square regression) of the residual followed as:

$$\beta = Arg \ \min \| \mathbf{R} - \beta^T \mathbf{\Omega} \|_2^2 \tag{28}$$

Solving Eq. (28), the coefficients are given by:

$$\beta = \left(\mathbf{\Omega}^T \mathbf{\Omega} \right)^{-1} \mathbf{\Omega}^T \mathbf{R} \tag{29}$$

2.6. Sensitivity analysis

In addition to the mere stochastic output of the beam model, the variance-based quantification of each random input parameter's influence on the model output is also discussed in this article. The sources of variance in the model output can be attributed to individual inputs, and thus, the importance of each input can be ranked accordingly. Among various sensitivity analysis methods, the Sobol indices (Sobol 1993) are the most widely used one. The Sobol's first-order and total-order indices are given by Saltelli et al. (2010) as follows:

$$\text{First} - \text{order Sobol index}: \quad S_i = \frac{Var_{\mathbf{q}^i}(E_{q_{\sim i}}(\bar{r}|\mathbf{q}^i))}{Var(\bar{r})} \mathbf{q}^{k \neq i} \tag{30a}$$

$$\text{Total} - \text{order Sobol index}: \quad S_{Ti} = 1 - \frac{Var_{\mathbf{q}^{\sim i}}(E_{\mathbf{q}^i}(\bar{r}|\mathbf{q}^{\sim i}))}{Var(\bar{r})} \tag{30b}$$

Both kinds of these Sobol indices are normalized by $Var(\bar{r})$ but the difference in meaning is first-order Sobol indices measure only the impact of a sole particular input variable $\mathbf{q}^i$, while total-order Sobol indices also take into account the impact of interactions between $\mathbf{q}^i$ and other variables $\mathbf{q}^{k \neq i}$. These indices can be computed using crude Monte Carlo simulation with the computational cost of $(N_{rv} + 2) \times N_s$ or using PCE with no additional cost. The Sobol's first-order and total-order indices can be estimated as follows:

$$S_i = \frac{D_i}{Var(\bar{r})} \tag{31a}$$

$$S_{Ti} = \frac{D_{Ti}}{Var(\bar{r})} \tag{31b}$$

where $D_i = \sum_{j \in \Gamma_i} \beta_j^2 \langle \Omega_j(\mathbf{q}^i), \Omega_j(\mathbf{q}^i) \rangle j$, Γ_i comprises all indices j such that the multivariate function Ω_j only contains the variable $\mathbf{q}^i$; $D_{Ti} = \sum_{j \in \Gamma_{Ti}} \beta_j^2 \langle \Omega_j(\text{II}), \Omega_j(\text{II}) \rangle$, Γ_{Ti} comprises all indices j such that the multivariate function Ω_j must contain variable $\mathbf{q}^i$; index j depends on how the list of multivariate functions is sorted.

2.7. Artificial neural network (ANN)

The Artificial Neural Network (ANN) in this article consists of layers of interconnected neurons organized into three main layers: the input layer, hidden layer(s), and the output layer. This architecture is shown in Figure 2. The input layer receives the raw input data whose each variable is assigned into a node. Each connection between an input node and a neuron in the hidden layer contributes to the weighted sum of inputs for that neuron. The initial weight values are random to avoid identical and redundant neurons in the network. The weighted sum is then passed through an activation function. Activation functions are preferably non-linear so that the neural network can learn complex models and their data relationship better. The weighted sum and activation function steps are repeated for the output layer, producing the final output of the neural
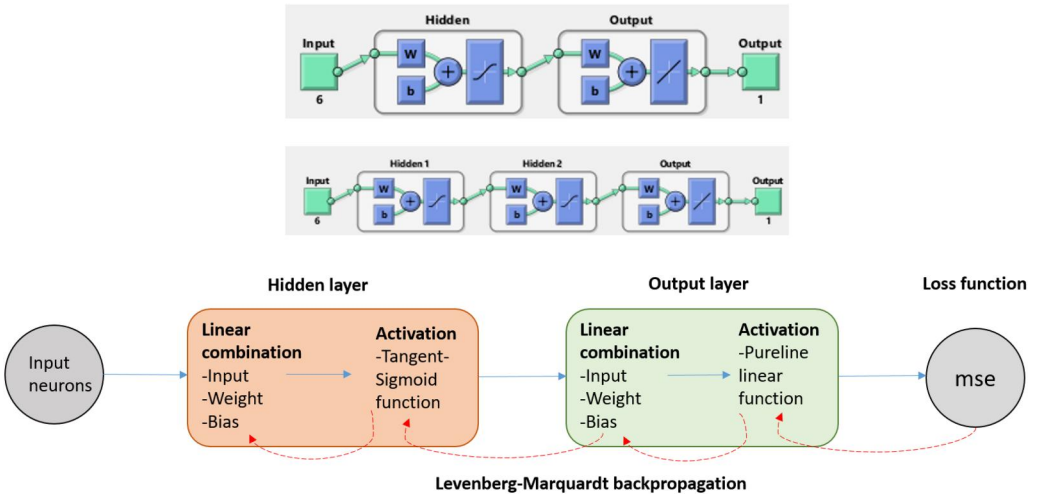

Figure 2. Architecture and workflow of the ANN with 1 and 2 hidden layers.

network. The difference between this predicted output and the true output obtained from the beam model are assessed using a loss function. Usually, further training iterations or epochs are needed to adjust the weight and minimize the loss function. In the present study, the mean square error (MSE) is used as the loss function. The root mean square error (RMSE) of the test set is also computed in this article for future references.

The network uses the computed loss to update its weights and bias through a process known as backpropagation. This involves calculating the gradient of the loss with respect to the weights and adjusting the weights in the opposite direction of the gradient to minimize the loss. This article applies the Levenberg–Marquardt backpropagation algorithm to train the ANN from the stochastic thin-walled beam data. The predicted output data of ANN and PCE are compared in terms of computing performance and accuracy.

3. Numerical results

The numerical studies in this section can be separated into two parts. First, the present thin-walled I-beam model with fixed material properties are analyzed and verified with other previous works. In the second part, the chosen beam's material properties are randomly generated to be the stochastic input variables for the Monte Carlo Simulation (MCS), Polynomial Chaos Expansion (PCE), and Artificial Neural Network (ANN) numerical analysis.

The beams studied throughout this section are laminated composite thin-walled I-beams composed of 16 angle plies with uniform thickness. Unless stated otherwise, these are made from glass-epoxy material whose mechanical properties are as follows: $E_1 = 53.78GPa$, $E_2 = E_3 = 17.93GPa$, $G_{12} = G_{13} = 8.96GPa$, $G_{23} = 3.45GPa$, $\nu_{12} = \nu_{13} = 0.25$. These material properties along with the applied uniformly distributed load (UDL) q are the six stochastic input parameters that are randomized based on the lognormal distribution and the coefficient of variation $CoV = 0.1$. This CoV is the ratio between the sample's standard deviation and mean. Referring to Figure 3, the dimensions of the top flange, bottom flange and the web are $h_1 = h_2 = h_3 = 0.00208m$ and $b_1 = b_2 = b_3 = 0.05m$. The beam's length-to-depth ratio varies between the forthcoming examples and can be from $L/b_3 = 5$ to $L/b_3 = 50$.

3.1. Deterministic beam model

Example 1: Convergence study
This example examines the convergence of the current solution for analyzing the displacement of laminated composite I-beams under different boundary conditions, namely, simply supported (S-S), clamped-free (C-F), and clamped-clamped (C-C). The angle-ply stacking sequence for the I-beams' flanges and web is $[45^o/-45^o]_{4s}$, and these 16 laminate plies have a uniform thickness. The beam is under a UDL $q = 1kN/m$. The results presented in Table 1 reveal that the proposed solutions converge with series number $m = 10$ for S-S and C-F boundary conditions and $m = 8$ for C-C boundary condition. These series numbers will be employed in subsequent analyses accordingly.

Example 2: Verification and parametric study
For the purpose of verification, this section compare the predictions made by the present thin-walled beam model with the past experimental test (Colombi and Poggi 2006) and other authors' results (Lee and Lee 2004; Lee 2005). The following tables and figures describe the static behaviors of isotropic steel beam and composite I-beams with different symmetrical lay-up $[\theta^o/-\theta^o]_{4s}$ in both flanges and the web.
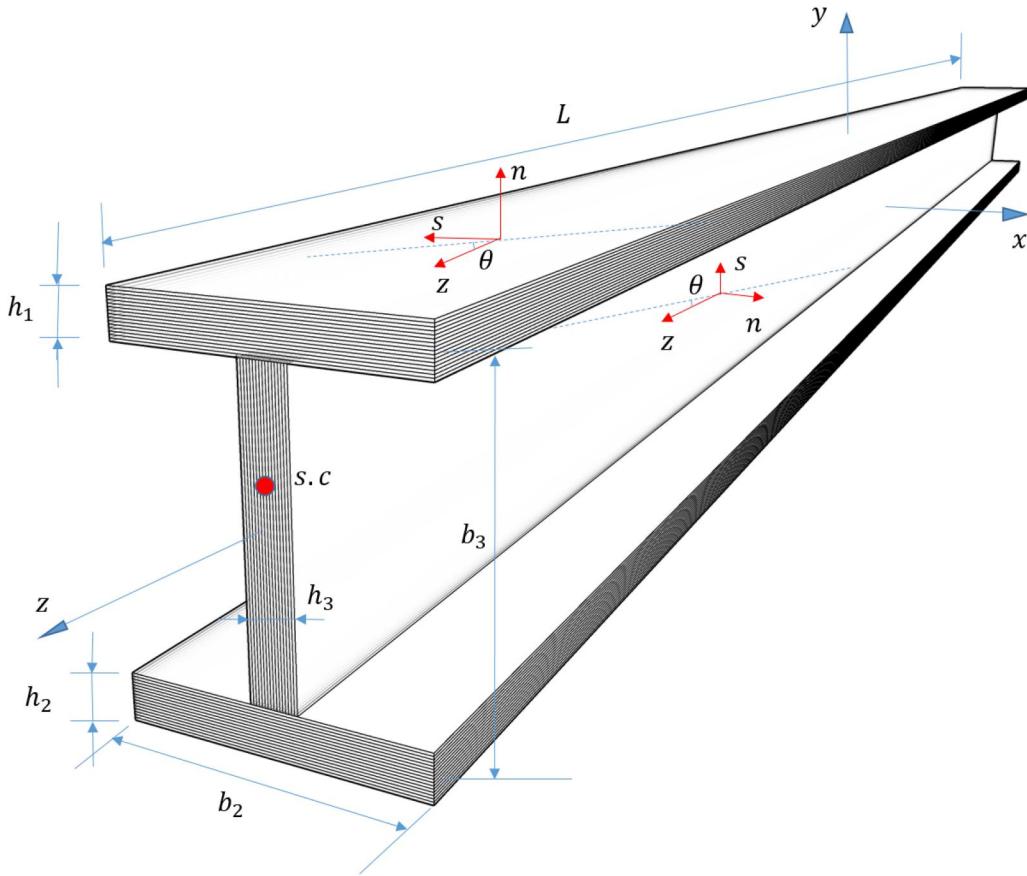
Figure 3. Geometry of laminated composite thin-walled I-beams.

Table 1. Convergence of deterministic mid-span displacement for laminated composite thin-walled I-beam with different boundary conditions.

BC	m					
	2	4	6	8	10	12
S-S	13.000	13.398	13.484	13.478	13.479	13.479
C-C	2.744	2.735	2.738	2.740	2.740	2.739
C-F	44.312	45.679	45.806	45.799	45.802	45.802

Figure 4 manifests the accuracy of the present thin-walled beam model in the matching of mid-span deflections with the test results conducted by Colombi and Poggi (2006). According to Colombi and Poggi, the standard hot rolled carbon steel profiles HEA 140 of quality Fe E 275 were used for the experiments. There is no definite specifications of the carbon steel used and its material properties can vary based on several factors such as heat treatment, manufacturing process and steel alloy composition. Therefore, the predictions computed in Figure 4 are for the isotropic steel beams with the following assumed properties: $E = 190GPa$, $G = 73GPa$ and $v = 0.3$.

Table 2 presents the simply supported laminated composite thin-walled beam's mid-span deflection under a UDL $q = 1kN/m$. It is evident that the current solutions for FTWT align exceptionally with the findings of previous studies and the ABAQUS software (Lee 2005; Lee and Lee 2004). Moreover, Table 3 further confirms the accuracy of the present deterministic beam model under C-C and C-F BCs by demonstrating that the present FTWT results are highly
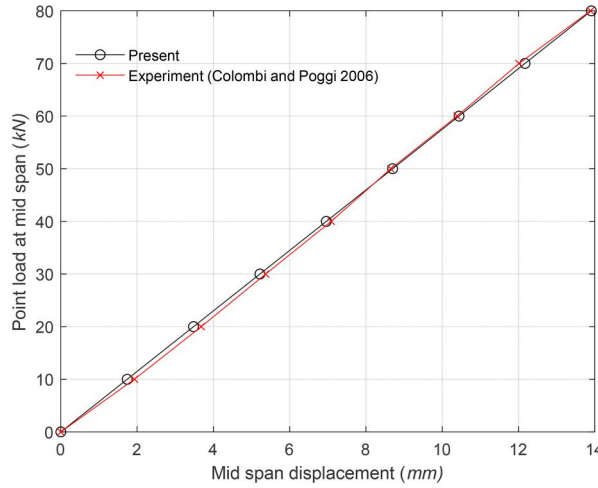
Figure 4. Verification with experimental static test of the HEA 140 carbon steel beam ($E = 190GPa$, $G = 73GPa$, $v = 0.3$).

Table 2. Verification of deterministic mid-span displacements for laminated composite thin-walled I-beam under a uniformly distributed load (cm, $L/b_3 = 50$, S-S BC).

	References				
Lay-ups	CTWT (Lee and Lee 2004)	FTWT (Lee 2005)	ABAQUS (Lee and Lee 2004)	Present (FTWT)	Present (STWT)
$[0]_{16}$	6.233	6.259	6.340	6.280	6.327
$[15/-15]_{4s}$	6.899	6.923	6.989	6.940	6.981
$[30/-30]_{4s}$	9.290	9.314	9.360	9.323	9.356
$[45/-45]_{4s}$	13.421	13.446	13.479	13.450	13.480
$[60/-60]_{4s}$	16.962	16.992	17.023	16.990	17.019
$[75/-75]_{4s}$	18.411	18.449	18.490	18.440	18.468
$[0/90]_{4s}$	9.299	9.381	9.400	9.383	9.416

Table 3. Verification of deterministic mid-span displacements for laminated composite thin-walled I-beam under a uniformly distributed load (cm, $L/b_3 = 50$, C-F and C-C BCs).

	C-F			C-C		
Lay-ups	Present (FTWT)	Present (STWT)	Nguyen and Nguyen (2020)	Present (FTWT)	Present (STWT)	Nguyen and Nguyen (2020)
$[0]_{16}$	21.332	21.472	21.274	1.292	1.344	1.274
$[15/-15]_{4s}$	23.577	23.699	23.535	1.420	1.459	1.406
$[30/-30]_{4s}$	31.685	31.783	31.666	1.890	1.922	1.884
$[45/-45]_{4s}$	45.718	45.805	45.718	2.712	2.741	2.713
$[60/-60]_{4s}$	57.755	57.839	57.777	3.420	3.447	3.427
$[75/-75]_{4s}$	62.682	62.765	62.728	3.709	3.737	3.724
$[0/90]_{4s}$	31.888	31.986	31.889	1.904	1.935	1.904

consistent with earlier study by Nguyen and Nguyen (2020). It can also be seen that the beam deflections increase as the ply angles increase, and the deflection of the $[0^o/90^o]_{4s}$ beam is similar to that of the $[30^o/-30^o]_{4s}$. However, due to the additional shear effect, the results for STWT in both Tables 2 and 3 are slightly higher than FTWT and CTWT. The discrepancies due to this shear effect particularly grow wider as the beam becomes thicker. To demonstrate this remark, Table 4 compares the FTWT and the STWT for the laminated composite thin-walled beams with $L/b_3 = 5$ and $L/b_3 = 10$ under all boundary conditions. The beam's mid-span displacements

Table 4. Comparison of the FTWT and the STWT when computing the deterministic mid-span displacements for laminated composite thin-walled I-beam under a uniformly distributed load (*mm*, $L/b_3 = 5$ and 10, $q = 100kN/m$).

| Lay-ups	S-S		C-C		CF	
	Present (FTWT)	Present (STWT)	Present (FTWT)	Present (STWT)	Present (FTWT)	Present (STWT)
$L/b_3 = 5$						
$[0]_{16}$	1.097	1.570	0.581	1.037	3.524	4.925
$[15/-15]_{4s}$	1.102	1.513	0.535	0.932	3.567	4.784
$[30/-30]_{4s}$	1.258	1.587	0.503	0.820	4.134	5.113
$[45/-45]_{4s}$	1.636	1.929	0.551	0.834	5.434	6.305
$[60/-60]_{4s}$	1.980	2.264	0.613	0.887	6.610	7.453
$[75/-75]_{4s}$	2.122	2.403	0.639	0.910	7.093	7.924
$[0/90]_{4s}$	1.286	1.615	0.526	0.843	4.221	5.195
$L/b_3 = 10$						
$[0]_{16}$	11.867	13.761	3.822	5.647	39.525	45.138
$[15/-15]_{4s}$	12.685	14.331	3.796	5.384	42.414	47.299
$[30/-30]_{4s}$	16.180	17.495	4.242	5.510	54.442	58.342
$[45/-45]_{4s}$	22.647	23.821	5.427	6.559	76.491	79.974
$[60/-60]_{4s}$	28.276	29.412	6.524	7.619	95.643	99.013
$[75/-75]_{4s}$	30.581	31.704	6.975	8.057	103.489	106.818
$[0/90]_{4s}$	16.363	17.680	4.348	5.617	55.025	58.926

computed using STWT are considerably higher than when using FTWT. Furthermore, the higher-order shear effect on the laminated composite thin-walled beam's mid-span displacement is computed for many cases of the beam's lay-up and length-to-height ratios L/b_3. This so-called higher-order shear effect is defined as the percentage difference between the beam responses yielded from the STWT and FTWT. It is observed from Figure 5 that the shear effect is the highest at $L/b_3 = 5$ and drastically drops as the L/b_3 increases to 10 and subsequently, 15. After the point where $L/b_3 = 15$, the plots for all cases of beam lay-ups reach a plateau with the increasing value of the abscissa. Apart from the aforementioned pattern, it is clear that the shear effect on the beam under C-C boundary condition is roughly more than double the shear effect on the cantilever beam. These findings are beneficial in accurately predicting the laminated composite thick thin-walled beam's behaviors under extremely high loads. These results indicate that the thick and short beams in bending are more likely to fail due to the transverse shear stress.

3.2. Stochastic analysis

The procedures for the stochastic analysis is presented in the Figure 6 flowchart. While Section 3.1 emphasizes the accuracy of the sinusoidal thin-walled beam model, this section aims to maximize the efficiency of the computational model and thus, reduce the computing time. On average, it takes authors' computer 100 s to run a case of thin-walled beam analysis. Most of this computing time is attributed to the evaluation of many integrals for the material coefficients and stiffness matrix. In order to make the MCS with 10^6 samples feasible, all these integrals are pre-computed and then later assembled every time a set of stochastic inputs is generated. The computing time displayed in Tables 5–7 are measured from the moment that the aforementioned integrals have been pre-computed to when all the desired outputs have been found. Apparently, the time measured here are subjected to the researchers' computer system but it should provide a good reference for comparing the methods' efficiency. The applied UDL q in this section are $q = 10kN/m$ for C-C boundary condition and $q = 1kN/m$ for S-S and C-F boundary conditions.
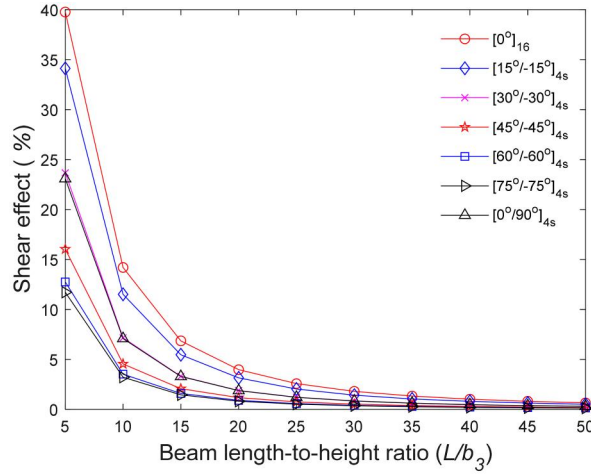
a) C-F
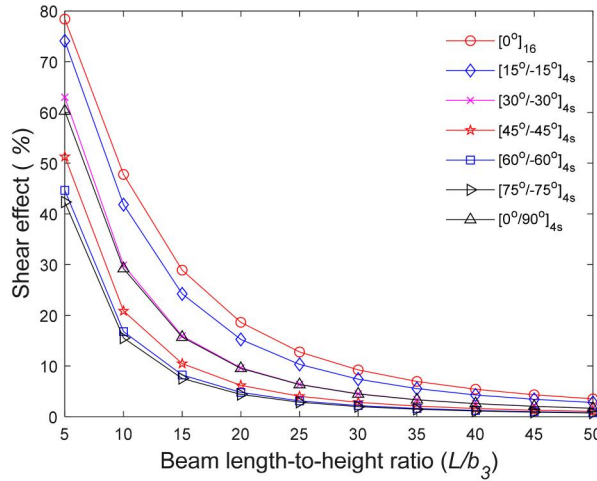
b) C-C

Figure 5. High-order shear effect (%) on the mid-span displacement of laminated composite glass-epoxy beam with various span-to-height (L/b_3) ratios and lay-ups (C-C and C-F BCs).

Example 3: Statistics of the laminated composite thin-walled beam outputs

The accuracy and efficiency of the Polynomial Chaos Expansion (PCE) surrogate model are verified through Monte Carlo Simulation (MCS) with $N_s = 100,000$ samples (S-S and CF boundary conditions) and $N_s = 1,000,000$ samples (C-C boundary condition). It would have taken days to compute the 100,000 outputs for a case of beam using MCS, but in this article, the time-consuming integrals of material coefficients and stiffness matrix are pre-computed. This leads to a great reduction in computing time, as shown in Tables 5–7 but this workaround might not be possible for other stochastic mechanical models. For the PCE method, the third-order Hermite polynomials with six variables are employed. To construct the PCE model, 252 and 4,096 output samples from the beam solver are needed for the Least-square regression (Shaker et al. 2008) approach and Spectral projection (SP) approaches, respectively. Tables 5–7 compare the four first statistical moments (mean, standard deviation, skewness, and kurtosis) of the mid-span and end-span displacements obtained from the MCS and PCE models.
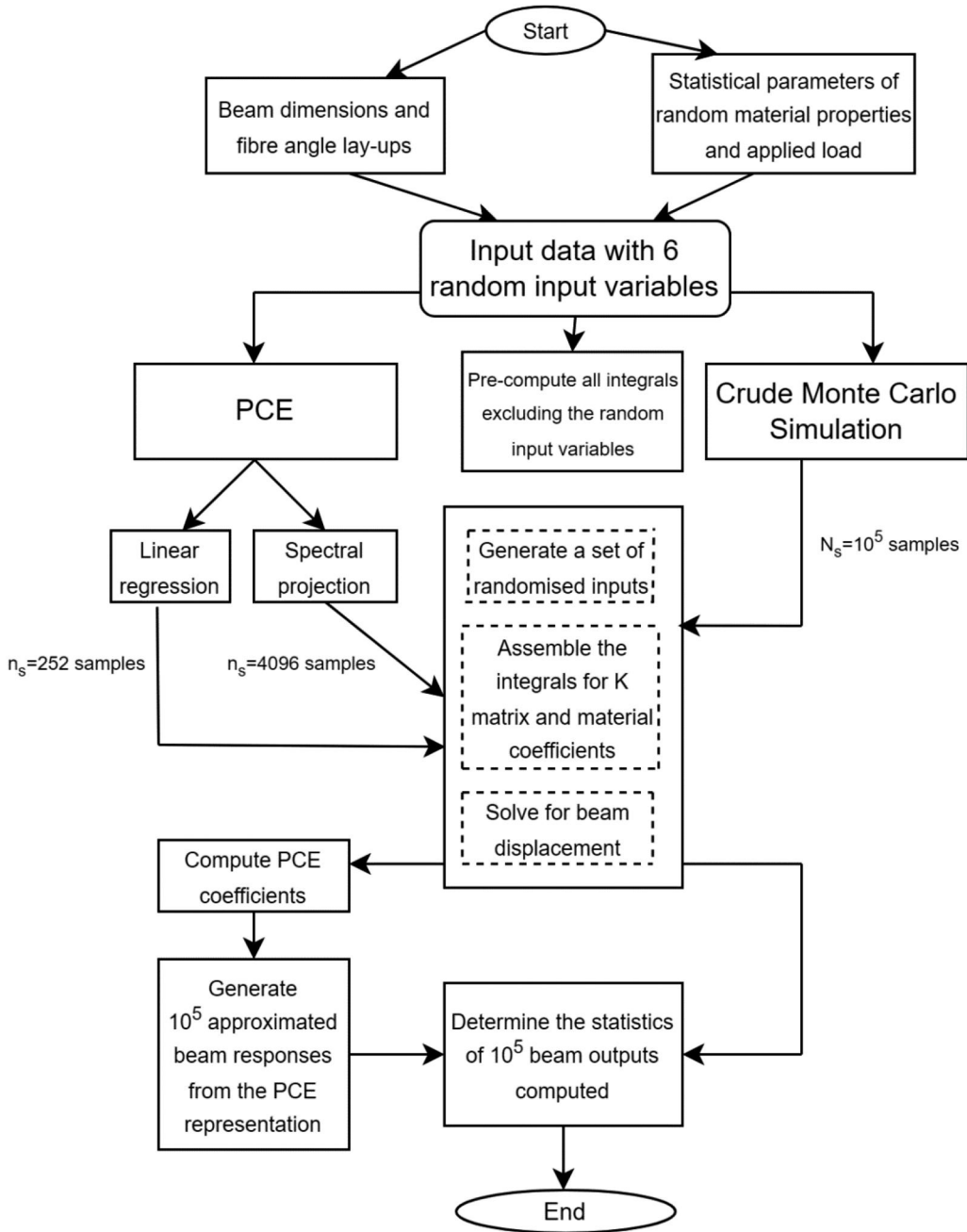
Figure 6. Flowchart for the stochastic static analysis of thin-walled I-beams using polynomial Chaos expansion and Monte Carlo simulation.

The mean and standard deviation of the fundamental frequencies from both the MCS and PCE models show excellent agreements in all cases. Most of the skewness and kurtosis values also closely match, with only a few cases showing slight differences in these higher-order statistical moments. Both the LR and SP approaches using the PCE method prove to be far more efficient than the MCS by reducing the computing time significantly while possessing closely similar key statistical metrics.

Table 5. Mean, standard deviation, kurtosis and skewness of mid-span transverse displacement (*mm*) for laminated composite thin-walled beams with different lay-ups and S-S boundary condition.

Lay-ups	Statistical moments	$L/b_3 = 20$			$L/b_3 = 50$		
		LR	SP	MC	LR	SP	MC
$[0/90]_{4s}$	Mean	1.76	1.76	1.77	63.87	63.94	63.93
	SD	0.24	0.24	0.24	9.00	8.99	9.04
	Kurtosis	3.33	3.32	3.31	3.29	3.32	3.34
	Skewness	0.42	0.42	0.42	0.42	0.42	0.43
	Computing time (s)	0.58	3.95	73.72	0.77	3.10	81.27
$[15/-15]_{4s}$	Mean	1.91	1.91	1.91	70.41	70.41	70.41
	SD	0.26	0.25	0.26	9.54	9.56	9.55
	Kurtosis	3.30	3.24	3.28	3.31	3.29	3.27
	Skewness	0.40	0.39	0.40	0.41	0.41	0.40
	Computing time (s)	0.46	3.60	89.91	0.46	3.40	96.35
$[30/-30]_{4s}$	Mean	2.50	2.50	2.50	94.20	94.28	94.31
	SD	0.31	0.31	0.31	11.62	11.60	11.66
	Kurtosis	3.28	3.28	3.25	3.23	3.21	3.22
	Skewness	0.38	0.38	0.38	0.37	0.36	0.36
	Computing time (s)	0.36	3.20	88.50	0.41	3.14	98.31
$[45/-45]_{4s}$	Mean	3.55	3.56	3.56	136.05	135.92	136.01
	SD	0.44	0.44	0.44	16.96	16.84	17.00
	Kurtosis	3.29	3.23	3.31	3.35	3.26	3.29
	Skewness	0.39	0.37	0.39	0.42	0.38	0.39
	Computing time (s)	0.39	2.90	92.68	0.38	3.19	98.40

Table 6. Mean, standard deviation, kurtosis and skewness of mid-span transverse displacement (*mm*) for laminated composite beams with different lay-ups and C-F boundary condition.

Lay-ups	Statistical moments	$L/b_3 = 10$			$L/b_3 = 20$		
		LR	SP	MC	LR	SP	MC
$[0/90]_{4s}$	Mean	1.12	1.12	1.12	16.07	16.08	16.08
	SD	0.15	0.15	0.15	2.24	2.24	2.23
	Kurtosis	3.29	3.32	3.31	33.14	3.34	3.36
	Skewness	0.40	0.42	0.41	4.19	0.43	0.43
	Computing time (s)	0.79	3.84	79.19	1.10	3.30	79.62
$[15/-15]_{4s}$	Mean	1.20	1.20	1.20	17.62	17.63	17.62
	SD	0.16	0.16	0.16	2.37	2.38	2.36
	Kurtosis	3.31	3.28	3.28	32.70	3.27	3.29
	Skewness	0.41	0.40	0.39	3.99	0.40	0.40
	Computing time (s)	0.50	3.01	88.34	0.90	3.15	87.62
$[30/-30]_{4s}$	Mean	1.54	1.54	1.54	23.42	23.41	23.39
	SD	0.19	0.19	0.19	2.88	2.89	2.88
	Kurtosis	3.27	3.21	3.26	32.38	3.26	3.22
	Skewness	0.37	0.37	0.38	3.68	0.39	0.38
	Computing time (s)	0.43	2.80	89.26	0.80	3.02	103.35
$[45/-45]_{4s}$	Mean	2.17	2.17	2.17	33.63	33.65	33.64
	SD	0.27	0.27	0.27	4.17	4.18	4.16
	Kurtosis	3.26	3.24	3.28	32.61	3.26	3.30
	Skewness	0.37	0.37	0.38	3.82	0.38	0.39
	Computing time (s)	0.48	2.78	88.30	0.92	3.38	100.93

To better visualize the output data, Figs. 7 and 8 show the probability density function (PDF) and cumulative distribution function (CDF) plots produced from the MCS and PCE methods for the quantity of interest (QoI). The PDF and CDF graphs for outputs from MCS and PCE are coincident in most beam displacement values. The only differences are at the peaks of the graphs for PDF and below the part where $P(X \leq x) < 10^{-3}$ for CDF. This is due to the lack of samples at those certain points in the output data distribution.

Zooming in the sample output data, Figs. 9–11 show the percentage difference between the MCS outputs and PCE-LR or SP outputs simulation-by-simulation. For every simulation, the random input parameters for both MCS and PCE methods are identical. For the S-S and C-F

Table 7. Mean, standard deviation, kurtosis and skewness of mid-span transverse displacement (*mm*) for laminated composite beams with different lay-ups and C-C boundary condition.

| Lay-ups	Statistical moments	$L/b_3 = 20$			$L/b_3 = 50$		
		LR	SP	MC	LR	SP	MC
$[0/90]_{4s}$	Mean	4.69	4.69	4.69	135.07	135.09	135.09
	SD	0.58	0.58	0.58	18.52	18.51	18.53
	Kurtosis	3.24	3.26	3.25	3.31	3.32	3.33
	Skewness	0.39	0.38	0.38	0.42	0.42	0.42
	Computing time (s)	0.71	3.59	521.79	1.04	4.00	521.69
$[15/-15]_{4s}$	Mean	4.83	4.84	4.84	147.12	147.11	147.13
	SD	0.60	0.60	0.61	19.64	19.68	19.66
	Kurtosis	3.22	3.26	3.27	3.29	3.28	3.29
	Skewness	0.37	0.38	0.38	0.41	0.40	0.41
	Computing time (s)	0.48	3.57	574.66	0.94	3.93	590.87
$[30/-30]_{4s}$	Mean	5.81	5.81	5.81	193.60	193.49	193.50
	SD	0.70	0.70	0.70	23.76	23.73	23.78
	Kurtosis	3.21	3.25	3.22	3.18	3.24	3.24
	Skewness	0.37	0.36	0.36	0.35	0.37	0.37
	Computing time (s)	0.31	3.08	582.50	0.88	3.78	590.42
$[45/-45]_{4s}$	Mean	7.83	7.84	7.84	276.39	276.40	276.35
	SD	0.95	0.96	0.96	34.30	34.26	34.29
	Kurtosis	3.40	3.24	3.26	3.27	3.27	3.26
	Skewness	0.40	0.37	0.38	0.38	0.39	0.38
	Computing time (s)	0.33	3.25	582.67	0.91	3.15	590.90
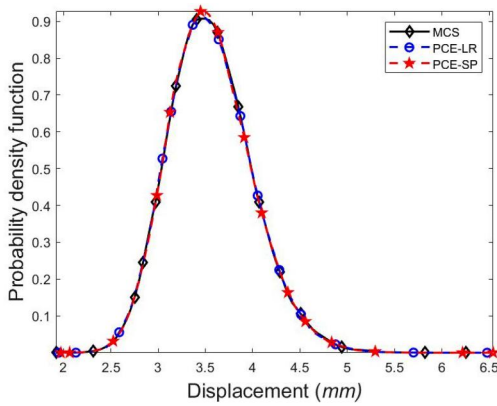
a. S-S boundary condition
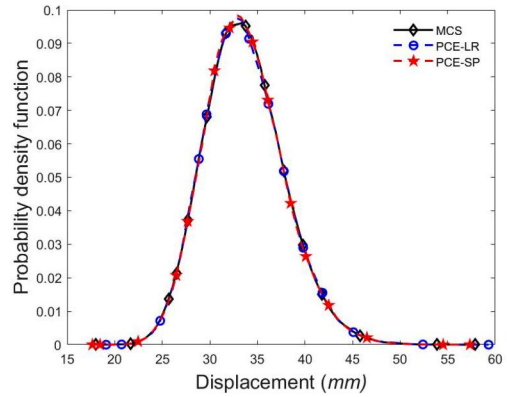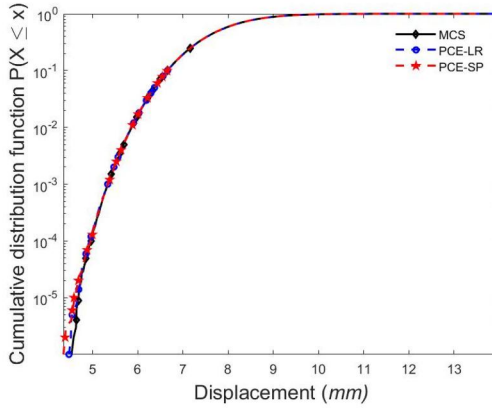
b. C-C boundary condition
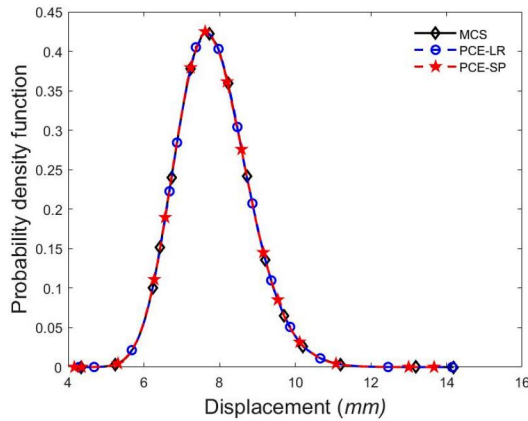
c. C-F boundary condition

Figure 7. Probability density function (PDF) of the MCS and PCE methods for the laminated composite thin-walled glass-epoxy beams' displacement (mm) with S-S, C-F ($N_s = 10^5$) boundary conditions ($N_s = 10^6$).
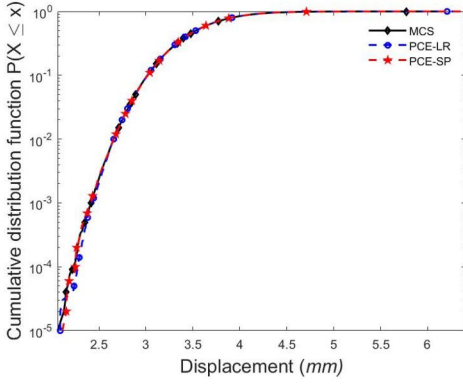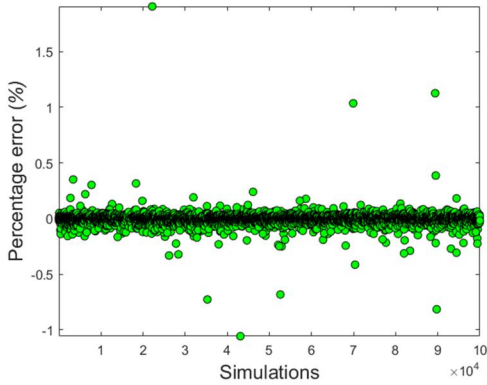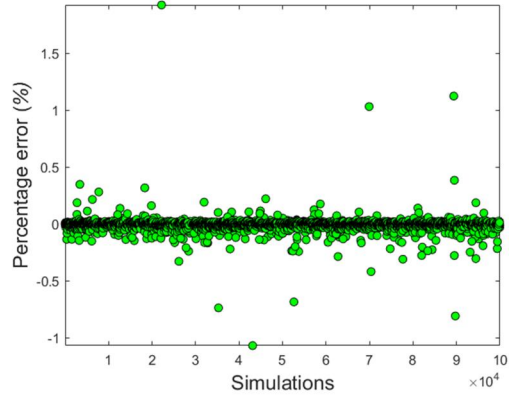
a. S-S boundary condition
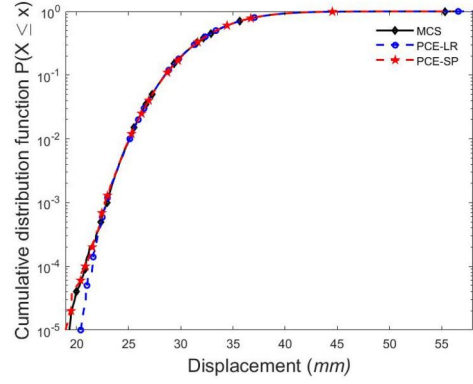
b. C-C boundary condition

c. C-F boundary condition

Figure 8. Cumulative distribution function (CDF) of the MCS and PCE methods for the laminated composite glass-epoxy thin-walled beam displacement (mm) with S-S, C-F ($N_s = 10^5$) boundary conditions ($N_s = 10^6$).

a. MCS vs PCE-LR

b. MCS vs PCE-SP

Figure 9. Percentage error in each simulation between the PCE surrogate responses and the deterministic glass-epoxy beam model responses computed from the same input parameters ($N_s = 10^5$, $[45^o/-45^o]_{4s}$, S-S boundary condition, $L/b_3 = 20$).

boundary conditions with $N_s = 100,000$, the error percentages are mostly from 0% to -0.2% with some outliers from $+1.5$% to -1.0%. For the C-C boundary conditions with a bigger sample
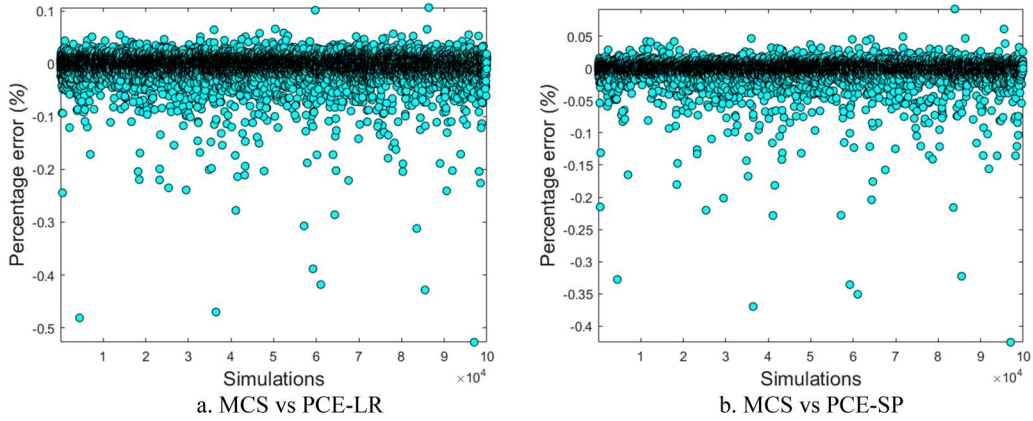
Figure 10. Percentage error in each simulation between the PCE surrogate responses and the deterministic glass-epoxy beam model responses computed from the same input parameters ($N_s = 10^5$, $[45^o/-45^o]_{4s}$, C-F boundary condition, $L/b_3 = 20$).
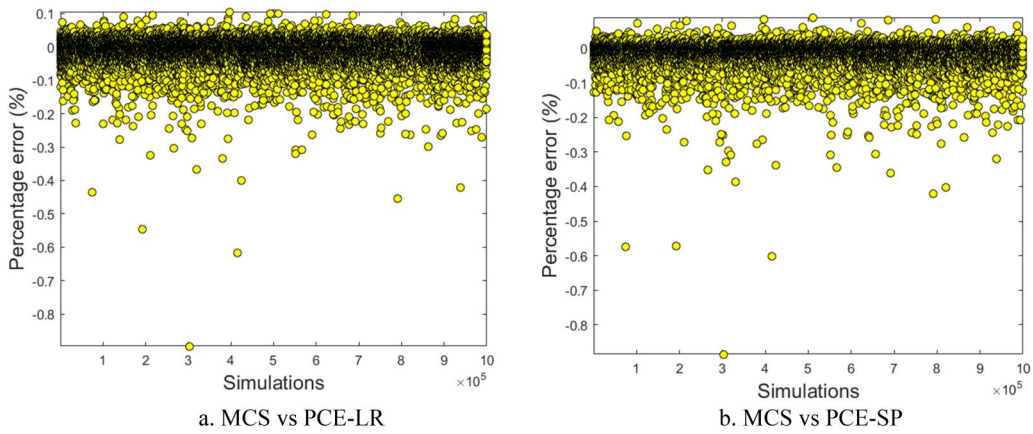

Figure 11. Percentage error in each simulation between the PCE surrogate responses and the deterministic beam model responses computed from the same input parameters ($N_s = 10^6$, $[45^o/-45^o]_{4s}$, C-C boundary condition, $L/b_3 = 20$).

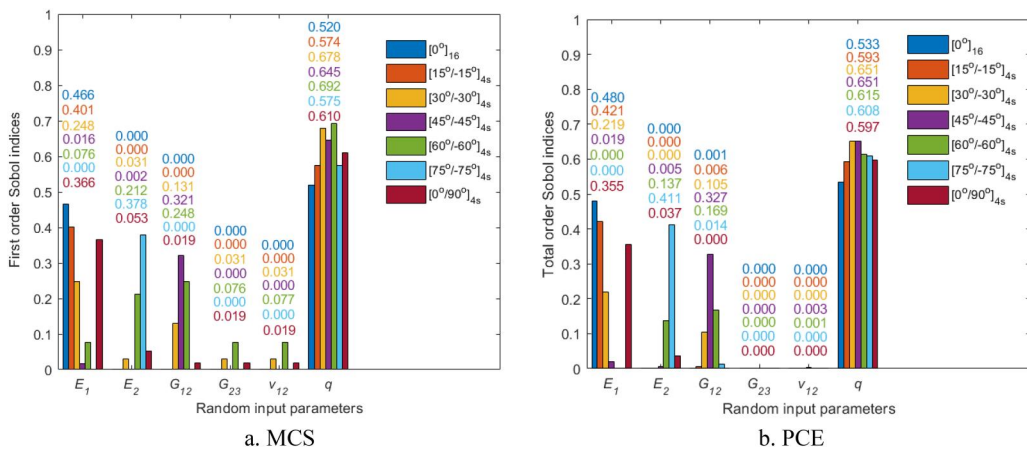
Figure 12. First order Sobol indices for six random input parameters of different thin-walled glass-epoxy beam lay-ups $[\theta^o/-\theta^o]_{4s}$ (C-F boundary condition, $L/b_3 = 20$).
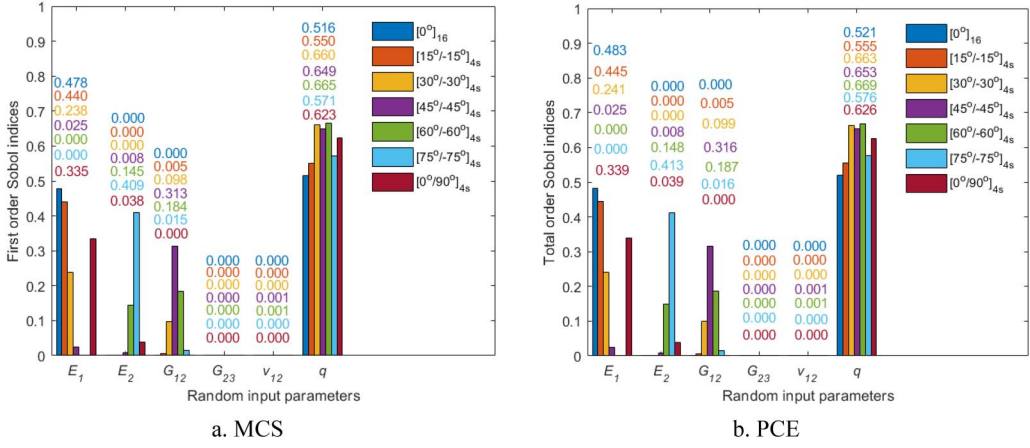
Figure 13. Total order Sobol indices for six random input parameters of different thin-walled beam lay-ups $[\theta^o/-\theta^o]_{4s}$ (C-F boundary condition, $L/b_3 = 20$).

Table 8. Comparison between the ANN, PCE and MCS for $N_S = 100,000$ samples of laminated composite thin-walled beams with $L/b_3 = 20$, $[45^o/-45^o]_{4S}$ lay-ups and C-F boundary condition.

| Method	Attribute	Training data (Ntrain)	Mean	SD	Kurtosis	Skewness	Time (s)	MSE	RMSE
ANN	1 hidden layer, 9 neurons	252	33.6121	4.1693	3.2833	0.3902	26.5	1.05E-5	3.24E-3
	1 hidden layer, 8 neurons	4096	33.6043	4.1668	3.2591	0.3818	25.2	8.76E-6	2.96E-3
	2 hidden layers, 7 neurons each	252	33.6113	4.1700	3.2666	0.3848	40.1	5.62E-5	7.49E-3
	2 hidden layers, 6 neurons each	4096	33.6139	4.1728	3.2711	0.3850	32.83	5.31E-5	7.29E-3
PCE	Least-square regression	252	33.6358	4.1855	3.2831	0.3888	1.8	7.99E-06	2.80E-03
	Spectral projection (SP)	4096	33.6359	4.1861	3.2870	0.3899	2.6	4.32E-06	2.10E-03
MCS	N_s=100,000	–	33.6449	4.1710	3.2858	0.3907	100.9	–	–

size $N_s = 10^6$, the percentage error points tend to lie on the negative side, with most being less than −0.2%.

It is not feasible for the structural designer to guarantee the absolute safety of the beam due to countless sources of uncertainties. Design calculations are based on the characteristic load and characteristic strength which have a reasonably low probability of nonconforming. For instance, the characteristic yield stress of steel is typically defined as the yield stress threshold below which no more than 5% of the test values are anticipated to fall. It is resource-intensive to conduct the beam's mechanical testing and produce the probability distribution of the load applied and the beam's strength. Therefore, the PCE method presented in this article helps save time and cost by significantly reducing the number of beam test samples, but still give a comparable results to the crude MCS testing.

Example 4: Sensitivity analysis

The study also examines the influence of each random input on the variation of the model responses. The first-order Sobol index is used to measure the parameters' influence on the variance of the model output without considering the effect of parameters' interaction. Since the Sobol indices are not affected by the boundary conditions, only Sobol indices for cantilever beams are shown. Figure 12 compares the first-order Sobol indices for static analysis using the MCS and PCE methods across all beam lay-ups. It is evident that the Sobol indices computed from the polynomial expansion coefficients closely match those calculated from the MCS. The sensitivity study reveals that the PCE method is significantly more efficient than the MCS. While the PCE method can compute the Sobol indices with no extra computing cost, the MCS demands at least $(N_{rv} + 2) \times N_s$ simulations based on several efficient algorithm proposed by Saltelli et al. (2010) and N_s^2 simulations based on the raw mathematical definition of Sobol indices. Figure 13
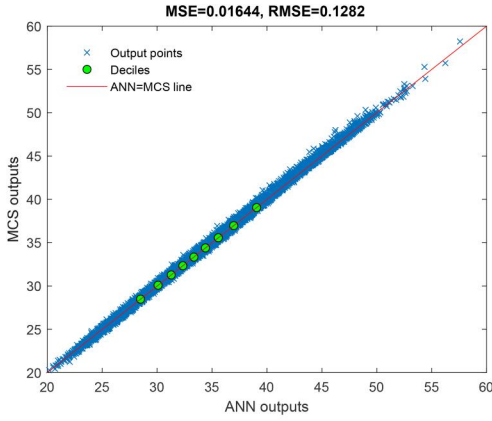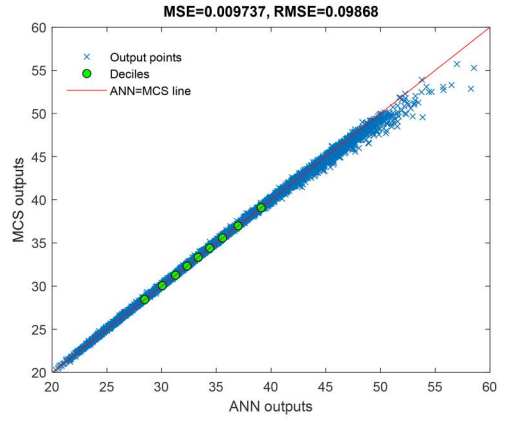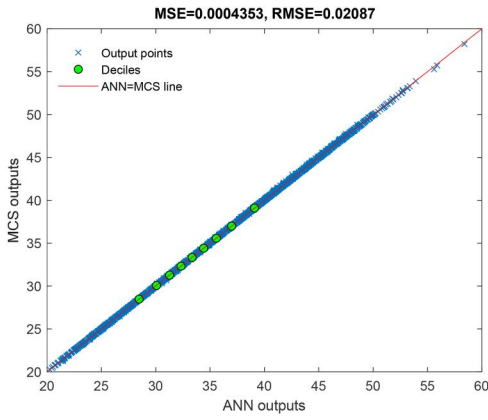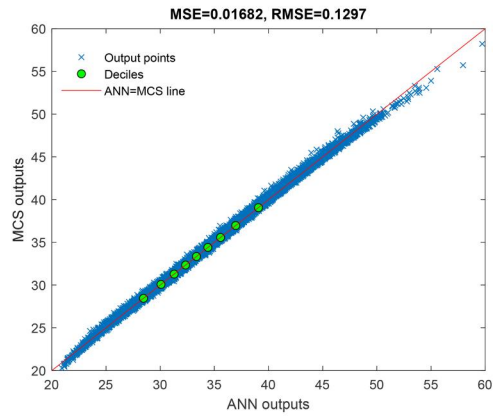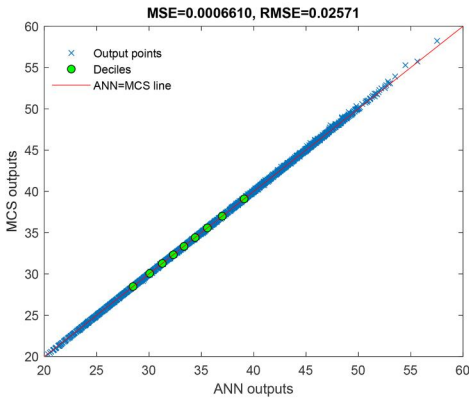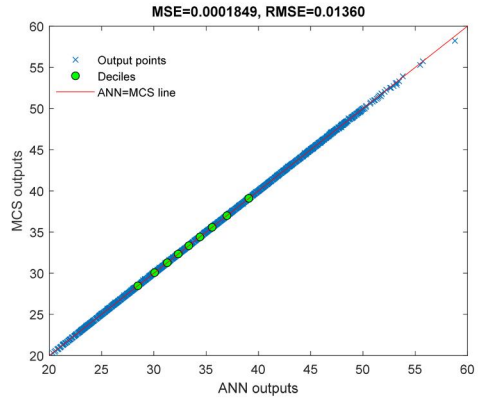
Figure 14. Quantile-quantile plot for comparing the 100,000 test outputs of MCS and ANN with different hidden layers' size ($[45^o / - 45^o]_{4s}$, C-F boundary condition, $L/b_3 = 20$).

presents the total Sobol indices bar graphs with the same settings and beam configurations as Figure 12. It is observed that the differences between the first- and total Sobol sensitivity indices are small for all variables.

Comparing the influences of the input variables, G_{23} and v_{12} play an insignificant role in the beam static responses with the Sobol indices equal to zero. The influence of E_1, E_2 and G_{12} change with the beam fiber-angle lay-ups and this information can be useful in the composite structure design. It is apparent that the variation in the applied UDL contributes the most to the beam's displacement, but the fluctuation of the Sobol indices for q as the fiber angle increases is interesting to see. These findings allow the structural designer to determine the most influential material properties on the static behavior of various laminated composite thin-walled beams' configurations. Thus, fewer mechanical testing is required to ensure the beams' quality.

3.3. Artificial neural network (ANN)

Example 5: Compare ANN with PCE and MCS

This example makes a comparison between the ANN, PCE, and MCS's accuracy and learning capability. The MCS with $N_S = 100,000$ samples are the input training data and test data for the predictions of PCE and ANN. Table 8 presents the statistical moments, computing time, and the mean square error of the three methods with various attributes. The ANN is computed by setting the number of epochs equal to 300. The hyperparameters, such as the number of hidden layers and the number of neurons, are calibrated so that the MSE and RMSE are close to the results of PCE. The ANN with 1 hidden layer and 8 neurons is sufficient compared to PCE. Even though the mean, standard deviation (SD), kurtosis and skewness of the output distribution for ANN and PCE are almost the same as the MCS, the ANN method takes much more time than the PCE. The PCE's advantage over ANN has been shown in Example 4, where Sobol's sensitivity indices can be computed from the coefficients for free of computing cost. While the ANN can produce much faster predictions than the MCS, it does require $(N_{rv} + 2) \times N_s$ more output data for the Sobol indices. Nonetheless, the PCE method suffers when the beam model contains a higher number of random input variables, which translates to a higher dimensional PCE model. The ANN otherwise can be conveniently tuned by changing many hyperparameters. Figure 14 displays the quantile-quantile plot between the outputs of MCS and ANN with different layer sizes. The output points in Figure 14a, b, and d create a thick line around the ANN = MCS line, which means the errors are high, especially at the upper part of the tenth deciles. The accuracy is observably improved in Figure 14c, e, and f when the number of neurons increases.

4. Conclusions

This article presented a stochastic model for analyzing the static behaviors of laminated composite thin-walled beams with an I-section based on a novel sinusoidal higher-order shear deformation thin-walled beam theory. The material properties of the laminated composite material are assumed to follow lognormal distributions, and their uncertainty is fed into a beam solver for the computation of sample stochastic outputs. The surrogate models based on Polynomial Chaos Expansion (PCE) and Artificial Neural Network (ANN) are developed to evaluate the stochastic responses efficiently. The benchmarks for accuracy and efficiency are the stochastic responses obtained from crude Monte Carlo simulation. The study also includes a sensitivity analysis to compare the importance of uncertainty in material properties to the stochastic responses. In conclusion, the present work's findings can be distilled into the following points:

- The proposed STWT is found to be efficient and accurate in predicting flexural behaviors of laminated composite thin-walled beams with open sections. The laminated composite thin-walled I-beam's displacements are higher than those from the CTWT and FTWT theories.

- The higher-order shear deformation effect on the displacement of thin-walled laminated composite beams is significant for thick beams ($L/b_3 < 15$).
- The PCE method has been shown to be able to preserve the stochastic output distribution with a considerably fewer required number of simulations, thus with much lower computing expense in which the LR and SP approaches only required 252 and 4,096 samples, respectively, in comparison with 100,000 samples from the MCS.
- The PCE method requires no extra computing cost to determine the Sobol indices, while the MCS, in the best case, demands more sample runs proportional to the number of random input parameters N_{rv} and the chosen base number of samples N_s ($(N_{rv} + 2) \times N_s$).
- The sensitivity analysis helps detect and eliminate insignificant variables, which in turn speeds up the stochastic model even more. The numerical results showed that the applied external load is the most critical variable affecting the flexural behaviors of the laminated composite thin-walled beams.
- Both supervised-learning ANN and PCE can accurately predict a high number of composite I-beams' outputs.
- The ANN costs more computational time than the PCE with a low number of random input variables.

Disclosure statement

No potential conflict of interest was reported by the authors.

References

Abdelmalek, A., M. Bouazza, M. Zidour, and N. Benseddiq. 2019. "Hygrothermal Effects on the Free Vibration Behavior of Composite Plate Using nth-Order Shear Deformation Theory: A Micromechanical Approach." *Iranian Journal of Science and Technology, Transactions of Mechanical Engineering* 43 (S1): 61–73. https://doi.org/10.1007/s40997-017-0140-y

Bauld, N. R., and T. Lih-Shyng. 1984. "A Vlasov Theory for Fiber-Reinforced Beams with Thin-Walled Open Cross Sections." *International Journal of Solids and Structures* 20 (3): 277–297. https://doi.org/10.1016/0020-7683(84)90039-8

Borges, R. A., L. F. F. Rodovalho, T. d P. Sales, and D. A. Rade. 2021. "Stochastic Eigenfrequency and Buckling Analyses of Plates Subjected to Random Temperature Distributions." *Mechanical Systems and Signal Processing* 147: 107088. https://doi.org/10.1016/j.ymssp.2020.107088

Bouazza, M., K. Amara, M. Zidour, A. Tounsi, and E. A. Adda-Bedia. 2015. "Hygrothermal Effects on the Postbuckling Response of Composite Beams." *Review of Information Engineering and Applications* 2 (1): 1–14. https://doi.org/10.18488/journal.79/2015.2.1/79.1.1.14

Boulal, A., T. Bensattalah, A. Karas, M. Zidour, H. Heireche, and E. A. A. Bedia. 2020. "Buckling of Carbon Nanotube Reinforced Composite Plates Supported by Kerr Foundation Using Hamilton's Energy Principle." *Structural Engineering and Mechanics* 73 (2): 209–223. https://doi.org/10.12989/sem.2020.9.73.209

Bui, X.-B., T.-K. Nguyen, N.-D. Nguyen, and T. P. Vo. 2022. "A General Higher-Order Shear Deformation Theory for Buckling and Free Vibration Analysis of Laminated Thin-Walled Composite I-Beams." *Composite Structures* 295: 115775. https://doi.org/10.1016/j.compstruct.2022.115775

Bui, X.-B., T.-K. Nguyen, and P. T. T. Nguyen. 2023. "Stochastic Vibration and Buckling Analysis of Functionally Graded Sandwich Thin-Walled Beams." *Mechanics Based Design of Structures and Machines*: 1–23. https://doi.org/10.1080/15397734.2023.2165101

Carrera, E., G. Giunta, and M. Petrolo. 2011. *Beam structures: Classical and advanced theories*. UK: John Wiley & Sons.

Chaikittiratana, A., and N. Wattanasakulpong. 2022. "Gram-Schmidt-Ritz Method for Dynamic Response of FG-GPLRC Beams under Multiple Moving Loads." *Mechanics Based Design of Structures and Machines* 50 (7): 2427–2448. https://doi.org/10.1080/15397734.2020.1778488

Chakraborty, S., B. Mandal, R. Chowdhury, and A. Chakrabarti. 2016. "Stochastic Free Vibration Analysis of Laminated Composite Plates Using Polynomial Correlated Function Expansion." *Composite Structures* 135: 236–249. https://doi.org/10.1016/j.compstruct.2015.09.044

Chandiramani, N. K., L. Librescu, and C. D. Shete. 2002. "On the Free-Vibration of Rotating Composite Beams Using a Higher-Order Shear Formulation." *Aerospace Science and Technology* 6 (8): 545–561. https://doi.org/10.1016/S1270-9638(02)01195-1

Colombi, P., and C. Poggi. 2006. "An Experimental, Analytical and Numerical Study of the Static Behavior of Steel Beams Reinforced by Pultruded CFRP Strips." *Composites Part B: Engineering* 37 (1): 64–73. https://doi.org/10.1016/j.compositesb.2005.03.002

Cottrell, J., T. Hughes, and Y. Bazilevs. 2009. *Isogeometric Analysis: Toward integration of CAD and FEA*.

Dalbey, K., M. S. Eldred, G. Geraci, J. D. Jakeman, K. A. Maupin, J. A. Monschke, D. T. Seidl, et al. 2020. "Dakota a Multilevel Parallel Object-Oriented Framework for Design Optimization Parameter Estimation Uncertainty Quantification and Sensitivity Analysis: Version 6.12 Theory Manual.; Sandia National Lab." (SNL-NM), Albuquerque, NM (United States).

Guessas, H., M. Zidour, M. Meradjah, and A. Tounsi. 2018. "The Critical Buckling Load of Reinforced Nanocomposite Porous Plates." *Structural Engineering and Mechanics* 67 (2): 115–123. https://doi.org/10.12989/sem.2018.67.2.115

Guo, H., X. Zhuang, and T. Rabczuk. 2019. "A Deep Collocation Method for the Bending Analysis of Kirchhoff Plate." *Computers, Materials & Continua* 59 (2): 433–456. https://doi.org/10.32604/cmc.2019.06660

Jagtap, K. R., A. Lal, and B. N. Singh. 2012. "Stochastic Nonlinear Bending Response of Functionally Graded Material Plate with Random System Properties in Thermal Environment." *International Journal of Mechanics and Materials in Design* 8 (2): 149–167. https://doi.org/10.1007/s10999-012-9183-9

Jakeman, J. D., M. Perego, and W. M. Severa. 2018. Neural Networks as Surrogates of Nonlinear High-Dimensional Parameter-to-Prediction Maps. United States.

Jung, S., and J.-Y. Lee. 2003. "Closed-Form Analysis of Thin-Walled Composite I-Beams considering Non-Classical Effects." *Composite Structures* 60 (1): 9–17. https://doi.org/10.1016/S0263-8223(02)00318-5

Kim, N.-I., and C.-K. Jeon. 2013. "Coupled Static and Dynamic Analyses of Shear Deformable Composite Beams with Channel-Sections#." *Mechanics Based Design of Structures and Machines* 41 (4): 489–511. https://doi.org/10.1080/15397734.2013.797332

Kim, N.-I., and D. K. Shin. 2008. "Coupled Deflection Analysis of Thin-Walled Timoshenko Laminated Composite Beams." *Computational Mechanics* 43 (4): 493–514. https://doi.org/10.1007/s00466-008-0324-9

Kumar, R. R., T. Mukhopadhyay, K. M. Pandey, and S. Dey. 2019. "Stochastic Buckling Analysis of Sandwich Plates: The Importance of Higher Order Modes." *International Journal of Mechanical Sciences* 152: 630–643. https://doi.org/10.1016/j.ijmecsci.2018.12.016

Latalski, J., and D. Zulli. 2020. "Generalized Beam Theory for Thin-Walled Beams with Curvilinear Open Cross-Sections." *Applied Sciences* 10 (21): 7802. https://doi.org/10.3390/app10217802

Lee, J. 2001. "Center of Gravity and Shear Center of Thin-Walled Open-Section Composite Beams." *Composite Structures* 52 (2): 255–260. https://doi.org/10.1016/S0263-8223(00)00177-X

Lee, J. 2005. "Flexural Analysis of Thin-Walled Composite Beams Using Shear-Deformable Beam Theory." *Composite Structures* 70 (2): 212–222. https://doi.org/10.1016/j.compstruct.2004.08.023

Lee, J., and S.-E. Kim. 2001. "Flexural–Torsional Buckling of Thin-Walled I-Section Composites." *Computers & Structures* 79 (10): 987–995. https://doi.org/10.1016/S0045-7949(00)00195-4

Lee, J., and S.-E. Kim. 2002. "Free Vibration of Thin-Walled Composite Beams with I-Shaped Cross-Sections." *Composite Structures* 55 (2): 205–215. https://doi.org/10.1016/S0263-8223(01)00150-7

Lee, J., and S-h Lee. 2004. "Flexural–Torsional Behavior of Thin-Walled Composite Beams." *Thin-Walled Structures* 42 (9): 1293–1305. https://doi.org/10.1016/j.tws.2004.03.015

Maddur, S. S., and S. K. Chaturvedi. 1999. "Laminated Composite Open Profile Sections: First Order Shear Deformation Theory." *Composite Structures* 45 (2): 105–114. https://doi.org/10.1016/S0263-8223(99)00005-7

Maddur, S. S., and S. K. Chaturvedi. 2000. "Laminated Composite Open Profile Sections: Non-Uniform Torsion of I-Sections." *Composite Structures* 50 (2): 159–169. https://doi.org/10.1016/S0263-8223(00)00093-3

Megson, T. H. G. 2021. *Aircraft Structures for Engineering Students*. 7th ed. United Kingdom: Butterworth-Heinemann.

Moreno-García, P., J. V. A. dos Santos, and H. Lopes. 2018. "A Review and Study on Ritz Method Admissible Functions with Emphasis on Buckling and Free Vibration of Isotropic and Anisotropic Beams and Plates." *Archives of Computational Methods in Engineering* 25 (3): 785–815. https://doi.org/10.1007/s11831-017-9214-7

Nguyen, H. X., T. Duy Hien, J. Lee, and H. Nguyen-Xuan. 2017. "Stochastic Buckling Behaviour of Laminated Composite Structures with Uncertain Material Properties." *Aerospace Science and Technology* 66: 274–283. https://doi.org/10.1016/j.ast.2017.01.028

Nguyen, N.-D., T.-K. Nguyen, T.-N. Nguyen, and H.-T. Thai. 2018. "New Ritz-Solution Shape Functions for Analysis of Thermo-Mechanical Buckling and Vibration of Laminated Composite Beams." *Composite Structures* 184: 452–460. https://doi.org/10.1016/j.compstruct.2017.10.003

Nguyen, N.-D., T.-K. Nguyen, T. P. Vo, and L. B. Nguyen. 2023. "Bending, Buckling and Free Vibration Behaviors of Thin-Walled Functionally Graded Sandwich and Composite Channel-Section Beams." *Mechanics Based Design of Structures and Machines* 51 (2): 932–960. https://doi.org/10.1080/15397734.2020.1859385

Nguyen, N. D., and T. K. Nguyen. 2020. "Ritz Solution for Static Analysis of Thin-Walled Laminated Composite I-Beams Based on First-Order Beam Theory." *2020 5th International Conference on Green Technology and Sustainable Development (GTSD)*, 27-28 Nov. 2020.

Oñate, E. 2013. "*Structural Analysis with the Finite Element Method.*" In *Linear Statics, Lecture Notes on Numerical Methods in Engineering and Sciences*. Spain: Springer Dordrecht.

Pandey, M. D., M. Z. Kabir, and A. N. Sherbourne. 1995. "Flexural-Torsional Stability of Thin-Walled Composite I-Section Beams." *Composites Engineering* 5 (3): 321–342. https://doi.org/10.1016/0961-9526(94)00101-E

Parhi, A., and B. N. Singh. 2014. "Stochastic Response of Laminated Composite Shell Panel in Hygrothermal Environment." *Mechanics Based Design of Structures and Machines* 42 (4): 454–482. https://doi.org/10.1080/15397734.2014.888006

Peng, X., D. Li, H. Wu, Z. Liu, J. Li, S. Jiang, and J. Tan. 2019. "Uncertainty Analysis of Composite Laminated Plate with Data-Driven Polynomial Chaos Expansion Method under Insufficient Input Data of Uncertain Parameters." *Composite Structures* 209: 625–633. https://doi.org/10.1016/j.compstruct.2018.11.015

Piovan, M. T., J. M. Ramirez, and R. Sampaio. 2013. "Dynamics of Thin-Walled Composite Beams: Analysis of Parametric Uncertainties." *Composite Structures* 105: 14–28. https://doi.org/10.1016/j.compstruct.2013.04.039

Qin, Z., and L. Librescu. 2002. "On a Shear-Deformable Theory of Anisotropic Thin-Walled Beams: Further Contribution and Validations." *Composite Structures* 56 (4): 345–358. https://doi.org/10.1016/S0263-8223(02)00019-3

Ramaprasad, S., B. Dattaguru, and G. Singh. 2022. "Exact Solutions for Thin-Walled Composite Open Section Beams Using a Unified State Space Coupled Field Formulation." *Mechanics Based Design of Structures and Machines* 51 (11): 5983–6007. https://doi.org/10.1080/15397734.2021.2024846

Reddy, J. N. 2003a. *Mechanics of Laminated Composite Plates and Shells*. 2nd ed. Boca Raton: CRC Press.

Reddy, J. N. 2003b. Mechanics of Laminated Composite Plates and Shells: Theory and Analysis. 2nd ed. Boca Raton: CRC Press.

Saltelli, A., P. Annoni, I. Azzini, F. Campolongo, M. Ratto, and S. Tarantola. 2010. "Variance Based Sensitivity Analysis of Model Output. Design and Estimator for the Total Sensitivity Index." *Computer Physics Communications* 181 (2): 259–270. https://doi.org/10.1016/j.cpc.2009.09.018

Samaniego, E., C. Anitescu, S. Goswami, V. M. Nguyen-Thanh, H. Guo, K. Hamdia, X. Zhuang, and T. Rabczuk. 2020. "An Energy Approach to the Solution of Partial Differential Equations in Computational Mechanics via Machine Learning: Concepts, Implementation and Applications." *Computer Methods in Applied Mechanics and Engineering* 362: 112790. https://doi.org/10.1016/j.cma.2019.112790

Sasikumar, P., A. Venketeswaran, R. Suresh, and S. Gupta. 2015. "A Data Driven Polynomial Chaos Based Approach for Stochastic Analysis of CFRP Laminated Composite Plates." *Composite Structures* 125: 212–227. https://doi.org/10.1016/j.compstruct.2015.02.010

Shaker, A., W. Abdelrahman, M. Tawfik, and E. A. Sadek. 2008. "Stochastic Finite Element Analysis of the Free Vibration of Laminated Composite Plates." *Computational Mechanics* 41 (4): 493–501. https://doi.org/10.1007/s00466-007-0205-7

Sobol, I. M. 1993. "Sensitivity Estimates for Nonlinear Mathematical Models." *Mathematical Modelling and Computational Experiments* 1 (4): 407–414.

Tayeb Tayeb, S., M. Zidour, T. Bensattalah, H. Heireche, A. Benahmed, and E. A. A. Bedia. 2020. "Mechanical Buckling of FG-CNTs Reinforced Composite Plate with Parabolic Distribution Using Hamilton's Energy Principle." *Advances in Nano Research* 8 (2): 135–148. https://doi.org/10.12989/ANR.2020.8.2.135

Tran, V.-T., T.-K. Nguyen, H. Nguyen-Xuan, and M. Abdel Wahab. 2023. "Vibration and Buckling Optimization of Functionally Graded Porous Microplates Using BCMO-ANN Algorithm." *Thin-Walled Structures* 182: 110267. https://doi.org/10.1016/j.tws.2022.110267

Trinh, M.-C., S.-N. Nguyen, H. Jun, and T. Nguyen-Thoi. 2021. "Stochastic Buckling Quantification of Laminated Composite Plates Using Cell-Based Smoothed Finite Elements." *Thin-Walled Structures* 163: 107674. https://doi.org/10.1016/j.tws.2021.107674

Tsokanas, N., T. Simpson, R. Pastorino, E. Chatzi, and B. Stojadinović. 2022. "Model Order Reduction for Real-Time Hybrid Simulation: Comparing Polynomial Chaos Expansion and Neural Network Methods." *Mechanism and Machine Theory* 178: 105072. https://doi.org/10.1016/j.mechmachtheory.2022.105072

Umesh, K., and R. Ganguli. 2013. "Material Uncertainty Effect on Vibration Control of Smart Composite Plate Using Polynomial Chaos Expansion." *Mechanics of Advanced Materials and Structures* 20 (7): 580–591. https://doi.org/10.1080/15376494.2011.643279

Vo, T. P., and J. Lee. 2009. "Flexural–Torsional Coupled Vibration and Buckling of Thin-Walled Open Section Composite Beams Using Shear-Deformable Beam Theory." *International Journal of Mechanical Sciences* 51 (9-10): 631–641. https://doi.org/10.1016/j.ijmecsci.2009.05.001

Wu, L., and M. Mohareb. 2011. "Finite Element Formulation for Shear Deformable Thin-Walled Beams." *Canadian Journal of Civil Engineering* 38 (4): 383–392. https://doi.org/10.1139/l11-007

Xiu, D., and G. E. Karniadakis. 2002. "The Wiener–Askey Polynomial Chaos for Stochastic Differential Equations." *SIAM Journal on Scientific Computing* 24 (2): 619–644. https://doi.org/10.1137/S1064827501387826

Yu, W., D. Hodges, V. Volovoi, and E. Fuchs. 2005. "A Generalized Vlasov Theory of Composite Beams." *Thin-Walled Structures* 43 (9): 1493–1511. https://doi.org/10.1016/j.tws.2005.02.003

Zerrouki, R., A. Karas, and M. Zidour. 2020. "Critical Buckling Analyses of Nonlinear FG-CNT Reinforced Nano-Composite Beam." *Advances in Nano Research* 9 (3): 211–220. https://doi.org/10.12989/ANR.2020.9.3.211

Zhuang, X., H. Guo, N. Alajlan, H. Zhu, and T. Rabczuk. 2021. "Deep Autoencoder Based Energy Method for the Bending, Vibration, and Buckling Analysis of Kirchhoff Plates with Transfer Learning." *European Journal of Mechanics - A/Solids* 87: 104225. https://doi.org/10.1016/j.euromechsol.2021.104225

Size-dependent behaviours of functionally graded sandwich thin-walled beams based on the modified couple stress theory

Xuan-Bach Bui [a], Trung-Kien Nguyen [b],[*], Armagan Karamanli [c], Thuc P. Vo [d]

[a] *Faculty of Civil Engineering, Ho Chi Minh City University of Technology and Education, 1 Vo Van Ngan Street, Thu Duc District, Ho Chi Minh City, Viet Nam*
[b] *CIRTech Institute, HUTECH University, 475A Dien Bien Phu Street, Binh Thanh District, Ho Chi Minh City, Viet Nam*
[c] *Department of Mechanical Engineering, Yildiz Technical University, Besiktas, Istanbul 34349, Turkey*
[d] *School of Computing, Engineering and Mathematical Sciences, La Trobe University, Bundoora, VIC 3086, Australia*

A B S T R A C T

This paper examines the static and vibration analysis of functionally graded sandwich thin-walled microbeams using the modified couple stress theory. The material properties in both web and flanges vary continuously through their thickness. The equations of motion are derived and solved by the Ritz method. Verification studies are performed on the bending and vibration responses of FG sandwich thin-walled beams. The effects of material distribution, span-to-height's ratio, and material length scale parameters on the responses of microbeams for various boundary conditions are investigated. The results of the analysis indicate that the deflections and natural frequencies of functionally graded sandwich thin-walled microbeams are greatly influenced by the variations of parameters mentioned earlier. The microbeams with the size effect are predicted to be much stiffer than their macro counterparts. Some benchmark results can be used as a reference for future studies.

Introduction

Owing to the high weight-to-stiffness ratio and performance of electro-thermo-mechanical properties, laminated composite and functionally graded (FG) structures have been employed in many engineering fields such as aerospace, automotive engineering, construction and many others. Inthe aerospace sector where the materials must undergo intense mechanical and thermal conditions, FG materials have proven to be applicable in numerous components. To name a few, some examples are the rocket nozzle, the spacecraft truss structure, the heat exchange panels, the reflector, the rocket engine and various micro-electro-mechanical systems [1–3]. The recent developments in the FG materials promise some important applications for thin-walled beams. In general, the behaviours of thin-walled beams can be predicted by classical thin-walled beam theory (CTWBT), first-order thin-walled beam theory (FTWBT) and higher-order thin-walled beam theory (HTWBT). Many papers related to thin-walled composite beams have been studied with different analytical and numerical methods as well as beam models; only some typical references are mentioned here [4–10]. The CTWBT initiated by Vlasov [11] was applied for FG thin-walled beams [12–15]. This theory neglects the shear effects and therefore, it underestimates the deflection and overestimates the frequencies/buckling loads. The

FTWBT accounts for the shear effects and thus predicts more accurately than the CTWBT. Based on the FTWBT, a number of papers have been dedicated to predicting the structural behaviours of FG thin-walled beams including the sandwich ones, some of which are cited here [16–24]. Kvaternik et al. [25] compared the thin-walled beam models developed from the Carrera Unified Formulation and Vlasov theory. Phi et al. [26] investigated the free vibration of FG thin-walled beams with open sections where the material properties vary along the contour direction. Librescu et al. [27] modeled the spinning thin-walled beam with a non-uniform cross-section. Fazelzadeh and Hosseini [28] investigated the aerothermoelastic behaviour of rotating FG thin-walled blades. Farsadi [29] optimized the static and dynamic responses of variable thickness rotating blades made of FG materials with porosities. The aforementioned literature review shows that although considerable number of studies have been carried out on static and dynamic responses of FG thin-walled beams, there is a limited number of works on their size-dependent behaviours. In order to take the size effects into account, advanced theories with material length scale parameters (MLSPs), in which the modified coupled stress theory (MCT) is the most popular one, have been proposed. The MCT initiated by Yang et al. [30] accounts for the size effects with only one MLSP. Thanks to its simplicity, many size-dependent FG microbeam and microplate models based on the MCT
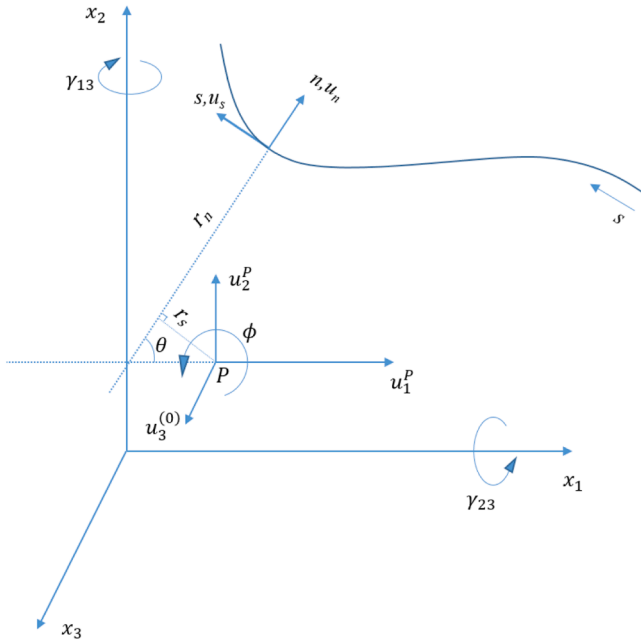
Fig. 1. Thin-walled coordinate systems.

have been developed [24,31–39]. Besides MCT, the modified strain gradient theory (MSGT) is also applied for microbeams [40–43]. Moreover, many experimental studies have also been conducted for different microbeam set-ups and provided a basis of comparison for theoretical studies [44–50]. Although many papers have been devoted to the analysis of FG microplates/microbeams, there are very few studies for FG thin-walled nanobeams. Soltani et al. [51–53] used CTWBT and non-local elasticity theory of Eringen to study the stability of FG nano I-beams. However, there is no other investigation for FG thin-walled microbeams, this interesting and complicated topic needs to be studied further.

This paper employs the FTWBT and MCT to investigate the static and vibration analysis of the FG sandwich thin-walled microbeams. The governing equations of motion are derived and then a hybrid series solution is developed. Verification studies are performed on the bending and vibration responses of FG sandwich thin-walled beams. A parametric study is carried out to depict the effects of material distribution and MLSP on their deflections and natural frequencies.

Theoretical formulation

Considering a FG sandwich thin-walled microbeam with length L and open sections, three sets of coordinate systems are examined in Figs. 1 and 2. The following assumptions are made: the strains are small, the section contour does not deform in its own plane, the shear and warping strains are uniform and local buckling and pre-buckling deformations are negligible.

Modified couple stress theory (MCT)

The total energy of system is composed of the strain energy Π_S, potential energy Π_W and kinetic energy Π_K as follows:

$$\Pi = \Pi_S + \Pi_W - \Pi_K \tag{1}$$

Based on the MCT, the strain energy of the system Π_S is given by:

$$\Pi_U = \int_V \left(\sigma_{ij}\varepsilon_{ij} + m_{ij}\chi_{ij}\right) dV \tag{2}$$

where $\varepsilon_{ij}, \chi_{ij}$ are strains and symmetric rotation gradients; σ_{ij} is Cauchy
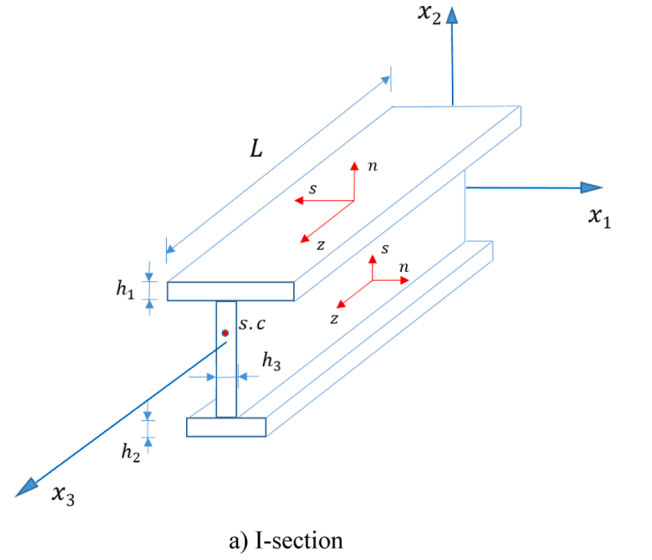
a) I-section
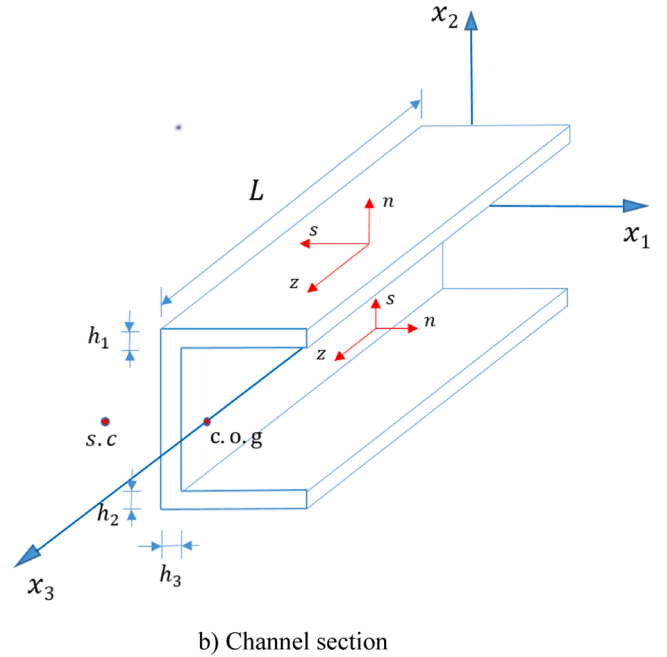
b) Channel section

Fig. 2. Geometry of FG thin-walled beams.

stress; m_{ij} is the high-order stress corresponding with strain gradients χ_{ij}. The components of strain ε_{ij} and strain gradients χ_{ij} are expressed in terms of the displacements u_i as follows:

$$\varepsilon_{ij} = \frac{1}{2}\left(u_{i,j} + u_{j,i}\right) \tag{3a}$$

$$\chi_{ij} = \frac{1}{4}\left(u_{n,mj}e_{imn} + u_{n,mi}e_{jmn}\right) \tag{3b}$$

where e_{imn} is the permutation symbol; the comma in the subscript indicates the differentiation with respect to the variable that follows.

The stress components σ_{ij} and m_{ij} are computed from constitutive equations as follows:

$$\sigma_{ij} = \lambda\varepsilon_{kk}\delta_{ij} + 2\mu\varepsilon_{ij} \tag{4a}$$

$$m_{ij} = 2\mu l^2\chi_{ij} \tag{4b}$$

where λ, μ are Lamé constants; δ_{ij} is the Knonecker delta; l is the MLSP

which can be determined by experimental works [54].

The potential energy of the system Π_W subjected to a transverse load q can be expressed as:

$$\Pi_W = -\int_0^L q u_2^P dx_3 \tag{5}$$

where u_2^P is the transverse displacement at P.

The kinetic energy of the system Π_K is expressed by:

$$\Pi_K = \frac{1}{2}\int_V \rho(x_3)\left(\dot{u}_1^2 + \dot{u}_2^2 + \dot{u}_3^2\right)dV \tag{6}$$

where $\rho(x_3)$ is the mass density; $\dot{u}_1 = u_{1,t}$, $\dot{u}_2 = u_{2,t}$, $\dot{u}_3 = u_{3,t}$ are the velocities in the x_1-, x_2- and x_3- directions, respectively.

Kinematics

The vertical and horizontal displacements $u_1(n,s,x_3)$ and $u_2(n,s,x_3)$ at any points in the contour coordinate system under a small rotation ϕ about the pole axis can be expressed in terms of those at the pole $u_1^P(x_3)$ and $u_2^P(x_3)$ in the x_1- and x_2- directions, respectively, as follows:

$$u_1(n,s,x_3) = u_1^P(x_3) - \left(X_2 - x_2^P\right)\phi(x_3) \tag{7a}$$

$$u_2(n,s,x_3) = u_2^P(x_3) + \left(X_1 - x_1^P\right)\phi(x_3) \tag{7b}$$

where $X_1 = x_1 + nx_{2,s}$ and $X_2 = x_2 - nx_{1,s}$. The displacements in the contour lines $u_n(n,s,x_3)$ and $u_s(n,s,x_3)$ can be derived from those in Eq. (7) as follows:

$$u_n(n,s,x_3) = u_1^P(x_3)X_{2,s} - u_2^P(x_3)X_{1,s} - R_s(n,x_3)\phi(x_3) \tag{8a}$$

$$u_s(n,s,x_3) = u_1^P(x_3)X_{1,s} + u_2^P(x_3)X_{2,s} + R_n(n,x_3)\phi(x_3) \tag{8b}$$

where $R_s(n,s) = r_s(s)$ and $R_n(n,s) = r_n(s) + n$ in which $r_s(s)$ and $r_n(s)$ are the lengths of the perpendiculars from P to the tangent and normal of the profile line center.

The shear strains $(\gamma_{s3}, \gamma_{n3})$ can be expressed via the transverse shear strains $(\gamma_{13}, \gamma_{23})$ and a direct shear strain caused by the change rate of twist angle $\phi_{,3}$ [55] as follows:

$$\gamma_{s3}(n,s,x_3) = \gamma_{13}(n,x_3)X_{1,s} + \gamma_{23}(n,x_3)X_{2,s} + 2n\phi_{,3}(x_3) = u_{s,3} + u_{3,s} \tag{9a}$$

$$\gamma_{n3}(n,s,x_3) = \gamma_{13}(n,x_3)X_{2,s} - \gamma_{23}(n,x_3)X_{1,s} = u_{n,3} + u_{3,n} \tag{9b}$$

It is assumed that γ_{13} and γ_{23} are constant in the wall thickness, i.e. $\gamma_{13}(n,x_3) = \gamma_{13}^{(0)}(x_3)$, $\gamma_{23}(n,x_3) = \gamma_{23}^{(0)}(x_3)$ where $\gamma_{13}^{(0)}, \gamma_{23}^{(0)}$ are mid-surface shear strains.

The axial displacement can be found by substituting Eq. (8) into Eq. (9) and then integrating with respect to s and n:

$$u_3(n,s,x_3) = u_3^{(0)}(x_3) + \theta_2(x_3)X_1(n,s) + \theta_1(x_3)X_2(n,s) - \phi_{,3}(x_3)\overline{F}_\omega(n,s) \tag{10}$$

where $\theta_1(x_3) = \gamma_{23}^{(0)} - u_{2,3}^P$ and $\theta_2(x_3) = \gamma_{13}^{(0)} - u_{1,3}^P$ are the rotations with respect to the x_1- and x_2- axes; $\overline{F}_\omega = F_\omega - nr_s$ where $F_\omega(s)$ is a warping function defined by:

$$F_\omega(s) = \int_{s_0}^s r_n(s)ds \tag{11}$$

The kinematics of FTWBT at any point of the section can be expressed by:

$$u_1(n,s,x_3) = u_1^P(x_3) - \left(x_2 - nx_{1,s} - x_2^P\right)\phi(x_3) \tag{12a}$$

$$u_2(n,s,x_3) = u_2^P(x_3) + \left(x_1 + nx_{2,s} - x_1^P\right)\phi(x_3) \tag{12b}$$

$$u_3(n,s,x_3) = u_3^{(0)}(x_3) + \theta_2(x_3)\left(x_1 + nx_{2,s}\right) + \theta_1(x_3)\left(x_2 - nx_{1,s}\right) - \phi_{,3}(x_3)\overline{F}_\omega \tag{12c}$$

It should be noted that the present FTWBT only depends on six variables. By setting $\gamma_{13}^{(0)} = 0$, $\gamma_{23}^{(0)} = 0$, the CTWBT can be recovered.

Strains

Using the displacements in Eq. (12), the non-zero linear strains are given by:

$$\varepsilon_{33}(n,s,x_3) = \varepsilon_{33}^{(0)} + n\varepsilon_{33}^{(1)} \tag{13a}$$

$$\gamma_{s3}(n,s,x_3) = \gamma_{s3}^{(0)} + n\gamma_{s3}^{(1)} \tag{13b}$$

$$\gamma_{n3}(n,s,x_3) = \gamma_{n3}^{(0)} \tag{13c}$$

where

$$\varepsilon_{33}^{(0)}(s,x_3) = u_{3,3}^{(0)} + \theta_{2,3}x_1 + \theta_{1,3}x_2 - \phi_{,33}F_\omega \tag{14a}$$

$$\varepsilon_{33}^{(1)}(s,x_3) = \theta_{2,3}x_{2,s} - \theta_{1,3}x_{1,s} + \phi_{,33}r_s \tag{14b}$$

$$\gamma_{s3}^{(0)}(s,x_3) = \gamma_{13}^{(0)}x_{1,s} + \gamma_{23}^{(0)}x_{2,s} \tag{14c}$$

$$\gamma_{s3}^{(1)}(s,x_3) = 2\phi_{,3} \tag{14d}$$

$$\gamma_{n3}^{(0)}(s,x_3) = \gamma_{13}^{(0)}x_{2,s} - \gamma_{23}^{(0)}x_{1,s} \tag{14e}$$

Moreover, the symmetric rotation gradients can be calculated by:

$$\chi_{ij} = \frac{1}{2}\left(\overline{\theta}_{i,j} + \overline{\theta}_{j,i}\right) \tag{15}$$

where $\overline{\theta}_i$ is defined as:

$$\overline{\theta}_1 = \frac{1}{2}\left(u_{3,2} - u_{2,3}\right) = \frac{1}{2}\left[\theta_1 - u_{2,3}^P - \left(X_1 - x_1^P\right)\phi_{,3}\right] \tag{16a}$$

$$\overline{\theta}_2 = \frac{1}{2}\left(u_{1,3} - u_{3,1}\right) = \frac{1}{2}\left[u_{1,3}^P - \theta_2 - \left(X_2 - x_2^P\right)\phi_{,3}\right] \tag{16b}$$

$$\overline{\theta}_3 = \frac{1}{2}\left(u_{2,1} - u_{1,2}\right) = \phi \tag{16c}$$

Substituting Eq. (16) into Eq. (15), the non-zero rotation gradients are expressed as follows:

$$\chi_{11} = -\frac{1}{2}\phi_{,3} \tag{17a}$$

$$\chi_{22} = -\frac{1}{2}\phi_{,3} \tag{17b}$$

$$\chi_{33} = \phi_{,3} \tag{17c}$$

$$\chi_{13} = \frac{1}{4}\left[\theta_{1,3} - u_{2,33}^P - \left(X_1 - x_1^P\right)\phi_{,33}\right] \tag{17d}$$

$$\chi_{23} = \frac{1}{4}\left[u_{1,33}^P - \theta_{2,3} - \left(X_2 - x_2^P\right)\phi_{,33}\right] \tag{17e}$$

Stresses

The constitutive equations can be written as:
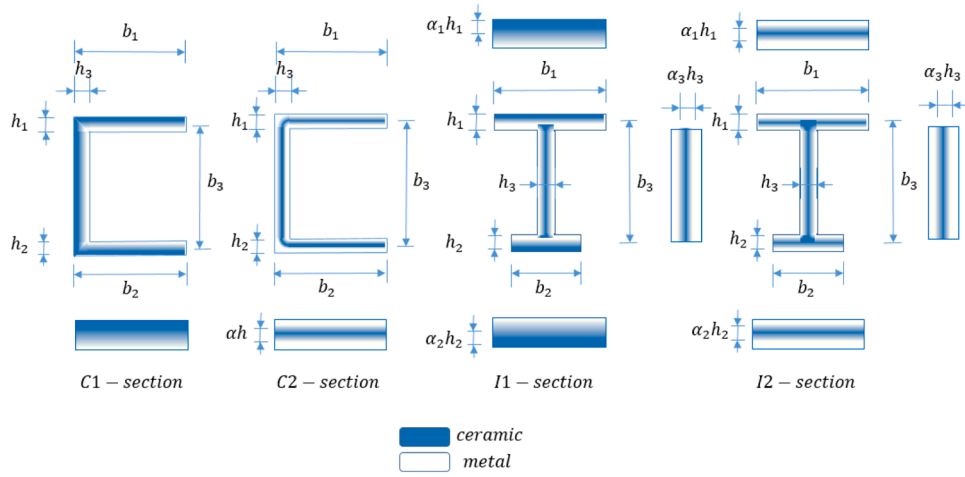
Fig. 3. Material distribution of thin-walled FG sandwich microbeams.

Table 1
Shape functions and essential BCs.

BC	$\varphi_j(x_3)$	$x_3 = 0$	$x_3 = L$
S-S	$\frac{z}{L}\left(1 - \frac{z}{L}\right)e^{\frac{-jz}{L}}$	$u_1^P = u_2^P = \phi = 0$	$u_1^P = u_2^P = \phi = 0$
C-F	$\left(\frac{z}{L}\right)^2 e^{\frac{-jz}{L}}$	$u_1^P = u_2^P = \phi = 0$ $u_{1,3}^P = u_{2,3}^P = \phi_{,3} = 0$ $u_3^{(0)} = \theta_2 = \theta_1 = 0$	
C—C	$\left(\frac{z}{L}\right)^2\left(1 - \frac{z}{L}\right)^2 e^{\frac{-jz}{L}}$	$u_1^P = u_2^P = \phi = 0$ $u_{1,3}^P = u_{2,3}^P = \phi_{,3} = 0$ $u_3^{(0)} = \theta_2 = \theta_1 = 0$	$u_1^P = u_2^P = \phi = 0$ $u_{1,3}^P = u_{2,3}^P = \phi_{,3} = 0$ $u_3^{(0)} = \theta_2 = \theta_1 = 0$

$$\begin{Bmatrix} \sigma_{33} \\ \sigma_{s3} \\ \sigma_{n3} \end{Bmatrix} = \begin{bmatrix} Q_{11} & 0 & 0 \\ 0 & Q_{66} & 0 \\ 0 & 0 & Q_{55} \end{bmatrix} \begin{Bmatrix} \varepsilon_{33} \\ \gamma_{s3} \\ \gamma_{n3} \end{Bmatrix} \quad (18a)$$

$$\begin{Bmatrix} m_{11} \\ m_{22} \\ m_{33} \\ m_{23} \\ m_{13} \end{Bmatrix} = 2\mu l^2 \begin{bmatrix} 1 & 0 & 0 & 0 & 0 \\ 0 & 1 & 0 & 0 & 0 \\ 0 & 0 & 1 & 0 & 0 \\ 0 & 0 & 0 & 1 & 0 \\ 0 & 0 & 0 & 0 & 1 \end{bmatrix} \begin{Bmatrix} \chi_{11} \\ \chi_{22} \\ \chi_{33} \\ \chi_{23} \\ \chi_{13} \end{Bmatrix} \quad (18b)$$

where $Q_{11} = E(n)$, $Q_{66} = Q_{55} = \mu = \frac{E(n)}{2(1+\nu)}$; $E(n)$ is the Young's modulus; ν is the Poisson's ratio, which is assumed to be constant. The effective mass density ρ and E are expressed by:

$$\rho = \rho_c V_c + \rho_m (1 - V_c) \quad (19a)$$

$$E = E_c V_c + E_m (1 - V_c) \quad (19b)$$

where the subscripts c and m indicate the ceramic and metal, V_c is the volume fraction of ceramic for I- and C-sections, which are given as follows:

- For C1 section (FG):

$$V_c = \left[\frac{n}{h_j} + 0.5\right]^p, \, -0.5h_j \leq n \leq 0.5h_j \quad (20)$$

- For C2, I2 sections and I1 section's web (FG sandwich):

$$V_c = \left[\frac{-|n| + 0.5h_j}{0.5\left(1 - \alpha_j\right)h_j}\right]^p, \, -0.5h_j \leq n \leq -0.5\alpha_j h_j \, \mathbf{or}, 0.5\alpha_j h_j \leq n \leq 0.5h_j, \quad (21a)$$

$$V_c = 1, \, -0.5\alpha_j h_j \leq n \leq 0.5\alpha_j h_j, \quad (21b)$$

- For I1-section's flanges (FG sandwich):

$$\mathbf{Flanges} : V_c = \left[\frac{n + 0.5h_j}{(1 - \alpha_j)h_j}\right]^p, \, -0.5h_j \leq n \leq \left(0.5 - \alpha_j\right)h_j \quad (22a)$$

Table 2
Convergence of fundamental frequencies and mid-span deflections of FG sandwich thin-walled C1-beams ($p = 5$).

b_3 /l	BC	m 2	4	6	8	10	12
Non-dimensional fundamental frequency							
1	S-S	8.157	8.051	8.020	8.020	8.020	8.020
	C-F	2.900	2.861	2.859	2.859	2.859	2.859
	C—C	18.186	18.121	18.118	18.116	18.115	18.115
0	S-S	2.039	2.012	2.005	2.005	2.005	2.005
	C-F	0.725	0.715	0.714	0.714	0.714	0.714
	C—C	4.546	4.529	4.529	4.529	4.529	4.529
Non-dimensional mid-span displacement							
1	S-S	26.205	26.993	27.164	27.151	27.153	27.153
	C-F	89.072	91.847	92.131	92.115	92.123	92.122
	C—C	5.704	5.696	5.714	5.722	5.723	5.722
0	S-S	86.280	88.895	89.461	89.418	89.424	89.423
	C-F	293.611	302.730	303.642	303.599	303.640	303.635
	C—C	18.550	18.514	18.561	18.589	18.589	18.590

Table 3

Verification on the mid-span deflections (*mm*) of FG sandwich C1- beams.

BC	Theory	p					
		0	0.5	1	2	5	10
$L/b_3 = 20$, Uniformly distributed load $q = 500N/m$							
S-S	Present	0.394	0.507	0.592	0.712	0.892	1.008
	Nguyen et al. (Shear) [19]	0.396	0.510	0.596	0.716	0.897	1.014
	Nguyen et al. (No shear) [19]	0.390	0.502	0.586	0.705	0.883	0.998
C-F	Present	1.337	1.722	2.011	2.418	3.030	3.424
	Nguyen et al. (Shear) [19]	1.343	1.730	2.021	2.429	3.044	3.440
	Nguyen et al. (No shear) [19]	1.325	1.706	1.993	2.396	3.003	3.393
C—C	Present	0.082	0.105	0.123	0.148	0.185	0.210
	Nguyen et al. (Shear) [19]	0.084	0.108	0.126	0.152	0.190	0.215
	Nguyen et al. (No shear) [19]	0.078	0.100	0.117	0.141	0.177	0.200
$L/b_3 = 50$, Uniformly distributed load $q = 500N/m$							
S-S	Present	15.249	19.637	22.939	27.572	34.554	39.047
	Nguyen et al. (Shear) [19]	15.261	19.654	22.958	27.596	34.583	39.080
	Nguyen et al. (No shear) [19]	15.223	19.605	22.900	27.527	34.496	38.982
C-F	Present	51.834	66.752	77.972	93.726	117.455	132.731
	Nguyen et al. (Shear) [19]	51.872	66.802	78.030	93.796	117.543	132.829
	Nguyen et al. (No shear) [19]	51.759	66.655	77.859	93.590	117.285	132.539
C—C	Present	3.069	3.952	4.617	5.550	6.955	7.859
	Nguyen et al. (Shear) [19]	3.082	3.969	4.637	5.573	6.984	7.893
	Nguyen et al. (No shear) [19]	3.045	3.921	4.580	5.505	6.899	7.797

Table 4

Verification on the fundamental frequencies of FG thin-walled S-S C1-beams ($L/b_3 = 40$).

Theory	$\overline{\omega}$	p					
		0	0.5	1	2	5	10
Present	$\overline{\omega}_1$	3.0659	2.7541	2.5543	2.3112	2.0047	1.8348
	$\overline{\omega}_2$	4.3456	3.8292	3.5581	3.2963	3.0128	2.8087
	$\overline{\omega}_3$	10.2076	9.1571	8.5057	7.7367	6.7841	6.2312
	$\overline{\omega}_4$	12.0947	10.7398	9.9695	9.1286	7.9979	7.3273
Nguyen et al. [13]	$\overline{\omega}_1$	3.0668	2.7612	2.5642	2.3227	2.0148	1.8421
	$\overline{\omega}_2$	4.3475	3.8641	3.6385	3.4141	3.1054	2.8575
	$\overline{\omega}_3$	10.2254	9.2060	8.5828	7.8407	6.8811	6.2951
	$\overline{\omega}_4$	12.1029	10.8223	10.1441	9.2903	8.0589	7.3684
Nguyen et al. [19] (Shear)	$\overline{\omega}_1$	3.0659	2.7541	2.5544	2.3114	2.0048	1.8349
	$\overline{\omega}_2$	4.3462	3.8270	3.5533	3.2895	3.0075	2.8059
	$\overline{\omega}_3$	10.1965	9.1416	8.4879	7.7173	6.7663	6.2169
	$\overline{\omega}_4$	12.0939	10.7356	9.9661	9.1447	8.0110	7.3327
Nguyen et al. [19] (No shear)	$\overline{\omega}_1$	3.0668	2.7549	2.5551	2.3119	2.0054	1.8354
	$\overline{\omega}_2$	4.3475	3.8653	3.6402	3.4168	3.1088	2.8599
	$\overline{\omega}_3$	10.2254	9.2126	8.5910	7.8480	6.8848	6.2971
	$\overline{\omega}_4$	12.1028	10.7996	10.1011	9.2302	8.0168	7.3391

Table 5

Verification on fundamental frequencies of FG thin-walled S-S C2- beams ($L/b_3 = 40$).

Theory	$\overline{\omega}$	p					
		0	0.5	1	2	5	10
Present	$\overline{\omega}_1$	3.0659	2.8667	2.7484	2.6137	2.4585	2.3796
	$\overline{\omega}_2$	4.3456	3.7623	3.4420	3.1188	2.8245	2.7139
	$\overline{\omega}_3$	10.2076	9.4192	8.9713	8.4818	7.9459	7.6852
	$\overline{\omega}_4$	12.0947	10.8030	10.0971	9.3697	8.6553	8.3493
Nguyen et al. [13]	$\overline{\omega}_1$	3.0668	2.8676	2.7492	2.6145	2.4592	2.3803
	$\overline{\omega}_2$	4.3475	3.7636	3.4431	3.1197	2.8252	2.7146
	$\overline{\omega}_3$	10.2254	9.4364	8.9881	8.4980	7.9612	7.7001
	$\overline{\omega}_4$	12.1029	10.8096	10.1029	9.3747	8.6598	8.3535

$$V_c = 1, -0.5h_j \leq n \leq (0.5 - \alpha_j)h_j, (0.5 - \alpha_j)h_j \leq n \leq 0.5h_j \qquad (22b)$$

where *p* is the power-law index, h_j $(j = 1, 2, 3)$ are the thicknesses of the top flange, bottom flange and web; α_j $(j = 1, 2, 3)$ are the thickness ratio of the ceramic for the top flange, bottom flange and web, respectively.

The notations of $h_1, h_2, h_3, \alpha_1, \alpha_2, \alpha_3$ in various sections are shown in Fig. 3.

Variational formulation

The characteristic equations of the system can be derived from Eq. (1) based on Hamilton's principle as follows:

Table 6

Verification on the deflections of FG thin-walled I1- beams under concentrated load *P* at mid-span.

BC	Reference	$L/b_3 = 10$				$L/b_3 = 20$			
		$p = 0$	1	2	5	$p = 0$	1	2	5
S-S	Present	82.9632	101.2863	109.8149	120.2931	80.3469	98.1423	106.4453	116.6634
	Nguyen et al. (Shear) [20]	82.9651	101.0141	109.4870	120.0059	80.3458	97.8696	106.1140	116.3724
	Nguyen et al. (No shear) [20]	79.4759	96.8193	104.9908	115.1634	79.4735	96.8217	104.9908	115.1618
C-F	Present	166.1572	202.8527	219.9295	240.9113	160.7956	196.4121	213.0255	233.4717
	Nguyen et al. (Shear) [20]	166.0264	202.1436	219.0958	240.1466	160.7613	195.8234	212.3202	232.8442
	Nguyen et al. (No shear) [20]	159.0095	193.7156	210.0585	230.4101	159.0071	193.7164	210.0609	230.4101
C—C	Present	23.3205	28.3885	30.7710	33.6108	20.7168	25.2846	27.4160	30.0292
	Nguyen et al. (Shear) [20]	23.2508	28.2537	30.5755	33.4169	20.6627	25.1701	27.2635	29.8981
	Nguyen et al. (No shear) [20]	19.8706	24.1872	26.2140	28.7219	19.8169	24.1543	26.1739	28.7235

Table 7

Verification on the mid-span deflections of FG thin-walled I2-beams under concentrated load at mid-span with different boundary conditions.

BC	Reference	$L/b_3 = 10$				$L/b_3 = 20$			
		$p = 0$	1	2	5	$p = 0$	1	2	5
S-S	Present	82.963	118.814	138.803	166.876	80.347	115.064	134.430	161.615
	Nguyen et al. (Shear) [20]	82.965	118.813	138.799	166.879	80.346	115.064	134.424	161.614
	Nguyen et al. (No shear) [20]	79.476	113.816	132.962	159.863	79.473	113.815	132.964	159.859
C-F	Present	166.157	237.953	277.989	334.219	160.796	230.275	269.020	323.436
	Nguyen et al. (Shear) [20]	166.026	237.761	277.765	333.951	160.761	230.227	268.963	323.367
	Nguyen et al. (No shear) [20]	159.009	227.716	266.027	319.841	159.007	227.715	266.028	319.839
C—C	Present	23.321	33.365	38.974	46.851	20.717	29.659	34.650	41.658
	Nguyen et al. (Shear) [20]	23.251	33.212	38.689	46.655	20.663	29.603	34.589	41.588
	Nguyen et al. (No shear) [20]	19.871	28.363	33.039	39.844	19.8169	24.1543	26.1739	28.7235

Table 8

Verification on the non-dimensional fundamental frequencies of FG thin-walled S-S I1- beams ($L/b_3 = 40$).

Section	Theory	p	α_3										
			0	0.1	0.2	0.3	0.4	0.5	0.6	0.7	0.8	0.9	1
M1 [13] ($\alpha_1 = 0.9, \alpha_2 = 0.1$)	Present	1	1.516	1.509	1.504	1.498	1.493	1.489	1.485	1.481	1.478	1.474	1.471
		5	1.511	1.498	1.486	1.476	1.468	1.461	1.455	1.450	1.446	1.442	1.438
	Nguyen et al. [13]	1	1.530	1.518	1.515	1.508	1.503	1.497	1.491	1.487	1.482	1.478	1.475
		5	1.559	1.539	1.522	1.506	1.493	1.482	1.472	1.464	1.456	1.450	1.444
M2 [13] ($\alpha_1 = 0.1, \alpha_2 = 0.9$)	Present	1	1.334	1.328	1.322	1.316	1.311	1.306	1.301	1.297	1.292	1.288	1.284
		5	1.165	1.154	1.144	1.134	1.125	1.116	1.108	1.100	1.093	1.086	1.079
	Nguyen et al. [13]	1	1.327	1.322	1.316	1.311	1.306	1.301	1.297	1.292	1.288	1.284	1.281
		5	1.153	1.143	1.133	1.125	1.116	1.108	1.101	1.094	1.087	1.081	1.074

$$\int_{t_1}^{t_2} (\delta\Pi_S + \delta\Pi_W - \delta\Pi_K)dt = 0 \tag{23}$$

The variation of the strain energy $\delta\Pi_S$ of the system is defined by:

$$\delta\Pi_S = \int_V (\sigma_{33}\delta\varepsilon_{33} + \sigma_{s3}\delta\gamma_{s3} + \sigma_{n3}\delta\gamma_{n3})dV$$
$$+ \int_V (m_{11}\delta\chi_{11} + m_{22}\delta\chi_{22} + m_{33}\delta\chi_{33} + 2m_{13}\delta\chi_{13} + 2m_{23}\delta\chi_{23})dV \tag{24}$$

where the shear correction coefficient is assumed to be unity. Substituting Eqs. (13) and (17) into Eq. (24) leads to have:

$$\delta\Pi_S = \int_0^L \left[T_{33}\delta u_{3,3}^{(0)} + M_{22}\delta\theta_{2,3} + M_{11}\delta\theta_{1,3} + M_\varpi\delta\phi_{,33} \right.$$
$$+ V_{11}\delta\left(u_{1,3}^P + \theta_2\right) + V_{22}\delta\left(u_{2,3}^P + \theta_1\right) + M_{33}\delta\phi_{,3} \right] dx_3$$
$$+ \int_0^L \left[M_{33}^\chi\delta\phi_{,3} + V_{11}^\chi\delta\left(u_{1,33}^P - \theta_{2,3}\right) + V_{22}^\chi\delta\left(\theta_{1,3} - u_{2,33}^P\right) + M_\varpi^\chi\delta\phi_{,33} \right] dx_3 \tag{25}$$

where the stress resultants $(T_{33}, M_{22}, M_{11}, M_\varpi, V_{11}, V_{22}, M_{33})$ and $(M_{33}^\chi, M_\varpi^\chi, V_{11}^\chi, V_{22}^\chi)$ are defined as follows:

$$(T_{33}, M_{22}, M_{11}, M_\varpi) = \int_A (1, X_1, X_2, nr_s - F_\omega)\sigma_{33}dsdn \tag{26a}$$

$$(V_{11}, V_{22}, M_{33}) = \int_A \left(\sigma_{s3}x_{1,s} + \sigma_{n3}x_{2,s}, \sigma_{s3}x_{2,s} - \sigma_{n3}x_{1,s}, 2n\sigma_{s3} \right)dsdn \tag{26b}$$

$$(M_{33}^\chi, V_{11}^\chi, V_{22}^\chi) = \int_A \left(m_{33} - \frac{m_{11}}{2} - \frac{m_{22}}{2}, \frac{m_{23}}{2}, \frac{m_{13}}{2} \right)dsdn \tag{26c}$$

$$M_\varpi^\chi = -\int_A \left[m_{13}\left(X_1 - x_1^P\right) + m_{23}\left(X_2 - x_2^P\right) \right]dsdn \tag{26d}$$

The stress resultants given above are related to the displacement as follows:
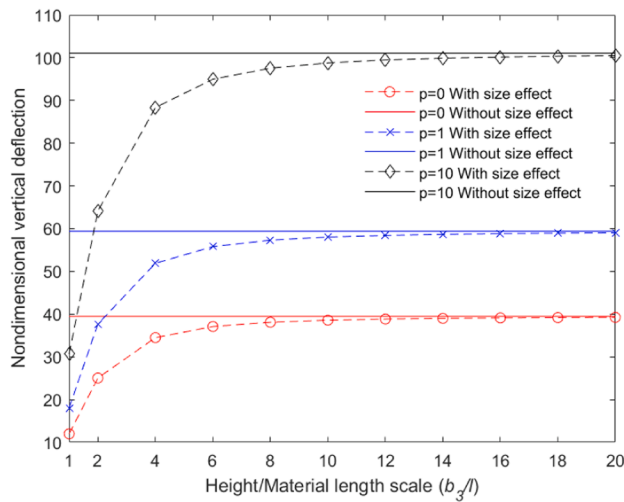
a) S-S
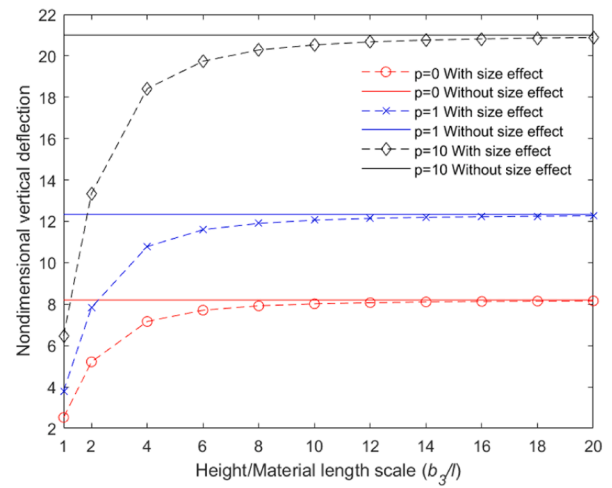
b) C-C
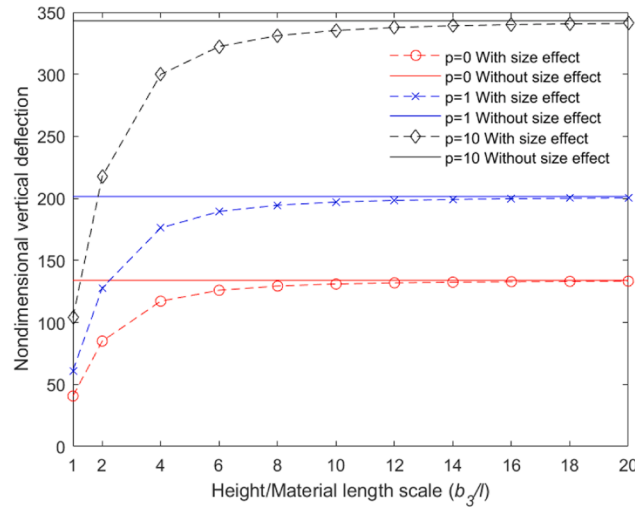
c) C-F

Fig. 4. Effects of b_3/l on the mid-span deflections of FG thin-walled C1-beams under uniformly distributed load ($L/b_3 = 20$).

$$
\left\{
\begin{array}{c}
T_{33} \\
M_{22} \\
M_{11} \\
V_{11} \\
V_{22} \\
M_{33} \\
M_{\varpi}
\end{array}
\right\}
=
\begin{bmatrix}
L_{11} & L_{12} & L_{13} & 0 & 0 & 0 & L_{17} \\
L_{12} & L_{22} & L_{23} & 0 & 0 & 0 & L_{27} \\
L_{13} & L_{23} & L_{33} & 0 & 0 & 0 & L_{37} \\
0 & 0 & 0 & L_{44} & L_{45} & L_{46} & 0 \\
0 & 0 & 0 & L_{45} & L_{55} & L_{56} & 0 \\
0 & 0 & 0 & L_{46} & L_{56} & L_{66} & 0 \\
0 & 0 & 0 & 0 & 0 & 0 & L_{77}
\end{bmatrix}
\left\{
\begin{array}{c}
u_{3,3}^{(0)} \\
\theta_{2,3} \\
\theta_{1,3} \\
u_{1,3}^{P} + \theta_2 \\
u_{2,3}^{P} + \theta_1 \\
\phi_{,3} \\
\phi_{,33}
\end{array}
\right\}
\quad (27a)
$$

$$
\left\{
\begin{array}{c}
M_{33}^{\chi} \\
V_{11}^{\chi} \\
V_{22}^{\chi} \\
M_{\varpi}^{\chi}
\end{array}
\right\}
=
\begin{bmatrix}
H_{11} & 0 & 0 & 0 \\
0 & H_{22} & 0 & H_{24} \\
0 & 0 & H_{33} & H_{34} \\
0 & H_{24} & H_{34} & H_{44}
\end{bmatrix}
\left\{
\begin{array}{c}
\phi_{,3} \\
u_{1,33}^{P} - \theta_{2,3} \\
\theta_{1,3} - u_{2,33}^{P} \\
\phi_{,33}
\end{array}
\right\}
\quad (27b)
$$

where the stiffness components are defined by:

$$L_{11} = \int_s A_{11} ds, L_{12} = \int_s (A_{11}x_1 + B_{11}x_{2,s}) ds, L_{13} = \int_s (A_{11}x_2 - B_{11}x_{1,s}) ds$$

$$L_{17} = \int_s (B_{11}r_s - A_{11}F_\omega) ds, L_{22} = \int_s \left(A_{11}x_1^2 + 2B_{11}x_1 x_{2,s} + D_{11}x_{2,s}^2\right) ds$$

$$L_{23} = \int_s \left[A_{11}x_1 x_2 + B_{11}\left(x_2 x_{2,s} - x_1 x_{1,s}\right) - D_{11}x_{1,s}x_{2,s}\right] ds$$

$$L_{27} = \int_s \left[-A_{11}x_1 F_\omega + B_{11}\left(x_1 r_s - x_{2,s}F_\omega\right) + D_{11}r_s x_{2,s}\right] ds$$

$$L_{33} = \int_s \left(A_{11}x_2^2 - 2B_{11}x_{1,s}x_2 + D_{11}x_{1,s}^2\right) ds$$

$$L_{37} = \int_s \left[-A_{11}x_2 F_\omega + B_{11}\left(x_2 r_s + x_{1,s}F_\omega\right) - D_{11}r_s x_{1,s}\right] ds$$

$$L_{44} = \int_s \left(A_{66}x_{1,s}^2 + A_{55}x_{2,s}^2\right) ds, L_{45} = \int_s (A_{66} - A_{55})x_{1,s}x_{2,s} ds, L_{46} = \int_s 2B_{66}x_{1,s} ds$$

$$L_{55} = \int_s \left(A_{66}x_{2,s}^2 + A_{55}x_{1,s}^2\right) ds, L_{56} = \int_s 2B_{66}x_{2,s} ds, L_{66} = \int_s 4D_{66} ds$$

$$L_{77} = \int_s \left(A_{11}F_\omega^2 - 2B_{11}r_s F_\omega + D_{11}r_s^2\right) ds$$

$$H_{11} = 3l^2 \int_A \mu dnds, H_{22} = \frac{l^2}{4}\int_A \mu dnds, H_{24} = -\frac{l^2}{4}\int_A \mu\left(X_2 - x_2^P\right) dnds$$

$$H_{33} = \frac{l^2}{4}\int_A \mu dnds, H_{34} = -\frac{l^2}{4}\int_A \mu\left(X_1 - x_1^P\right) dnds$$

$$H_{44} = \frac{l^2}{4}\int_A \mu\left[\left(X_1 - x_1^P\right)^2 + \left(X_2 - x_2^P\right)^2\right] dnds$$

$$\left(A_{ij}, B_{ij}, D_{ij}\right) = \int_s \left(1, n, n^2\right) Q_{ij} ds$$

(28)

The variation of potential energy Π_W of the system subjected to a transverse load q can be expressed as:

$$\delta\Pi_W = -\int_0^L q\delta u_2^P dx_3$$

(29)

The variation of kinetic energy Π_K of the system is given by:

$$\delta\Pi_K = \int_\Omega \rho(n)(\dot{u}_1\delta\dot{u}_1 + \dot{u}_2\delta\dot{u}_2 + \dot{u}_3\delta\dot{u}_3) d\Omega$$

$$= \int_0^L \left\{\delta\dot{u}_1^P\left(m_1\dot{u}_1^P - m_2\dot\phi\right) + \delta\dot{u}_2^P\left(m_1\dot{u}_2^P + m_3\dot\phi\right) + \delta\dot{u}_3^{(0)}\left(m_1\dot{u}_3^{(0)} + m_6\dot\theta_2 + m_{10}\dot\theta_1 - m_{13}\dot\phi_{,3}\right)\right.$$

$$+\delta\dot\theta_2\left(m_6\dot{u}_3^{(0)} + m_7\dot\theta_2 + m_8\dot\theta_1 - m_9\dot\phi_{,3}\right) + \delta\dot\theta_1\left(m_{10}\dot{u}_3^{(0)} + m_8\dot\theta_2 + m_{11}\dot\theta_1 - m_{12}\dot\phi_{,3}\right)$$

$$\left.+\delta\dot\phi\left[-m_2\dot{u}_1^P + m_3\dot{u}_2^P + (m_4 + m_5)\dot\phi\right] + \delta\dot\phi_{,3}\left[-m_{13}\dot{u}_3^{(0)} - m_9\dot\theta_2 - m_{12}\dot\theta_1 + m_{14}\dot\phi_{,3}\right]\right\} dx_3$$

(30)

where the terms of mass m_i are given as follows:

$$\{m_1, m_2, m_3, m_4, m_5\} = \int_A \rho\left\{1, X_2 - x_2^P, X_1 - x_1^P, \left(X_2 - x_2^P\right)^2, \left(X_1 - x_1^P\right)^2\right\} dnds$$

(31a)

$$\{m_6, m_7, m_8, m_9\} = \int_A \rho X_1\{1, X_1, X_2, \overline{F}_\omega\} dnds$$

(31b)

$$\{m_{10}, m_{11}, m_{12}\} = \int_A \rho X_2\{1, X_2, \overline{F}_\omega\} dnds$$

(31c)

$$\{m_{13}, m_{14}\} = \int_A \rho\left\{\overline{F}_\omega, \overline{F}_\omega^2\right\} dnds$$

(31d)

Hybrid series solution

The displacement field is approximated via unknowns $(u_{1j}^P(t), u_{2j}^P(t), u_{3j}(t), \theta_{2j}(t), \theta_{1j}(t)$ and $\phi_j(t))$ and shape functions $(\psi_j(x_3))$ as follows:

$$\{u_1^P, u_2^P, \phi\}(x_3, t) = \sum_{j=1}^m \psi_j(x_3)\{u_{1j}^P, u_{2j}^P, \phi_j\}(t)$$

(32a)

$$\left\{u_3^{(0)}, \theta_1, \theta_2\right\}(x_3, t) = \sum_{j=1}^m \psi_{j,3}(x_3)\{u_{3j}, \theta_{1j}, \theta_{2j}\}(t)$$

(32b)

It should be noted that hybrid shape functions are proposed in Table 1 by a combination of exponential and admissible trigonometric functions to satisfy various BCs such as simply-supported (S-S), clamped-free (C-F) and clamped-clamped (C—C).

Substituting Eq. (32) into Eqs. (25), (29) and (30), and then plugging the subsequent results into Eq. (23) leads to the characteristic equations for bending and vibration analysis of FG sandwich thin-walled micro-beams as follows:

$$\mathbf{Kd} + \mathbf{M\ddot{d}} = \mathbf{F}$$

(33)

where $\mathbf{K}, \mathbf{M}, \mathbf{F}$ are the stiffness matrix, mass matrix and force vector, respectively; $\mathbf{d} = \begin{bmatrix} \mathbf{u_1^P} & \mathbf{u_2^P} & \mathbf{u_3} & \boldsymbol{\theta_2} & \boldsymbol{\theta_1} & \boldsymbol{\Phi} \end{bmatrix}^T$ is the displacement vector. It is noted that the stiffness matrix $\mathbf{K}$ can be divided into that of strain part $\mathbf{K}^\varepsilon$ and that of strain gradient $\mathbf{K}^\chi$, i.e. $\mathbf{K} = \mathbf{K}^\varepsilon + \mathbf{K}^\chi$ as follows:

$$\mathbf{K}^\varepsilon = \begin{bmatrix} \mathbf{K}^{\varepsilon 11} & \mathbf{K}^{\varepsilon 12} & \mathbf{0} & \mathbf{K}^{\varepsilon 14} & \mathbf{K}^{\varepsilon 15} & \mathbf{K}^{\varepsilon 16} \\ \mathbf{K}^{\varepsilon 12} & \mathbf{K}^{\varepsilon 22} & \mathbf{0} & \mathbf{K}^{\varepsilon 24} & \mathbf{K}^{\varepsilon 25} & \mathbf{K}^{\varepsilon 26} \\ \mathbf{K}^{\varepsilon 13} & \mathbf{K}^{\varepsilon 23} & \mathbf{K}^{\varepsilon 33} & \mathbf{K}^{\varepsilon 34} & \mathbf{K}^{\varepsilon 35} & \mathbf{K}^{\varepsilon 36} \\ \mathbf{K}^{\varepsilon 14} & \mathbf{K}^{\varepsilon 24} & \mathbf{K}^{\varepsilon 34} & \mathbf{K}^{\varepsilon 44} & \mathbf{K}^{\varepsilon 45} & \mathbf{K}^{\varepsilon 46} \\ \mathbf{K}^{\varepsilon 15} & \mathbf{K}^{\varepsilon 25} & \mathbf{K}^{\varepsilon 35} & \mathbf{K}^{\varepsilon 45} & \mathbf{K}^{\varepsilon 55} & \mathbf{K}^{\varepsilon 56} \\ \mathbf{K}^{\varepsilon 16} & \mathbf{K}^{\varepsilon 26} & \mathbf{K}^{\varepsilon 36} & \mathbf{K}^{\varepsilon 46} & \mathbf{K}^{\varepsilon 56} & \mathbf{K}^{\varepsilon 66} \end{bmatrix}$$

(34a)

$$\mathbf{K}^\chi = \begin{bmatrix} \mathbf{K}^{\chi 11} & \mathbf{0} & \mathbf{0} & \mathbf{K}^{\chi 14} & \mathbf{0} & \mathbf{K}^{\chi 16} \\ \mathbf{K}^{\chi 12} & \mathbf{K}^{\chi 22} & \mathbf{0} & \mathbf{0} & \mathbf{K}^{\chi 25} & \mathbf{K}^{\chi 26} \\ \mathbf{0} & \mathbf{0} & \mathbf{0} & \mathbf{0} & \mathbf{0} & \mathbf{0} \\ \mathbf{K}^{\chi 14} & \mathbf{0} & \mathbf{0} & \mathbf{K}^{\chi 44} & \mathbf{0} & \mathbf{K}^{\chi 46} \\ \mathbf{0} & \mathbf{K}^{\chi 25} & \mathbf{0} & \mathbf{0} & \mathbf{K}^{\chi 55} & \mathbf{K}^{\chi 56} \\ \mathbf{K}^{\chi 16} & \mathbf{K}^{\chi 26} & \mathbf{0} & \mathbf{K}^{\chi 46} & \mathbf{K}^{\chi 56} & \mathbf{K}^{\chi 66} \end{bmatrix}$$
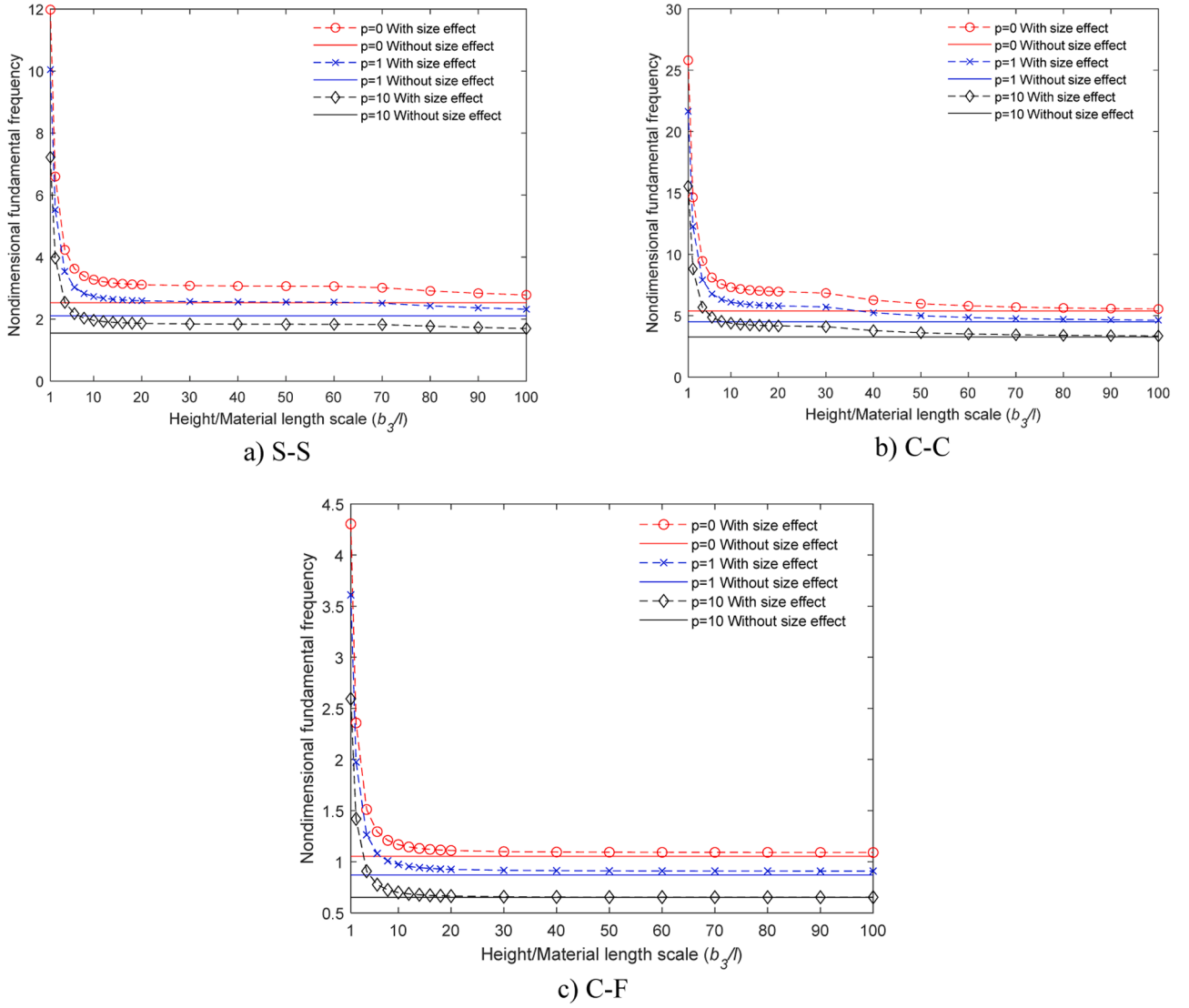
(34b)

a) S-S

b) C-C

c) C-F

Fig. 5. Effects of b_3/l on the fundamental frequency of FG thin-walled C1-beams ($L/b_3 = 10$).

where

$$K_{ij}^{\varepsilon 11} = L_{44}S_{ij}^{11}, K_{ij}^{\varepsilon 12} = L_{45}S_{ij}^{11}, K_{ij}^{\varepsilon 14} = L_{44}S_{ij}^{11}, K_{ij}^{\varepsilon 15} = L_{45}S_{ij}^{11}, K_{ij}^{\varepsilon 16} = L_{46}S_{ij}^{11}$$

$$K_{ij}^{\varepsilon 22} = L_{55}S_{ij}^{11}, K_{ij}^{\varepsilon 24} = L_{45}S_{ij}^{11}, K_{ij}^{\varepsilon 25} = L_{55}S_{ij}^{11}, K_{ij}^{\varepsilon 26} = L_{56}S_{ij}^{11}$$

$$K_{ij}^{\varepsilon 33} = L_{11}S_{ij}^{22}, K_{ij}^{\varepsilon 34} = L_{12}S_{ij}^{22}, K_{ij}^{\varepsilon 35} = L_{13}S_{ij}^{22}, K_{ij}^{\varepsilon 36} = L_{17}S_{ij}^{22}$$

$$K_{ij}^{\varepsilon 44} = L_{22}S_{ij}^{22} + L_{44}S_{ij}^{11}, K_{ij}^{\varepsilon 45} = L_{23}S_{ij}^{22} + L_{45}S_{ij}^{11}$$

$$K_{ij}^{\varepsilon 46} = L_{27}S_{ij}^{22} + L_{46}S_{ij}^{11}, K_{ij}^{\varepsilon 55} = L_{33}S_{ij}^{22} + L_{55}S_{ij}^{11}$$

$$K_{ij}^{\varepsilon 56} = L_{37}S_{ij}^{22} + L_{56}S_{ij}^{11}, K_{ij}^{\varepsilon 66} = L_{77}S_{ij}^{22} + L_{66}S_{ij}^{11}$$

$$K_{ij}^{\chi 11} = H_{22}S_{ij}^{22}, K_{ij}^{\chi 14} = -H_{22}S_{ij}^{22}, K_{ij}^{\chi 16} = H_{24}S_{ij}^{22}$$

$$K_{ij}^{\chi 22} = H_{23}S_{ij}^{22}, K_{ij}^{\chi 25} = -H_{23}S_{ij}^{22}, K_{ij}^{\chi 26} = -H_{34}S_{ij}^{22}$$

$$K_{ij}^{\chi 44} = H_{22}S_{ij}^{22}, K_{ij}^{\chi 46} = -H_{24}S_{ij}^{22}, K_{ij}^{\chi 55} = H_{23}S_{ij}^{22}$$

$$K_{ij}^{\chi 55} = H_{23}S_{ij}^{22}, K_{ij}^{\chi 56} = H_{34}S_{ij}^{22}, K_{ij}^{\chi 66} = H_{11}S_{ij}^{11} + H_{44}S_{ij}^{22}$$

$$S_{ij}^{rs} = \int_0^L \frac{\partial^r \psi_i}{\partial x_3^r} \frac{\partial^s \psi_j}{\partial x_3^s} dx_3$$

(35)

The components of mass matrix **M** are given by:

$$\mathbf{M} = \begin{bmatrix} \mathbf{M}^{11} & \mathbf{0} & \mathbf{0} & \mathbf{0} & \mathbf{0} & \mathbf{M}^{16} \\ \mathbf{0} & \mathbf{M}^{22} & \mathbf{0} & \mathbf{0} & \mathbf{0} & \mathbf{M}^{26} \\ \mathbf{0} & \mathbf{0} & {}^T\mathbf{M}^{33} & \mathbf{M}^{34} & \mathbf{M}^{35} & \mathbf{M}^{36} \\ \mathbf{0} & \mathbf{0} & {}^T\mathbf{M}^{34} & \mathbf{M}^{44} & \mathbf{M}^{45} & \mathbf{M}^{46} \\ \mathbf{0} & \mathbf{0} & {}^T\mathbf{M}^{35} & {}^T\mathbf{M}^{45} & \mathbf{M}^{55} & \mathbf{M}^{56} \\ {}^T\mathbf{M}^{16} & {}^T\mathbf{M}^{26} & {}^T\mathbf{M}^{36} & {}^T\mathbf{M}^{46} & {}^T\mathbf{M}^{56} & \mathbf{M}^{66} \end{bmatrix}$$

(36)

where

$$M_{ij}^{11} = m_1 S_{ij}^{00}, M_{ij}^{16} = -m_2 S_{ij}^{00}, M_{ij}^{22} = m_1 S_{ij}^{00}, M_{ij}^{26} = m_3 S_{ij}^{00}, M_{ij}^{33} = m_1 S_{ij}^{11}$$

$$M_{ij}^{34} = m_6 S_{ij}^{11}, M_{ij}^{35} = M_{10} S_{ij}^{11}, M_{ij}^{36} = -m_{13} S_{ij}^{11}, M_{ij}^{44} = m_7 S_{ij}^{11}, M_{ij}^{45} = m_8 S_{ij}^{11}$$

$$M_{ij}^{46} = -m_9 S_{ij}^{11}, M_{ij}^{55} = m_{11} S_{ij}^{11}, M_{ij}^{56} = -m_{12} S_{ij}^{11}, M_{ij}^{66} = m_{14} S_{ij}^{11} + (m_4 + m_5) S_{ij}^{00}$$

(37)

The non-zero components of load vector $\mathbf{F} = \begin{bmatrix} \mathbf{0} & \mathbf{f} & \mathbf{0} & \mathbf{0} & \mathbf{0} & \mathbf{0} \end{bmatrix}^T$ are given by:

$$f_i = \int_0^L q\psi_i dx_3$$

(38)

9

a) S-S

b) C-C

c) C-F
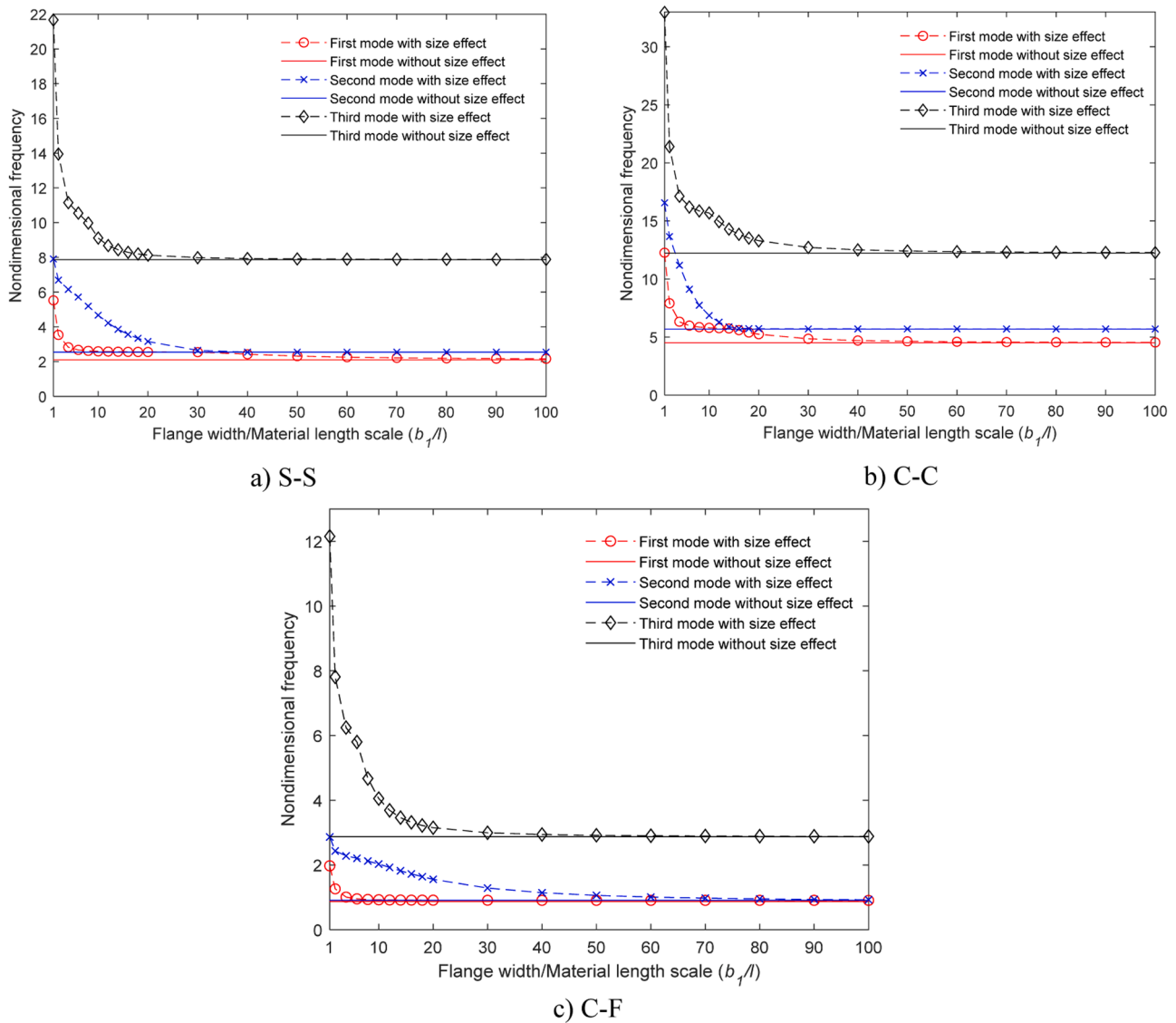
Fig. 6. Effects of b_1/l on the first three natural frequencies of FG thin-walled C1-beams ($L/b_3 = 10, p = 1$).

Table 9
Size effects on the mid-span deflections of FG thin-walled C1-section microbeams under uniformly distributed load.

BC	b_3 / l	$L/b_3 = 10$				$L/b_3 = 20$			
		$p = 0$	1	2	5	$p = 0$	1	2	5
S-S	0	40.682	61.198	73.563	92.187	39.463	59.364	71.358	89.424
	1	12.501	18.805	22.604	28.327	11.983	18.025	21.667	27.153
	2	25.858	38.898	46.756	58.595	25.042	37.670	45.281	56.745
	4	35.563	53.497	64.305	80.586	34.492	51.885	62.367	78.158
C-F	0	137.612	207.009	248.835	311.834	133.997	201.570	242.296	303.640
	1	42.090	63.315	76.107	95.377	40.654	61.154	73.510	92.123
	2	87.326	131.362	157.903	197.883	85.012	127.882	153.719	192.639
	4	120.218	180.842	217.380	272.417	117.110	176.165	211.757	265.371
C—C	0	9.383	14.117	16.965	21.483	8.209	12.341	14.834	18.592
	1	2.982	4.485	5.392	6.758	2.526	3.799	4.566	5.723
	2	5.965	8.963	10.774	13.507	5.214	7.843	9.426	11.815
	4	8.182	12.309	14.788	18.540	7.163	10.786	12.965	16.249

Numerical results

In this section, several numerical examples for FG thin-walled sandwich microbeams with and without the size-effect are presented. The geometries of I- and C-sections are given in Fig. 3 by $h = h_1 = h_2 = h_3$; $b_3 = 40h$ For C1 and C2-section, $b_1 = b_2 = 20h$ while for I1 and I2-section, $b_1 = 20h$, $b_2 = 10h$. Unless stated otherwise, the thickness ratios of ceramic material are given as: for I1, $\alpha_1 = 0.9, \alpha_2 = 0.1, \alpha_3 = 0.4$, for I2 $\alpha_1 = \alpha_2 = \alpha_3 = 0.1$ and for C2, $\alpha_1 = \alpha_2 = \alpha_3 = 0.3$. The following material properties are used for the static analysis: $E_c = 320.7$ GPa, $E_m =$

Table 10
Size effects on the lowest frequencies of FG thin-walled S-S C1-section microbeams ($L/b_3 = 10$).

b_3/l	$\overline{\omega}$	p					
		0	0.5	1	2	5	10
0	$\overline{\omega}_1$	2.530	2.267	2.106	1.917	1.685	1.549
	$\overline{\omega}_2$	3.053	2.743	2.544	2.302	1.997	1.828
	$\overline{\omega}_3$	9.406	8.475	7.874	7.136	6.193	5.661
	$\overline{\omega}_4$	9.509	8.553	7.944	7.207	6.275	5.746
1	$\overline{\omega}_1$	11.982	10.809	10.049	9.110	7.903	7.219
	$\overline{\omega}_2$	13.597	12.269	11.408	10.343	8.972	8.195
	$\overline{\omega}_3$	45.890	41.402	38.490	34.896	30.270	27.651
	$\overline{\omega}_4$	49.831	44.968	41.810	37.910	32.886	30.037
2	$\overline{\omega}_1$	6.595	5.945	5.525	5.007	4.344	3.969
	$\overline{\omega}_2$	9.432	8.511	7.914	7.175	6.224	5.685
	$\overline{\omega}_3$	25.859	23.315	21.667	19.638	17.035	15.565
	$\overline{\omega}_4$	34.818	31.422	29.216	26.492	22.980	20.989
4	$\overline{\omega}_1$	4.231	3.809	3.537	3.204	2.779	2.541
	$\overline{\omega}_2$	7.977	7.199	6.694	6.070	5.265	4.809
	$\overline{\omega}_3$	16.682	15.020	13.948	12.634	10.959	10.020
	$\overline{\omega}_4$	28.861	26.050	24.224	21.968	19.057	17.404

105.69 GPa, $\nu = \nu_c = \nu_m = 0.3$ and the vibration analysis: $E_c = 380$ GPa, $E_m = 70$ GPa, $\nu = \nu_c = \nu_m = 0.3$, $\rho_c = 3960 kg/m^3$, $\rho_m = 2702 kg/m^3$. The MLSP is assumed to be $l = 15\mu m$ for the analysis of all subsequent sections. The non-dimensional deflections and frequencies of micro-beams are revealed as follows.

Non-dimensional deflection under point load (P):

$$\overline{u}_2^P = 1000 \frac{E_c hb^3}{PL^3} u_2^P \tag{39}$$

Non-dimensional deflection under uniform distributed load (q):

$$\overline{u}_2^P = 1000 \frac{E_c hb^3}{qL^4} u_2^P \tag{40}$$

Non-dimensional frequency:

$$\overline{\omega} = \frac{L^2}{b_3} \sqrt{\frac{\rho_m}{E_m}} \omega \tag{41}$$

Convergence study

FG thin-walled C1-beams ($p = 5$, $L/b_3 = 20$ and 40) under uniformly distributed load q with various BCs are analysed. Their fundamental frequencies and mid-span deflections are presented in Table 2. The beam height-to-material length scale ratio $b_3/l = 0$ refers to macrobeam while $b_3/l = 1$ is for microbeam. It can be seen that in all cases, the series number $m = 10$ ensures the convergence of the present solution. For that reason, $m = 10$ will be used in the subsequent sections.

Verification studies

Since there is no available results on the FG sandwich thin-walled microbeams, the verification is carried out with those of macrobeams ($b_3/l = 0$).

Example 1. FG thin-walled C1- and C2-beams are considered. Tables 3 and 4 display the mid-span deflection (*mm*) under a uniformly distributed load $q = 500N/m$ and fundamental frequencies of the C1-beam. The first four natural frequencies of the C2-beam with various material power index p are given in Table 5. In Table 3, the bending results show good agreements with those given by Nguyen et al. [19] for both cases of $L/b_3 = 20$ and 50. As predicted, the deflections increase with

the increase of the power index p. In Tables 4 and 5, the fundamental frequencies are compared with those from Nguyen et al. [13] and Nguyen et al. [19]. It can be seen that the results align well with those from previous studies, especially the ones using shear deformable theory.

Example 2. FG thin-walled sandwich I1- and I2-beams with $L/b_3 = 10$ and 20 are considered and their maximum displacements under a concentrated load at mid span are presented in Tables 6 and 7. Good agreement is observed between the present results and those accounting for shear effect given by Kim and Lee [21] and Nguyen et al. [20]. Furthermore, Table 8 compares the fundamental frequencies between the present model and those from Nguyen et al. [13]. Again, excellent agreement between these results is found for different values of ceramic thickness ratio α_j and power index p.

Parametric study

In this section, the results are computed for the FG thin-walled microbeams with various $b_3/l = 1, 2, 4$ along with those from macrobeam $b_3/l = 0$ to investigate the size effect.

Example 3. The mid-span deflections and fundamental frequencies of FG thin-walled C1-beams are shown in Tables 9 and 10. As seen in Table 8, in the cases where $b_3/l = 1, 2, 4$, the size-dependent effect is significant. The size effect makes the beam stiffer which results in a smaller mid-span deflection and larger frequencies. It can also be seen from Figs. 4 and 5 that under all boundary conditions, the beam's bending and vibration responses experience a drastic change from $b_3/l = 1$ to $b_3/l = 2$ but the slope quickly becomes less steep when $b_3/l > 2$. To better understand the influences of the flange-width-to –MLSP ratio (b_1/l) on the dynamic behaviours of these FG C1 microbeams, the first three natural frequencies are shown in Fig. 6. Since the microbeam's geometrical shape is preserved and is set with $b_3 = 2b_1$, the b_1/l ratio's effects on the frequencies at all modes are proportional to the b_3/l ratio, which can be deduced by comparing Figs. 5 and 6. Additionally, it is interesting to see the very sharp drop of the frequencies in the third mode compared to first one in all boundary conditions when $b_1/l < 5$. Besides, the second frequencies approach to those of macro beams when $b_1/l = 20$, which is much faster than the other two modes.

a) S-S

b) C-C

c) C-F
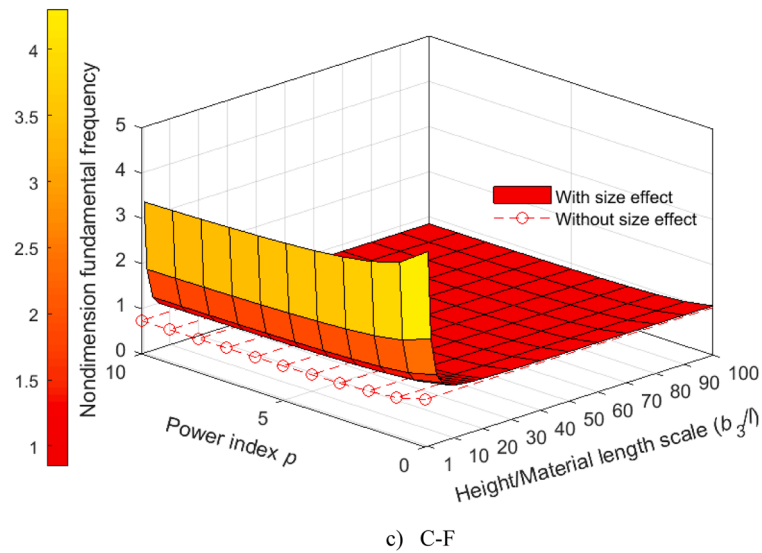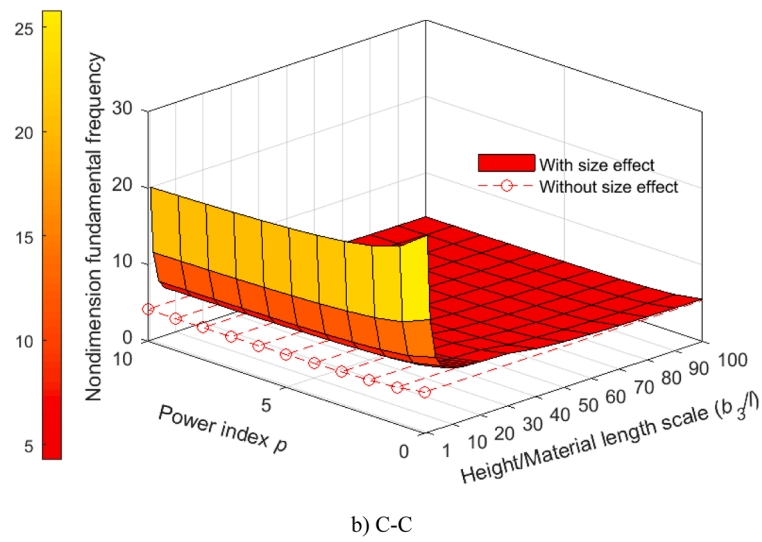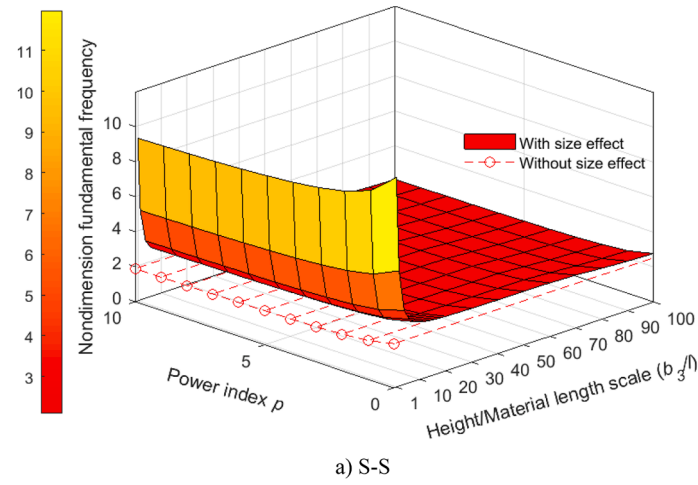
Fig. 7. Effects of b_3/l and p on the fundamental frequency of FG sandwich thin-walled C2-beams ($L/b_3 = 10$) under various boundary conditions.

12
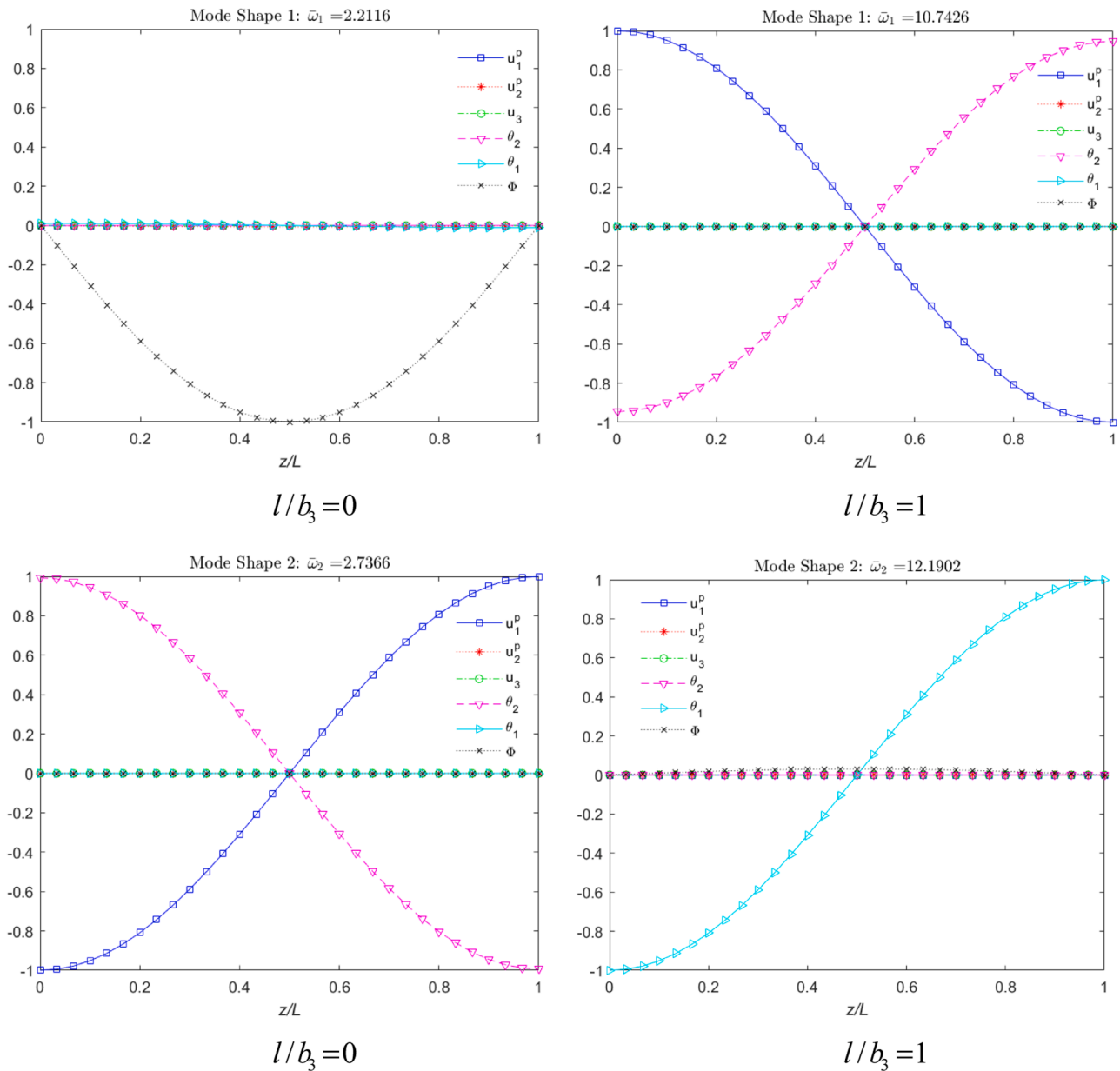
Fig. 8. The first two mode shapes of FG thin-walled C2-section macro- and micro- beams ($p = 1$, $L/b_3 = 10$, S-S boundary condition).

Table 11
Size effects on the fundamental frequencies of FG C2-section microbeams ($L/b_3 = 10$).

BC	b_3/l	p					
		$p = 0$	0.5	1	2	5	10
S-S	0	2.530	2.327	2.212	2.086	1.951	1.887
	1	11.982	11.205	10.743	10.217	9.610	9.302
	2	6.595	6.167	5.912	5.623	5.289	5.119
	4	4.231	3.956	3.793	3.607	3.393	3.284
C-C	0	5.393	5.020	4.802	4.557	4.280	4.141
	1	25.804	24.130	23.135	22.002	20.696	20.032
	2	14.637	13.687	13.123	12.481	11.740	11.363
	4	9.458	8.844	8.479	8.064	7.585	7.342
C-F	0	1.053	0.945	0.885	0.823	0.762	0.735
	1	4.305	4.025	3.859	3.670	3.453	3.342
	2	2.358	2.205	2.114	2.011	1.891	1.831
	4	1.511	1.413	1.355	1.288	1.212	1.173

a) S-S

b) C-C

c) C-F

Fig. 9. Effects of b_3/l and p on the mid-span displacement of the FG sandwich thin-walled I2-beams ($L/b_3 = 10$) under various boundary conditions.
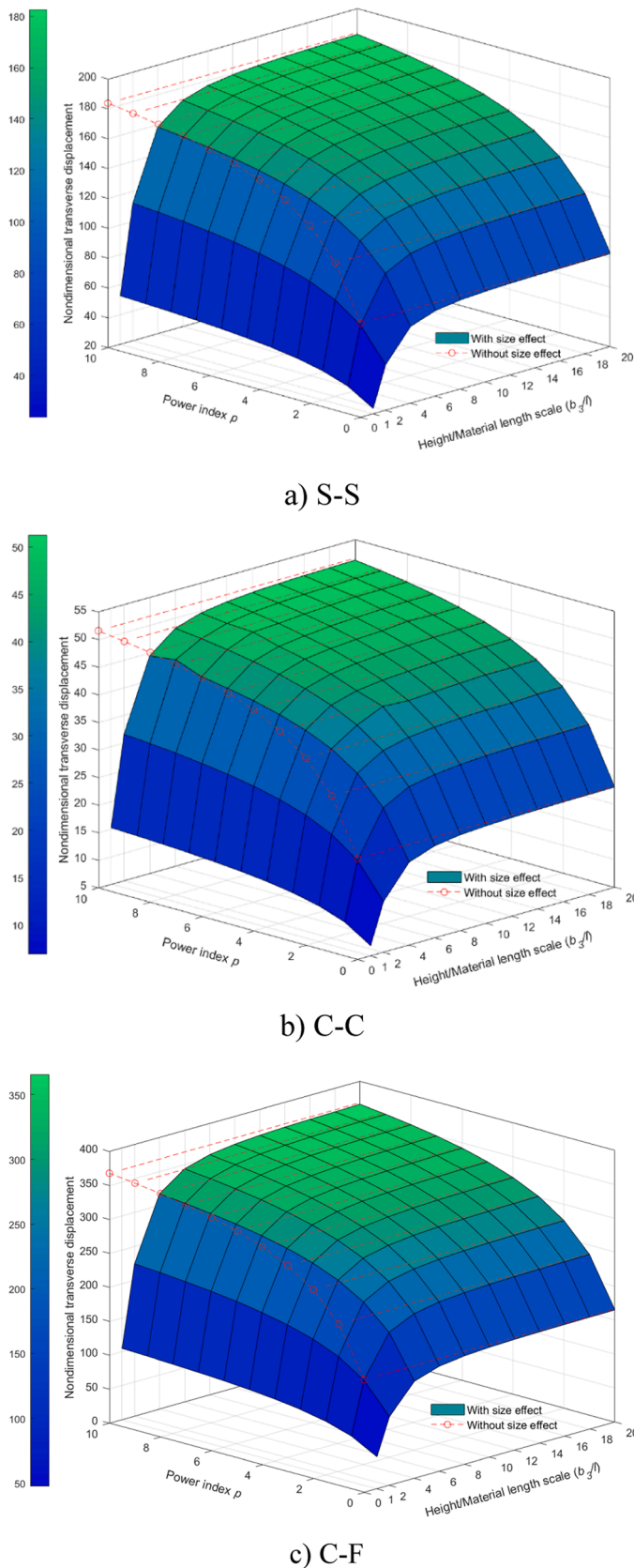
Example 4. This example investigates the vibration of FG thin-walled C2-beam. The present solution in Table 11 shows that when taking the size-dependent effect into account, the fundamental frequencies at $b_3/l = 1$ are more than 4 times greater than at $b_3/l = 0$. As b_3/l ratio increases, the vibration responses decrease and become closer to those of the macrobeam model. This pattern applies for all values of power index p and all three boundary conditions as can be seen in Table 10 and Fig. 7. It is also worth pointing out that in Fig. 7, at $b_3/l = 0$, there is only a slight decrease in fundamental frequency when the power index p changes from 0 to 1. Nonetheless, at $b_3/l = 1$, a big difference in the fundamental frequencies compared between the microbeam and macrobeam model can be observed. Fig. 8 shows the first two mode shapes when $b_3/l = 0$ and $b_3/l = 1$. It is noticeable that the first mode of the macrobeam is torsion mode. The second mode of marcobeam can be observed to be very similar to the first one of microbeams which are bending mode. The second mode of microbeam is also bending mode. The understanding of the beam vibrational mode can help detect defects and prevent structural failures.

Example 5. The size-dependent effect is investigated on the FG thin-walled I1- and I2-beams subjected to a concentrated load at mid-span and their mid-span displacements are provided in Tables 12 and 13. The lower values demonstrate a stiffer beam, the microbeams again show an increase in stiffness compared to its macro beam counterpart. The lower b_3/l ratio is, the stiffer the microbeam becomes. As shown in Table 12, the mid-span displacement when $b_3/l = 0$ is four to five times greater than when $b_3/l = 1$. Fig. 9 further demonstrates the variation of the mid span displacement with different values of power index p and b_3/l ratios.

Example 6. Vibration analysis of the FG sandwich I1- and I2-microbeams is carried out. Tables 14 and 15 display the first four natural frequencies of simply-supported beams when $b_3/l = 0$, 1, 2, 4. At $p = 0$, both sections are fully made of ceramic material and therefore, the results for both sections are identical. Nonetheless, across all values of p, the size-dependent effects on the microbeam are conspicuous as observed in previous examples. The beam becomes stiffer and thus, has higher dimensionless fundamental frequencies when the b_3/l ratio gets smaller. Besides, Fig. 10 shows the first two mode shapes of the micro- and macro-I1 S-S beams. Both the mode shapes of the macro I1-beam are torsion mode while those of micro I1-beam are bending mode. In Tables 14 and 15, the frequencies in all modes of both I1- and I2- microbeam at $b_3/l = 1$ are 5 to 12 times more than those of the macrobeam at $b_3/l = 0$.

Conclusions

By using the first-order shear deformation theory and modified couple stress theory, this paper studied for the first time the size-dependent behaviours of functionally graded sandwich thin-walled C and I-beams. The effects of boundary conditions, material distribution, beam length-to-height ratio and material length scale parameter were investigated. The following findings were drawn from the numerical results:

- The size-dependent effect made the FG thin-walled microbeams considerably stiffer, which in turn reduced the beam's bending transverse deflections and increased the beam's fundamental frequencies.
- The mid-span displacements of the C1 and I2 microbeams converged to the values of their macro-beam counterparts at $b_3/l = 20$ under all three boundary conditions.
- The fundamental frequency of the C1 and C2 microbeams converged to their macrobeam values quickly under C-F condition at $b_3/l = 20$

Table 12
Size effects on the mid-span deflections of FG thin-walled I1-section microbeams under concentrated load at mid-span.

BC	b_3/l	$L/b_3 = 10$				$L/b_3 = 20$			
		$p = 0$	1	2	5	$p = 0$	1	2	5
S-S	0	82.963	118.814	138.803	166.876	80.347	98.142	106.445	116.663
	1	23.664	33.889	39.590	47.599	22.620	27.298	29.354	31.773
	2	50.620	72.491	84.688	101.818	48.952	59.403	64.125	69.799
	4	71.483	102.372	119.597	143.787	69.231	84.371	91.351	99.879
C-F	0	166.157	202.853	219.929	240.911	160.796	196.412	213.026	233.472
	1	47.307	57.068	61.350	66.380	45.262	54.622	58.738	63.579
	2	101.263	122.821	132.542	144.202	97.956	118.867	128.318	139.673
	4	143.087	174.283	188.641	206.135	138.546	168.838	182.814	199.870
C—C	0	23.321	28.389	30.771	33.611	20.717	25.285	27.416	30.029
	1	6.889	8.299	8.915	9.633	5.908	7.126	7.671	8.290
	2	14.244	17.237	18.592	20.184	12.638	15.327	16.455	17.993
	4	20.045	24.371	26.899	28.627	17.848	21.739	24.020	25.721

Table 13
Size effects on the mid-span deflections of FG I2-section microbeams under concentrated load at mid-span.

| BC	b_3/l	$L/b_3 = 10$				$L/b_3 = 20$			
		$p = 0$	1	2	5	0	1	2	5
S-S	0	82.963	118.814	138.803	166.876	80.347	115.064	134.431	161.617
	1	23.664	33.889	39.590	47.599	22.620	32.393	37.843	45.497
	2	50.620	72.491	84.688	101.818	48.952	70.103	81.897	98.463
	4	71.483	102.372	119.597	143.787	69.232	99.152	115.827	139.259
C-F	0	166.157	237.953	277.989	334.219	160.796	230.276	269.020	323.436
	1	47.307	67.746	79.144	95.153	45.262	64.818	75.723	91.040
	2	101.263	145.017	169.416	203.684	97.956	140.281	163.883	197.033
	4	143.087	204.914	239.391	287.814	138.546	198.410	231.793	278.679
C—C	0	23.321	33.365	38.974	46.851	20.713	29.668	34.652	41.675
	1	6.889	9.866	11.525	13.857	5.907	8.462	9.884	11.882
	2	14.242	20.389	23.814	28.632	12.643	18.102	21.161	25.421
	4	20.066	28.614	33.572	40.320	17.851	25.553	29.860	35.902
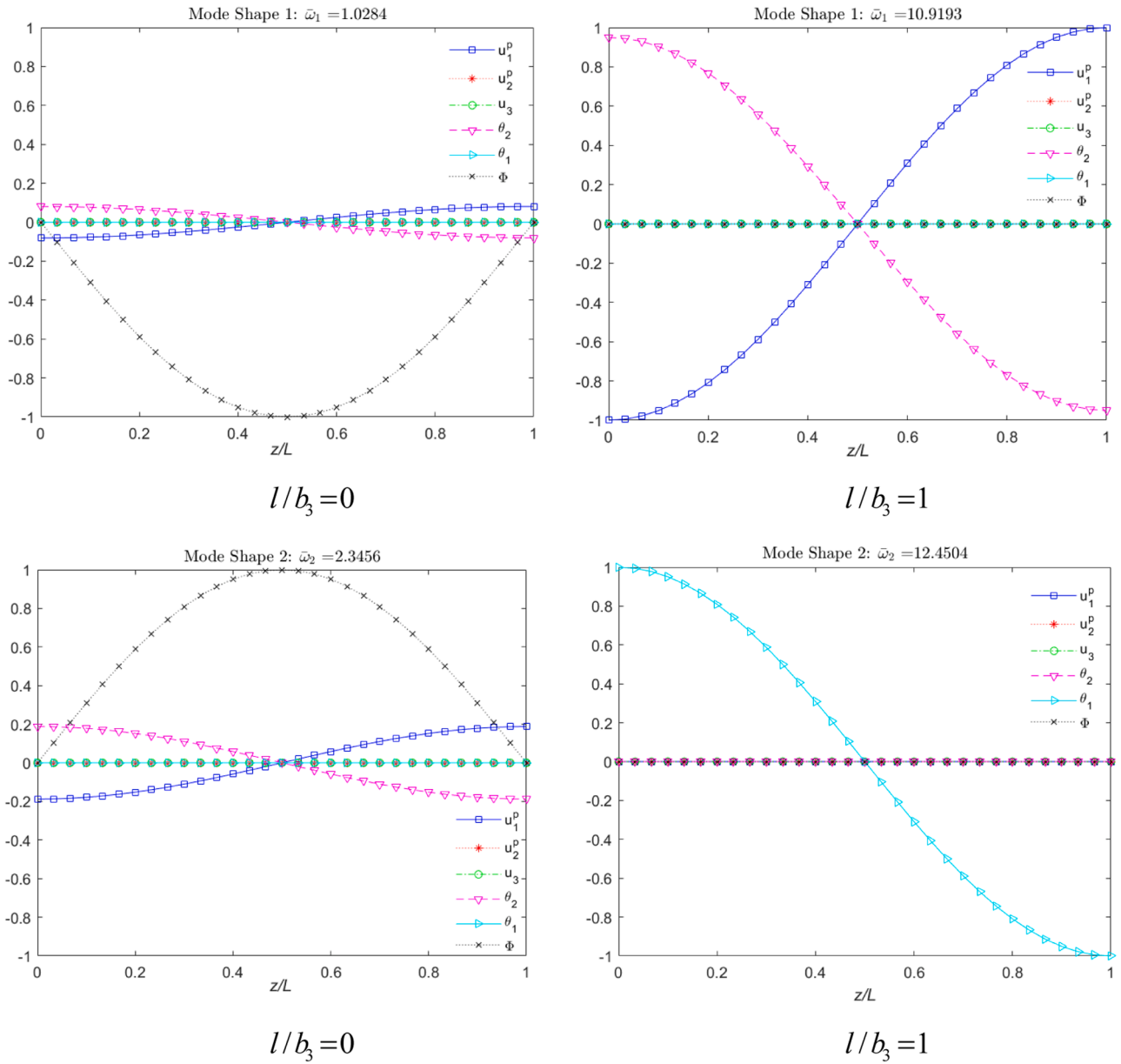
Fig. 10. The first two mode shapes of FG thin-walled I1-section macro- and micro- beams ($p = 1$, $L/b_3 = 10$, S-S boundary condition).

Table 14

Size effects on the lowest frequencies of FG thin-walled S-S I1-section micro-beams ($L/b_3 = 10$).

b_3/l	$\overline{\omega}$	p					
		0	0.5	1	2	5	10
0	$\overline{\omega}_1$	1.178	1.084	1.028	0.967	0.899	0.867
	$\overline{\omega}_2$	2.440	2.374	2.346	2.322	2.303	2.295
	$\overline{\omega}_3$	3.959	3.590	3.370	3.119	2.831	2.683
	$\overline{\omega}_4$	7.163	6.802	6.583	6.328	5.946	5.601
1	$\overline{\omega}_1$	11.728	11.211	10.919	10.602	10.255	10.086
	$\overline{\omega}_2$	13.429	12.808	12.450	12.052	11.605	11.382
	$\overline{\omega}_3$	45.203	43.201	42.074	40.847	39.503	38.848
	$\overline{\omega}_4$	49.542	47.269	45.966	44.522	42.906	42.103
2	$\overline{\omega}_1$	6.068	5.814	5.671	5.516	5.346	5.263
	$\overline{\omega}_2$	9.171	8.730	8.469	8.172	7.829	7.654
	$\overline{\omega}_3$	23.986	22.976	22.408	21.791	21.117	20.789
	$\overline{\omega}_4$	34.271	32.639	31.678	30.589	29.336	28.698
4	$\overline{\omega}_1$	3.326	3.210	3.145	3.075	2.999	2.962
	$\overline{\omega}_2$	7.716	7.334	7.104	6.838	6.524	6.362
	$\overline{\omega}_3$	13.232	12.768	12.508	12.227	11.922	11.774
	$\overline{\omega}_4$	28.860	27.445	26.596	25.618	24.471	23.878

Table 15

Size effects on the lowest frequencies of FG thin-walled S-S I2-section micro-beams ($L/b_3 = 10$).

b_3/l	$\overline{\omega}$	p					
		0	0.5	1	2	5	10
0	$\overline{\omega}_1$	1.178	1.032	0.947	0.856	0.766	0.726
	$\overline{\omega}_2$	2.440	2.168	2.011	1.838	1.648	1.555
	$\overline{\omega}_3$	3.959	3.533	3.283	3.004	2.694	2.541
	$\overline{\omega}_4$	7.163	6.544	6.155	5.688	5.113	4.801
1	$\overline{\omega}_1$	11.728	10.715	10.078	9.314	8.372	7.861
	$\overline{\omega}_2$	13.429	12.270	11.540	10.665	9.586	9.002
	$\overline{\omega}_3$	45.203	41.301	38.844	35.900	32.267	30.300
	$\overline{\omega}_4$	49.542	45.266	42.573	39.346	35.365	33.209
2	$\overline{\omega}_1$	6.068	5.544	5.214	4.819	4.331	4.067
	$\overline{\omega}_2$	9.171	8.379	7.881	7.283	6.546	6.147
	$\overline{\omega}_3$	23.986	21.915	20.611	19.048	17.121	16.077
	$\overline{\omega}_4$	34.271	31.313	29.450	27.217	24.464	22.972
4	$\overline{\omega}_1$	3.326	3.038	2.857	2.641	2.373	2.229
	$\overline{\omega}_2$	7.716	7.050	6.631	6.128	5.508	5.172
	$\overline{\omega}_3$	13.232	12.089	11.369	10.507	9.444	8.868
	$\overline{\omega}_4$	28.860	26.369	24.800	22.920	20.601	19.345

but converged much slower under S-S and C—C condition at $b_3/l = 100$.

- The first two mode shapes of the C2 macrobeam and microbeam were torsion and bending mode.

The present model was found to be simple and efficient in predicting the static and dynamic responses of functionally graded sandwich thin-walled microbeams.

Declaration of Competing Interest

The authors declare that they have no known competing financial interests or personal relationships that could have appeared to influence the work reported in this paper.

Data availability

No data was used for the research described in the article.

References

[1] R.M. Mahamood, E.T. Akinlabi, Types of functionally graded materials and their areas of application. Functionally Graded Materials, Springer International Publishing, Cham, 2017, pp. 9–21. R.M. Mahamood and E.T. Akinlabi.

[2] A. Miteva, A. Bouzekova-Penkova, Some aerospace applications of functionally graded materials, Aerosp. Res. Bull. 33 (2021).

[3] R. Osiander, M.A.G. Darrin, J.L. Champion, MEMS and Microstructures in Aerospace Applications, CRC Press, 2018.

[4] T.P. Vo, J. Lee, Flexural–torsional coupled vibration and buckling of thin-walled open section composite beams using shear-deformable beam theory, Int. J. Mech. Sci. 51 (9) (2009) 631–641.

[5] X.B. Bui, T.K. Nguyen, N.D. Nguyen, T.P. Vo, A general higher-order shear deformation theory for buckling and free vibration analysis of laminated thin-walled composite I-beams, Compos. Struct. 295 (2022), 115775.

[6] E.J. Barbero, R. Lopez-Anido, J.F. Davalos, On the mechanics of thin-walled laminated composite beams, J. Compos. Mater. 27 (8) (1993) 806–829.

[7] E. Carrera, M. Filippi, P.K. Mahato, A. Pagani, Advanced models for free vibration analysis of laminated beams with compact and thin-walled open/closed sections, J. Compos. Mater. 49 (17) (2015) 2085–2101.

[8] N.I. Kim, D.K. Shin, Dynamic stiffness matrix for flexural-torsional, lateral buckling and free vibration analyses of mono-symmetric thin-walled composite beams, Int. J. Struct. Stab. Dyn. 09 (03) (2009) 411–436.

[9] N.I. Kim, D.K. Shin, Y.S. Park, Dynamic stiffness matrix of thin-walled composite I-beam with symmetric and arbitrary laminations, J. Sound Vib. 318 (1) (2008) 364–388.

[10] M. Petrolo, M. Nagaraj, E. Daneshkhah, R. Augello, E. Carrera, Static analysis of thin-walled beams accounting for nonlinearities, Proc. Inst. Mech. Eng. Part C J. Mech. Eng. Sci. 236 (6) (2022) 2967–2980.

[11] V.Z. Vlasov, Thin-Walled Elastic Beams, National Technical Information Service, 1984.

[12] T.T. Nguyen, J. Lee, Interactive geometric interpretation and static analysis of thin-walled bi-directional functionally graded beams, Compos. Struct. 191 (2018) 1–11.

[13] T.T. Nguyen, N.I. Kim, J. Lee, Free vibration of thin-walled functionally graded open-section beams, Compos. Part B Eng. 95 (2016) 105–116.

[14] D. Lanc, G. Turkalj, T.P. Vo, J. Brnić, Nonlinear buckling behaviours of thin-walled functionally graded open section beams, Compos. Struct. 152 (2016) 829–839.

[15] T.T. Nguyen, N.I. Kim, J. Lee, Analysis of thin-walled open-section beams with functionally graded materials, Compos. Struct. 138 (2016) 75–83.

[16] N.I. Kim, J. Lee, Investigation of coupled instability for shear flexible FG sandwich I-beams subjected to variable axial force, Acta Mech. 229 (1) (2018) 47–70.

[17] N.I. Kim, J. Lee, Coupled vibration characteristics of shear flexible thin-walled functionally graded sandwich I-beams, Compos. Part B Eng. 110 (2017) 229–247.

[18] N.D. Nguyen, T.K. Nguyen, T.P. Vo, T.N. Nguyen, S. Lee, Vibration and buckling behaviours of thin-walled composite and functionally graded sandwich I-beams, Compos. Part B Eng. 166 (2019) 414–427.

[19] N.D. Nguyen, T.K. Nguyen, T.P. Vo, L.B. Nguyen, Bending, buckling and free vibration behaviors of thin-walled functionally graded sandwich and composite channel-section beams, Mech. Based Des. Struct. Mach. (2020) 1–29.

[20] N.D. Nguyen, T.P. Vo, T.K. Nguyen, An improved shear deformable theory for bending and buckling response of thin-walled FG sandwich I-beams resting on the elastic foundation, Compos. Struct. 254 (2020), 112823.

[21] N.I. Kim, J. Lee, Flexural-torsional analysis of functionally graded sandwich I-beams considering shear effects, Compos. Part B Eng. 108 (2017) 436–450.

[22] D. Lanc, T.P. Vo, G. Turkalj, J. Lee, Buckling analysis of thin-walled functionally graded sandwich box beams, Thin Walled Struct. 86 (2015) 148–156.

[23] T.T. Nguyen, N.L. Nguyen, J. Lee, Q.H. Nguyen, Analysis of non-uniform polygonal cross-sections for thin-walled functionally graded straight and curved beams, Eng. Struct. 226 (2021) 111366.

[24] J. Kim, K. Żur, J.N. Reddy, Bending, free vibration, and buckling of modified couples stress-based functionally graded porous micro-plates, Compos. Struct. 209 (2018).

[25] S. Kvaternik, M. Filippi, D. Lanc, G. Turkalj, E. Carrera, Comparison of classical and refined beam models applied on isotropic and FG thin-walled beams in nonlinear buckling response, Compos. Struct. 229 (2019), 111490.

[26] L.T.M. Phi, T.T. Nguyen, J. Lee, Free vibration of thin-walled open-section beams with functionally graded materials along the contour direction, Thin Walled Struct. 159 (2021), 107146.

[27] L. Librescu, S.Y. Oh, O. Song, Spinning thin-walled beams made of functionally graded materials: modeling, vibration and instability, Eur. J. Mech. A. Solids 23 (3) (2004) 499–515.

[28] S.A. Fazelzadeh, M. Hosseini, Aerothermoelastic behavior of supersonic rotating thin-walled beams made of functionally graded materials, J. Fluids Struct. 23 (8) (2007) 1251–1264.

[29] T. Farsadi, Variable thickness thin-walled rotating blades made of functionally graded porous materials, Proc. Inst. Mech. Eng. Part C J. Mech. Eng. Sci. 236 (14) (2022) 7674–7689.

[30] F. Yang, A.C.M. Chong, D.C.C. Lam, P. Tong, Couple stress based strain gradient theory for elasticity, Int. J. Solids Struct. 39 (10) (2002) 2731–2743.

[31] J. Fang, J. Gu, H. Wang, Size-dependent three-dimensional free vibration of rotating functionally graded microbeams based on a modified couple stress theory, Int. J. Mech. Sci. 136 (2018) 188–199.

[32] L.L. Ke, Y.S. Wang, Size effect on dynamic stability of functionally graded microbeams based on a modified couple stress theory, Compos. Struct. 93 (2) (2011) 342–350.

[33] M. Şimşek, J.N. Reddy, Bending and vibration of functionally graded microbeams using a new higher order beam theory and the modified couple stress theory, Int. J. Eng. Sci. 64 (2013) 37–53.

[34] H.T. Thai, T.P. Vo, T.K. Nguyen, J. Lee, Size-dependent behavior of functionally graded sandwich microbeams based on the modified couple stress theory, Compos. Struct. 123 (2015) 337–349.

[35] F. Fan, Y. Xu, S. Sahmani, B. Safaei, Modified couple stress-based geometrically nonlinear oscillations of porous functionally graded microplates using NURBS-based isogeometric approach, Comput. Methods Appl. Mech. Eng. 372 (2020), 113400.

[36] A. Farzam, B. Hassani, Isogeometric analysis of in-plane functionally graded porous microplates using modified couple stress theory, Aerosp. Sci. Technol. 91 (2019) 508–524.

[37] H. Liu, Q. Zhang, Nonlinear dynamics of two-directional functionally graded microbeam with geometrical imperfection using unified shear deformable beam theory, Appl. Math. Model. 98 (2021) 783–800.

[38] X. Chen, Y. Lu, Y. Li, Free vibration, buckling and dynamic stability of bi-directional FG microbeam with a variable length scale parameter embedded in elastic medium, Appl. Math. Model. 67 (2019) 430–448.

[39] F. Ebrahimi, F. Mahmoodi, A modified couple stress theory for buckling analysis of higher order inhomogeneous microbeams with porosities, Proc. Inst. Mech. Eng. Part C J. Mech. Eng. Sci. 233 (8) (2019) 2855–2866.

[40] A. Ghorbani Shenas, S. Ziaee, P. Malekzadeh, Nonlinear vibration analysis of pre-twisted functionally graded microbeams in thermal environment, Thin Walled Struct. 118 (2017) 87–104.

[41] A. Karamanli, T.P. Vo, A quasi-3D theory for functionally graded porous microbeams based on the modified strain gradient theory, Compos. Struct. 257 (2021), 113066.

[42] S. Mirzaei, M. Hejazi, R. Ansari, Isogeometric analysis of small-scale effects on the vibration of functionally graded porous curved microbeams based on the modified strain gradient elasticity theory, Acta Mech. (2023).

[43] B. Ramazani Darvazi, J. Rezapour, S. Rouhi, R. Gholami, Nonlinear vortex induced vibration analysis of electrostatic actuated microbeam based on modified strain gradient theory, J. Vib. Eng. Technol. (2023).

[44] J. Lei, Y. He, S. Guo, Z. Li, D. Liu, Size-dependent vibration of nickel cantilever microbeams: experiment and gradient elasticity, AIP Adv. 6 (10) (2016), 105202.

[45] S. Ilyas, M.I. Younis, Theoretical and experimental investigation of mode localization in electrostatically and mechanically coupled microbeam resonators, Int. J. Non Linear Mech. 125 (2020), 103516.

[46] Z. Li, Y. He, J. Lei, S. Han, S. Guo, D. Liu, Experimental investigation on size-dependent higher-mode vibration of cantilever microbeams, Microsyst. Technol. 25 (8) (2019) 3005–3015.

[47] L. Placidi, U. Andreaus, A.D. Corte, T. Lekszycki, Gedanken experiments for the determination of two-dimensional linear second gradient elasticity coefficients, Z. Angew. Math. Phys. 66 (6) (2015) 3699–3725.

[48] N.A. Fleck, G.M. Muller, M.F. Ashby, J.W. Hutchinson, Strain gradient plasticity: theory and experiment, Acta Metall. Mater. 42 (2) (1994) 475–487.

[49] J.S. Stölken, A.G. Evans, A microbend test method for measuring the plasticity length scale, Acta Mater. 46 (14) (1998) 5109–5115.

[50] Z. Li, Y. He, J. Lei, S. Guo, D. Liu, L. Wang, A standard experimental method for determining the material length scale based on modified couple stress theory, Int. J. Mech. Sci. 141 (2018) 198–205.

[51] M. Soltani, F. Atoufi, Non-local finite element formulation for stability analysis of thin-walled nanobeams with varying I-section, Acta Mech. 233 (2) (2022) 789–811.

[52] M. Soltani, F. Atoufi, F. Mohri, R. Dimitri, F. Tornabene, Nonlocal elasticity theory for lateral stability analysis of tapered thin-walled nanobeams with axially varying materials, Thin Walled Struct. 159 (2021), 107268.

[53] M. Soltani, A. Soltani, O. Civalek, Interaction of the lateral buckling strength with the axial load for FG micro-sized I-section beam–columns, Thin Walled Struct. 179 (2022), 109616.

[54] D.C.C. Lam, F. Yang, A.C.M. Chong, J. Wang, P. Tong, Experiments and theory in strain gradient elasticity, J. Mech. Phys. Solids 51 (8) (2003) 1477–1508.

[55] T.H.G. Megson, Aircraft Structures for Engineering Students, 7th ed., 649, Butterworth-Heinemann, United Kingdom, 2021.

ORIGINAL

Xuan-Bach Bui · Phong T. T. Nguyen · Trung-Kien Nguyen

Spectral projection and linear regression approaches for stochastic flexural and vibration analysis of laminated composite beams

Abstract This paper presents a novel approach for assessing the uncertainty in vibration and static responses of laminated composite beams resulting from uncertainty in material properties and distributed loads. The proposed method utilizes surrogate models developed using polynomial chaos expansion (PCE) based on a relatively small sample size. These training samples are computed using a high-order shear beam model in which the governing equations are derived using Hamilton's principle, and solved by Ritz's approach using a trigonometric series approximation. The proposed PCE model's coefficients are estimated using the spectral projection and linear regression techniques. The first four statistical moments and probability distributions of the mid-span displacement and the fundamental frequency of laminated composite beams are predicted. Global sensitivity analysis is also conducted to assess how material property variation and stochastic loads affect the beam's deflection and the fundamental frequency. The accuracy and efficiency of the proposed PCE models are compared with those from Monte Carlo simulation (MCS). A remarkable reduction in the computational cost of PCE models compared to MCS is observed without compromising the predictions' accuracy. As most real-world systems are subjected to multiple sources of uncertainty, this study provides a state-of-the-art method to quantify such uncertain parameters more efficiently and allow for a better reliability assessment in composite beam design.

Keywords Bending · Vibration · Stochastic behaviours · Laminated composite beams · Higher-order shear deformation theory

1 Introduction

Composite materials have steadily increased their applications across various engineering disciplines. This can be attributed to their mechanical benefits, including superior strength- and stiffness-to-weight ratios compared to conventional materials. The static and dynamic behaviors of macro [1–5] and nano [6, 7] composite structural elements have captured the attention of numerous researchers, leading to further investigations involving various loading conditions, namely mechanical [8, 9], electric, magnet [10–13] and thermal loads [14–18]. Moreover, different methods and solutions such as the finite element method [19–21], analytical series solution

X.-B. Bui
Faculty of Civil Engineering, Ho Chi Minh City University of Technology and Education, 1 Vo Van Ngan Street, Thu Duc City, Ho Chi Minh City, Viet Nam

P. T. T. Nguyen
Faculty of International Education, Ho Chi Minh City University of Technology and Education, 1 Vo Van Ngan Street, Thu Duc City, Ho Chi Minh City, Viet Nam

T.-K. Nguyen (✉)
CIRTech Institute, HUTECH University, 475A Dien Bien Phu Street, Binh Thanh District, Ho Chi Minh City, Viet Nam
e-mail: ntkien@hutech.edu.vn

[1, 2, 4, 18, 22–24] have been proposed to accurately predict laminated composite (LC) structures' responses. Nonetheless, due to the complex fabrication processes and random load fluctuations, these composite structures exhibit inherent variability in their theoretical performance predictions and actual experimental values. The uncertainty sources can be material, geometrical, and loading parameters. These uncertainties significantly influence vibration and static response characteristics such as frequencies and displacements. The deterministic approaches with no uncertainty accounted for are adjusted with a safety factor in design. Meanwhile, the probabilistic modeling approaches study the stochastic responses and assess the structures' performance based on the input uncertainties. A literature review shows that though there have been many researches concerning stochastic structural mechanics, the study on stochastic analysis of LC beams is extremely limited.

In order to investigate stochastic behaviors of structures with uncertainties, the most straightforward and intuitive method is the crude Monte Carlo Simulation method (MCS) which simply runs the structural model repetitively to achieve the desired level of accuracy. However, in cases where the physical model is complex, employing the MCS becomes impractical for its substantial computational time. Therefore, to overcome this drawback, many numerical methods for stochastic analysis, such as the stochastic finite element method [25, 26], perturbation method [27, 28], support vector machine [29], and polynomial chaos expansion (PCE) method [30] have been proposed to reduce the computational cost and maintain accuracy. The main idea of PCE approach is to approximate the stochastic outputs by representing them as a series in an orthogonal space, including the chosen basis polynomials and their corresponding coefficients. It allows for efficient and accurate calculation of statistics and probability distributions for computational models involving random input parameters.

Herein presents an overview of the previously published works on applying stochastic analysis methods for mechanical systems. Based on the MCS, Nguyen et al. [31] investigated the effects of uncertain material properties on the buckling responses of LC plates based on the isogeometric analysis. Elishakoff and Archaud [32] proposed a modified MCS method that significantly reduces simulation size to analyze the buckling of imperfect beams on softening foundations. Recently, Avíla and Squarcio [33] presented the Neuman-Monte Carlo methodology for the stochastic bending analysis of the Levinson–Bickford beam. Naskar et al. [34] proposed a stochastic approach to study the natural frequencies of thin-walled LC beams with spatially varying matrix cracking damage in a multi-scale framework in which a concept of stochastic representative volume element has been introduced and verified against the traditional MCS. As for the perturbation-based methods, Li et al. [35] analyzed the effect of random system properties on the critical thermal buckling temperature of LC plates with temperature-dependent properties using the perturbation technique. Onkar et al. [36] proposed a stochastic buckling analysis of LC plates with random material properties under uniaxial compressive loading. It is based on the layerwise plate model to solve both pre-buckling and buckling problems, while the stochastic analysis has been done based on the mean-centered first-order perturbation technique. Meanwhile, the PCE has been used extensively for various mechanical problems. Peng et al. [30] presented an uncertainty analysis method for LC plates using a data-driven PCE method under insufficient input data related to uncertain design parameters. Based on this approach, Verma and Singh [37] studied the thermal buckling responses of LC plates with random geometric and material properties. Chandra et al. [38] presented a stochastic dynamic response analysis of LC plates using generalized polynomial chaos expansion due to random mean temperature increment. Then a stochastic finite element method was developed based on the first-order shear deformation theory (FSDT). Chakraborty et al. [39] presented an improved PCE approach based on a polynomial correlated function expansion for stochastic vibration analysis of LC plates. Bhattacharyya [40] used the Bayesian learning-based PCE to analyze the global reliability sensitivity of a general system. Despite the broad applications of PCE in many areas, its implementation in analyzing the stochastic responses of LC beams under stochastic loads is extremely limited and therefore needs to be explored further. Particularly, how material properties variation and load variability influence LC beams' fundamental frequency and mid-span displacement have yet to be sufficiently assessed. For those reasons, it calls for a deeper exploration of future research.

This paper aims to develop surrogate models using polynomial chaos expansion for uncertainty quantification and sensitivity analysis of LC beams with random material properties and stochastic loads. These input uncertainties are given by defined lognormal distributions. The proposed PCE models consist of multivariate Hermite polynomials and unknown associated coefficients. A set of realizations of random input parameters is generated from which the deterministic beam model gives the corresponding realizations of output responses. These realizations are then used to estimate the PCE coefficients by either the spectral projection using the Gaussian quadrature rule or the ordinary least-square regression approach. The deterministic beam model is derived based on a higher-order shear deformation theory (HSDT) that satisfies the traction-free boundary
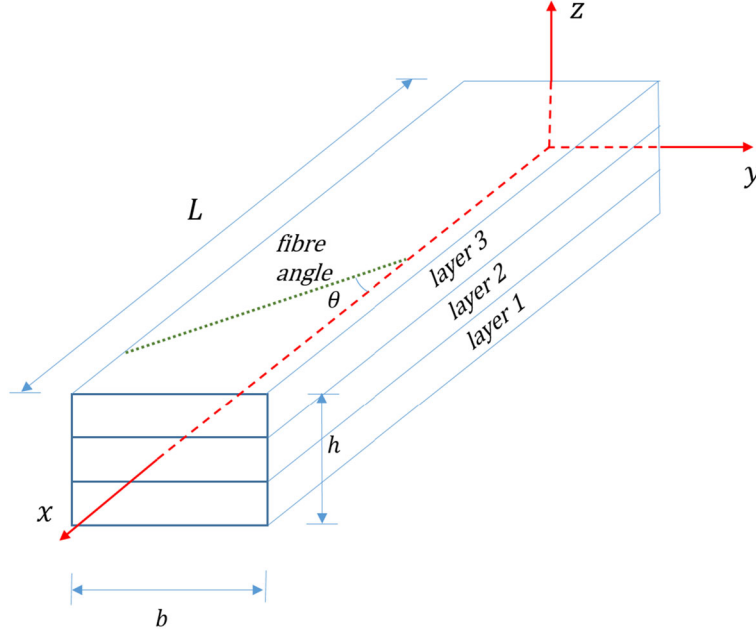
Fig. 1 Geometry of a laminated composite beam

condition on the top and bottom surfaces of the LC beams. Numerical results are presented to investigate the effects of the stochasticity, fiber angle, span-to-thickness ratio, and boundary conditions on the probabilistic deflection and natural frequencies of the LC beams. Additionally, Sobol's sensitivity indices are computed to rank the most significant random variables affecting both static and vibration responses of the LC beams. All numerical and statistical results are validated with those obtained from one million samples of the Monte Carlo simulation.

2 Theoretical formulation

Consider a LC beam with length L and rectangular cross-section $b \times h$ as shown in Fig. 1. It is made of n plies of orthotropic materials in different fibre angles with respect to the x-axis.

2.1 Kinematic, strain and stress

The displacement field of LC beams based on the higher-order shear deformation theory is given by ([22]):

$$u(x,z) = \overline{u}(x) - z\overline{w}_{,x} + \left(\frac{5z}{4} - \frac{5z^3}{3h^2}\right)\overline{\varphi}(x) = \overline{u}(x) - z\overline{w}_{,x} + \psi(z)\overline{\varphi}(x) \tag{1}$$

$$w(x,z) = \overline{w}(z) \tag{2}$$

where $\overline{u}(x)$, $\overline{w}(x)$ are axial and transverse displacements at mid-plane of the LC beams, respectively; $\overline{\varphi}(x)$ is the rotation of a transverse normal about the y-axis; $\psi(z)$ is the shear function that reveals a higher-order variation of axial displacement; the comma indicates partial differentiation with respect to the coordinate subscript that follows.

The non-zero strains of LC beams derived from Eqs. (1, 2) are given by:

$$\varepsilon_x = \overline{\varepsilon}_x^{(0)} + z\overline{\varepsilon}_x^{(1)} + \psi\overline{\varepsilon}_x^{(2)} \tag{3}$$

$$\gamma_{xz} = \psi_{,z}\overline{\varphi} \tag{4}$$

where

$$\overline{\varepsilon}_x^{(0)} = \overline{u}_{,x}, \overline{\varepsilon}_x^{(1)} = -\overline{w}_{,xx}, \overline{\varepsilon}_x^{(2)} = \overline{\varphi}_{,x} \tag{5}$$

The elastic strain and stress relation of kth-layer in global coordinates is given by:

$$\left\{ \begin{matrix} \sigma_x \\ \sigma_{xz} \end{matrix} \right\}^{(k)} = \left(\begin{matrix} \overline{Q}_{11} & 0 \\ 0 & \overline{Q}_{55} \end{matrix} \right)^{(k)} \left\{ \begin{matrix} \varepsilon_x \\ \gamma_{xz} \end{matrix} \right\}^{(k)} \tag{6}$$

where the $\overline{Q}_{ij}^{(k)}$ are the plane stress-reduced stiffness coefficients in global coordinates (see [22] for details).

2.2 Energy formulation

Hamilton's principle is used to derive characteristic equations of the LC beams in which the total potential energy Λ of the LC beams is composed of the strain energy U, work done by external forces V and kinetic energy K.

$$\int_{t_1}^{t_2} \delta \Lambda dt = \int_{t_1}^{t_2} (\delta U + \delta V - \delta K) dt = 0 \tag{7}$$

The variation of strain energy of the LC beams is given by:

$$\delta U = \int_V (\sigma_x \delta \varepsilon_x + \sigma_{xz} \delta \gamma_{xz}) dV = \int_0^L \left(N_x \delta \overline{\varepsilon}_x^{(0)} + M_x^{(1)} \delta \overline{\varepsilon}_x^{(1)} + M_x^{(2)} \delta \overline{\varepsilon}_x^{(2)} + Q_x \delta \overline{\varphi} \right) dx$$

$$= \int_0^L \left(N_x \delta \overline{u}_{,x} - M_x^{(1)} \delta \overline{w}_{,xx} + M_x^{(2)} \delta \overline{\varphi}_{,x} + Q_x \delta \overline{\varphi} \right) dx \tag{8}$$

where the stress resultants $\left(N_x, M_x^{(1)}, M_x^{(2)}, Q_x \right)$ are defined by:

$$N_x = \int_{-h/2}^{h/2} \sigma_x b dz = A \overline{u}_{,x} - B \overline{w}_{,xx} + B^s \overline{\varphi}_{,x} \tag{9}$$

$$M_x^{(1)} = \int_{-h/2}^{h/2} z \sigma_x b dz = B \overline{u}_{,x} - D \overline{w}_{,xx} + D^s \overline{\varphi}_{,x} \tag{10}$$

$$M_x^{(2)} = \int_{-h/2}^{h/2} \psi \sigma_x b dz = B^s \overline{u}_{,x} - D^s \overline{w}_{,xx} + H^s \overline{\varphi}_{,x} \tag{11}$$

$$Q_x = \int_{-h/2}^{h/2} \psi_{,z} \sigma_{xz} b dz = A^s \overline{\varphi} \tag{12}$$

where the stiffness coefficients of the LC beams are determined as follows:

$$\left(A, B, D, B^s, D^s, H^s \right) = \int_{-h/2}^{h/2} \overline{Q}_{11} \left(1, z, z^2, \psi, z\psi, \psi^2 \right) b dz \tag{13}$$

$$A^s = \int_{-h/2}^{h/2} \overline{Q}_{55} \psi_{,z}^2 b dz \tag{14}$$

The variation of work done by a transvers distributed force $\overline{f}$ of LC beams is written in the following form:

$$\delta V = -\int_0^L \overline{f}\delta\overline{w}dx \tag{15}$$

The variation of kinetic energy of the LC beams is expressed by:

$$\delta K = \int_V \rho(\dot{u}\delta\dot{u} + \dot{w}\delta\dot{w})dV$$

$$= \int_0^L \left[I_0\dot{\overline{u}}\delta\dot{\overline{u}} - I_1\left(\dot{\overline{u}}\delta\dot{\overline{w}}_{,x} + \dot{\overline{w}}_{,x}\delta\dot{\overline{u}}\right) + I_2\dot{\overline{w}}_{,x}\delta\dot{\overline{w}}_{,x} + J_1\left(\dot{\overline{u}}\delta\dot{\overline{\varphi}} + \dot{\overline{\varphi}}\delta\dot{\overline{u}}\right) \right.$$

$$\left. - J_2\left(\dot{\overline{w}}_{,x}\delta\dot{\overline{\varphi}} + \dot{\overline{\varphi}}\delta\dot{\overline{w}}_{,x}\right) + K_2\dot{\overline{\varphi}}\delta\dot{\overline{\varphi}} + I_0\dot{\overline{w}}\delta\dot{\overline{w}} \right]dx \tag{16}$$

where dot-superscript denotes the differentiation with respect to the time t; ρ is the mass density of each layer, and $I_0, I_1, I_2, J_1, J_2, K_2$ are the inertia coefficients defined by:

$$(I_0, I_1, I_2, J_1, J_2, K_2) = \int_{-h/2}^{h/2} \rho\left(1, z, z^2, \psi, z\psi, \psi^2\right)bdz \tag{17}$$

Substituting Eqs. (8), (15) and (16) into Eq. (7) leads to:

$$\int_{t_1}^{t_2}\int_0^L \left[\left(A\overline{u}_{,x} - B\overline{w}_{,xx} + B^s\overline{\varphi}_{,x}\right)\delta\overline{u}_{,x} - \left(B\overline{u}_{,x} - D\overline{w}_{,xx} + D^s\overline{\varphi}_{,x}\right)\delta\overline{w}_{,xx} \right.$$

$$\left. + \left(B^s\overline{u}_{,x} - D^s\overline{w}_{,xx} + H^s\overline{\varphi}_{,x}\right)\delta\overline{\varphi}_{,x} + A^s\overline{\varphi}\delta\overline{\varphi} \right]dx - \int_0^L q\delta\overline{w}dx$$

$$- \int_0^L \left[I_0\dot{\overline{u}}\delta\dot{\overline{u}} - I_1\left(\dot{\overline{u}}\delta\dot{\overline{w}}_{,x} + \dot{\overline{w}}_{,x}\delta\dot{\overline{u}}\right) + I_2\dot{\overline{w}}_{,x}\delta\dot{\overline{w}}_{,x} + J_1\left(\dot{\overline{u}}\delta\dot{\overline{\varphi}} + \dot{\overline{\varphi}}\delta\dot{\overline{u}}\right) \right.$$

$$\left. - J_2\left(\dot{\overline{w}}_{,x}\delta\dot{\overline{\varphi}} + \dot{\overline{\varphi}}\delta\dot{\overline{w}}_{,x}\right) + K_2\dot{\overline{\varphi}}\delta\dot{\overline{\varphi}} + I_0\dot{\overline{w}}\delta\dot{\overline{w}} \right]dxdt = 0 \tag{18}$$

2.3 Ritz method

Based on the Ritz method ([41]), the displacement field in Eq. (18) is approximated in the following forms:

$$\overline{u}(x,t) = \sum_{j=1}^m N_j^u(x)u_j e^{i\omega t} \tag{19}$$

$$\overline{w}(x,t) = \sum_{j=1}^m N_j^w(x)w_j e^{i\omega t} \tag{20}$$

$$\overline{\varphi}(x,t) = \sum_{j=1}^m N_j^\varphi(x)\varphi_j e^{i\omega t} \tag{21}$$

where ω is the natural frequency, $i^2 = -1$ the imaginary unit; u_j, w_j, φ_j are unknown values to be determined; $N_j^u(x), N_j^w(x)$ and $N_j^\varphi(x)$ are shape functions. It is known that the accuracy and convergence of the Ritz method depend on the choice of these approximate functions ([1, 22]). Trigonometric shape functions which satisfy different boundary conditions (BCs): simply-supported (S–S), clamped-free (C–F) and clamped–clamped (C–C), are given as follows ([22]):

- S–S: $N_u = \cos \frac{j\pi x}{L}$, $N_w = \sin \frac{j\pi x}{L}$, $N_\varphi = \cos \frac{j\pi x}{L}$
- C–F: $N_u = \sin \frac{(2j-1)\pi}{2L}x$, $N_w = 1 - \cos \frac{(2j-1)\pi}{2L}x$, $N_\varphi = \sin \frac{(2j-1)\pi}{2L}x$
- C–C: $N_u = \sin \frac{2j\pi x}{L}$, $N_w = \sin^2 \frac{j\pi x}{L}$, $N_\varphi = \sin \frac{2j\pi x}{L}$

Substituting Eqs. (19, 20, 21) into Eq. (18) leads to:

$$\left(\begin{bmatrix} \mathbf{K}^{11} & \mathbf{K}^{12} & \mathbf{K}^{13} \\ {}^T\mathbf{K}^{12} & \mathbf{K}^{22} & \mathbf{K}^{23} \\ {}^T\mathbf{K}^{13} & {}^T\mathbf{K}^{23} & \mathbf{K}^{33} \end{bmatrix} - \omega^2 \begin{bmatrix} \mathbf{M}^{11} & \mathbf{M}^{12} & \mathbf{M}^{13} \\ {}^T\mathbf{K}^{12} & \mathbf{M}^{22} & \mathbf{M}^{23} \\ {}^T\mathbf{K}^{13} & {}^T\mathbf{M}^{23} & \mathbf{M}^{33} \end{bmatrix} \right) \left\{ \begin{array}{c} \mathbf{\bar{u}} \\ \mathbf{\bar{w}} \\ \mathbf{\bar{\jmath}} \end{array} \right\} = \left\{ \begin{array}{c} \mathbf{0} \\ \mathbf{f} \\ \mathbf{0} \end{array} \right\} \tag{22}$$

where the components of stiffness matrix $\mathbf{K}$, mass matrix $\mathbf{M}$ and force vector $\mathbf{f}$ are given by:

$$K_{ij}^{11} = A \int_0^L N_{i,x}^u N_{j,x}^u dx, \quad K_{ij}^{12} = -B \int_0^L N_{i,x}^u N_{j,xx}^w dx, \quad K_{ij}^{13} = B^s \int_0^L N_{i,x}^u N_{j,x}^\varphi dx$$

$$K_{ij}^{22} = D \int_0^L N_{i,xx}^w N_{j,xx}^w dx, \quad K_{ij}^{23} = -D^s \int_0^L N_{i,xx}^w N_{j,x}^\varphi dx$$

$$K_{ij}^{33} = -H^s \int_0^L N_{i,x}^\varphi N_{j,x}^\varphi dx + A^s \int_0^L N_i^\varphi N_j^\varphi dx, \quad f_i = \int_0^L \overline{f} N_j^\varphi dx$$

$$M_{ij}^{11} = I_0 \int_0^L N_i^u N_j^u dx, \quad M_{ij}^{12} = -I_1 \int_0^L N_i^u N_{j,x}^w dx, \quad M_{ij}^{13} = -J_1 \int_0^L N_i^u N_j^\varphi dx$$

$$M_{ij}^{22} = I_0 \int_0^L N_i^w N_j^w dx + I_2 \int_0^L N_{i,x}^w N_{j,x}^w dx, \quad M_{ij}^{23} = -J_2 \int_0^L N_{i,x}^w N_j^\varphi dx, \quad M_{ij}^{33} = K_2 \int_0^L N_i^\varphi N_j^\varphi dx \tag{23}$$

2.4 Polynomial chaos expansion

For computational models involving random input parameters, the uncertainty in model responses can be characterized by representing them as a series of orthogonal functions as follows ([42]):

$$\bar{r}(\mathbf{q}) = \sum_{i=0}^{\infty} \beta_i \Omega_i(\mathbf{q}) \tag{24}$$

where $\mathbf{q}$ is a vector of d independent random variables mapped to physical random parameters; Ω_i are multivariate orthogonal basis functions; β_i are coefficients to be determined. In order to determine these components, two main following approaches can be considered: polynomial chaos expansion (PCE) and stochastic collocation, in which the PCE estimates the coefficients in a suitable set of basis functions using either spectral projection or linear regression, whereas the stochastic collocation approach forms the interpolation polynomials for the known coefficients under collocation points ([43]). For the present manuscript, the PCE method with both projection and linear regression methods will be developed. The multivariate Hermite polynomials are used as the basis functions, and $\mathbf{q}$ is used as a vector of standard normal variables.

In practice, Eq. (24) is typically truncated using a finite number of terms. If the number of random variables is d, the qualified order of polynomial is p, and for the total-degree truncation scheme, the number of full polynomial terms N is the permutation of p and $d + p$, determined as follows: $N = \frac{(d+p)!}{d!p!}$ ([42]), Eq. (24) therefore becomes:

$$\bar{r}(\mathbf{q}) = \sum_{i=0}^{N-1} \beta_i \Omega_i(\mathbf{q}) + \varepsilon \tag{25}$$

in which the basis functions Ω_i are considered under multivariate Hermite polynomials, and their associated coefficients β_i should be determined so that the residual ε is minimized. Among different methods, spectral projection and linear regression approaches are applied in this paper.

2.4.1 Spectral projection approach

For spectral projection, the residual minimum requires that it must be orthogonal with the projection of response in the selected space or the inner product of the residual and each basis function is zero. From Eq. (25), taking the inner product of both sides with respect to Ω_j and enforcing orthogonality yields:

$$\langle \bar{r}, \Omega_j \rangle = \sum_{i=0}^{N-1} \beta_i \langle \Omega_i, \Omega_j \rangle \tag{26}$$

Because Ω_j are mutually orthogonal, Eq. (26) becomes:

$$\beta_i = \frac{\langle \bar{r}, \Omega_i \rangle}{\langle \Omega_i, \Omega_i \rangle} = \frac{1}{\langle \Omega_i, \Omega_i \rangle} \int \bar{r} \Omega_i \rho_Q(\mathbf{q}) d\mathbf{q} \tag{27}$$

It is noted that all coefficients can be theoretically obtained by solving Eq. (27); however, the random response $\bar{r}$ is unknown. Moreover, Eq. (27) involves a multidimensional integral evaluated numerically using either probabilistic techniques (sampling) or deterministic techniques (quadrature rules, sparse grid approaches). In the present paper, the probabilistic Gauss-Hermite quadrature will be used to compute β_i. Note that the normalization factor $\langle \Omega_i, \Omega_i \rangle$ in Eq. (27) can be analytically estimated. It is worth to noticing that if the order of the output $\bar{r}$ is p, the highest order of the integrands in Eq. (27) is at least $2p$, so the minimum number of Gauss point for each dimension is $N_{gp} = p + 1$ and the total number of quadrature points is $(p+1)^d$. Hence, if the model response $\bar{r}\left(q_{j_1}^1 ... q_{j_d}^d\right)$ is obtained from the Ritz solution, $(p+1)^d$ deterministic problems need to be solved. In consequence, this method is quite expensive for multidimensional and higher-order problems.

2.4.2 Linear regression approach

Let $\Re = \left\{\mathbf{q}^1, ..., \mathbf{q}^{N_s}\right\}$ be a set of $N_s(N_s > N)$ realizations of input random vector, and $\mathbf{R} = \left\{\bar{r}^1, ..., \bar{r}^{N_s}\right\}$ be corresponding output evaluations $\left(\bar{r}^i = \bar{r}(\mathbf{q}^i), i = 1, ..., N_s\right)$. The vector of residuals can be estimated from Eq. (25) in the compact form:

$$\Upsilon = \mathbf{R} - \beta^T \mathbf{\Omega} \tag{28}$$

where $\mathbf{\Omega}$ is the matrix whose elements are given by $\Omega_{ij} = \Omega_j(\mathbf{q}^i)$, $i = 1, ..., N_s$; $j = 1, ..., N$. The coefficients β are estimated by minimizing the L_2- norm (least-square regression) of the residual followed as:

$$\beta = Arg \min \left\| \mathbf{R} - \beta^T \mathbf{\Omega} \right\|_2^2 \tag{29}$$

Solving Eq. (29), the coefficients are given by:

$$\beta = \left(\mathbf{\Omega}^T \mathbf{\Omega}\right)^{-1} \mathbf{\Omega}^T \mathbf{R} \tag{30}$$

2.5 Sensitivity analysis

Apart from the LC beams' responses concerning the input uncertainty, the degree to which each random variable contributes to the model output uncertainty is of great interest. The sensitivity analysis is a branch of study that quantifies how much the uncertainty of each random input variable, either as an individual or with other variable interaction, contributes to the model output uncertainty. The sensitivity analysis can be carried out effectively by the variance-based method, which has been developed by Sobol [44] and has been further studied by Satelli et al. [45, 46] and Sudret [47]. Sobol's first-order and total-order indices are given by Satelli et al. [45] as follows:

$$\text{First-order Sobol index}: \quad S_i = \frac{Var_{\mathbf{q}^i}(E_{q_{\sim i}}(\bar{r}|\mathbf{q}^i))}{Var(\bar{r})} \mathbf{q}^{k \neq i} \tag{31}$$

Table 1 Random input material properties and statistical distribution

Material properties and load	Mean		COV	Distribution
	MAT I [18]	MAT II [22]		
E_1(GPa)	138	100	0.1	Lognormal
$E_2 = E_3$(GPa)	6.9	4	0.1	Lognormal
$G_{12} = G_{13}$(GPa)	4.14	2	0.1	Lognormal
G_{23}(GPa)	3.45	0.8	0.1	Lognormal
$\nu_{12} = \nu_{13}$	0.25	0.25	0.1	Lognormal
ρ(kg/m^3)	1550.1	–	0.1	Lognormal
q(N/m)	–	10^6	0.1	Lognormal

$$\text{Total-order Sobol index}: \quad S_{Ti} = 1 - \frac{Var_{\mathbf{q}^{\sim i}}(E_{\mathbf{q}^i}(\overline{r}|\mathbf{q}^{\sim i}))}{Var(\overline{r})} \tag{32}$$

Both kinds of these Sobol indices are normalised by $Var(\overline{r})$ but the difference in meaning is first-order Sobol indices measure only the impact of a sole particular input variable $\mathbf{q}^i$, while total-order Sobol indices also take into account the impact of interactions between $\mathbf{q}^i$ and other variables $\mathbf{q}^{k \neq i}$. These indices can be computed using crude Monte Carlo simulation with the computational cost of $(d+2)N_s$ or using PCE with no additional cost. The Sobol's first-order and total-order indices can be estimated as follows:

$$S_i = \frac{D_i}{Var(\overline{r})} \tag{33}$$

$$S_{Ti} = \frac{D_{Ti}}{Var(\overline{r})} \tag{34}$$

where $D_i = \sum_{j \in \Gamma_i} \beta_j^2 \langle \Omega_j(\mathbf{q}^i), \Omega_j(\mathbf{q}^i) \rangle j$, Γ_i comprises all indices j such that the multivariate function Ω_j only contains the variable $\mathbf{q}^i$; $D_{Ti} = \sum_{j \in \Gamma_{Ti}} \beta_j^2 \langle \Omega_j(\boldsymbol{q}), \Omega_j(\boldsymbol{q}) \rangle$, Γ_{Ti} comprises all indices j such that the multivariate function Ω_j must contain variable $\mathbf{q}^i$; index j depends on how the list of multivariate functions is sorted.

3 Numerical results

Several numerical examples are performed in this section to investigate the accuracy and efficiency of the present theory. The effects of material properties uncertainty on the bending and free vibration behaviors of LC beams are observed with different lay-ups and boundary conditions. Two types of material MAT I [18] and MAT II [31] shown in Table 1 are considered for the vibration and bending analysis, respectively. The non-dimensional fundamental frequency and mid-span displacement are given as: $\hat{\omega} = \frac{\omega L^2}{b_3}\sqrt{\frac{\rho}{E_2}}$ and $\hat{w} = \frac{100E_2bh^3}{qL^4}w$.

3.1 Convergence study

In order to investigate the convergence of the present solution with an increasing number of series, both non-dimensional first fundamental frequencies (MAT I) and mid-span displacements (MAT II) of $[0^o/90^o/0^o]$ LC beams are computed with increasing Ritz series numbers and different boundary conditions. It can be seen from Table 2 that the convergence of the present Ritz-based trigonometric series solution is fairly achieved at $m = 8$. Therefore, $m = 8$ would be used in subsequent calculations.

Additionally, to verify the convergence of the present solution with respect to the polynomial order p, Table 3 introduces fundamental frequencies of $[0^o/90^o/0^o]$ LC beams with MAT I and for the linear regression (LR), spectral projection (SP), and MCS methods. The first four statistical moments, including the mean μ, standard deviation σ, kurtosis, and skewness are calculated for C–C boundary conditions. The span-to-depth ratio $L/h = 10$ is considered and the order of polynomial p is increased from 2 to 5. In the LR method,

Table 2 Convergence of the non-dimensional fundamental frequency (MAT I) and non-dimensional mid-span displacement (MAT II) of $[0^o/90^o/0^o]$ laminated composite beams

BC	m					
	2	4	6	8	10	12
Non-dimensional fundamental frequency						
S–S	10.76	10.76	10.76	10.76	10.76	10.76
C–C	18.07	17.70	17.59	17.54	17.52	17.51
C–F	4.18	4.15	4.14	4.14	4.14	4.14
Non-dimensional mid-span displacement						
S–S	1.11	1.10	1.10	1.10	1.10	1.10
C–C	0.48	0.52	0.53	0.53	0.53	0.53
C–F	3.13	3.36	3.41	3.43	3.44	3.45

Table 3 Convergence of fundamental frequency (Hz) of $[0^o/90^o/0^o]$ laminated composite beams with respect to the polynomial order p of the PCE ($L/h = 10$, C–C)

Polynomial order p	Properties	LR	SP	MCS
2	μ	1549.373	1549.321	1549.233
	σ	89.566	89.628	
	Kurtosis	3.037	3.045	
	Skewness	0.165	0.176	
3	μ	1549.286	1549.233	89.719
	σ	89.656	89.687	
	Kurtosis	3.051	3.059	
	Skewness	0.172	0.178	
4	μ	1549.364	1549.425	3.061
	σ	89.565	89.568	
	Kurtosis	3.058	3.055	
	Skewness	0.176	0.177	
5	μ	1549.285	1549.432	0.172
	σ	89.595	89.635	
	Kurtosis	3.056	3.049	
	Skewness	0.175	0.173	

a higher-order polynomial gives a higher number of terms N, and the number of simulation runs in the LR method N_s is set to be 3 N. Besides, for the SP method, the number of Gauss quadrature points N_{gp} is equal to the order of polynomial plus one for each variable (i.e.,$N_{gp} = p + 1$) and the N_s is equal to N_{gp}^d. For both LR and SP, the higher-order polynomial clearly gives a higher degree of accuracy but also requires more computing time. Based on the results in Table 3, this study considers the polynomial order of 3 to be sufficient and will be used in the subsequent sections. The convergence study of the static analysis gives a similar trend and also achieves sufficient accuracy when the polynomial order is 3. As a result, for the LC beam responses of LR, SP and MCS methods in all subsequent Tables, the numbers of simulations are $N_s = 252$, $N_s = 4096$ and $N_s = 10^6$, respectively.

3.2 Verification of the model accuracy

Before demonstrating the efficiency of the proposed stochastic analysis for the LC beams, the accuracy of the beam solver model with and without uncertainties in material properties is investigated. Symmetric and asymmetric cross-ply LC beams with different layer-ups of the same thickness are considered. It is noted that the deterministic solution results in Table 4 and 5 are derived from the mean values of the input parameters in Table 1. To verify the vibration behaviors of the LC beams, Table 4 presents the mean, standard deviation, and deterministic fundamental frequencies of $[0^o/90^o/0^o]$ and $[0^o/90^o]$ LC beams with $L = 0.381$m, $h = 0.0381$m and MAT I. The mean values obtained from the MCS, LR and SP are compared with those obtained from previous works of Nguyen et al. [18] and Jun et al. [15]. It can be seen that there are excellent agreements between the models.

Similarly, the reliability of the present theory in predicting static behaviors is carried out in Table 5 for both cross-ply 0°/90°/0° and 0°/90° LC beams made of the MAT II with $L = 0.381$m, $h = 0.0381$m. The

Table 4 Mean and standard deviation of fundamental frequency (Hz) of $[0^o/90^o/0^o]$ and $[0^o/90^o]$ laminated composite beams with C–C boundary conditions ($L = 0.381$m, $h = 0.0381$m, MAT I)

Theory	$0°/90°/0°$		$0°/90°$	
	μ	σ	μ	σ
Deterministic	1546.8	–	1000.7	–
Nguyen et al. [18]	1552.4	–	1001.2	–
Jun et al. [15]	–	–	999.6	–
Present (LR)	1549.4	89.6	1003.0	58.3
Present (SP)	1549.2	89.5	1002.9	58.2
Present (MCS)	1549.2	89.6	1003.0	58.3

Table 5 Mean and standard deviation of mid-span displacement (mm) of $[0^o/90^o/0^o]$ and $[0^o/90^o]$ laminated composite beams with C–C boundary conditions ($L = 0.381$m, $h = 0.0381$m, MAT II)

Theory	$0°/90°/0°$		$0°/90°$	
	μ	σ	μ	σ
Deterministic	0.504	–	0.955	–
Nguyen et al. [22]	0.506	–	0.956	–
Khdeir and Reddy [24]	0.507	–	0.957	–
Present (LR)	0.507	0.059	0.961	0.111
Present (SP)	0.507	0.059	0.960	0.111
Present (MC)	0.507	0.059	0.960	0.111

mean, standard deviation and deterministic results of the transverse mid-span displacement are compared with those derived from Nguyen et al. [22] and Khdeir and Reddy [24] based on the HSDT. In comparison, good agreements with the earlier works are again found. In the following sections, where the uncertainties in material properties are accounted for, the MCS with one million simulation $N_s = 10^6$ is deemed the reference for result verification of the LR and SP methods.

3.3 Static analysis

The static behaviors of LC beams with various boundary conditions, span-to-depth ratios, and fiber angles are investigated in this section. These beams are made of MAT II and subjected to a uniformly distributed load. In this stochastic analysis, there are six lognormal-distributed random variables with a coefficient of variation (COV) of 0.1, where COV is the ratio between the standard deviation and mean of an input variable. In order to verify the accuracy of LR and SP methods, as mentioned above, four statistical moments consisting of the mean, standard deviation, skewness, and kurtosis of the mid-span displacement are computed and compared with those of the Monte Carlo simulations. Regarding the computational cost, the MCS, LR, and SP, respectively, require 10^6, 252 and 4096 simulations of the beam analysis model.

It can be seen from Tables 6, 7, 8 that the results obtained from LR and SP agree well with the MCS. Although the SP method runs 16 times more simulations than the LR, the improvement in accuracy is only noticeable in a few cases of thin beam ($L/h = 20$) where the lay-ups are $[45^o/-45^o]$ and $[-45^o/45^o/-45^o]$. These results ascertain the accuracy of the LR and SP methods. Furthermore, the average computing time is also displayed for each method. The time taken to pre-compute the integrals of stiffness and mass matrices is excluded. Even though this recorded time can vary considerably depending on the computer specifications or programming languages, the ratios between the run-time of MCS and PCE methods are evaluated. Both LR and SP approaches for the PCE method take the authors' computer less than a second, while the MCS requires slightly over a minute. This remark demonstrates the efficiency of the current PCE method. In addition, the LC beam deflections under various boundary conditions are plotted in Figs. 2, 3 shows the probability density function (PDF) and probability of exceedance (PoE) curves of the mid-span displacements. The PDF graph shows identical data distribution across three methods, whereas in the PoE figures, all three methods only give the matching results up to $P(X > 10^{-4})$. This discrepancy is due to the lack of samples whose probability of occurrence is less than 10^{-4}. In Fig. 4, the PoE curves of the output distribution computed by MCS, SP and LR are plotted 10 times and all of them show visible variation pass the point where $P(X < 10^{-4})$.

Table 6 Mean, standard deviation, kurtosis and skewness of mid-span transverse displacement (mm) for laminated composite beams with different lay-ups (MAT II) and S–S boundary condition

Lay-ups	Statistical moments	$L/h = 5$			$L/h = 20$		
		LR	SP	MC	LR	SP	MC
$[0^o/90^o]$	Mean	0.573	0.573	0.573	26.228	26.222	26.223
	SD	0.066	0.066	0.066	3.256	3.254	3.255
	Kurtosis	3.219	3.215	3.211	3.248	3.251	3.255
	Skewness	0.351	0.351	0.346	0.370	0.372	0.377
$[45^o/-45^o]$	Mean	1.671	1.670	1.670	91.799	91.821	91.808
	SD	0.202	0.202	0.202	11.417	11.424	11.413
	Kurtosis	3.244	3.232	3.265	3.260	3.252	3.254
	Skewness	0.372	0.365	0.375	0.380	0.381	0.378
$[0^o/90^o/0^o]$	Mean	0.289	0.289	0.289	5.851	5.852	5.852
	SD	0.034	0.034	0.034	0.773	0.774	0.773
	Kurtosis	3.221	3.223	3.236	3.306	3.301	3.306
	Skewness	0.354	0.350	0.356	0.408	0.411	0.409
$[45^o/-45^o/45^o]$	Mean	1.671	1.670	1.671	91.798	91.798	91.802
	SD	0.202	0.202	0.202	11.407	11.423	11.430
	Kurtosis	3.253	3.247	3.250	3.249	3.255	3.271
	Skewness	0.373	0.371	0.372	0.375	0.381	0.385
Average computing time (s)		0.5	0.8	65.4	0.5	0.8	61.7

Table 7 Mean, standard deviation, kurtosis and skewness of mid-span transverse displacement (mm) for laminated composite beams with different lay-ups (MAT II) and C–C boundary condition

| Lay-ups	Statistical moments	$L/h = 5$			$L/h = 20$		
		LR	SP	MC	LR	SP	MC
$[0^o/90^o]$	Mean	0.230	0.230	0.230	5.764	5.766	5.765
	SD	0.026	0.026	0.026	0.696	0.696	0.697
	Kurtosis	3.216	3.213	3.217	3.244	3.236	3.242
	Skewness	0.351	0.346	0.344	0.364	0.362	0.369
$[45^o/-45^o]$	Mean	0.517	0.517	0.517	19.116	19.112	19.106
	SD	0.061	0.061	0.061	2.356	2.356	2.352
	Kurtosis	3.244	3.221	3.220	3.272	3.256	3.253
	Skewness	0.362	0.356	0.357	0.380	0.379	0.376
$[0^o/90^o/0^o]$	Mean	0.184	0.184	0.184	1.802	1.802	1.802
	SD	0.022	0.022	0.022	0.215	0.215	0.215
	Kurtosis	3.210	3.217	3.222	3.222	3.236	3.230
	Skewness	0.349	0.356	0.354	0.359	0.361	0.364
$[45^o/-45^o/45^o]$	Mean	0.517	0.517	0.517	19.115	19.115	19.107
	SD	0.061	0.061	0.061	2.357	2.359	2.356
	Kurtosis	3.233	3.227	3.233	3.243	3.263	3.252
	Skewness	0.373	0.379	0.378	0.373	0.379	0.378
Average computing time (s)		0.4	0.9	61.2	0.5	0.9	63.0

3.4 Vibration analysis

In this section, the fundamental frequencies (Hz) of LC beams with various boundary conditions, span-to-depth ratio, and fiber angles are given in Tables 9, 10, 11. These beams made of the MAT I have six lognormal-distributed random variables with a COV of 0.1. Similar to the static analysis, four statistical moments of mean, standard deviation, skewness, and kurtosis of the fundamental frequency (Hz) are computed and verified with those of the Monte Carlo simulations. While both the LR and SP methods give matching results for the mean and standard deviation, there is an apparent discrepancy of the skewness and kurtosis between the LR method and the other two. Tables 9, 10, 11 show that the kurtosis and skewness obtained from the LR method in the cases of 45°/− 45° and 0°/90° beams differ from the kurtosis and skewness of the SP and MCS methods. This difference in the skewness and kurtosis does not mean the whole output distributions from these methods differ. Concerning efficiency, like the static analysis section above, the PCE methods show considerable improvement in the average computing time compared to the MCS for all cases of the LC beams.
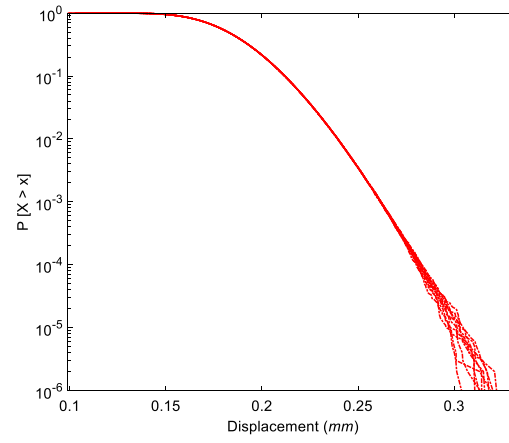
Table 8 Mean, standard deviation, kurtosis and skewness of mid-span transverse displacement (*mm*) for laminated composite beams with different lay-ups (MAT II) and C-F boundary condition

Lay-ups	Statistical moment	$L/h = 5$			$L/h = 20$		
		LR	SP	MC	LR	SP	MC
$[0^o/90^o]$	Mean	1.824	1.825	1.824	88.711	88.719	88.717
	SD	0.214	0.214	0.214	11.004	11.023	11.027
	Kurtosis	3.233	3.226	3.223	3.237	3.244	3.242
	Skewness	0.355	0.355	0.354	0.367	0.370	0.371
$[45^o/-45^o]$	Mean	5.523	5.522	5.524	311.433	311.427	311.449
	SD	0.671	0.670	0.671	38.729	38.727	38.747
	Kurtosis	3.256	3.253	3.259	3.253	3.253	3.257
	Skewness	0.376	0.375	0.374	0.378	0.377	0.378
$[0^o/90^o/0^o]$	Mean	0.813	0.813	0.813	19.358	19.363	19.360
	SD	0.095	0.095	0.094	2.584	2.585	2.587
	Kurtosis	3.206	3.222	3.202	3.297	3.309	3.302
	Skewness	0.349	0.348	0.344	0.408	0.413	0.414
$[45^o/-45^o/45^o]$	Mean	5.522	5.522	5.522	311.447	311.381	311.389
	SD	0.671	0.670	0.670	38.707	38.727	38.702
	Kurtosis	3.243	3.261	3.246	3.250	3.265	3.265
	Skewness	0.371	0.373	0.371	0.375	0.380	0.379
Average computing time (s)		0.4	0.9	62.4	0.5	0.8	59.4
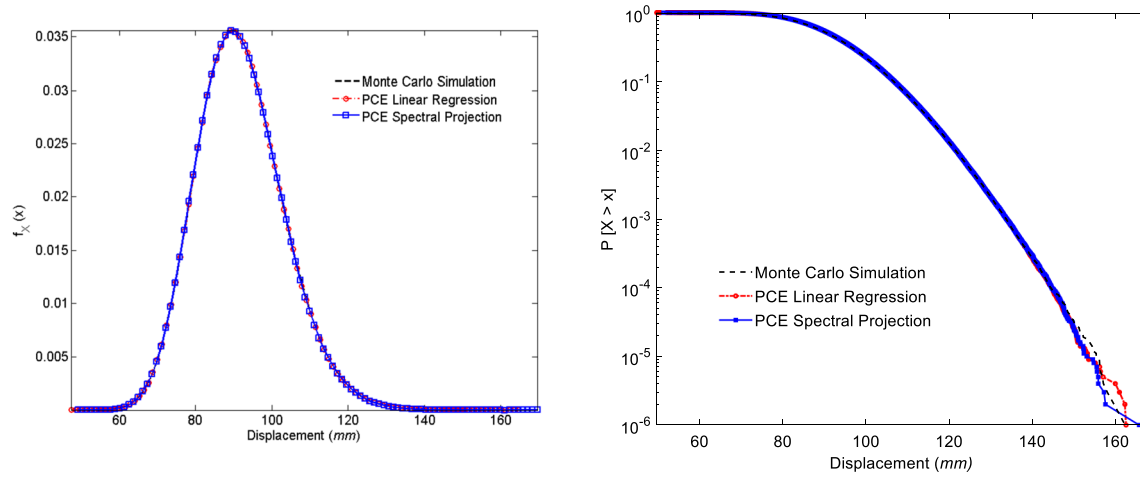
Fig. 2 Probability density function (PDF) and Probability of exceedance (PoE) of three numerical methods (MCS, LR, SP) of the mid-span displacement (mm) for $[45^o/-45^o/45^o]$ laminated composite beam (*L/h* = 20, S–S boundary condition)
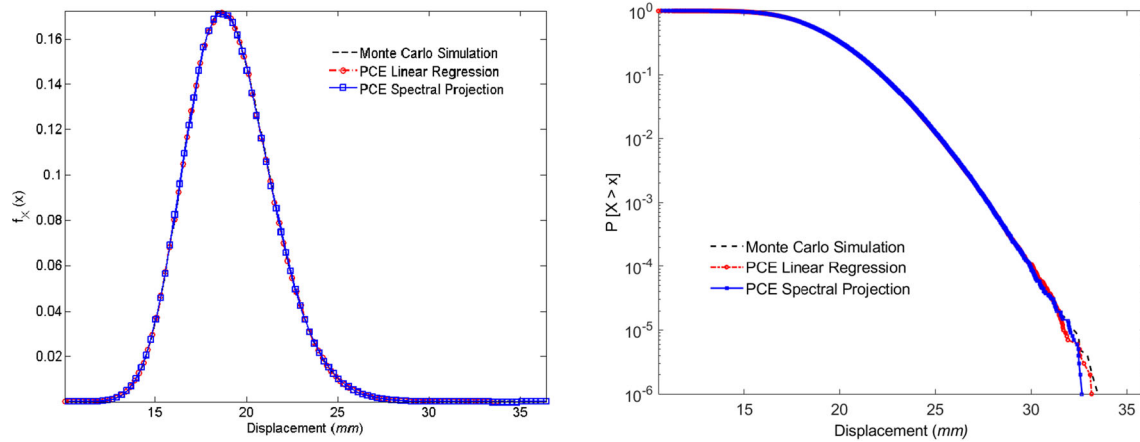
Fig. 3 Probability density function (PDF) and Probability of exceedance (PoE) of three numerical methods (MCS, LR, SP) of the mid-span displacement (mm) for $[45^o/-45^o/45^o]$ laminated composite beam (*L/h* = 20, C–C boundary condition)
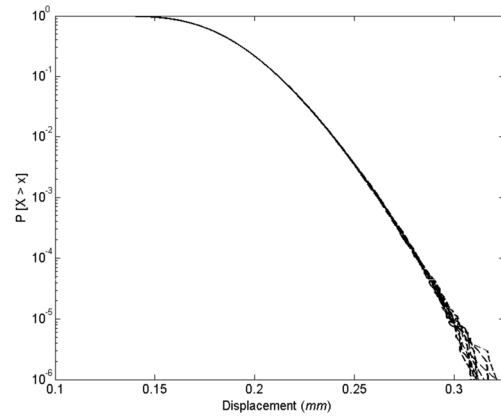
(a) MCS

(b) LR
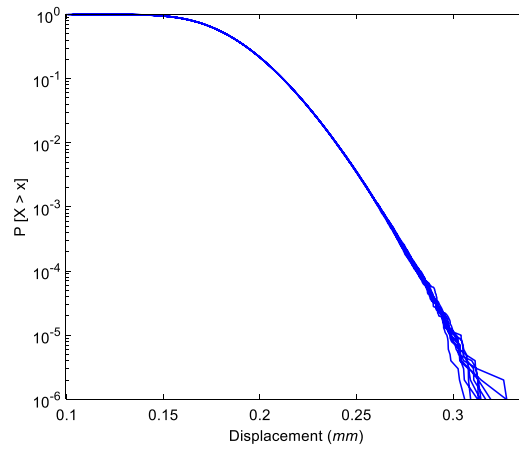
(c) SP

Fig. 4 Variation in probability of exceedance (PoE) of mid-span displacement (mm) for the $[0^o/90^o/0^o]$ laminated composite beam ($L/h = 5$, C–C boundary condition)

Table 9 Mean, standard deviation, kurtosis and skewness of fundamental frequency (Hz) of laminated composite beams with different lay-ups (MAT I) and S–S boundary condition

| Lay-ups	Statistical moments	$L/h = 5$			$L/h = 20$		
		LR	SP	MC	LR	SP	MC
$[0^o/90^o]$	Mean	891.230	891.265	891.345	251.138	251.107	251.122
	SD	52.197	52.210	52.186	15.478	15.465	15.436
	Kurtosis	3.046	3.054	3.054	2.942	3.072	3.057
	Skewness	0.170	0.176	0.174	0.222	0.187	0.185
$[45^o/-45^o]$	Mean	574.380	574.405	574.391	152.486	152.481	152.472
	SD	34.893	34.908	34.892	9.380	9.374	9.389
	Kurtosis	3.061	3.056	3.060	2.887	3.058	3.065
	Skewness	0.180	0.177	0.179	0.207	0.183	0.185
$[0^o/90^o/0^o]$	Mean	1433.000	1433.202	1433.094	529.764	529.855	529.840
	SD	83.171	83.156	83.169	35.966	35.948	35.927
	Kurtosis	3.059	3.060	3.054	3.070	3.075	3.068
	Skewness	0.169	0.175	0.170	0.201	0.202	0.191
$[45^o/-45^o/45^o]$	Mean	574.429	574.418	574.417	152.500	152.484	152.484
	SD	34.925	34.890	34.910	9.391	9.387	9.371
	Kurtosis	3.056	3.064	3.059	3.063	3.057	3.073
	Skewness	0.179	0.181	0.180	0.182	0.187	0.183
Average computing time (s)		1.4	1.9	117.5	1.3	2.5	120.3

Table 10 Mean, standard deviation, kurtosis and skewness of fundamental frequency (Hz) of laminated composite beams with different lay-ups (MAT I) and C–C boundary condition

Lay-ups	Statistical moments	$L/h = 5$			$L/h = 20$		
		LR	SP	MC	LR	SP	MC
$[0^o/90^o]$	Mean	1558.420	1558.239	1558.318	552.984	552.986	552.989
	SD	87.957	87.872	87.812	33.448	33.478	33.501
	Kurtosis	3.042	3.055	3.053	2.668	3.057	3.056
	Skewness	0.171	0.171	0.169	0.185	0.183	0.180
$[45^o/-45^o]$	Mean	1119.291	1119.101	1119.239	341.336	341.318	341.307
	SD	66.516	66.533	66.471	20.931	20.892	20.888
	Kurtosis	3.044	3.047	3.059	2.937	3.058	3.052
	Skewness	0.170	0.175	0.175	0.120	0.178	0.176
$[0^o/90^o/0^o]$	Mean	1903.023	1902.896	1903.137	1052.855	1053.112	1053.129
	SD	110.435	110.430	110.547	65.283	65.372	65.372
	Kurtosis	3.056	3.058	3.061	3.063	3.065	3.056
	Skewness	0.173	0.171	0.179	0.181	0.178	0.178
$[45^o/-45^o/45^o]$	Mean	1119.214	1119.171	1119.285	341.353	341.308	341.353
	SD	66.382	66.429	66.480	20.911	20.920	20.945
	Kurtosis	3.053	3.043	3.055	3.061	3.049	3.058
	Skewness	0.170	0.173	0.173	0.181	0.177	0.181
Average computing time (s)		1.3	3.5	114.2	0.8	1.2	117.1

Instead of comparing the PDF and PoE as above, Fig. 5 shows the quantile–quantile plots of 10^6 sample outputs obtained from MCS compared with the outputs of LR and SP methods in each of the two graphs. In a quantile–quantile plot, the two samples plotted have the same distribution when the plot is linear and lies along the 45-degree reference line. The straight lines shown in Fig. 5 further confirm that compared with the computationally-expensive MCS, the output distribution of LR and SP methods are accurate despite the much fewer simulations. In addition, the PoE curves of the output from all three methods are plotted ten times in Fig. 6 to demonstrate how the lack of samples pass the point $P(X < 10^{-4})$ causes the variation in the vibration output distribution. This also explains the deviation of data points from the 45-degree reference line at the lower- and upper-extreme quantiles in Fig. 5.

Table 11 Mean, standard deviation, kurtosis and skewness of fundamental frequency (*Hz*) of laminated composite beams with different lay-ups (MAT I) and C-F boundary condition

Lay-ups	Statistical moments	$L/h = 5$			$L/h = 20$		
		LR	SP	MC	LR	SP	MC
$[0^o/90^o]$	Mean	338.969	338.930	338.967	89.918	89.933	89.922
	SD	20.346	20.336	20.345	5.548	5.553	5.558
	Kurtosis	3.061	3.057	3.049	2.724	3.073	3.071
	Skewness	0.180	0.181	0.177	0.045	0.190	0.191
$[45^o/-45^o]$	Mean	211.651	211.635	211.629	54.453	54.456	54.458
	SD	12.952	12.956	12.939	3.351	3.354	3.353
	Kurtosis	3.049	3.062	3.063	2.770	3.049	3.062
	Skewness	0.178	0.181	0.185	0.032	0.178	0.183
$[0^o/90^o/0^o]$	Mean	617.404	617.420	617.421	193.115	193.109	193.121
	SD	37.323	37.290	37.282	13.374	13.389	13.375
	Kurtosis	3.055	3.056	3.060	3.069	3.077	3.080
	Skewness	0.172	0.175	0.175	0.203	0.207	0.206
$[45^o/-45^o/45^o]$	Mean	211.646	211.644	211.633	54.454	54.461	54.460
	SD	12.955	12.942	12.944	3.353	3.354	3.353
	Kurtosis	3.043	3.047	3.047	3.062	3.051	3.059
	Skewness	0.179	0.180	0.177	0.182	0.182	0.179
Average computing time (s)		0.4	1.0	112.0	0.5	1.1	119.8
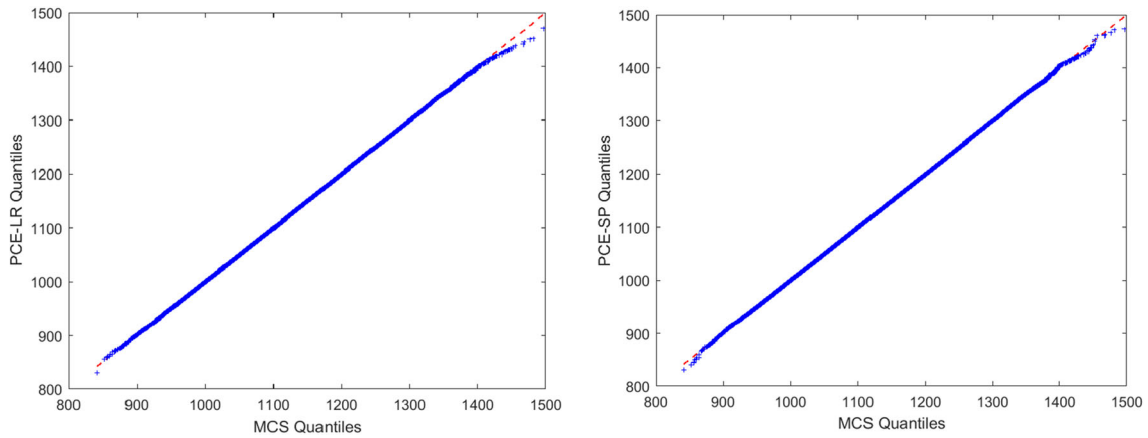
Fig. 5 Quantile–quantile plot of Linear regression (LR) and Spectral projection (SP) methods with respect to the Monte Carlo Simulation (MCS) for the fundamental frequencies of $[45^o/-45^o]$ laminated composite beam ($L/h=5$, C–C boundary condition)

3.5 Sensitivity analysis

This section discusses the impact of each random input variable on the beam's deflection and fundamental frequency. In all cases, total-order Sobol indices computed are very similar to the first-order Sobol indices which infer that there is almost no interaction between the random input variables. Therefore, only the first-order Sobol indices are presented in Figs. 7 and 8. While these Sobol indices can be derived effortlessly from the PCE coefficients, they theoretically require two nested loops of N_s^2 beam solver runs in the crude MCS method. Several improved MCS algorithms proposed [45] can reduce the complexity to $(N_{rv} + 2)N_s$ which is still nowhere near the efficiency of the PCE method presented in this paper. In both figures, the three bars represent the first-order Sobol indices of the variable underneath computed using the MCS, PCE-SP and PCE-LR methods. The values above each group of bars are, respectively, for the MCS, PCE-SP and PCE-LR from top to bottom. It can be seen from both Figs. 7 and 8 that the PCE-SP and PCE-LR methods give the same results, all of which agree well with the MCS. Figure 7 indicates the variation of applied distributed load q affects the beam's deflection the most.

Interestingly, to a lesser extent, the variation of the material's shear modulus G_{12} also influences the model outputs in the case of $[45^o/-45^o]$ lay-up while in the case of $[0^o/90^o]$ lay-up, the second most impactful variable is E_1. All the other four variables in both cases of lay-ups are considered insignificant and
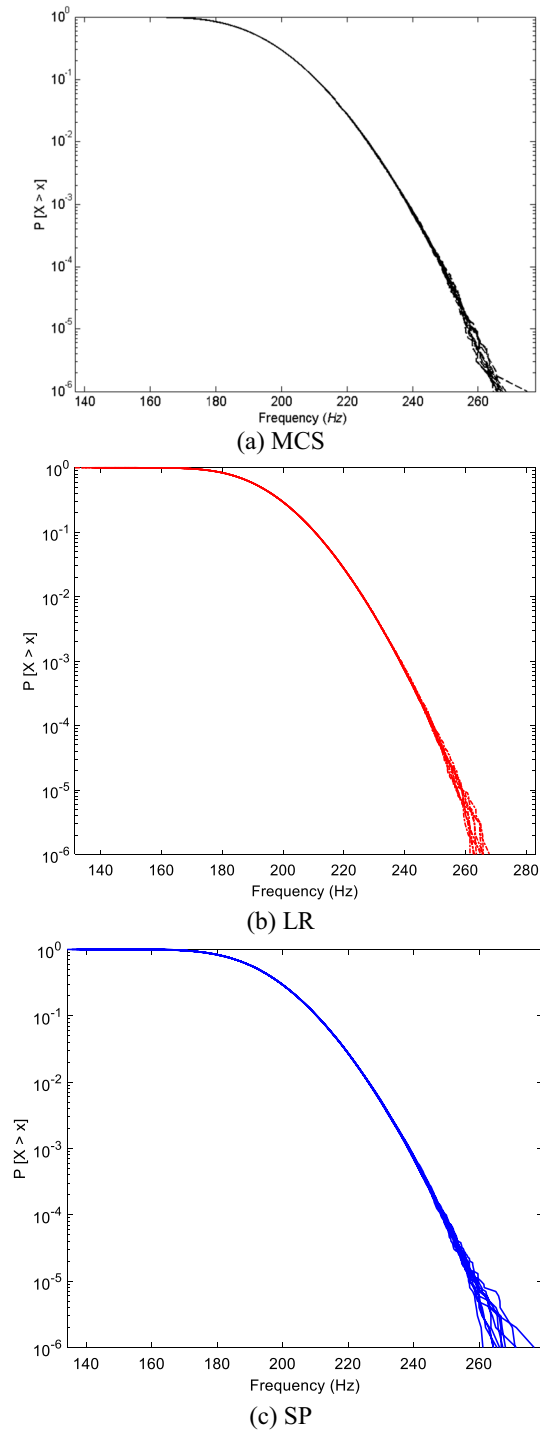
Fig. 6 Variation in probability of exceedance (PoE) of fundamental frequencies (Hz) for the $[0^o/90^o/0^o]$ laminated composite beam ($L/h = 20$, C-F boundary condition)
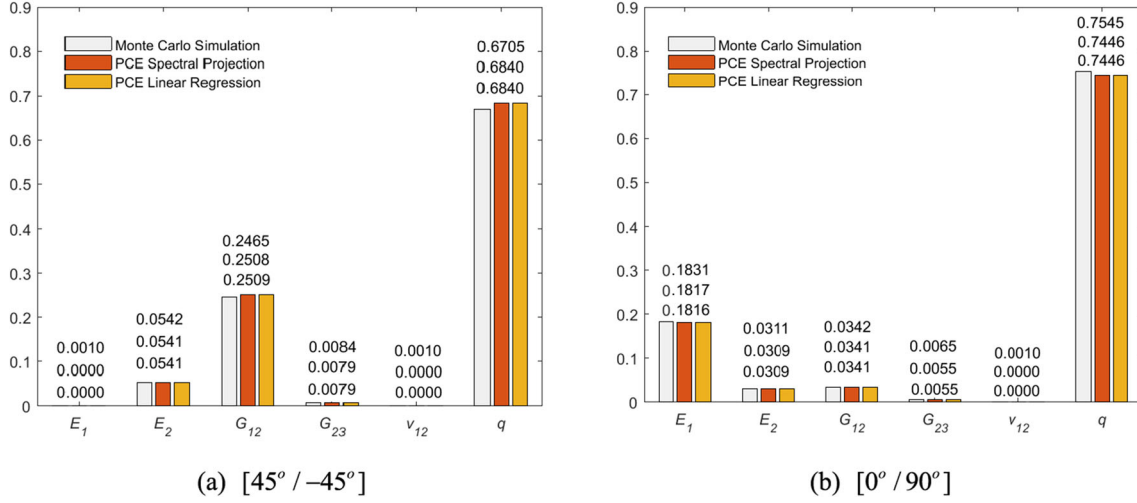
(a) $[45^o / -45^o]$ (b) $[0^o / 90^o]$

Fig. 7 First-order Sobol indices of the random input variables with respect to the mid-span displacement (mm) of the LC beam model obtained from MCS and PCE ($L/h = 5$, S–S boundary condition)
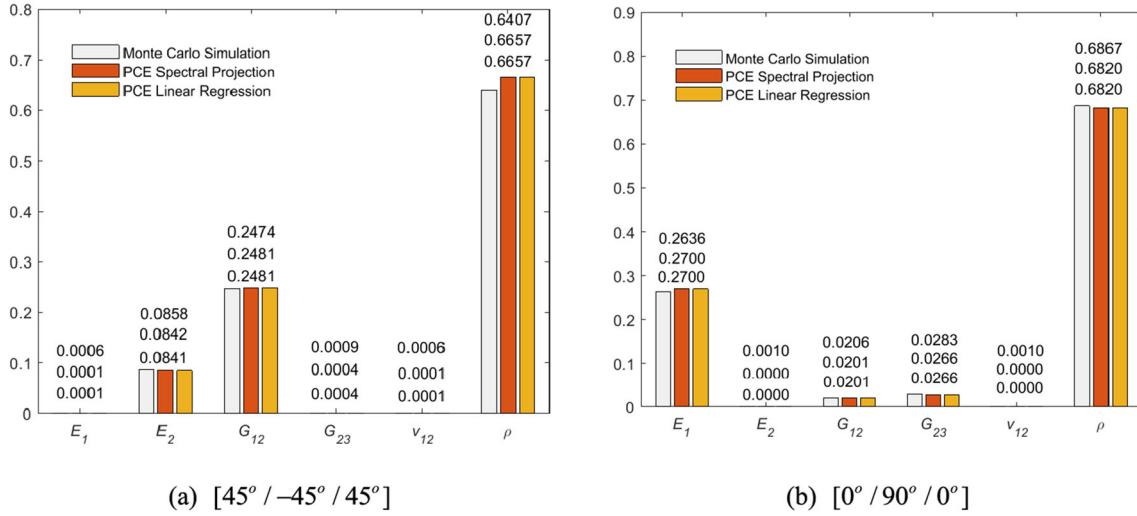

(a) $[45^o / -45^o / 45^o]$ (b) $[0^o / 90^o / 0^o]$

Fig. 8 First-order Sobol indices of the random input variables with respect to the first fundamental frequency (Hz) of the LC beam model obtained from MCS and PCE ($L/h = 5$, C–F boundary condition)

can be ignored to reduce the computational cost. Figure 8 shows a similar pattern for the vibration analysis of the beam. For both $[45^o / - 45^o / 45^o]$ and $[0^o / 90^o / 0^o]$ lay-ups, the material mass density ρ affects the fundamental frequencies the most. The second most important variable is G_{12} for $[45^o / - 45^o / 45^o]$ lay-up and E_1 for $[0^o / 90^o / 0^o]$ lay-up. There is a small difference compared to the static analysis that in the case of $[45^o / - 45^o / 45^o]$ lay-up, E_2 plays a minor role in altering the beam's vibration responses. Knowing the lay-up arrangement, the sensitivity analysis is thus valuable for filtering the critical variables in a beam model, reducing the size of the random input vector and saving computing time.

4 Conclusion

This paper investigated the stochastic static and vibration characteristics of laminated composite beams considering the uncertainty in material properties and applied loads. The random input parameters are modeled within a given range of the lognormal distributions. A metamodel-based polynomial chaos expansion with spectral projection and linear regression approaches was constructed using a few training samples simulated from the deterministic beam model. The higher-order shear deformation theory and Hamilton's principle are employed

to derive the beam's governing equations which are then solved by Ritz's method. The results from the PCE are validated against the crude Monte Carlo simulation regarding different statistical metrics and input parameters' sensitivity. The following conclusions could be drawn from the observations of the numerical results:

- The proposed PCE method has been demonstrated to accurately capture the stochastic output distribution while significantly reducing the number of required simulations and substantially reducing computing expenses.
- The linear regression approach requires fewer simulations than the spectral projection approach.
- The proposed methods can estimate Sobol's indices in global sensitivity analysis without incurring additional computing costs beyond those necessary for constructing the PCE model.
- The variability in the applied load influences the mid-span displacement most, while mass density variation significantly affects the vibration characteristics of LC beams.

The proposed use of PCE in this paper for laminated composite beams can be extended to stochastic analysis of other composite structures. This approach is particularly valuable in cases where the complexity of calculations or the cost of practical experiments hinder efficient data collection.

References

1. Aydogdu, M.: Vibration analysis of cross-ply laminated beams with general boundary conditions by Ritz method. Int. J. Mech. Sci. **47**(11), 1740–1755 (2005)
2. Kant, T., Marur, S.R., Rao, G.S.: Analytical solution to the dynamic analysis of laminated beams using higher order refined theory. Compos. Struct. **40**(1), 1–9 (1997)
3. Karama, M., Afaq, K.S., Mistou, S.: Mechanical behaviour of laminated composite beam by the new multi-layered laminated composite structures model with transverse shear stress continuity. Int. J. Solids Struct. **40**(6), 1525–1546 (2003)
4. Khdeir, A.A., Reddy, J.N.: Free vibration of cross-ply laminated beams with arbitrary boundary conditions. Int. J. Eng. Sci. **32**(12), 1971–1980 (1994)
5. Nguyen, N.-D., Nguyen, T.-K., Thai, H.-T., Vo, T.P.: A Ritz type solution with exponential trial functions for laminated composite beams based on the modified couple stress theory. Compos. Struct. **191**, 154–167 (2018)
6. Ebrahimi, F., Ahari, M.F.: Magnetostriction-assisted active control of the multi-layered nanoplates: effect of the porous functionally graded facesheets on the system's behavior. Eng. Comput. **39**(1), 269–283 (2023)
7. Dhore, N., Khalsa, L., Varghese, V.: Hygrothermoelastic analysis of non-simple nano-beam induced by ramp-type heating. Archive Appl. Mechan. **93**, 3379–3393 (2023)
8. Vo, T.P., Lee, J.: Geometrical nonlinear analysis of thin-walled composite beams using finite element method based on first order shear deformation theory. Arch. Appl. Mech. **81**(4), 419–435 (2011)
9. Zhang, Y., Zhang, L., Zhang, S.: Exact series solutions of composite beams with rotationally restrained boundary conditions: static analysis. Arch. Appl. Mech. **92**(12), 3999–4015 (2022)
10. Ebrahimi, F., Hosseini, S.H.S.: Nonlinear vibration and dynamic instability analysis nanobeams under thermo-magneto-mechanical loads: a parametric excitation study. Eng. Comput. **37**(1), 395–408 (2021)
11. Ebrahimi, F., Karimiasl, M., Mahesh, V.: Chaotic dynamics and forced harmonic vibration analysis of magneto-electro-viscoelastic multiscale composite nanobeam. Eng. Comput. **37**(2), 937–950 (2021)
12. Selvamani, R., Loganathan, R., Ebrahimi, F.: Nonlocal state-space strain gradient approach to the vibration of piezoelectric functionally graded nanobeam. Eng. Trans. **70**(4), 319–338 (2022)
13. Selvamani, R., Rexy, J., Ebrahimi, F.: Vibration analysis of a magneto thermo electrical nano fiber reinforced with graphene oxide powder under refined beam model. J. Solid Mechan. **13**(1), 80–94 (2021)
14. Ellali, M., Bouazza, M., Amara, K.: Thermal buckling of a sandwich beam attached with piezoelectric layers via the shear deformation theory. Arch. Appl. Mech. **92**(3), 657–665 (2022)
15. Jun, L., Yuchen, B., Peng, H.: A dynamic stiffness method for analysis of thermal effect on vibration and buckling of a laminated composite beam. Arch. Appl. Mech. **87**(8), 1295–1315 (2017)
16. Li, X., Yu, K., Zhao, R.: Thermal post-buckling and vibration analysis of a symmetric sandwich beam with clamped and simply supported boundary conditions. Arch. Appl. Mech. **88**(4), 543–561 (2018)
17. Liu, L., Yang, W., Chai, Y., Zhai, G.: Vibration and thermal buckling analyses of multi-span composite lattice sandwich beams. Arch. Appl. Mech. **91**(6), 2601–2616 (2021)
18. Nguyen, N.-D., Nguyen, T.-K., Nguyen, T.-N., Thai, H.-T.: New Ritz-solution shape functions for analysis of thermo-mechanical buckling and vibration of laminated composite beams. Compos. Struct. **184**, 452–460 (2018)
19. Beheshti-Aval, S.B., Lezgy-Nazargah, M.: A coupled refined high-order global-local theory and finite element model for static electromechanical response of smart multilayered/sandwich beams. Arch. Appl. Mech. **82**(12), 1709–1752 (2012)
20. Vo, T.P., Thai, H.-T., Inam, F.: Axial-flexural coupled vibration and buckling of composite beams using sinusoidal shear deformation theory. Arch. Appl. Mech. **83**(4), 605–622 (2013)
21. Vo, T.P., Thai, H.-T.: Static behavior of composite beams using various refined shear deformation theories. Compos. Struct. **94**(8), 2513–2522 (2012)
22. Nguyen, T.-K., Nguyen, N.-D., Vo, T., Thai, T.: Trigonometric-series solution for analysis of laminated composite beams. Compos. Struct. **160**, 142–151 (2016)
23. Nguyen, N.-D., Nguyen, T.-K., Vo, T.P., Thai, H.-T.: Ritz-based analytical solutions for bending, buckling and vibration behavior of laminated composite beams. Int. J. Struct. Stab. Dyn. **18**(11), 1850130 (2018)

24. Khdeir, A.A., Reddy, J.N.: An exact solution for the bending of thin and thick cross-ply laminated beams. Compos. Struct. **37**(2), 195–203 (1997)
25. Liu, X., Jiang, L., Xiang, P., Zhou, W., Lai, Z., Feng, Y.: Stochastic finite element method based on point estimate and Karhunen-Loéve expansion. Arch. Appl. Mech. **91**(4), 1257–1271 (2021)
26. Stefanou, G.: The stochastic finite element method: past, present and future. Comput. Methods Appl. Mech. Eng. **198**(9), 1031–1051 (2009)
27. Rahman, S., Rao, B.N.: A perturbation method for stochastic meshless analysis in elastostatics. Int. J. Numer. Meth. Eng. **50**(8), 1969–1991 (2001)
28. Sahoo, R., Grover, N., Singh, B.N.: Random vibration response of composite–sandwich laminates. Arch. Appl. Mech. **91**(9), 3755–3771 (2021)
29. Li, H.-S., Lü, Z.-Z., Yue, Z.-F.: Support vector machine for structural reliability analysis. Appl. Math. Mech. **27**(10), 1295–1303 (2006)
30. Peng, X., Li, D., Wu, H., Liu, Z., Li, J., Jiang, S., Tan, J.: Uncertainty analysis of composite laminated plate with data-driven polynomial chaos expansion method under insufficient input data of uncertain parameters. Compos. Struct. **209**, 625–633 (2019)
31. Nguyen, H.X., Duy Hien, T., Lee, J., Nguyen-Xuan, H.: Stochastic buckling behaviour of laminated composite structures with uncertain material properties. Aerosp. Sci. Technol. **66**, 274–283 (2017)
32. Elishakoff, I., Archaud, E.: Modified Monte Carlo method for buckling analysis of nonlinear imperfect structures. Arch. Appl. Mech. **83**(9), 1327–1339 (2013)
33. da Claudio, S.R.Á., Squarcio, R.M.F.: The Neumann-Monte Carlo methodology applied to the quantification of uncertainty in the problem stochastic bending of the Levinson-Bickford beam. Archive Appl. Mechan. **93**(5), 2009–2024 (2023)
34. Naskar, S., Mukhopadhyay, T., Sriramula, S., Adhikari, S.: Stochastic natural frequency analysis of damaged thin-walled laminated composite beams with uncertainty in micromechanical properties. Compos. Struct. **160**, 312–334 (2017)
35. Li, J., Tian, X., Han, Z., Narita, Y.: Stochastic thermal buckling analysis of laminated plates using perturbation technique. Compos. Struct. **139**, 1–12 (2016)
36. Onkar, A.K., Upadhyay, C.S., Yadav, D.: Stochastic finite element buckling analysis of laminated plates with circular cutout under uniaxial compression. J. Appl. Mech. **74**(4), 798–809 (2006)
37. Verma, V.K., Singh, B.N.: Thermal buckling of laminated composite plates with random geometric and material properties. Int. J. Struct. Stabil. Dyn. **09**(02), 187–211 (2009)
38. Chandra, S., Sepahvand, K., Matsagar, V.A., Marburg, S.: Stochastic dynamic analysis of composite plate with random temperature increment. Compos. Struct. **226**, 111159 (2019)
39. Chakraborty, S., Mandal, B., Chowdhury, R., Chakrabarti, A.: Stochastic free vibration analysis of laminated composite plates using polynomial correlated function expansion. Compos. Struct. **135**, 236–249 (2016)
40. Bhattacharyya, B.: On the use of sparse Bayesian learning-based polynomial chaos expansion for global reliability sensitivity analysis. J. Comput. Appl. Math. **420**, 114819 (2023)
41. Reddy, J.N.: Mechanics of laminated composite plates and shells: theory and analysis, 2nd edn. CRC Press, Boca Raton (2003)
42. Xiu, D., Karniadakis, G.E.: The wiener-askey polynomial chaos for stochastic differential equations. SIAM J. Sci. Comput. **24**(2), 619–644 (2002)
43. Dalbey, K., Eldred, M.S., Geraci, G., Jakeman, J.D., Maupin, K.A., Monschke, J.A., Seidl, D.T., Swiler, L.P., Tran, A., Menhorn, F., Zeng, X.: Dakota A Multilevel Parallel Object-Oriented Framework for Design Optimization Parameter Estimation Uncertainty Quantification and Sensitivity Analysis: Version 6.12 Theory Manual. 2020, ; Sandia National Lab. (SNL-NM), Albuquerque, NM (United States). p. Medium: ED; Size, p 128
44. Sobol, I.M.: Sensitivity estimates for nonlinear mathematical models. Mathe. Modell. Comput. Exp. **1**, 407 (1993)
45. Saltelli, A., Annoni, P., Azzini, I., Campolongo, F., Ratto, M., Tarantola, S.: Variance based sensitivity analysis of model output. Design and estimator for the total sensitivity index. Comput. Phys. Commun. **181**(2), 259–270 (2010)
46. Saltelli, A., Ratto, M., Tarantola, S., Campolongo, F.: Update 1 of: sensitivity analysis for chemical models. Chem. Rev. **112**(5), PR1–PR21 (2012)
47. Sudret, B.: Global sensitivity analysis using polynomial chaos expansions. Reliab. Eng. Syst. Saf. **93**(7), 964–979 (2008)

A novel two-variable model for bending analysis of laminated composite beams

Xuan-Bach Bui
Faculty of Civil Engineering
Ho Chi Minh City University of Technology and Education
Ho Chi Minh City, Viet Nam

Trung-Kien Nguyen
Faculty of Civil Engineering
Ho Chi Minh City University of Technology and Education
Ho Chi Minh City, Viet Nam

Quoc-Cuong Le
Faculty of Engineering - Technology
Thu Dau Mot University
Binh Duong Province, Viet Nam
cuongtd91@gmail.com

T. Truong-Phong Nguyen
Faculty of Civil Engineering
Ho Chi Minh City University of Technology and Education
Ho Chi Minh City, Viet Nam

Abstract—A novel two-variable model for static analysis of laminated composite beams is proposed in this paper. The kinematics of the beam having only two variables are expanded in a hybrid form under polynomial and trigonometric series in thickness and axial directions, respectively. Lagrange's equations are then used to derive characteristic equations of the beams. Numerical results for laminated composite beams are compared with previous studies and are used to investigate the effects of length-to-depth ratio, fibre angles and material anisotropy on the deflection and stresses of laminated composite beams.

Index Terms—Laminated composite beams; Bending; Elasticity solution.

I. INTRODUCTION

Laminated composite materials are fabricated by assembling multiple layers of fibrous materials to achieve the superior engineering properties such as bending stiffness, strength-to-weight ratio and thermal performance. As a result, laminate composite has been widely applied in aerospace engineering, mechanical engineering as well as construction technology. In order to maximise the potential advantage of this multilayered material, numerous studies and computation modelling have been conducted to fine-tune the static and dynamic behaviours of laminated composite beams. Various beam theories have been developed in order to predict accurately their structural responses and capture anisotropy of laminated composite materials. Classical beam theory (CBT) is the simplest one in analyzing responses of laminated composite beams. Nonetheless, this theory underestimates deflections and overestimates natural frequencies of the beams due to neglecting effects of transverse shear deformation. In order to account for this effect, thanks to its simplicity in formulation and programming, the first-order shear deformation beam theory (FSBT) is commonly used by researchers and commercial softwares for the analysis of laminated composite beams ([1], [2], [3], [4], [5]). However, in this theory, the inadequate distribution of

transverse shear stress in the beam thickness requires a shear correction factor to calculate the shear force. This adverse in practice could be overcome by using higher-order deformation beam theory (HSBT) ([6], [7], [8], [9], [10], [11], [12], [13], [14], [15]) or Quasi-3D beam theory (Quasi-3D) ([16], [17], [18], [19], [20], [21], [22]) owing to the higher-order variation of axial displacement or both axial and transverse displacements, respectively. In such approach, stresses of the beam can be directly computed from constitutive equations without shear coefficient requirement. Many higher-order shear deformation theories have been developed with different approaches in which its kinematics could be expressed in terms of polynomial ([23], [24], [25], [26], [27]), trigonometric ([28], [29], [30], [31], [32], [33], [34]), exponential ones ([35], [36]), hyperbolic ([37], [38], [39]) and hybrid higher-order shear functions ([40], [41]). A literature review shows that a vast number of researches on development HSBT and Quasi-3D have been developed, however the accuracy of these theories strictly depends on the choice of shear functions and number of variables defining the problem. The development of new beam theories as well as suitable solution methods is a complicated problem and needs to study further.

The objective of this paper is to develop a bi-directional elasticity solution for static analysis of laminated composite beams. Based on the elasticity equations, the proposed theory only requires two unknowns in which the axial and transverse displacements are approximated in series terms in its two in-plane directions for different boundary conditions and Lagrange's equations are used to derive characteristic equations. Numerical results are presented to investigate the effects of length-to-depth ratio, fibre angle and material anisotropy on the deflections and stresses of laminated composite beams.

II. THEORETICAL FORMULATION

Considering a laminated composite beam with rectangular section $b \times h$ and length L, the beam is composed of n layers of orthotropic materials.

A. Kinematic, strain and stress

Denoting u and w are axial and transverse displacements at location (x, z) of the beam. The linear displacement-strain relations of the beam are given by:

$$\epsilon_x = \frac{\partial u}{\partial x} \tag{1a}$$

$$\epsilon_z = \frac{\partial w}{\partial z} \tag{1b}$$

$$\gamma_{xz} = \frac{\partial u}{\partial z} + \frac{\partial w}{\partial x} \tag{1c}$$

Based on an assumption of the plan stress in the plane (x, z) of the beam, i.e $\sigma_y = \sigma_{yz} = \sigma_{xy} = 0$, the elastic constitutive equation at the kth-layer in the global coordinate system is expressed by:

$$\left\{ \begin{array}{c} \sigma_x \\ \sigma_z \\ \sigma_{xz} \end{array} \right\} = \left[\begin{array}{ccc} \bar{\bar{C}}_{11} & \bar{\bar{C}}_{13} & 0 \\ \bar{\bar{C}}_{13} & \bar{\bar{C}}_{33} & 0 \\ 0 & 0 & \bar{\bar{C}}_{55} \end{array} \right] \left\{ \begin{array}{c} \epsilon_x \\ \epsilon_z \\ \gamma_{xz} \end{array} \right\} \tag{2}$$

where $\bar{\bar{C}}_{11}$, $\bar{\bar{C}}_{13}$ and $\bar{\bar{C}}_{55}$ are the reduced in-plane and out-of-plane elastic stiffness coefficients of the laminated composite beam in the global coordinates (see [22] for more details).

B. Energy formulation

The total static energy Π of the beam under an external transverse loading comprises the strain energy $\mathcal{U}$ and work done by the external load $\mathcal{V}$. The strain energy $\mathcal{U}$ of the beam is given by:

$$\begin{aligned} \mathcal{U} &= \frac{1}{2} \int_V \left(\sigma_x \epsilon_x + \sigma_z \epsilon_z + \sigma_{xz} \gamma_{xz} \right) dV \\ &= \frac{1}{2} \int_V \left\{ \bar{\bar{C}}_{11} \left(\frac{\partial u}{\partial x} \right)^2 + 2\bar{\bar{C}}_{13} \frac{\partial u}{\partial x} \frac{\partial w}{\partial z} + \bar{\bar{C}}_{33} \left(\frac{\partial w}{\partial z} \right)^2 \right. \\ &\quad + \left. \bar{\bar{C}}_{55} \left[\left(\frac{\partial u}{\partial z} \right)^2 + 2\frac{\partial u}{\partial z} \frac{\partial w}{\partial x} + \left(\frac{\partial w}{\partial x} \right)^2 \right] \right\} dV \end{aligned} \tag{3}$$

The work done by a transverse load q at the bottom surface of the beam is given by:

$$\mathcal{V} = -\int_0^L qw\,dx \tag{4}$$

The total energy of the beam is therefore expressed by:

$$\begin{aligned} \Pi &= \frac{1}{2} \int_V \left\{ \bar{\bar{C}}_{11} \left(\frac{\partial u}{\partial x} \right)^2 + 2\bar{\bar{C}}_{13} \frac{\partial u}{\partial x} \frac{\partial w}{\partial z} + \bar{\bar{C}}_{33} \left(\frac{\partial w}{\partial z} \right)^2 \right. \\ &\quad + \left. \bar{\bar{C}}_{55} \left[\left(\frac{\partial u}{\partial z} \right)^2 + 2\frac{\partial u}{\partial z} \frac{\partial w}{\partial x} + \left(\frac{\partial w}{\partial x} \right)^2 \right] \right\} dV \\ &\quad - \int_0^L qw\,dx \end{aligned} \tag{5}$$

C. Bi-directional Ritz solution

Based on the Ritz method, the axial and transverse displacements at location (x, z) of the beam can be generally approximated in the following forms:

$$u(x, z, t) = \sum_{r=1}^R \sum_{s=1}^S \psi_{rs}(x, z) u_{rs} \tag{6a}$$

$$w(x, z, t) = \sum_{r=1}^R \sum_{s=1}^S \varphi_{rs}(x, z) w_{rs} \tag{6b}$$

where u_{rs}, w_{rs} are unknown displacement values to be determined; $\psi_{rs}(x, z)$, $\varphi_{rs}(x, z)$ are the bi-directional shape functions which are composed of admissible hybrid exponential-trigonometric function in the x−axis and polynomial function in the z−axis as follows:

$$\text{S-S} \quad : \quad \psi_{rs}(x, z) = \cos\frac{\pi x}{L} e^{-rx/L} z^{s-1}$$

$$\varphi_{rs}(x, z) = \sin\frac{\pi x}{L} e^{-rx/L} z^{s-1} \tag{7a}$$

$$\text{C-F} \quad : \quad \psi_{rs}(x, z) = \sin\frac{\pi x}{2L} e^{-rx/L} z^{s-1}$$

$$\varphi_{rs}(x, z) = \left(1 - \cos\frac{\pi x}{2L} \right) e^{-rx/L} z^{s-1} \tag{7b}$$

$$\text{C-C} \quad : \quad \psi_{rs}(x, z) = \sin\frac{\pi x}{L} e^{-rx/L} z^{s-1}$$

$$\varphi_{rs}(x, z) = \sin^2\frac{\pi x}{L} e^{-rx/L} z^{s-1} \tag{7c}$$

It is noted that the shape functions in Eqs. (7) satisfy kinetic boundary conditions of the beams (S-S: siply supported beams, C-F: clamped-free beams, C-C: clamped-clamped beans). The characteristic equations of the beam can be obtained by substituting Eqs. (6) into Eq. (5) and using Lagrange's equations:

$$\frac{\partial \Pi}{\partial q_{rs}} = 0 \tag{8}$$

where $q_{rs} = (u_{rs}, w_{rs})$ are displacement vector of the beam. The characteristic equations of the beam are obtained as follows:

$$\left[\begin{array}{cc} \mathbf{K}^{11} & \mathbf{K}^{12} \\ {}^T\mathbf{K}^{12} & \mathbf{K}^{22} \end{array} \right] \left\{ \begin{array}{c} \mathbf{u} \\ \mathbf{w} \end{array} \right\} = \left\{ \begin{array}{c} \mathbf{0} \\ \mathbf{F} \end{array} \right\} \tag{9}$$

where the components of stiffness matrix $\mathbf{K}$ and load vector

F are defined as follows:

$$K_{rspq}^{11} = \int_0^L \int_{-h/2}^{h/2} \bar{\bar{C}}_{11} \frac{\partial \psi_{rs}}{\partial x} \frac{\partial \psi_{pq}}{\partial x} \, bdxdz$$

$$+ \int_0^L \int_{-h/2}^{h/2} \bar{\bar{C}}_{55} \frac{\partial \psi_{rs}}{\partial z} \frac{\partial \psi_{pq}}{\partial z} \, bdxdz,$$

$$K_{rspq}^{12} = \int_0^L \int_{-h/2}^{h/2} \bar{\bar{C}}_{13} \frac{\partial \psi_{rs}}{\partial x} \frac{\partial \varphi_{pq}}{\partial z} \, bdxdz$$

$$+ \int_0^L \int_{-h/2}^{h/2} \bar{\bar{C}}_{55} \frac{\partial \psi_{rs}}{\partial z} \frac{\partial \varphi_{pq}}{\partial x} \, bdxdz,$$

$$K_{rspq}^{22} = \int_0^L \int_{-h/2}^{h/2} \bar{\bar{C}}_{33} \frac{\partial \varphi_{rs}}{\partial z} \frac{\partial \varphi_{pq}}{\partial z} \, bdxdz$$

$$+ \int_0^L \int_{-h/2}^{h/2} \bar{\bar{C}}_{55} \frac{\partial \varphi_{rs}}{\partial x} \frac{\partial \varphi_{pq}}{\partial x} \, bdxdz,$$

$$F_{rs} = \int_0^L q\varphi_{rs} \, dx \tag{10}$$

III. NUMERICAL EXAMPLES

A range of numerical examples are performed in this section to verify the efficiency of the present theory with different boundary conditions. The laminated composite beam is subjected to a uniformly distributed load applied on the bottom surface and in the $z-$direction of the beam. Laminates are assumed to have equal thicknesses and are made of the same orthotropic materials whose properties are given as follows: material I ($E_1/E_2 = 40$, $E_2 = E_3$, $G_{12} = G_{13} = 0.6E_2$, $G_{23} = 0.5E_2$, $\nu_{12} = \nu_{13} = \nu_{23} = 0.25$), material II ($E_1/E_2 = 25$, $E_2 = E_3$, $G_{12} = G_{13} = 0.5E_2$, $G_{23} = 0.2E_2$, $\nu_{12} = \nu_{13} = \nu_{23} = 0.25$). Except special mentions, for convenience, the following nondimensional parameters are used in numerical examples:

$$\bar{w} = \frac{100wE_2bh^3}{qL^4}, \bar{\sigma}_x = \frac{bh^2}{qL^2}\sigma_x\left(\frac{L}{2}, \frac{h}{2}\right)$$

$$\bar{\sigma}_z = \frac{b}{q}\sigma_z\left(\frac{L}{2}, \frac{h}{2}\right), \bar{\sigma}_{xz} = \frac{bh}{qL}\sigma_{xz}(0,0) \tag{11}$$

In order to verify the convergence of solution field, Table I presents variations of non-dimensional mid-span transverse displacement with respect to the number of series in $x-$direction (R) and $z-$direction (S) of $0^o/90^o/0^o$ symmetric laminated composite beams. The results are calculated with with $L/h = 5$, Material I and $E_1/E_2 = 40$ for S-S, C-F and C-C boundary conditions. It can be seen that the responses converge quickly in $x-$direction and number of series in this direction $R = 10$ can be the point of convergence of the displacement for the boundary conditions, whereas the beam appears softer and converges with an increase of the number of series in z-direction. As an example for further verification, $R = 10$ and $S = 4$ will be used in the following computations.

Static responses of cross-ply laminated composite beams is investigated in Tables II and III. The nondimensional transverse displacements at $x = L/2$ are calculated for $0^o/90^o/0^o$ symmetric and $0^o/90^o$ un-symmetric composite beams with different boundary conditions and span-to-thickness ratios

TABLE I
CONVERGENCE STUDIES FOR NORMALIZED MID-SPAN TRANSVERSE DISPLACEMENT OF $0^o/90^o/0^o$ LAMINATED COMPOSITE BEAMS ($L/h = 5$, MATERIAL I, $E_1/E_2 = 40$).

BC	S	R					
		2	4	6	8	10	12
S-S	1	0.9050	0.8794	0.8821	0.8827	0.8825	0.8826
	2	1.2946	1.2836	1.2867	1.2873	1.2871	1.2872
	3	1.2852	1.2765	1.2790	1.2793	1.2791	1.2793
	4	1.4654	1.4568	1.4594	1.4596	1.4594	1.4595
	5	1.4644	1.4559	1.4586	1.4587	1.4585	1.4586
	6	1.4647	1.4555	1.4582	1.4584	1.4581	1.4582
	7	1.4648	1.4556	1.4582	1.4584	1.4582	1.4583
C-F	1	2.2812	2.4497	2.5823	2.5810	2.5908	2.6161
	2	3.5129	3.8151	3.9580	3.9567	3.9663	3.9729
	3	3.5036	3.8114	3.9529	3.9528	3.9626	3.9693
	4	3.9105	4.2195	4.3625	4.3616	4.3713	4.3778
	5	3.9102	4.2183	4.3618	4.3620	4.3715	4.3777
	6	3.9163	4.2293	4.3739	4.3740	4.3833	4.3897
	7	3.9166	4.2295	4.3740	4.3741	4.3834	4.3897
C-C	1	0.6891	0.7536	0.8154	0.8482	0.8468	0.8469
	2	0.7495	0.8344	0.8962	0.9292	0.9278	0.9278
	3	0.7403	0.8287	0.8896	0.9222	0.9207	0.9207
	4	0.8256	0.9306	0.9919	1.0251	1.0235	1.0238
	5	0.8251	0.9294	0.9913	1.0243	1.0227	1.0235
	6	0.8306	0.9351	0.9970	1.0308	1.0285	1.0292
	7	0.8309	0.9353	0.9972	1.0309	1.0287	1.0293

TABLE II
NONDIMENSIONAL MID-SPAN DISPLACEMENTS OF $0^o/90^o/0^o$ AND $0^o/90^o$ LAMINATED COMPOSITE BEAMS (MATERIAL II)

BC	Theory	$0^o/90^o/0^o$			$0^o/90^o$		
		$L/h=5$	10	50	$L/h=5$	10	50
S-S	HSBT [22]	2.414	1.098	0.666	4.785	3.697	3.345
	HSBT [6]	2.412	1.096	0.666	4.777	3.688	3.336
	HSBT [7]	2.398	1.090	0.661	4.750	3.668	3.318
	Quasi-3D [22]	2.405	1.097	0.666	4.764	3.694	3.345
	Quasi-3D [17]	2.405	1.097	0.666	4.828	3.763	3.415
	Quasi-3D [21]	-	1.097	-	-	3.731	-
	Present	2.418	1.105	0.666	4.918	3.730	3.346
C-F	HSBT [22]	6.830	3.461	2.257	15.308	12.371	11.365
	HSBT [6]	6.824	3.455	2.251	15.279	12.343	11.337
	HSBT [7]	6.836	3.466	2.262	15.334	12.398	11.392
	Quasi-3D [22]	6.844	3.451	2.256	15.260	12.339	11.343
	Quasi-3D [21]	-	3.459	-	-	12.475	-
	Present	7.077	3.496	2.257	15.889	12.452	11.333
C-C	HSBT [22]	1.538	0.532	0.147	1.924	1.007	0.680
	HSBT [6]	1.537	0.532	0.147	1.922	1.005	0.679
	Quasi-3D [22]	1.543	0.532	0.147	1.916	1.005	0.679
	Quasi-3D [21]	-	0.532	-	-	1.010	-
	Present	1.629	0.540	0.147	2.150	1.041	0.677

TABLE III
NONDIMENSIONAL STRESSES OF $0^o/90^o/0^o$ AND $0^o/90^o$ LAMINATED COMPOSITE BEAMS (S-S, MATERIAL II)

Stress	Theory	$0^o/90^o/0^o$			$0^o/90^o$		
		$L/h=5$	10	50	$L/h=5$	10	50
$\bar{\sigma}_x$	HSBT [22]	1.0669	0.8500	0.8705	0.2361	0.2342	0.2336
	HSBT [42]	1.0670	0.8503	-	0.2361	0.2342	-
	HSBT [17]	1.0669	0.8500	0.7805	0.2362	0.2343	0.2336
	Quasi-3D [22]	1.0732	0.8504	0.7806	0.2380	0.2346	0.2336
	Quasi-3D [17]	1.0732	0.8506	0.7806	0.2276	0.2246	0.2236
	Quasi-3D [21]	-	0.8501	-	-	0.2227	-
	Present	1.1820	0.8668	0.7796	0.2564	0.2392	0.2335
$\bar{\sigma}_{xz}$	HSBT [22]	0.4057	0.4311	0.4523	0.9205	0.9565	0.9878
	HSBT [42]	0.4057	0.4311	-	0.9187	0.9484	-
	HSBT [17]	0.4057	0.4311	0.4514	0.9211	0.9572	0.9860
	Quasi-3D [22]	0.4013	0.4286	0.4521	0.9052	0.9476	0.9869
	Quasi-3D [17]	0.4013	0.4289	0.4509	0.9038	0.9469	0.9814
	Quasi-3D [21]	-	-	-	-	0.9503	-
	Present	0.4182	0.4613	0.4946	0.8068	0.8558	0.8869
$\bar{\sigma}_z$	Quasi-3D [22]	0.1833	0.1787	0.1804	0.2966	0.2911	0.3046
	Quasi-3D [17]	0.1833	0.1803	0.1804	0.2988	0.2982	0.2983
	Present	0.1262	0.1117	0.0880	0.0550	0.0683	0.0122

TABLE IV

NONDIMENSIONAL MID-SPAN DISPLACEMENTS OF $0^o/\theta/0^o$ LAMINATED
COMPOSITE BEAMS (MATERIAL II)

BC	Theory	Fiber angle θ						
		0°	15°	30°	45°	60°	75°	90°
S-S	Quasi-3D [22]	1.7930	1.8626	2.0140	2.1762	2.3030	2.3796	2.4049
	Quasi-3D [43]	1.7930	1.8626	2.0140	2.1762	2.3030	2.3796	2.4049
	Present	1.7933	1.8622	2.0119	2.1767	2.3091	2.3908	2.4180
C-F	Quasi-3D [22]	5.2683	5.4840	5.8705	6.2780	6.5930	6.7820	6.8442
	Quasi-3D [43]	5.2774	5.4898	5.8804	6.2879	6.6029	6.7919	6.8541
	Present	5.4658	5.6682	6.0602	6.4790	6.8093	7.0103	7.0769
C-C	Quasi-3D [22]	1.0866	1.1485	1.2616	1.3801	1.4711	1.5253	1.5431
	Quasi-3D [43]	1.0998	1.1537	1.2670	1.3856	1.4766	1.5309	1.5487
	Present	1.1842	1.2325	1.3446	1.4638	1.5559	1.6111	1.6293

TABLE V

NONDIMENSIONAL MID-SPAN DISPLACEMENTS OF $0^o/\theta/0^o$ LAMINATED
COMPOSITE BEAMS (MATERIAL II)

BC	Theory	Fiber angle θ						
		0°	15°	30°	45°	60°	75°	90°
S-S	Quasi-3D [22]	0.6370	0.6554	0.6608	0.6634	0.6650	0.6658	0.6661
	Quasi-3D [43]	0.6370	0.6554	0.6608	0.6634	0.6650	0.6658	0.6661
	Present	0.6369	0.6554	0.6608	0.6635	0.6652	0.6662	0.6665
C-F	Quasi-3D [22]	2.1599	2.2225	2.2402	2.2480	2.2529	2.2554	2.2562
	Quasi-3D [43]	2.1602	2.2228	2.2405	2.2483	2.2531	2.2557	2.2565
	Present	2.1593	2.2218	2.2396	2.2477	2.2528	2.2557	2.2566
C-C	Quasi-3D [22]	0.1367	0.1408	0.1431	0.1449	0.1462	0.1470	0.1473
	Quasi-3D [43]	0.1367	0.1408	0.1431	0.1449	0.1462	0.1470	0.1472
	Present	0.1362	0.1403	0.1425	0.1444	0.1458	0.1466	0.1469

$L/h=5$ and 50. The results are examined with earlier those derived from the HSBTs (Nguyen et al. [22], Khdeir and Reddy [6], Murthy et al. [7]), Quasi-3Ds (Nguyen et al. [22], Mantari and Canales [21], Zenkour [17]). It can be seen that there are differences of the transverse displacements between the present model and those from the HSBTs and Quasi-3Ds for the thickness beam ($L/h = 5$), however the theories are similar with an increase of the span-to-thickness ratio. It can be explained by the fact that with an increase of L/h, the transverse deformation effects become smaller and the theories converge to the conventional ones. Moreover, it is interesting to observe that the present beam model clearly predicts lower stiffness than the previous ones for symmetric and un-symmetric laminated composite beams under all boundary conditions. Moreover, the nondimensional axial, transverse shear and transverse normal stresses of symmetric and unsymmetric cross-ply composite beams with S-S boundary condition are reported in Table III and compared with other works based on the HSBTs and Quasi-3Ds. In comparison, the effect of transverse normal and transverse strains are again found for the normalized axial stress $\bar{\sigma}_x$. For the transverse normal stress $\bar{\sigma}_z$ and transverse shear stress $\bar{\sigma}_{xz}$, there exist deviations of the present theory and other one, especially for transverse normal stress. However, as expected the present solution tends to approach to the free-traction condition on the top surface of the beams.

As a mean to study effects of transverse normal and shear strains on the displacement and stresses further, Tables IV and V introduce variations of the nondimensional center transverse displacement with respect to the boundary conditions, span-to-thickness ratio and different fiber angles of $0^o/\theta^o/0^o$ and

$0^o/\theta^o$ laminated composite beams. The results are compared to those obtained from Quasi-3Ds of Nguyen et al. [22] and Vo et al. [43]. Considerable differences between the present model and Quasi-3D ones are again observed for thick laminated composite beams ($L/h = 5$) and no significant deviations are found between the theories for thin beams ($L/h = 50$). Moreover, the increase of fiber angles makes the beam softer and leads to the increase of the transverse displacement.

IV. CONCLUSIONS

The authors proposed a new two-unknown model for static analysis of laminated composite beams. The axial and transverse displacements of the beam are expanded in a hybrid form under polynomial and trigonometric series. Lagrange's equations are used to derive characteristic equations of the beams. Numerical results for laminated composite beams with different boundary conditions are compared with previous studies and to investigate the effects of length-to-depth ratio, fibre angles and material anisotropy on the deflection and stresses of laminated composite beams. The obtained results showed that the proposed beam model is found to simple and efficient in predicting bending responses of laminated composite beams with various boundary conditions.

REFERENCES

[1] M. KOMIJANI, J. N. REDDY, M. R. ESLAMI, M. BATENI, An analytical approach for thermal stability analysis of two-layer timoshenko beams, International Journal of Structural Stability and Dynamics 13 (08) (2013) 1350036.

[2] K. Chandrashekhara, K. Krishnamurthy, S. Roy, Free vibration of composite beams including rotary inertia and shear deformation, Composite Structures 14 (4) (1990) 269 – 279.

[3] C. Santiuste, S. Snchez-Sez, E. Barbero, Dynamic analysis of bending-torsion coupled composite beams using the flexibility influence function method, International Journal of Mechanical Sciences 50 (12) (2008) 1611 – 1618.

[4] T.-K. Nguyen, T. P. Vo, H.-T. Thai, Static and free vibration of axially loaded functionally graded beams based on the first-order shear deformation theory, Composites Part B: Engineering 55 (0) (2013) 147 – 157.

[5] T.-K. Nguyen, B.-D. Nguyen, T. P. Vo, H.-T. Thai, A novel unified model for laminated composite beams, Composite Structures 238 (2020) 111943.

[6] A. Khdeir, J. Reddy, An exact solution for the bending of thin and thick cross-ply laminated beams, Composite Structures 37 (2) (1997) 195 – 203.

[7] M. Murthy, D. R. Mahapatra, K. Badarinarayana, S. Gopalakrishnan, A refined higher order finite element for asymmetric composite beams, Composite Structures 67 (1) (2005) 27 – 35.

[8] M. Aydogdu, Buckling analysis of cross-ply laminated beams with general boundary conditions by ritz method, Composites Science and Technology 66 (10) (2006) 1248 – 1255.

[9] M. Aydogdu, Free vibration analysis of angle-ply laminated beams with general boundary conditions, Journal of Reinforced Plastics and Composites 25 (15) (2006) 1571–1583.

[10] L. Jun, L. Xiaobin, H. Hongxing, Free vibration analysis of third-order shear deformable composite beams using dynamic stiffness method, Archive of Applied Mechanics 79 (12) (2009) 1083–1098.

[11] M. Simsek, Fundamental frequency analysis of functionally graded beams by using different higher-order beam theories, Nuclear Engineering and Design 240 (4) (2010) 697 – 705.

[12] L. Jun, H. Hongxing, Free vibration analyses of axially loaded laminated composite beams based on higher-order shear deformation theory, Meccanica 46 (6) (2011) 1299–1317.

[13] J. Li, Z. Wu, X. Kong, X. Li, W. Wu, Comparison of various shear deformation theories for free vibration of laminated composite beams with general lay-ups, Composite Structures 108 (2014) 767 – 778.

[14] T. Vo, H.-T. Thai, T.-K. Nguyen, F. Inam, Static and vibration analysis of functionally graded beams using refined shear deformation theory, Meccanica 49 (1) (2014) 155–168.

[15] T.-K. Nguyen, N.-D. Nguyen, T. P. Vo, H.-T. Thai, Trigonometric-series solution for analysis of laminated composite beams, Composite Structures 160 (2017) 142 – 151.

[16] H. MATSUNAGA, Vibration and buckling of multilayered composite beams according to higher order deformation theories, Journal of Sound and Vibration 246 (1) (2001) 47 – 62.

[17] A. M. Zenkour, Transverse shear and normal deformation theory for bending analysis of laminated and sandwich elastic beams, Mechanics of Composite Materials and Structures 6 (3) (1999) 267–283.

[18] W. Chen, C. Lv, Z. Bian, Free vibration analysis of generally laminated beams via state-space-based differential quadrature, Composite Structures 63 (34) (2004) 417 – 425.

[19] T. P. Vo, H.-T. Thai, T.-K. Nguyen, F. Inam, J. Lee, A quasi-3d theory for vibration and buckling of functionally graded sandwich beams, Composite Structures 119 (0) (2015) 1 – 12.

[20] J. Mantari, F. Canales, Free vibration and buckling of laminated beams via hybrid ritz solution for various penalized boundary conditions, Composite Structures 152 (2016) 306 – 315.

[21] J. Mantari, F. Canales, Finite element formulation of laminated beams with capability to model the thickness expansion, Composites Part B: Engineering 101 (2016) 107 – 115.

[22] N.-D. Nguyen, T.-K. Nguyen, T. P. Vo, H.-T. Thai, Ritz-based analytical solutions for bending, buckling and vibration behavior of laminated composite beams, International Journal of Structural Stability and Dynamics 18 (11) (2018) 1850130.

[23] S. Ambartsumian, On the theory of bending of anisotropic plates and shallow shells, Journal of Applied Mathematics and Mechanics 24 (2) (1960) 500 – 514.

[24] E. Reissner, On transverse bending of plates, including the effect of transverse shear deformation, International Journal of Solids and Structures 11 (5) (1975) 569 – 573.

[25] M. Levinson, An accurate, simple theory of the statics and dynamics of elastic plates, Mechanics Research Communications 7 (6) (1980) 343 – 350.

[26] J. N. Reddy, A simple higher-order theory for laminated composite plates, Journal of Applied Mechanics 51 (1984) 745–752.

[27] T. N. Nguyen, C. H. Thai, H. Nguyen-Xuan, On the general framework of high order shear deformation theories for laminated composite plate structures: A novel unified approach, International Journal of Mechanical Sciences 110 (2016) 242 – 255.

[28] M. Murthy, An improved transverse shear deformation theory for laminated anisotropic plates, National Aeronautics and Space Administration, Washington DC, 1981.

[29] M. STEIN, Nonlinear theory for plates and shells including the effects of transverse shearing, AIAA Journal 24 (9) (1986) 1537–1544.

[30] M. Touratier, An efficient standard plate theory, International Journal of Engineering Science 29 (8) (1991) 901 – 916.

[31] H. Arya, R. Shimpi, N. Naik, A zigzag model for laminated composite beams, Composite Structures 56 (1) (2002) 21 – 24.

[32] C. H. Thai, A. Ferreira, S. Bordas, T. Rabczuk, H. Nguyen-Xuan, Isogeometric analysis of laminated composite and sandwich plates using a new inverse trigonometric shear deformation theory, European Journal of Mechanics - A/Solids 43 (2014) 89 – 108.

[33] J. Mantari, A. Oktem, C. G. Soares, A new trigonometric shear deformation theory for isotropic, laminated composite and sandwich plates, International Journal of Solids and Structures 49 (1) (2012) 43 – 53.

[34] V.-H. Nguyen, T.-K. Nguyen, H.-T. Thai, T. P. Vo, A new inverse trigonometric shear deformation theory for isotropic and functionally graded sandwich plates, Composites Part B: Engineering 66 (0) (2014) 233 – 246.

[35] M. Karama, K. Afaq, S. Mistou, Mechanical behaviour of laminated composite beam by the new multi-layered laminated composite structures model with transverse shear stress continuity, International Journal of Solids and Structures 40 (6) (2003) 1525 – 1546.

[36] M. Aydogdu, A new shear deformation theory for laminated composite plates, Composite Structures 89 (1) (2009) 94 – 101.

[37] K. Soldatos, A transverse shear deformation theory for homogeneous monoclinic plates, Acta Mechanica 94 (3-4) (1992) 195–220.

[38] N. E. Meiche, A. Tounsi, N. Ziane, I. Mechab, E. A. Adda.Bedia, A new hyperbolic shear deformation theory for buckling and vibration of functionally graded sandwich plate, International Journal of Mechanical Sciences 53 (4) (2011) 237 – 247.

[39] S. S. Akavci, A. H. Tanrikulu, Buckling and free vibration analyses of laminated composite plates by using two new hyperbolic shear-deformation theories, Mechanics of Composite Materials 44 (2) (2008) 145.

[40] J. Mantari, A. Oktem, C. G. Soares, A new higher order shear deformation theory for sandwich and composite laminated plates, Composites Part B: Engineering 43 (3) (2012) 1489 – 1499.

[41] C. H. Thai, S. Kulasegaram, L. V. Tran, H. Nguyen-Xuan, Generalized shear deformation theory for functionally graded isotropic and sandwich plates based on isogeometric approach, Computers & Structures 141 (2014) 94 – 112.

[42] T. P. Vo, H.-T. Thai, Static behavior of composite beams using various refined shear deformation theories, Composite Structures 94 (8) (2012) 2513 – 2522.

[43] T. P. Vo, H.-T. Thai, T.-K. Nguyen, D. Lanc, A. Karamanli, Flexural analysis of laminated composite and sandwich beams using a four-unknown shear and normal deformation theory, Composite Structures 176 (2017) 388 – 397.

Metadata of the chapter that will be visualized in SpringerLink

Book Title	ICSCEA 2021	
Series Title		
Chapter Title	Stochastic Vibration Responses of Laminated Composite Beams Based on a Quasi-3D Theory	
Copyright Year	2023	
Copyright HolderName	The Author(s), under exclusive license to Springer Nature Singapore Pte Ltd.	

Corresponding Author	Family Name	**Bui**
	Particle	
	Given Name	**Xuan-Bach**
	Prefix	
	Suffix	
	Role	
	Division	Faculty of Civil Engineering
	Organization	Ho Chi Minh City University of Technology and Education
	Address	Ho Chi Minh City, Vietnam
	Email	bachbx@hcmut.edu.vn
Author	Family Name	**Nguyen**
	Particle	
	Given Name	**Trung-Kien**
	Prefix	
	Suffix	
	Role	
	Division	Faculty of Civil Engineering
	Organization	Ho Chi Minh City University of Technology and Education
	Address	Ho Chi Minh City, Vietnam
	Email	
Author	Family Name	**Nguyen**
	Particle	
	Given Name	**T. Truong-Phong**
	Prefix	
	Suffix	
	Role	
	Division	Faculty of Civil Engineering
	Organization	Ho Chi Minh City University of Technology and Education
	Address	Ho Chi Minh City, Vietnam
	Email	
Author	Family Name	**Nguyen**
	Particle	
	Given Name	**Van-Trien**
	Prefix	
	Suffix	

Role	
Division	Faculty of Civil Engineering
Organization	Ho Chi Minh City University of Technology and Education
Address	Ho Chi Minh City, Vietnam
Email	

Abstract	Stochastic vibration responses of laminated composite beams based on a quasi-3D shear deformation theory are proposed in this paper. The mechanical properties of constituent materials are assumed to be uncertain, thus the free vibration responses can be modeled as random variables. A very large number of simulations is performed for propagating the overall uncertainty in the material properties to vibration behaviours by Monte Carlo simulation method. The higher-order shear deformation beam theory with nonlinear variations of both axial and transverse displacements is used and a trigonometric-series solution is developed to solve characteristic equations of motions. Novel numerical results are obtained to investigate the effects of uncertain material properties on the natural frequencies of the laminated composite beams.

Keywords (separated by '-')	Stochastic responses - Laminated composite beams - Vibration

Stochastic Vibration Responses of Laminated Composite Beams Based on a Quasi-3D Theory

Xuan-Bach Bui, Trung-Kien Nguyen, T. Truong-Phong Nguyen, and Van-Trien Nguyen

Abstract Stochastic vibration responses of laminated composite beams based on a quasi-3D shear deformation theory are proposed in this paper. The mechanical properties of constituent materials are assumed to be uncertain, thus the free vibration responses can be modeled as random variables. A very large number of simulations is performed for propagating the overall uncertainty in the material properties to vibration behaviours by Monte Carlo simulation method. The higher-order shear deformation beam theory with nonlinear variations of both axial and transverse displacements is used and a trigonometric-series solution is developed to solve characteristic equations of motions. Novel numerical results are obtained to investigate the effects of uncertain material properties on the natural frequencies of the laminated composite beams.

Keywords Stochastic responses · Laminated composite beams · Vibration

1 Introduction

Thanks to the performance in high strength- and stiffness-to-weight ratios, multi-layered composite materials under beam structures have been used in many engineering fields such as mechanical engineering, aerospace engineering, construction, etc. Practically however, the mechanical performance of composite materials can be inconsistent, that probably results in the fabrication process or other unexpected factors. It is therefore necessary to account for these uncertainties in the behaviour analysis of laminated composite beams. Large applications of laminated composite beams led to the development of computational theories and methods with different approaches, only some representative references are herein cited [1–9]. For stochastic analysis, several methods have been used to model and propagate the uncertainty in stochastic computational simulations. Monte Carlo simulation method is known as the most straightforward and intuitive one which simply run the computational

X.-B. Bui (✉) · T.-K. Nguyen · T. T.-P. Nguyen · V.-T. Nguyen
Faculty of Civil Engineering, Ho Chi Minh City University of Technology and Education, Ho Chi Minh City, Vietnam
e-mail: bachbx@hcmut.edu.vn

26 model as many times as the accuracy required [10–12]. Nonetheless, when the phys-
27 ical model is complicated, the Monte Carlo method demands much computing time
28 and infeasible to obtain desired sample outputs. In other word, stochastic numerical
29 methods based on polynomial chaos expansion that speeds up the computing process
30 while maintaining the accuracy have attracted considerable attention in predicting
31 stochastic responses of laminated composite plates [13–16]. Though the polynomial
32 chaos expansion requires a priori less computational cost, this approach appears to
33 be complicated to implement and program. A literature review showed that there
34 were still gaps in current research on stochastic behaviours of laminated composite
35 beams and therefore, it motivates the investigation in this paper.

36   The objective of this paper is to propose stochastic vibration behaviours of lami-
37 nated composite beams considering uncertainties in the material properties. It is
38 based on a higher-order shear deformation theory which accounts for a higher-order
39 variation of both axial and transverse displacements. The uncertainty of material
40 properties are described through a probability distribution. This uncertainty will be
41 propagated through the Ritz-method-based quasi-3D beam model to obtain the statis-
42 tics of the outputs. The Monte Carlo simulation method will be used to propagate
43 the uncertainty of material properties. Numerical results are presented to investigate
44 the effects of uncertain material properties on the natural frequencies of laminated
45 composite beams.

46 2 Theoretical Formulation

47 Consider a laminated composite beam with length L and rectangular cross-section
48 $b \times h$ as shown in Fig. 1. It is made of n plies of orthotropic materials in different
49 fibre angles with respect to the x-axis.

50 2.1 Displacements, Strains and Stresses

51 The displacement field of the present theory is given by:

$$u(x, z, t) = u_0(x, t) - z w_{0,x} + f(z)\theta_0(x, t) \tag{1a}$$

$$w(x, z, t) = w_0(x, t) + g(z)w_{z0}(x, t) \tag{1b}$$

56 where u_0, w_0, w_{z0}, θ_0 are four variables to be determined; $g(z) = f'(z)$ where $f(z) =$
57 $\frac{5z}{4} - \frac{5z^3}{3h^2}$ is the nonlinear shear function satisfying the condition $f'(z = \pm h/2) = 0$;
58 the comma in subscript is used to indicate the differentiation of coordinate that
59 follows.

60   The non-zero strains related to the displacements in Eq. (1) are given by:
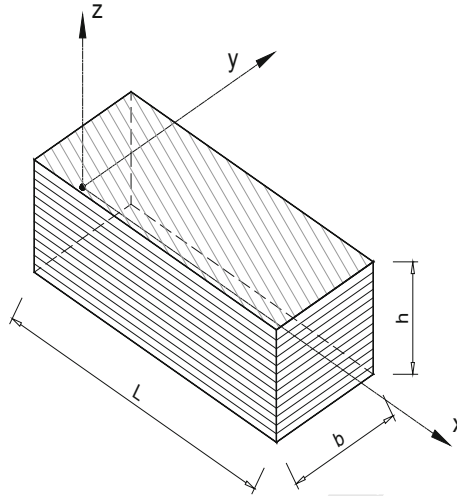
Fig. 1 Geometry of a laminated composite beam

$$\varepsilon_x(x, z) = u_{,x} = u_{0,x} - zw_{0,xx} + f\theta_{0,x} \tag{2a}$$

$$\varepsilon_z(x, z) = g''(z)w_{0z} \tag{2b}$$

$$\gamma_{xz}(x, z) = g(z)\left(w_{z0,x} + \theta_0\right) \tag{2c}$$

Moreover, the assumption of a plane stress state in (x, z)-plan leads to the stress–strain relation as follows:

$$\begin{Bmatrix} \sigma_x \\ \sigma_z \\ \sigma_{xz} \end{Bmatrix} = \begin{pmatrix} Q'_{11} & Q'_{13} & 0 \\ Q'_{13} & Q'_{33} & 0 \\ 0 & 0 & Q'_{55} \end{pmatrix} \begin{Bmatrix} \varepsilon_x \\ \varepsilon_z \\ \gamma_{xz} \end{Bmatrix} \tag{3}$$

where $Q'_{11}, Q'_{13}, Q'_{33}, Q'_{55}$ are reduced stiffness constants of materials. These coefficients are related to the stiffness components of materials in global coordinates C'_{ij} as follows [9]:

$$Q'_{11} = C'_{11} + \frac{C'^2_{16}C'_{22} - 2C'_{12}C'_{16}C'_{26} + C'^2_{12}C'_{66}}{C'^2_{26} - C'_{22}C'_{66}} \tag{4a}$$

$$Q'_{13} = C'_{13} + \frac{C'_{16}C'_{22}C'_{36} + C'_{12}C'_{23}C'_{66} - C'_{16}C'_{23}C'_{26} - C'_{12}C'_{26}C'_{36}}{C'^2_{26} - C'_{22}C'_{66}} \tag{4b}$$

$$Q'_{33} = C'_{33} + \frac{C'^2_{36}C'_{22} - 2C'_{23}C'_{26}C'_{36} + C'^2_{23}C'_{66}}{C'^2_{26} - C'_{22}C'_{66}} \tag{4c}$$

80

$$Q'_{55} = C'_{55} - \frac{C'^{2}_{45}}{C'_{44}} \tag{4d}$$

2.2 Energy Formulation

The total energy of the laminated composite beams is composed of the strain energy Π_S and kinetic energy Π_K. The strain energy of the laminated composite beams is given by:

$$\Pi_S = \frac{1}{2} \int_V (\sigma_x \varepsilon_x + \sigma_z \varepsilon_z + \sigma_{xz} \gamma_{xz}) dV$$

$$= \frac{1}{2} \int_0^L \Big[A_{11} u_{0,x}^2 + D_{11} w_{0,xx}^2 + H_{11}^s \theta_{0,x}^2 - 2B_{11} u_{0,x} w_{0,xx} + 2B_{11}^s u_{0,x} \theta_{0,x} - 2D_{11}^s w_{0,xx} \theta_{0,x}$$

$$+ N_{33}^s w_{0z}^2 + 2T_{13}^s u_{0,x} w_{z0} - 2M_{13}^s w_{0,xx} w_{z0} + 2E_{13}^s \theta_{0,x} w_{z0} + A_{55}^s (\theta_0 + w_{z0,x})^2 \Big] dx \tag{5}$$

where the stiffness components of laminated composite beams are defined as follows:

$$\big(A_{ij}, B_{ij}, D_{ij}, B_{ij}^s, D_{ij}^s, H_{ij}^s\big) = \int_{-h/2}^{h/2} (1, z, z^2, f, zf, f^2) Q'_{ij} b dz \tag{6a}$$

$$\big(A_{ij}^s, E_{ij}^s, T_{ij}^s, M_{ij}^s, N_{ij}^s\big) = \int_{-h/2}^{h/2} \big(g^2, fg_{,z}, g_{,z}, zg_{,z}, g_{,z}^2\big) Q'_{ij} b dz \tag{6b}$$

The kinetic energy of the laminated composite beams is given by:

$$\Pi_K = \frac{1}{2} \int_V \rho(z) \big(\dot{u}^2 + \dot{w}^2\big) dV$$

$$= \frac{1}{2} \int_0^L \Big[I_0 \dot{u}_0^2 + I_2 \dot{w}_{0,x}^2 + K_2 \dot{\theta}_0^2 - 2I_1 \dot{u}_0 \dot{w}_{0,x} + 2J_1 \dot{u}_0 \dot{\theta}_0 - 2J_2 \dot{w}_{0,x} \dot{\theta}_0 + I_0 \dot{w}_0^2 + 2L_1 \dot{w}_0 \dot{w}_{z0} + L_2 w_{z0}^2 \Big] dx$$

$$\tag{7}$$

where the superscript dot is used to indicate the differentiation of the variable with the time t; ρ is the mass density; $(I_0, I_1, I_2, J_1, J_2, K_2, L_1, L_2)$ are terms of inertia defined as follows:

$$(I_0, I_1, I_2, J_1, J_2, K_2, L_1, L_2) = \int\limits_{-h/2}^{h/2} \rho(1, z, z^2, f, zf, f^2, g, g^2) b\, dz \qquad (8)$$

By combining Eqs. (5) and (7), the total energy of the laminated composite beams is given by:

$$\Pi = \frac{1}{2} \int\limits_0^L \Big[A_{11} u_{0,x}^2 + D_{11} w_{0,xx}^2 + H_{11}^s \theta_{0,x}^2 - 2B_{11} u_{0,x} w_{0,xx} + 2B_{11}^s u_{0,x} \theta_{0,x} - 2D_{11}^s w_{0,xx}\theta_{0,x}$$

$$+ N_{33}^s w_{0z}^2 + 2T_{13}^s u_{0,x} w_{z0} - 2M_{13}^s w_{0,xx} w_{z0} + 2E_{13}^s \theta_{0,x} w_{z0} + A_{55}^s (\theta_0 + w_{z0,x})^2 \Big] dx$$

$$- \frac{1}{2} \int\limits_0^L \Big[I_0 \dot{u}_0^2 + I_2 \dot{w}_{0,x}^2 + K_2 \dot{\theta}_0^2 - 2I_1 \dot{u}_0 \dot{w}_{0,x} + 2J_1 \dot{u}_0 \dot{\theta}_0 - 2J_2 \dot{w}_{0,x}\dot{\theta}_0 + I_0 \dot{w}_0^2 + 2L_1 \dot{w}_0 \dot{w}_{z0} + L_2 w_{z0}^2 \Big] dx$$

$$(9)$$

2.3 Trigonometric-Series Solutions

The solution field u_0, w_0, θ_0, w_{z0} can be approximated under series of shape functions and associated variables as follows:

$$\{u_0(x, t), \theta_0(x, t)\} = \sum_{j=1}^m \psi_j(x)\{u_j(t), \theta_j(t)\} \qquad (10a)$$

$$\{w_0(x, t), w_{z0}(x, t)\} = \sum_{j=1}^m \varphi_j(x)\{w_j(t), w_{zj}(t)\} \qquad (10b)$$

where u_j, w_j, θ_j, w_{zj} are variables to be determined; $\psi_j(x)$, $\varphi_j(x)$ are shape functions. The approximations in Eq. (10) are known as Ritz's one in which it is noted that the accuracy of this approach depends on the construction of shape functions. These functions should be continuous, complete and orthogonal. In the present study, the functions of approximation $\psi_j(x)$, $\varphi_j(x)$ are selected under trigonometric ones that satisfy kinematic boundary conditions. Three typical boundary conditions (simply-supported: S-S, clamped-clamped: C-C, clamped-free: C-F) are considered as Table 1.

Substituting Eq. (10) into Eq. (9) and using Lagrange's equations lead to:

$$Kp + M\ddot{p} = F(t) \qquad (11)$$

where $p = \begin{bmatrix} u_0 & w_0 & w_{z0} & theta_0 \end{bmatrix}^T$; K and M are stiffness and mass matrix, respectively, which are given by:

Table 1 Kinematic boundary conditions and trigonometric shape functions

BCs	$x = 0$	$x = L$	$\psi_j(x)$	$\varphi_j(x)$
S-S	$w_0 = 0,\ w_{z0} = 0$	$w_0 = 0,\ w_{z0} = 0$	$\cos \frac{j\pi x}{L}$	$\sin \frac{j\pi x}{L}$
C-F	$u_0 = 0,\ w_0 = 0,\ w_{0,x} = 0, \theta_0 = 0,\ w_{z0} = 0$		$\sin \frac{(2j-1)\pi}{2L} x$	$1 - \cos \frac{(2j-1)\pi}{2L} x$
C-C	$u_0 = 0,\ w_0 = 0,\ w_{0,x} = 0, \theta_0 = 0,\ w_{z0} = 0$	$u_0 = 0,\ w_0 = 0,\ w_{0,x} = 0, \theta_0 = 0,\ w_{z0} = 0$	$\sin \frac{2j\pi x}{L}$	$\sin^2 \frac{j\pi x}{L}$

$$K = \begin{bmatrix} K^{11} & K^{12} & K^{13} & K^{14} \\ {}^{T}K^{12} & K^{22} & K^{23} & K^{24} \\ {}^{T}K^{13} & {}^{T}K^{23} & K^{33} & K^{34} \\ {}^{T}K^{14} & {}^{T}K^{24} & {}^{T}K^{34} & K^{44} \end{bmatrix}, \quad M = \begin{bmatrix} M^{11} & M^{12} & M^{13} & 0 \\ {}^{T}M^{12} & M^{22} & M^{23} & M^{24} \\ {}^{T}M^{13} & {}^{T}M^{23} & M^{33} & 0 \\ 0 & {}^{T}M^{24} & 0 & M^{44} \end{bmatrix} \tag{12}$$

The components of stiffness and mass matrix are determined as follows:

$$K_{ij}^{11} = A_{11} \int_0^L \psi_{i,x} \psi_{i,x} dx, \ K_{ij}^{12} = -B_{11} \int_0^L \psi_{i,x} \varphi_{i,xx} dx, \ K_{ij}^{13} = B_{11}^s \int_0^L \psi_{i,x} \psi_{j,x} dx, \ K_{ij}^{14} = T_{13}^s \int_0^L \psi_{i,x} \varphi_j dx \tag{13a}$$

$$K_{ij}^{22} = D_{11} \int_0^L \varphi_{i,xx} \varphi_{j,xx} dx, \ K_{ij}^{23} = -D_{11}^s \int_0^L \varphi_{i,xx} \psi_{j,x} dx, \ K_{ij}^{24} = -M_{13}^s \int_0^L \varphi_{i,xx} \varphi_j dx \tag{13b}$$

$$K_{ij}^{33} = H_{11}^s \int_0^L \psi_{i,x} \psi_{j,x} dx + A_{55}^s \int_0^L \psi_i \psi_j dx, \ K_{ij}^{34} = E_{13}^s \int_0^L \psi_{i,x} \varphi_j dx + A_{55}^s \int_0^L \psi_i \varphi_{j,x} dx \tag{13c}$$

$$K_{ij}^{44} = N_{33}^s \int_0^L \varphi_i \varphi_j dx + A_{55}^s \int_0^L \varphi_{i,x} \varphi_{j,x} dx \tag{13d}$$

$$M_{ij}^{11} = I_0 \int_0^L \psi_i \psi_j dx, \ M_{ij}^{12} = -I_1 \int_0^L \psi_i \varphi_{j,x} dx, \ M_{ij}^{13} = J_1 \int_0^L \psi_i \psi_j dx \tag{13e}$$

$$M_{ij}^{22} = I_0 \int_0^L \varphi_i \varphi_j dx + I_2 \int_0^L \varphi_{i,x} \varphi_{j,x} dx, \ M_{ij}^{23} = -J_2 \int_0^L \varphi_{i,x} \psi_j dx, \ M_{ij}^{24} = L_1 \int_0^L \varphi_i \varphi_j dx \tag{13f}$$

$$M_{ij}^{33} = K_2 \int_0^L \psi_i \psi_j dx, \ M_{ij}^{44} = L_2 \int_0^L \psi_i \psi_j dx \tag{13g}$$

It is worth noticing that the free vibration responses can be derived by expressing $p(t) = p e^{i\omega t}$ and solving the characteristic equation $(K - \omega^2 M) p = 0$ in which ω is natural frequencies of the laminated composite beams; $i^2 = -1$ is imaginary part.

2.4 Monte Carlo Simulation

The material properties of laminated composite beams are supposed to be random according to a required distribution. In order to propagate the variability in material properties to the vibration responses of laminated composite beams, Monte Carlo simulation method will be used. This technique requires a generation of random numbers set from material properties and then these are used to obtain the vibration responses and its statistics. The following statistics of the responses of the laminated composite beams are used for computations:

$$E[X] = \int_{-\infty}^{\infty} x f(x) dx \tag{14a}$$

$$SD = \sqrt{\sigma} = \sqrt{\frac{\sum_{i=1}^{n}(x_i - \mu)^2}{n-1}} \tag{14b}$$

where $E[X]$ is expectation of the variable set X; x is the value in the sample space; $f(x)$ is probability density function (PDF); σ is standard deviation of the set of random numbers; n is number of samples. In addition to the expectation and variance, higher-order statistics such as the skewness $\tilde{\mu}_3$ and kurtosis $Kurt$, confidence interval CI are also measured as follows:

$$\tilde{\mu}_3 = \frac{\sum_{i}^{N}(x_i - \mu)^3}{(n-1) \times \sigma^3} \tag{15a}$$

$$Kurt = \frac{E(x - \mu)^4}{\sigma^4} \tag{15b}$$

$$CI = \mu \pm z \frac{SD}{\sqrt{n}} \tag{15c}$$

where z is the required confidence interval (%).

3 Numerical Examples

A number of numerical examples are performed in this section to investigate the accuracy and efficiency of the present theory. The laminated composite beams are composed of orthotropic material layers of the same thickness. The means, standard-to-mean ratio (COV) and distribution of material properties are given in Table 2. The effects of material properties uncertainty on the vibration behaviours of laminated composite beams are observed with different lay-ups and boundary conditions.

As a first example, in order to study the convergence, laminated composite beams with mean material properties given in Table 2 are considered. The results are computed with three boundary conditions (BC) S-S, C-C and C-F, and different fiber orientations, [0°/90°], [0°/90°/0°], [45°/−45°] and [45°/−45°/45°]. The fundamental frequencies are reported in Table 3 for various values of number of series m. The results obtained from Table 3 show that the solutions converge quickly for all responses and boundary conditions, the number of series $m = 10$ can be considered as the convergence point for the natural frequencies of the laminated composite beams, therefore this value will be used for the sequel computations.

As a second example, in order to investigate stochastic responses of the laminated composite beams, Monte Carlo simulation method with number of samples $N_s = 10^5$

Table 2 Material properties and geometry of the laminated composite beams

Properties	Mean [9]	COV	Distribution
E_1 (GPa)	120	0.1	Lognormal
E_2 (GPa)	3	0.1	Lognormal
$G_{12} = G_{13}$ (GPa)	$0.6E_2$	0.1	Lognormal
G_{23} (GPa)	$0.5E_2$	0.1	Lognormal
ν_{12}	0.25	0.1	Lognormal
ρ (kg/m^2)	1500	0.1	Lognormal
L (m)	0.381	–	–
h (m)	0.1905	–	–
b (m)	0.0254	–	–

Table 3 Convergence of the fundamental frequencies (Hz)

BC	Lay-ups	m						
		2	4	6	8	10	12	14
S-S	0°/90°	213.754	213.754	213.754	213.754	213.754	213.754	213.754
	45°/−45°	102.389	102.389	102.389	102.389	102.389	102.389	102.389
	0°/90°/0°	482.307	482.307	482.307	482.307	482.307	482.307	482.307
	−45°/45°/−45°	102.389	102.389	102.389	102.389	102.389	102.389	102.389
C-C	0°/90°	469.254	465.780	464.802	464.361	464.124	463.986	463.900
	45°/−45°	231.998	230.455	229.993	229.764	229.625	229.532	229.467
	0°/90°/0°	900.487	885.486	880.776	878.679	877.582	876.941	876.535
	−45°/45°/−45°	231.998	230.455	229.993	229.764	229.625	229.532	229.467
C-F	0°/90°	77.200	76.927	76.848	76.811	76.790	76.776	76.766
	45°/−45°	36.969	36.767	36.699	36.665	36.644	36.630	36.620
	0°/90°/0°	180.377	179.600	179.375	179.272	179.215	179.179	179.156
	−45°/45°/−45°	36.969	36.767	36.699	36.665	36.644	36.630	36.620

is performed in which six parameters in Table 2 are randomly varied according to the lognormal distribution. It is noted that the lognormal distribution is chosen instead of normal distribution to avoid negative values in material property input. Besides, the coefficient $COV = 0.1$ is applied for all parameters. Table 4 presents four statistical moments of simulation outputs computed for laminated composite beams with different lay-ups and boundary conditions. The mean μ, standard deviation σ, skewness $\tilde{\mu}_3$ and kurtosis $Kurt$ are calculated with four layer-ups 0°/90°, 45°/−45°, 0°/90°/0°, −45°/45°/−45°, and three boundary conditions S-S, C-F and C-C. The means and deterministic values obtained from the present theory are compared to those of Nguyen et al. [9] based on a quasi-3D deterministic beam model. It can be seen that there are excellent agreements between the deterministic models, no significant differences of the means of fundamental frequencies and those of Nguyen

Table 4 Fundamental frequencies (Hz) of laminated composite beams with arbitrary lay-ups and boundary conditions

BC	Lay-ups	Present				Present (deterministic)	Nguyen [9]
		μ	σ	Kurtosis	Skewness		
S–S	0°/90°	214.300	13.538	3.054	0.193	213.754	213.116
	45°/−45°	102.468	6.293	3.036	0.170	102.389	–
	0°/90°/0°	483.159	31.689	3.060	0.184	482.307	482.295
	−45°/45°/−45°	102.472	6.320	3.064	0.174	102.389	–
C–C	0°/90°	465.298	28.570	3.056	0.169	464.124	462.889
	45°/−45°	229.812	14.113	3.040	0.167	229.625	–
	0°/90°/0°	878.536	51.876	3.046	0.174	877.582	876.952
	−45°/45°/−45°	229.722	14.075	3.029	0.168	229.625	–
C-F	0°/90°	77.006	4.877	3.040	0.195	76.790	76.562
	45°/−45°	36.665	2.262	3.077	0.199	36.644	–
	0°/90°/0°	179.557	12.256	3.082	0.199	179.215	179.177
	−45°/45°/−45°	36.670	2.254	3.041	0.184	36.644	–

et al. [9] are found. Moreover, it is observed that the ratios of standard deviation and mean is about 6%. The kurtosis values are slightly higher than 3, which indicates that the present distribution of responses has rather heavier tail and more outliers than the normal distribution. The positive skewness in Table 4 means the data is right-skewed which is a characteristic of lognormal distribution (Fig. 2).

AQ2

Furthermore, the effect of number of simulations on the accuracy of output distribution is demonstrated in Fig. 3. The curves are plotted for 0°/90°/0° laminated composite beams with the span-to-thickness ratio $L/h = 20$, C-C and C-F boundary conditions. The 80% and 99% confidence interval of the mean value of simulation
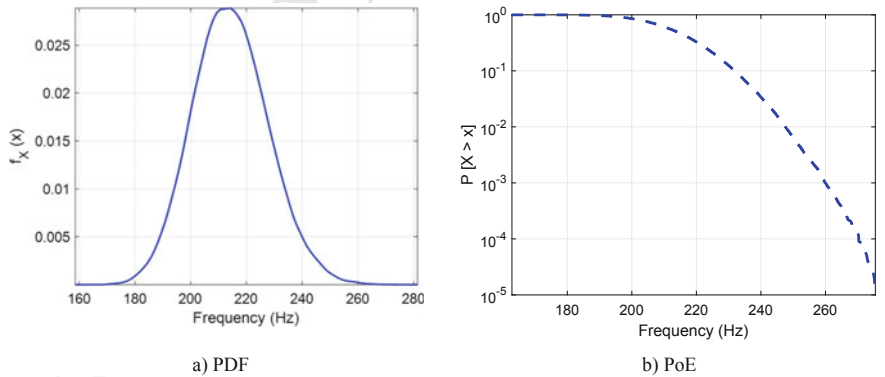

a) PDF   b) PoE

Fig. 2 Probability density function (PDF) and Probability of exceedance (PoE) of the fundamental frequency (Hz) for 0°/90° laminated composite beam ($L/h = 20$, S-S boundary condition)
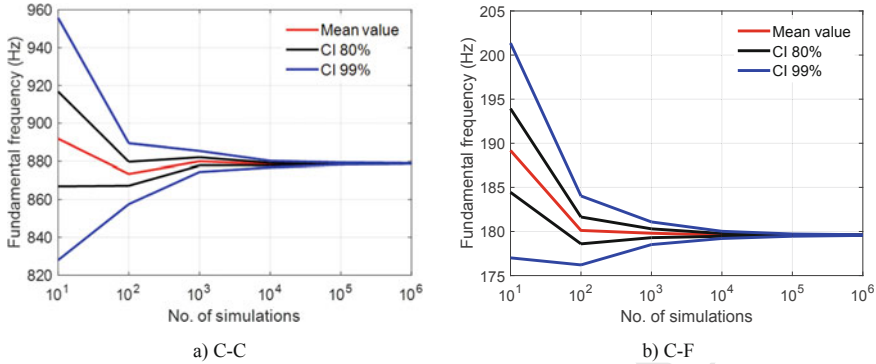
a) C-C   b) C-F

Fig. 3 Mean and confidence interval of the fundamental frequencies (Hz) of 0°/90°/0° laminated composite beam ($L/h = 20$, C-C and C-F boundary conditions)

outputs are shown for the number of simulations 10^1, 10^2, 10^3, 10^4, 10^5 and 10^6. It can be observed from these graphs that in the present beam model, the true value of mean fundamental frequencies can be achieved when the Monte Carlo simulation has 10^5 or more samples.

Figure 4 presents the probability of exceedance (PoE) of the fundamental frequencies for the composite beam with $-45°/45°/-45°$ ply composition and S-S boundary condition. In Fig. 4a, the PoE is plotted 10 times each of which has the number of samples $N_s = 10^5$. Noticingly, the tails of the plots past $P[X > x] = 10^{-3}$ have fluctuations. This is due to there are very few samples at the very small probability of occurrence. In Fig. 4b, the setup is similar to that of Fig. 4a but with the number of samples $N_s = 10^4$. The similar fluctuation is seen past the horizontal line where $P[X > x] = 10^{-2}$. Therefore, by plain observation, the outputs of Monte Carlo simulation is stable up to the point where $P[X > x] = 10^{-(\log(Ns)-2)}$.
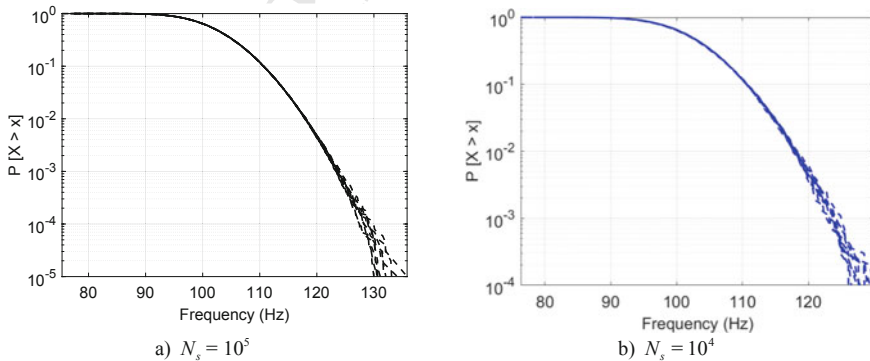

a) $N_s = 10^5$ b) $N_s = 10^4$

Fig. 4 Probability of exceedance (PoE) of the fundamental frequencies (Hz) of $-45°/45°/-45°$ laminated composite beam ($L/h = 20$, S-S boundary conditions)

4 Conclusions

This article presents stochastic vibration behaviours of laminated composite beams based on a quasi-3D theory. The stochastic mechanical properties of component materials are propagated into the vibrational responses of the composite beams with arbitrary lay-ups and boundary conditions. The beam model is based on the higher-order shear deformation theory with nonlinear formulation of axial and transverse displacements. A trigonometric-series solution is utilised to solve the equations of motion. A high number of Monte Carlo simulations is conducted to investigate the effects of stochastic uncertainties on the natural frequencies of the laminated composite beams. The outputs of these simulations are presented as probability density functions, probability of exceedance and several statistical moments. The numerical results obtained from this paper showed that the present model is simple and efficient in predicting stochastic vibration responses of the laminated composite beams. Novel results can be used as benchmarks for the future researches.

References

1. Aydogdu M (2005) Vibration analysis of cross-ply laminated beams with general boundary conditions by Ritz method. Int J Mech Sci 47(11):1740–1755
2. Kant T, Marur SR, Rao GS (1997) Analytical solution to the dynamic analysis of laminated beams using higher order refined theory. Compos Struct 40(1):1–9
3. Khdeir A, Reddy J (1994) Free vibration of cross-ply laminated beams with arbitrary boundary conditions. Int J Eng Sci 32(12):1971–1980
4. Nguyen T-K et al (2017) Trigonometric-series solution for analysis of laminated composite beams. Compos Struct 160:142–151
5. Vo TP, Thai H-T (2012) Static behavior of composite beams using various refined shear deformation theories. Compos Struct 94(8):2513–2522
6. Nguyen N-D et al (2018) New Ritz-solution shape functions for analysis of thermo-mechanical buckling and vibration of laminated composite beams. Compos Struct 184:452–460
7. Jun L, Yuchen B, Peng H (2017) A dynamic stiffness method for analysis of thermal effect on vibration and buckling of a laminated composite beam. Arch Appl Mech 87(8):1295–1315
8. Khdeir AA, Reddy JN (1997) An exact solution for the bending of thin and thick cross-ply laminated beams. Compos Struct 37(2):195–203
9. Nguyen N-D et al (2018) Ritz-based analytical solutions for bending, buckling and vibration behavior of laminated composite beams. Int J Struct Stab Dyn 18(11):1850130
10. Nguyen HX et al (2017) Stochastic buckling behaviour of laminated composite structures with uncertain material properties. Aerosp Sci Technol 66:274–283
11. Li J et al (2016) Stochastic thermal buckling analysis of laminated plates using perturbation technique. Compos Struct 139:1–12
12. Grover N et al (2017) Influence of parametric uncertainties on the deflection statistics of general laminated composite and sandwich plates. Compos Struct 171:158–169

13. Peng X et al (2019) Uncertainty analysis of composite laminated plate with data-driven polynomial chaos expansion method under insufficient input data of uncertain parameters. Compos Struct 209:625–633
14. Chandra S et al (2019) Stochastic dynamic analysis of composite plate with random temperature increment. Compos Struct 226:111159
15. Chen N-Z, Guedes Soares C (2008) Spectral stochastic finite element analysis for laminated composite plates. Comput Methods Appl Mech Eng 197(51):4830–4839
16. Chakraborty S et al (2016) Stochastic free vibration analysis of laminated composite plates using polynomial correlated function expansion. Compos Struct 135:236–249

Author Queries

Chapter 83

Query Refs.	Details Required	Author's response
AQ1	Please check and confirm if the author names and initials are correct.	
AQ2	Please check and confirm if the inserted citation of Fig. 2 is correct. If not, please suggest an alternate citation. Please note that figures and tables should be cited sequentially in the text.	

BUCKLING ANALYSIS OF LAMINATED COMPOSITE THIN-WALLED I-BEAM UNDER MECHANICAL AND THERMAL LOADS

Xuan-Bach Bui[1] , **Anh-Cao Nguyen**[1] , **Ngoc-Duong Nguyen**[1,*] ,
Tien-Tho Do[1]**, Trung-Kien Nguyen**[2]
[1]*Ho Chi Minh City University of Technology and Education,*
1 Vo Van Ngan Street, Thu Duc City, Ho Chi Minh City, Vietnam
[2]*CIRTech Institute, HUTECH University,*
475A Dien Bien Phu Street, Binh Thanh District, Ho Chi Minh City, Vietnam
*E-mail: duongnn@hcmute.edu.vn

Abstract. Despite the extensive use of thin-walled structures, the studies on their behaviours when exposed to extreme thermal environment are relatively scarce. Therefore, this paper aims to present the buckling analysis of thin-walled composite I-beams under thermo-mechanical loads. The thermal effects are investigated for the case of studied beams undergoing a uniform temperature rise through their thickness. The theory is based on the first-order shear deformation thin-walled beam theory with linear variation of displacements in the wall thickness. The governing equations of motion are derived from Hamilton's principle and are solved by series-type solutions with hybrid shape functions. Numerical results are presented to investigate the effects of fibre angle, material distribution, span-to-height's ratio and shear deformation on the critical buckling load and temperature rise. These results for several cases are verified with available references to demonstrate the present beam model's accuracy.

Keywords: thin-walled beam, thermal buckling, buckling analysis, series solution.

1. INTRODUCTION

The application of anisotropic laminated composite materials is increasing in many engineering fields such as aerospace, aircrafts and civil [1–4]. Thanks to its excellent mechanical properties, especially the strength-to-weight ratio, such structures have become

a topic of interest for many researchers, some of which, can be found in [5, 6]. Comparable to the Euler-Bernoulli theory for solid beam, Vlasov [7] developed the classical thin-walled beam theory (CTWBT) which ignores the effects of shear deformation. Vlasov's theory is easy to implement and analyse LC thin-walled beams [7–10]. Nonetheless, in the case of thick short beam, Vlasov's theory deliver inaccurate beam responses predictions such as the deflection, natural frequencies and critical buckling loads. Razaqpur and Li [11] developed a finite element model for thin-walled box girder that can analyse the extension, flexure, torsion, torsional warping, distortion, distortional warping, and shear lag effects using an extended version of Vlasov's thin-walled beam theory. Pavazza et al. [12] proposed a novel torsion theory for shear deformable thin-walled beams of arbitrary open cross-sections based on the classical Vlasov's theory of thin-walled beams and the Timoshenko's beam bending theory. Comparable to the first-order shear deformation beam theory, the first-order thin-walled beam theory (FTWBT) takes the transverse shear into account and allow the transverse displacement vary linearly across the thin wall thickness. The FTWBT gives better beam responses' predictions for beam with $L/b_3 < 10$ and has been studied in multiple researches [13–23]. The FTWBT demands a shear correction factor [24] to be calculated but it can also be a source of error. To overcome this setback, the high-order deformation thin-walled beam theory (HTWBT) has been proposed [25–27]. Though the HTWBT predicts more accurate results than the FTWBT, it appears to be too complicated to implement.

Besides, in practical engineering contexts, thin-walled beams are exposed to high-temperature environments. Therefore, the predictions of the thin-walled beams' responses to the thermal load in such contexts are of utmost importance. Many models and approaches on this matter have been studied in recent years for solid beams with rectangle sections, some representative references are herein cited. Trinh et al. [28] presented an analytical method for the vibration and buckling of functionally graded beams under mechanical and thermal loads. Nguyen et al. [29] investigated the hygro-thermal effects on vibration and thermal buckling behaviours of functionally graded beams. Li et al. [30] studied the free vibration characteristics of a spinning composite thin-walled beam under hygrothermal environment. Sun et al. [31] investigated the buckling and post-buckling behaviors of functionully graded Timoshenko beams on non-linear elastic foundation. A brief literature study shows that although many researches on thermal responses of laminated composite and functionally graded beams with rectangle sections have been performed, thermal buckling behaviors of thin-walled beams are extremely limited, Simonetti et al. [32] recently presented the thermal buckling analysis of thin-walled closed section functionally graded beam-type structures [32]. Pantousa [33] conducted a numerical study on thermal buckling of empty thin-walled steel tanks under multiple pool-fire scenarios.

This paper aims to investigate the elastic buckling of laminated composite thin-walled beams with I-section in thermo-mechanical environments. It is based on the FTWBT with a uniform temperature rise. The characteristic equations are derived from Hamilton's principle and solved by Ritz method with hybrid shape functions. Numerical results are presented for the laminated composite I-beams with various boundary conditions, fibre angles and length-to-height ratios.

2. THEORETICAL FORMULATION
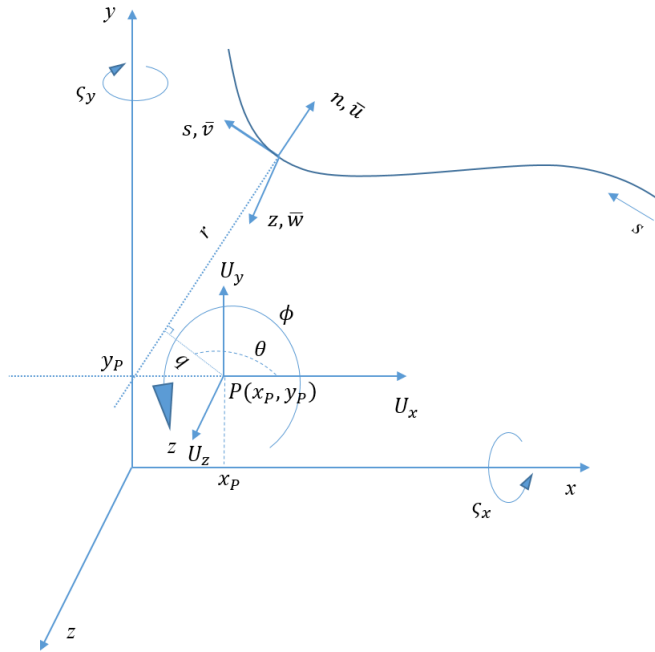
Fig. 1. Coordinate systems of a thin-walled beam

To analyse the thin-walled beam, the variables are defined in three set of coordinate systems as displayed in Fig. 1. These are the Cartesian coordinate system (x, y, z) , the local plate coordinate system (n, s, z) and the contour coordinate s along the profile of the section. The angle θ is the angle between s- and x-axes. The pole $P(x_P, y_P)$ is optimally chosen to be at the shear center of the section. The assumptions made in this beam model are: the effects of geometrical nonlinearity are ignored, the section contour remains undeformed in its own plane and the transverse shear strains are constant in the wall thickness. Fig. 2 shows how the aforementioned coordinate systems fit in to the thin-walled I-beam in this paper. The widths (b_1, b_2, b_3) and the thicknesses (h_1, h_2, h_3) with lower index 1, 2, 3 are for the beam's top, bottom flange, and web, respectively.
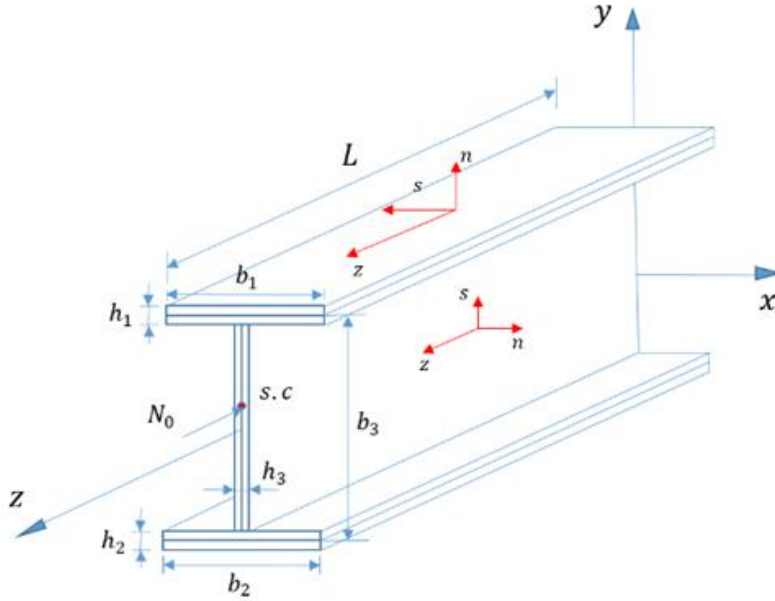
Fig. 2. Geometry of a thin-walled I-beam

2.1. Kinematics

The displacements $(\bar{u}, \bar{v}, \bar{w})$ at any point on the midsurface of the laminated composite thin-walled beams under a small rotation ϕ about the pole axis can be expressed in terms of those at the pole (U, V, W) as follows

$$\bar{u}(s,z) = U_x(z) \sin\theta(s) - U_y(z) \cos\theta(s) - \phi(z) q(s), \tag{1a}$$

$$\bar{v}(s,z) = U_x(z) \cos\theta(s) + U_y(z) \sin\theta(s) - \phi(z) r(s), \tag{1b}$$

$$\bar{w}(s,z) = U_z(z) + \varsigma_y(z) x(s) + \varsigma_x(z) y(s) + \varsigma_\omega(z) \omega(s), \tag{1c}$$

where $\varsigma_x, \varsigma_y, \varsigma_\omega$ are the rotations of the cross-section with respect to and, respectively, which are defined by

$$\varsigma_y = \gamma_{xz}^0 - U_x', \quad \varsigma_x = \gamma_{yz}^0 - U_y', \quad \varsigma_\omega = \gamma_\omega^0 - \phi'. \tag{2}$$

The warping function ω is given by

$$\omega(s) = \int_{s_0}^{s} r(s) \mathrm{d}s. \tag{3}$$

Moreover, the displacements (u, v, w) at a point on the beam section are expressed in term of the mid-surface displacements $(\bar{u}, \bar{v}, \bar{w})$ as follows

$$u(n,s,z) = \bar{u}(s,z), \tag{4a}$$

$$v\left(n,s,z\right) = \bar{v}\left(s,z\right) + n\bar{\zeta}_s\left(s,z\right), \tag{4b}$$

$$w\left(n,s,z\right) = \bar{w}\left(s,z\right) + n\bar{\zeta}_z\left(s,z\right), \tag{4c}$$

where $\bar{\zeta}_s$ and $\bar{\zeta}_z$ are expressed as follows

$$\bar{\zeta}_z = \varsigma_y \sin\theta - \varsigma_x \cos\theta - \varsigma_\omega q, \quad \bar{\psi}_s\left(s,z,t\right) = -\frac{\partial u}{\partial s}. \tag{5}$$

2.2. Strains

From the displacements defined in Eq. (4), the strain field can be written as

$$\varepsilon_s\left(n,s,z\right) = \bar{\varepsilon}_s\left(s,z\right) + n\bar{\kappa}_s\left(s,z\right), \tag{6a}$$

$$\varepsilon_z\left(n,s,z\right) = \bar{\varepsilon}_z\left(s,z\right) + n\bar{\kappa}_z\left(s,z\right), \tag{6b}$$

$$\gamma_{sz}\left(n,s,z\right) = \bar{\gamma}_{sz}\left(s,z\right) + n\bar{\kappa}_{sz}\left(s,z\right), \tag{6c}$$

$$\gamma_{nz}\left(n,s,z\right) = \bar{\gamma}_{nz}\left(s,z\right) + n\bar{\kappa}_{nz}\left(s,z\right), \tag{6d}$$

where

$$\bar{\varepsilon}_s = 0, \quad \bar{\varepsilon}_z = \frac{\partial\bar{w}}{\partial z} = \varepsilon_z^0 + x\kappa_y + y\kappa_x + \omega\kappa_\omega, \quad \bar{\kappa}_s = 0, \tag{7a}$$

$$\bar{\kappa}_z = \frac{\partial\bar{\zeta}_z}{\partial z} = \kappa_y \sin\theta - \kappa_x \cos\theta - \kappa_\omega q, \quad \bar{\kappa}_{sz} = \kappa_{sz}, \quad \bar{\kappa}_{nz} = 0, \tag{7b}$$

$$\varepsilon_z^0 = W', \quad \kappa_x = \varsigma_x', \quad \kappa_y = \varsigma_y', \quad \kappa_\omega = \varsigma_\omega', \quad \kappa_{sz} = \phi' - \varsigma_\omega, \tag{7c}$$

$$\varepsilon_z = \varepsilon_0^z + \left(x + n\sin\theta\right)\kappa_y + \left(y - n\cos\theta\right)\kappa_x + \left(\omega - nq\right)\kappa_\omega, \tag{7d}$$

$$\gamma_{sz} = \gamma_{xz}^0 \cos\theta + \gamma_{yz}^0 \sin\theta + \gamma_\omega^0 r + n\kappa_{sz}, \quad \gamma_{nz} = \gamma_{xz}^0 \sin\theta - \gamma_{yz}^0 \cos\theta - \gamma_\omega^0 q. \tag{7e}$$

2.3. Stress-strains relation

For laminated composite thin-walled beams, it is supposed to be constituted by a number of orthotropic material layers with the same thickness. The reduced constitutive equations at the kth-layer is given by

$$\left\{\begin{array}{c} \sigma_z \\ \sigma_{sz} \\ \sigma_{nz} \end{array}\right\} = \left(\begin{array}{ccc} P_{11} & P_{16} & 0 \\ P_{16} & P_{66} & 0 \\ 0 & 0 & P_{55} \end{array}\right) \left\{\begin{array}{c} \varepsilon_z \\ \gamma_{sz} \\ \gamma_{nz} \end{array}\right\}, \tag{8a}$$

where $P_{11} = \bar{Q}_{11} - \frac{\bar{Q}_{12}^2}{\bar{Q}_{22}}$, $P_{16} = \bar{Q}_{16} - \frac{\bar{Q}_{12}\bar{Q}_{26}}{\bar{Q}_{22}}$, $P_{66} = \bar{Q}_{66} - \frac{\bar{Q}_{26}^2}{\bar{Q}_{22}}$, $P_{55} = \bar{Q}_{55}$; $\bar{Q}_{ij}$ are the transformed reduced stiffness matrix elements which can be computed based on the fibre lay-up as follows

$$\bar{Q}_{11} = Q_{11}c^4 + Q_{22}s^4 + 2(Q_{12} + 2Q_{66})s^2c^2, \tag{8b}$$

$$\bar{Q}_{12} = (Q_{11} + Q_{22} - 4Q_{66})s^2c^2 + Q_{12}(s^4 + c^4), \tag{8c}$$

$$\bar{Q}_{22} = Q_{11}s^4 + 2(Q_{12} + 2Q_{66})s^2c^2 + Q_{22}c^4, \tag{8d}$$

$$\bar{Q}_{16} = (Q_{11} - Q_{12} - 2Q_{66})sc^3 + (Q_{12} - Q_{22} + 2Q_{66})s^3c, \tag{8e}$$

$$\bar{Q}_{26} = (Q_{12} - Q_{22} + 2Q_{66})sc^3 + (Q_{11} - Q_{12} - 2Q_{66})s^3c, \tag{8f}$$

$$\bar{Q}_{55} = Q_{55}c^2 + Q_{44}s^2, \tag{8g}$$

$$\bar{Q}_{66} = (Q_{11} + Q_{22} - 2Q_{12} - 2Q_{66})s^2c^2 + Q_{66}(s^4 + c^4), \tag{8h}$$

$$Q_{11} = E_1/(1 - \nu_{12}\nu_{21}), \quad Q_{22} = E_2/(1 - \nu_{12}\nu_{21}), \quad Q_{12} = \nu_{12}Q_{22}, \tag{8i}$$

$$Q_{44} = G_{23}, \quad Q_{55} = G_{13}, \quad Q_{66} = G_{12}, \quad s = \sin\theta, \quad c = \cos\theta, \tag{8j}$$

where θ is the fibre orientation angle of the current laminated layer, E_1 and E_2 are the Young's moduli, ν_{12} and ν_{21} are the Poisson's ratio values, G_{12}, G_{13} and G_{23} are the shear moduli of the laminated composite material.

2.4. Variational formulation

The characteristic equations of the laminated composite thin-walled beams can be derived by Hamilton's principle in which the total energy of the system Π is composed of the strain energy Π_S and work done by external force Π_W. The strain energy Π_S of the laminated composite thin-walled beam is expressed by

$$\Pi_S = \frac{1}{2} \int_\Omega (\sigma_z \varepsilon_z + \sigma_{sz}\gamma_{sz} + \sigma_{nz}\gamma_{nz}) \, d\Omega, \tag{9}$$

where Ω is the beam volume. Substitution of Eqs. (6), (7) and (8) into Eq. (9) gives

$$
\begin{aligned}
\Pi_S = \frac{1}{2} \int_0^L \big[& E_{11}U'^2_z + 2E_{16}U'_zU'_x + 2E_{17}U'_zU'_y + 2\,(E_{15} + E_{18})\,U'_z\phi' \\
& + 2E_{12}U'_z\varsigma'_y + 2E_{16}U'_z\varsigma_y + 2E_{13}U'_z\varsigma'_x + 2E_{17}U'_z\varsigma_x + 2E_{14}U'_z\varsigma'_\omega \\
& + 2\,(E_{18} - E_{15})\,U'_z\varsigma'_\omega + E_{66}U'^2_x + 2E_{67}U'_xU'_y + 2\,(E_{56} + E_{68})\,U'_x\phi' \\
& + 2E_{26}U'_x\varsigma'_y + 2E_{66}U'_x\varsigma_y + 2E_{36}U'_x\varsigma'_x + 2E_{67}U'_x\varsigma_x + 2E_{46}U'_x\varsigma'_\omega \\
& + 2\,(E_{68} - E_{56})\,U'_x\varsigma_\omega + E_{77}U'^2_y + 2\,(E_{57} + E_{78})\,U'_y\phi' + 2E_{27}U'_y\varsigma'_y \\
& + 2E_{67}U'_y\varsigma'_y + 2E_{37}U'_y\varsigma'_x + 2E_{77}U'_y\varsigma_x + 2E_{47}U'_y\varsigma_\omega + 2\,(E_{78} - E_{57})\,U'_y\varsigma_\omega \\
& + (E_{55} + 2E_{58} + E_{88})\,\phi'^2 + 2\,(E_{25} + E_{28})\,\phi'\varsigma'_y + 2\,(E_{56} + E_{68})\,\phi'\varsigma_y \\
& + 2\,(E_{78} - E_{57})\,U'_y\varsigma_\omega + (E_{55} + 2E_{58} + E_{88})\,\phi'^2 + 2\,(E_{25} + E_{28})\,\phi'\varsigma'_y \\
& + 2\,(E_{56} + E_{68})\,\phi'\varsigma_\omega + 2\,(E_{35} + E_{38})\,\phi'\varsigma'_x + 2\,(E_{57} + E_{78})\,\phi'\varsigma_x \\
& + 2\,(E_{45} + E_{48})\,\phi'\varsigma'_\omega + 2\,(E_{88} - E_{55})\,\phi'\varsigma_\omega + E_{22}\psi'^2_y + 2E_{26}\varsigma'_y\varsigma_y \\
& + E_{66}\varsigma^2_y + 2E_{23}\varsigma'_y\varsigma'_x + 2E_{27}\varsigma'_y\varsigma_x + 2E_{36}\varsigma_y\varsigma'_x + 2E_{67}\varsigma_y\varsigma_x \\
& + E_{24}\varsigma'_y\varsigma'_\omega + 2\,(E_{28} - E_{25})\,\varsigma'_y\varsigma_\omega + 2E_{46}\varsigma_y\varsigma_\omega + 2\,(E_{68} - E_{56})\,\varsigma_y\varsigma_\omega \\
& + E_{33}\varsigma'^2_\omega + 2E_{37}\varsigma'_x\varsigma_x + E_{77}\varsigma^2_x + 2E_{34}\varsigma'_x\varsigma'_\omega + 2\,(E_{38} - E_{35})\,\varsigma'_x\varsigma_\omega \\
& + 2E_{47}\varsigma_x\varsigma'_\omega + 2\,(E_{78} - E_{57})\,\varsigma_x\varsigma_\omega + + E_{44}\varsigma'^2_\omega 2\,(E_{48} - E_{45})\,\varsigma'_\omega\varsigma_\omega \\
& + (E_{88} - 2E_{58} + E_{55})\,\varsigma^2_\omega \big] \, dz,
\end{aligned} \tag{10}
$$

where E_{ij} are the stiffness coefficients of the laminated composite thin-walled composite beams [34].

The work done by the external mechanical axial load N_0^m and thermal load N_0^t is defined as

$$
\begin{aligned}
\Pi_W &= \frac{1}{2} \int_\Omega \frac{\left(N_0^m + N_0^t\right)}{A} \left(u'^2 + v'^2\right) d\Omega \\
&= \frac{1}{2} \int_0^L \left(N_0^m + N_0^t\right) \left(U'^2_x + U'^2_y + 2y_p U'_x \phi' - 2x_p U'_y \phi' + \frac{I_p}{A} \phi'^2\right) dz,
\end{aligned}
\tag{11}
$$

where A is the cross-sectional area; I_p is the polar moment of inertia about the centroid given by

$$
I_p = I_x + I_y,
\tag{12}
$$

where I_x and I_y are the second moment of inertia with respect to the x- and y-axes, respectively

$$
I_x = \int_A y^2 dA, \quad I_y = \int_A x^2 dA.
\tag{13}
$$

The axial thermal load is given as

$$
N_0^t = \int_n \left(\alpha_z P_{11} + 2\alpha_{sz} P_{16}\right) \Delta T dn,
\tag{14}
$$

where $\Delta T = T - T_0$ is the temperature difference; T_0 is the initial temperature; α_z, α_{sz} are the thermal expansion coefficients in the (n, s, z) coordinate system. The components (α_z, α_{sz}) are derived from the thermal expansion coefficients of the studied fibre materials (α_1, α_2) as follows

$$
\alpha_z = \alpha_1 \cos^2 \theta + \alpha_2 \sin^2 \theta,
\tag{15a}
$$

$$
\alpha_{sz} = (\alpha_1 - \alpha_2) \sin \theta \cos \theta.
\tag{15b}
$$

2.5. Hybrid series solution

Based on the Ritz method, the displacement field can be approximated as follows

$$
\{U_x, U_y, \phi\} (z) = \sum_{j=1}^m \phi_j (z) \{U_{xj}, U_{yj}, \phi_j\},
\tag{16a}
$$

$$
\{U_z, \varsigma_y, \varsigma_x, \varsigma_\omega\} (z) = \sum_{j=1}^m \phi'_j (z) \{U_{zj}, \varsigma_{yj}, \varsigma_{xj}, \varsigma_{\omega j}\},
\tag{16b}
$$

where $U_{xj}, U_{yj}, \phi_j, U_{zj}, \varsigma_{yj}, \varsigma_{xj}, \varsigma_{\omega j}$ are the unknowns to be computed; $\phi_j (z)$ is the shape functions which satisfy the boundary conditions (BCs) (Table 1).

Table 1. Shape functions and essential BCs of laminated composite thin-walled I-beams

BC	$\phi_j(x)/e^{\frac{-jx}{L}}$	$x = 0$	$x = L$
S-S	$\sin\left(\dfrac{\pi x}{L}\right)$	$U_x = U_y = \phi = 0$	$U = V = \phi = 0$
C-F	$\sin^2\left(\dfrac{\pi x}{2L}\right)$	$U_x = U_y = \phi = 0$ $U'_x = U'_y = \phi' = 0$ $U_z = \varsigma_y = \varsigma_x = \varsigma_\omega = 0$	
C-C	$\sin^2\left(\dfrac{\pi x}{L}\right)$	$U_x = U_y = \phi = 0$ $U'_x = U'_y = \phi' = 0$ $U_z = \varsigma_y = \varsigma_x = \varsigma_\omega = 0$	$U_x = U_y = \phi = 0$ $U'_x = U'_y = \phi' = 0$ $U_z = \varsigma_y = \varsigma_x = \varsigma_\omega = 0$

Substituting Eq. (16) in to Eqs. (10) and (11), and then applying Hamilton's principle lead to the characteristic equation for the buckling analysis of the laminated composite thin-walled beams as follows

$$\mathbf{Kp} = \mathbf{0}, \tag{17}$$

where $\mathbf{p} = \begin{bmatrix} \mathbf{U}_z & \mathbf{U}_x & \mathbf{U}_y & \mathbf{\Phi} & \varsigma_x & \varsigma_y & \varsigma_\omega \end{bmatrix}^T$ is the displacement vector; $\mathbf{K}$ is the stiffness matrix and is given as

$$\mathbf{K} = \begin{bmatrix}
\mathbf{K}^{11} & \mathbf{K}^{12} & \mathbf{K}^{13} & \mathbf{K}^{14} & \mathbf{K}^{15} & \mathbf{K}^{16} & \mathbf{K}^{17} \\
{}^T\mathbf{K}^{12} & \mathbf{K}^{22} & \mathbf{K}^{23} & \mathbf{K}^{24} & \mathbf{K}^{25} & \mathbf{K}^{26} & \mathbf{K}^{27} \\
{}^T\mathbf{K}^{13} & {}^T\mathbf{K}^{23} & \mathbf{K}^{33} & \mathbf{K}^{34} & \mathbf{K}^{35} & \mathbf{K}^{36} & \mathbf{K}^{37} \\
{}^T\mathbf{K}^{14} & {}^T\mathbf{K}^{24} & {}^T\mathbf{K}^{34} & \mathbf{K}^{44} & \mathbf{K}^{45} & \mathbf{K}^{46} & \mathbf{K}^{47} \\
{}^T\mathbf{K}^{15} & {}^T\mathbf{K}^{25} & {}^T\mathbf{K}^{35} & {}^T\mathbf{K}^{45} & \mathbf{K}^{55} & \mathbf{K}^{56} & \mathbf{K}^{57} \\
{}^T\mathbf{K}^{16} & {}^T\mathbf{K}^{26} & {}^T\mathbf{K}^{36} & {}^T\mathbf{K}^{46} & {}^T\mathbf{K}^{56} & \mathbf{K}^{66} & \mathbf{K}^{67} \\
{}^T\mathbf{K}^{17} & {}^T\mathbf{K}^{27} & {}^T\mathbf{K}^{37} & {}^T\mathbf{K}^{47} & {}^T\mathbf{K}^{57} & {}^T\mathbf{K}^{67} & \mathbf{K}^{77}
\end{bmatrix}, \tag{18}$$

with the following matrix elements

$$K_{ij}^{11} = E_{11} \int_0^L \phi_i'' \phi_j'' \, dz, \quad K_{ij}^{12} = E_{16} \int_0^L \phi_i'' \phi_j' \, dz, \quad K_{ij}^{13} = E_{17} \int_0^L \phi_i'' \phi_j' \, dz,$$

$$K_{ij}^{14} = (E_{15} + E_{18}) \int_0^L \phi_i'' \phi_j' \, dz, \quad K_{ij}^{15} = E_{12} \int_0^L \phi_i'' \phi_j'' \, dz + E_{16} \int_0^L \phi_i' \phi_j \, dz,$$

$$K_{ij}^{16} = E_{13} \int_0^L \phi_i'' \phi_j'' \, dz + E_{17} \int_0^L \phi_i'' \phi_j' \, dz, \quad K_{ij}^{17} = E_{14} \int_0^L \phi_i'' \phi_j'' \, dz + (E_{18} - E_{15}) \int_0^L \phi_i'' \phi_j' \, dz,$$

$$K_{ij}^{22} = E_{66} \int_0^L \phi_i' \phi_j' \mathrm{d}z + \left(N_0^m + N_0^t\right) \int_0^L \phi_i' \phi_j' \mathrm{d}z, \quad K_{ij}^{23} = E_{67} \int_0^L \phi_i' \phi_j' \mathrm{d}z,$$

$$K_{ij}^{24} = (E_{56} + E_{68}) \int_0^L \phi_i' \phi_j' \mathrm{d}z + \left(N_0^m + N_0^t\right) y_p \int_0^L \phi_i' \phi_j' \mathrm{d}z,$$

$$K_{ij}^{25} = E_{26} \int_0^L \phi_i' \phi_j'' \mathrm{d}z + E_{66} \int_0^L \phi_i' \phi_j' \mathrm{d}z, \quad K_{ij}^{26} = E_{36} \int_0^L \phi_i' \phi_j' \mathrm{d}z + E_{67} \int_0^L \phi_i' \phi_j' \mathrm{d}z,$$

$$K_{ij}^{27} = E_{46} \int_0^L \phi_i' \phi_j'' \mathrm{d}z + (E_{68} - E_{56}) \int_0^L \phi_i' \phi_j' \mathrm{d}z, \quad K_{ij}^{33} = E_{77} \int_0^L \phi_i' \phi_j' \mathrm{d}z + \left(N_0^m + N_0^t\right) \int_0^L \phi_i' \phi_j' \mathrm{d}z,$$

$$K_{ij}^{34} = (E_{57} + E_{78}) \int_0^L \phi_i' \phi_j' \mathrm{d}z - \left(N_0^m + N_0^t\right) x_p \int_0^L \phi_i' \phi_j' \mathrm{d}z, \quad K_{ij}^{35} = E_{27} \int_0^L \phi_i' \phi_j'' \mathrm{d}z + E_{67} \int_0^L \phi_i' \phi_j' \mathrm{d}z,$$

$$K_{ij}^{36} = E_{37} \int_0^L \phi_i' \phi_j'' \mathrm{d}z + E_{77} \int_0^L \phi_i' \phi_j' \mathrm{d}z, \quad K_{ij}^{37} = E_{47} \int_0^L \phi_i' \phi_j'' \mathrm{d}z + (E_{78} - E_{57}) \int_0^L \phi_i' \phi_j' \mathrm{d}z,$$

$$K_{ij}^{44} = (E_{55} + 2E_{58} + E_{88}) \int_0^L \phi_i' \phi_j' \mathrm{d}z + \frac{\left(N_0^m + N_0^t\right) I_p}{A} \int_0^L \phi_i' \phi_j' \mathrm{d}z,$$

$$K_{ij}^{45} = (E_{25} + E_{28}) \int_0^L \phi_i' \phi_j'' \mathrm{d}z + (E_{56} + E_{68}) \int_0^L \phi_i' \phi_j' \mathrm{d}z,$$

$$K_{ij}^{46} = (E_{35} + E_{38}) \int_0^L \phi_i' \phi_j'' \mathrm{d}z + (E_{57} + E_{78}) \int_0^L \phi_i' \phi_j' \mathrm{d}z,$$

$$K_{ij}^{47} = (E_{45} + E_{48}) \int_0^L \phi_i' \phi_j'' \mathrm{d}z + (E_{88} - E_{55}) \int_0^L \phi_i' \phi_j' \mathrm{d}z,$$

$$K_{ij}^{55} = E_{22} \int_0^L \phi_i'' \phi_j'' \mathrm{d}z + E_{26} \int_0^L \left(\phi_i'' \phi_j' + \phi_i' \phi_j''\right) \mathrm{d}z + E_{66} \int_0^L \phi_i' \phi_j' \mathrm{d}z,$$

$$K_{ij}^{56} = E_{23} \int_0^L \phi_i'' \phi_j'' \mathrm{d}z + E_{27} \int_0^L \phi_i'' \phi_j' \mathrm{d}z + E_{36} \int_0^L \phi_i' \phi_j'' \mathrm{d}z + E_{67} \int_0^L \phi_i' \phi_j' \mathrm{d}z,$$

$$K_{ij}^{57} = E_{24} \int_0^L \phi_i'' \phi_j'' \mathrm{d}z + (E_{28} - E_{25}) \int_0^L \phi_i'' \phi_j' \mathrm{d}z + E_{46} \int_0^L \phi_i' \phi_j'' \mathrm{d}z + (E_{68} - E_{56}) \int_0^L \phi_i' \phi_j' \mathrm{d}z,$$

$$K_{ij}^{66} = E_{33} \int_0^L \phi_i'' \phi_j'' \mathrm{d}z + E_{37} \int_0^L \left(\phi_i'' \phi_j' + \phi_i' \phi_j'' \right) \mathrm{d}z + E_{77} \int_0^L \phi_i' \phi_j' \mathrm{d}z,$$

$$K_{ij}^{67} = E_{34} \int_0^L \phi_i'' \phi_j'' \mathrm{d}z + (E_{38} - E_{35}) \int_0^L \phi_i'' \phi_j' \mathrm{d}z + E_{47} \int_0^L \phi_i' \phi_j'' \mathrm{d}z + (E_{78} - E_{57}) \int_0^L \phi_i' \phi_j' \mathrm{d}z,$$

$$K_{ij}^{77} = E_{44} \int_0^L \phi_i'' \phi_j'' \mathrm{d}z + (E_{48} - E_{45}) \int_0^L \left(\phi_i'' \phi_j' + \phi_i' \phi_j'' \right) \mathrm{d}z + (E_{88} - 2E_{58} + E_{55}) \int_0^L \phi_i' \phi_j' \mathrm{d}z.$$

$$(19)$$

The buckling responses of the laminated composite thin-walled beam can be obtained by solving $\det(\mathbf{K}) = \mathbf{0}$.

3. NUMERICAL RESULTS

The laminated composite thin-walled I-beam in this numerical study is made of glass-epoxy materials with the following properties: $E_1 = 53.78$ GPa, $E_2 = 17.93$ GPa, $G_{12} = G_{13} = 8.96$ GPa, $G_{23} = 3.45$ GPa, $\nu_{12} = 0.25$. The thermal expansion coefficients of glass and epoxy are $\alpha_1 = 6.7 \times 10^{-7}$ K^{-1} and $\alpha_2 = 3.6 \times 10^{-6}$ K^{-1} respectively. The geometry of the laminated composite thin-walled I-beam is shown in Fig. 2 with $b_1 = b_2 = b_3 = 0.05$ m, $h_1 = h_2 = h_3 = 0.00208$ m.

3.1. Convergence and verification study

This section conducts convergence study of the present solution for buckling analysis of laminated composite thin-walled I-beams under mechanical loads. For Table 2, the laminated composite I-beam's length is expressed as $L/b_3 = 40$. The laminated angle-ply for all the flanges and web is $[45°/ - 45°]_{4s}$. It can be observed in Table 2 that the results of this paper's approach achieve numerical convergence at $m = 8$ and agree with the results of Nguyen et al. [34]. Therefore, the series number $m = 8$ is applied in subsequent analyses.

To further verify the current solution in mechanical environment, Table 3 presents the effects of the various fibre angle lay-ups, boundary conditions and the length-to-depth ratio on the laminated composite I-beam's critical buckling loads. It can be seen that in both cases of $L/b_3 = 20$ and $L/b_3 = 80$, the critical buckling loads decrease with the increasing fibre angle $\theta°$ of the $[\theta°, -\theta°]_{4s}$ lay-up. The buckling results of the laminated composite I-beam with S-S boundary condition and $L/b_3 = 80$, C-F boundary condition and $L/b_3 = 20$ show good agreements with past researches from Kim et al. [35] and Vo

and Lee [18]. More results are computed for the laminated composite I-beam set-up in Table 3 but with more cases of fibre angle θ°. These results are plotted for $L/b_3 = 20$ and $L/b_3 = 80$ in Fig. 3.

Table 2. Convergence of critical buckling loads (*kN*) for the laminated composite thin-walled I-beams under mechanical load

BCs	Reference	*m*					
		2	4	6	8	10	12
S-S	Present	2.931	2.679	2.671	2.671	2.671	2.671
	Nguyen et al. (Shear) [34]	2.752	2.690	2.671	2.671	2.671	2.671
	Nguyen et al. (No shear) [34]	2.755	2.692	2.673	2.673	2.673	2.673
C-F	Present	3.852	1.564	0.738	0.671	0.668	0.669
	Nguyen et al. (Shear) [34]	0.706	0.668	0.668	0.668	0.668	0.668
	Nguyen et al. (No shear) [34]	0.706	0.668	0.668	0.668	0.668	0.668
C-C	Present	10.768	10.659	10.657	10.657	10.657	10.657
	Nguyen et al. (Shear) [34]	10.797	10.678	10.657	10.657	10.657	10.657
	Nguyen et al. (No shear) [34]	10.832	10.712	10.691	10.691	10.691	10.691

Table 3. Comparison of critical buckling loads (*N*) of the thin-walled composite I-beams under mechanical loads

| BC	Reference	Fibre angle							
		$[0]_{16}$	$[15/-15]_{4s}$	$[30/-30]_{4s}$	$[45/-45]_{4s}$	$[60/-60]_{4s}$	$[75/-75]_{4s}$	$[90/-90]_{4s}$	$[0/90]_{4s}$
$L/b_3 = 80$									
S-S	Present (Shear)	1438.1	1299.4	965.0	668.1	528.6	487.0	479.6	959.0
	Kim et al. (No shear) [35]	1438.8	1300.0	965.2	668.2	528.7	487.1	-	959.3
C-F	Present (Shear)	361.2	326.4	242.4	167.8	132.7	122.3	120.4	240.9
C-C	Present (Shear)	5743.3	5191.0	3856.8	2670.6	2113.2	1946.7	1917.1	3831.4
$L/b_3 = 20$									
S-S	Present (Shear)	22832.7	20660.1	15376.7	10657.3	8433.9	7767.7	7648.6	15255.8
C-F	Present (Shear)	5768.6	5213.8	3873.7	2682.4	2122.5	1955.2	1925.5	3848.3
	Vo and Lee (Shear) [18]	5741.5	5189.0	3854.5	2668.4	2111.3	1945.1	-	3829.8
	Kim et al. (No shear) [35]	5755.2	5199.8	3861.0	2672.7	2114.7	1948.3	-	3857.8
C-C	Present (Shear)	77772.9	72116.0	57102.8	42069.5	33438.5	30632.4	29873.4	53993.2

(a) $L/b_3 = 80$

(b) $L/b_3 = 20$
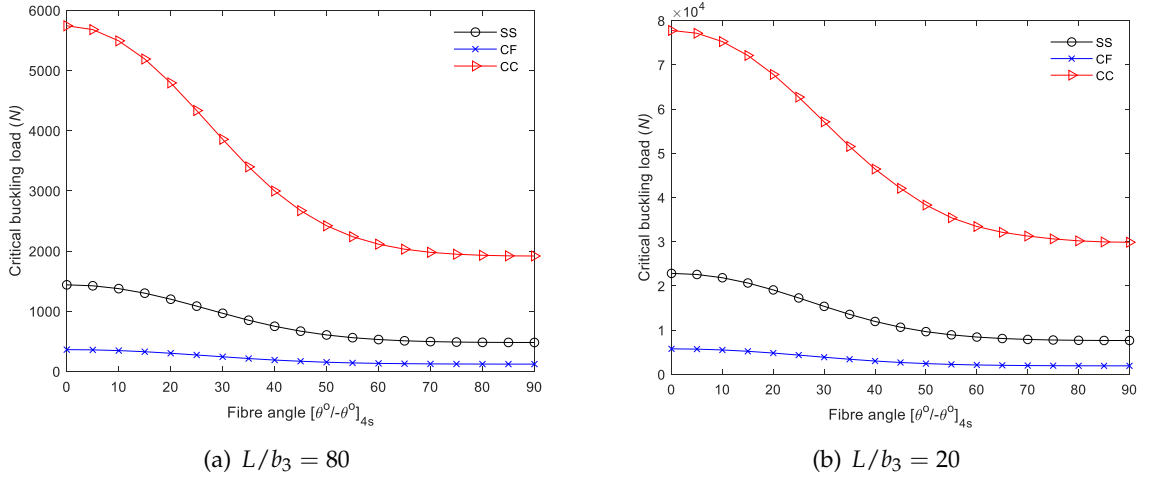
Fig. 3. Critical buckling loads (N) for the glass-epoxy composite I-beam with respect to fibre angle for different boundary conditions

3.2. Thermal buckling stability

This section aims to study the effect of fibre angle, length-to-depth ratio and boundary conditions on the thermal buckling stability of the laminated composite thin-walled I-beams. The critical buckling temperature for various fibre angle lay-ups, boundary conditions and length-to-depth ratios are plotted in Fig. 4. It can be seen that the critical buckling temperature slightly increases when θ° goes from 0° to 20° and drop sharply
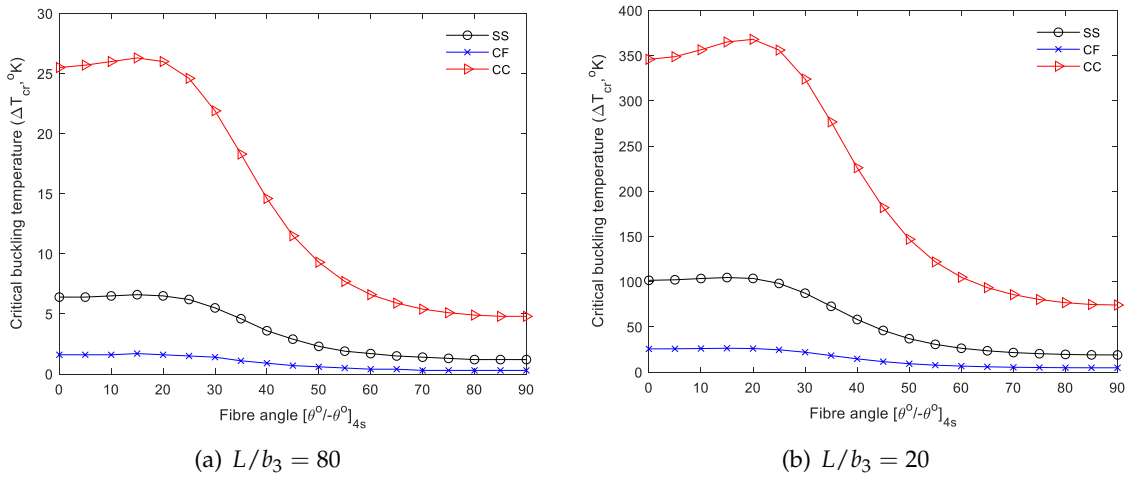

(a) $L/b_3 = 80$

(b) $L/b_3 = 20$

Fig. 4. Critical buckling temperature ΔT_{cr} ($^\circ$K) for the glass-epoxy composite I-beam

when θ° is in the range of 20°–70° before plateauing afterwards. This trend is particularly clearer when the beam is under C-C boundary condition.

Moreover, the laminated composite I-beam can withstand much more temperature rise and thermal load with $L/b_3 = 20$ compared to $L/b_3 = 80$. Fig.5 demonstrates better the effects of length-to-depth ratios on the thermal buckling stability of the laminated composite I-beams. The thin-walled beam is drastically more stable at low L/b_3 and the L/b_3 becomes less significant when $L/b_3 > 30$.
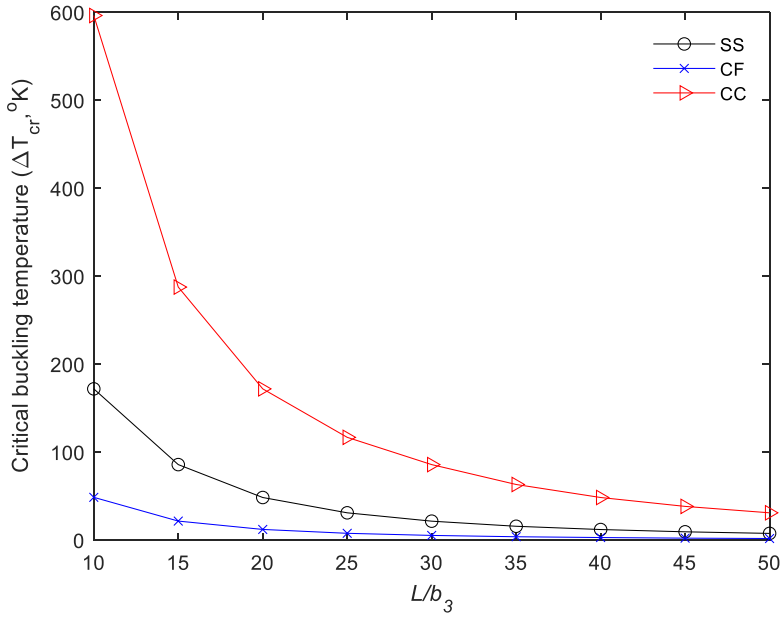

Fig. 5. Critical buckling temperature ΔT_{cr} ($^\circ$K) for the laminated composite I-beam with various length-to-depth ratios ($[0^\circ/90^\circ]_{4s}$)

4. CONCLUSION

A shear-deformable thin-walled beam model and a hybrid series solution are presented in this study. The glass-epoxy composite I-beam is investigated for its mechanical and thermal buckling stability. This model can predict accurately the critical buckling loads and critical buckling temperature for different beam configurations. The effects of fibre angle lay-up, boundary conditions and length-to-depth ratios are shown in the numerical results. The beam's buckling capacity is higher for low fibre angle, low length-to-depth ratios and clamped-clamped boundary condition. The present model is shown to be valid for buckling analysis of laminated composite I-beam under mechanical and thermal loads.

DECLARATION OF COMPETING INTEREST

FUNDING

REFERENCES

[1] O. A. Bauchau and J. I. Craig. *Structural analysis: with applications to aerospace structures*. Springer Netherlands, (2009).

[2] T. H. G. Megson. *Aircraft structures for engineering students*. United Kingdom: Butterworth-Heinemann, seventh edition, (2021).

[3] S. Eken. Free vibration analysis of composite aircraft wings modeled as thin-walled beams with NACA airfoil sections. *Thin-Walled Structures*, **139**, (2019), pp. 362–371. https://doi.org/10.1016/j.tws.2019.01.042.

[4] Z. K. Awad, T. Aravinthan, Y. Zhuge, and F. Gonzalez. A review of optimization techniques used in the design of fibre composite structures for civil engineering applications. *Materials & Design*, **33**, (2012), pp. 534–544. https://doi.org/10.1016/j.matdes.2011.04.061.

[5] C. Mittelstedt. Buckling and post-buckling of thin-walled composite laminated beams—a review of engineering analysis methods. *Applied Mechanics Reviews*, **72**, (2020). https://doi.org/10.1115/1.4045680.

[6] L. Librescu and O. Song. *Thin-walled composite beams*. Springer Netherlands, (2006). https://doi.org/10.1007/1-4020-4203-5.

[7] N. R. Bauld and T. Lih-Shyng. A Vlasov theory for fiber-reinforced beams with thin-walled open cross sections. *International Journal of Solids and Structures*, **20**, (3), (1984), pp. 277–297. https://doi.org/10.1016/0020-7683(84)90039-8.

[8] M. D. Pandey, M. Z. Kabir, and A. N. Sherbourne. Flexural-torsional stability of thin-walled composite I-section beams. *Composites Engineering*, **5**, (1995), pp. 321–342. https://doi.org/10.1016/0961-9526(94)00101-e.

[9] J. Lee and S.-E. Kim. Free vibration of thin-walled composite beams with I-shaped cross-sections. *Composite Structures*, **55**, (2002), pp. 205–215. https://doi.org/10.1016/s0263-8223(01)00150-7.

[10] J. Lee and S.-E. Kim. Flexural–torsional buckling of thin-walled I-section composites. *Computers & Structures*, **79**, (2001), pp. 987–995. https://doi.org/10.1016/s0045-7949(00)00195-4.

[11] A. G. Razaqpur and H. Li. Thin-walled multicell box-girder finite element. *Journal of Structural Engineering*, **117**, (1991), pp. 2953–2971. https://doi.org/10.1061/(asce)0733-9445(1991)117:10(2953).

[12] R. Pavazza, A. Matoković, and M. Vukasović. A theory of torsion of thin-walled beams of arbitrary open sections with influence of shear. *Mechanics Based Design of Structures and Machines*, **50**, (2020), pp. 206–241. https://doi.org/10.1080/15397734.2020.1714449.

[13] S. Y. Back and K. M. Will. Shear-flexible thin-walled element for composite I-beams. *Engineering Structures*, **30**, (2008), pp. 1447–1458. https://doi.org/10.1016/j.engstruct.2007.08.002.

[14] S. S. Maddur and S. K. Chaturvedi. Laminated composite open profile sections: non-uniform torsion of I-sections. *Composite Structures*, **50**, (2000), pp. 159–169. https://doi.org/10.1016/s0263-8223(00)00093-3.

[15] S. S. Maddur and S. K. Chaturvedi. Laminated composite open profile sections: first order shear deformation theory. *Composite Structures*, **45**, (1999), pp. 105–114. https://doi.org/10.1016/s0263-8223(99)00005-7.

[16] J. Lee. Flexural analysis of thin-walled composite beams using shear-deformable beam theory. *Composite Structures*, **70**, (2005), pp. 212–222. https://doi.org/10.1016/j.compstruct.2004.08.023.

[17] Z. Qin and L. Librescu. On a shear-deformable theory of anisotropic thin-walled beams: further contribution and validations. *Composite Structures*, **56**, (2002), pp. 345–358. https://doi.org/10.1016/s0263-8223(02)00019-3.

[18] T. P. Vo and J. Lee. Flexural–torsional coupled vibration and buckling of thin-walled open section composite beams using shear-deformable beam theory. *International Journal of Mechanical Sciences*, **51**, (2009), pp. 631–641. https://doi.org/10.1016/j.ijmecsci.2009.05.001.

[19] J. Lee. Center of gravity and shear center of thin-walled open-section composite beams. *Composite Structures*, **52**, (2001), pp. 255–260. https://doi.org/10.1016/s0263-8223(00)00177-x.

[20] S. N. Jung and J.-Y. Lee. Closed-form analysis of thin-walled composite I-beams considering non-classical effects. *Composite Structures*, **60**, (2003), pp. 9–17. https://doi.org/10.1016/s0263-8223(02)00318-5.

[21] N.-I. Kim and D. K. Shin. Coupled deflection analysis of thin-walled Timoshenko laminated composite beams. *Computational Mechanics*, **43**, (2008), pp. 493–514. https://doi.org/10.1007/s00466-008-0324-9.

[22] L. Wu and M. Mohareb. Finite element formulation for shear deformable thin-walled beams. *Canadian Journal of Civil Engineering*, **38**, (2011), pp. 383–392. https://doi.org/10.1139/l11-007.

[23] A. Prokić. On fivefold coupled vibrations of Timoshenko thin-walled beams. *Engineering Structures*, **28**, (2006), pp. 54–62. https://doi.org/10.1016/j.engstruct.2005.07.002.

[24] S. J. Kim, K. W. Yoon, and S. N. Jung. Shear correction factors for thin-walled composite boxbeam considering nonclassical behaviors. *Journal of Composite Materials*, **30**, (1996), pp. 1132–1149. https://doi.org/10.1177/002199839603001004.

[25] X.-B. Bui, T.-K. Nguyen, N.-D. Nguyen, and T. P. Vo. A general higher-order shear deformation theory for buckling and free vibration analysis of laminated thin-walled composite I-beams. *Composite Structures*, **295**, (2022). https://doi.org/10.1016/j.compstruct.2022.115775.

[26] R. F. Vieira, F. B. E. Virtuoso, and E. B. R. Pereira. A higher order thin-walled beam model including warping and shear modes. *International Journal of Mechanical Sciences*, **66**, (2013), pp. 67–82. https://doi.org/10.1016/j.ijmecsci.2012.10.009.

[27] N.-L. Nguyen, G.-W. Jang, S. Choi, J. Kim, and Y. Y. Kim. Analysis of thin-walled beam-shell structures for concept modeling based on higher-order beam theory. *Computers & Structures*, **195**, (2018), pp. 16–33. https://doi.org/10.1016/j.compstruc.2017.09.009.

[28] L. C. Trinh, T. P. Vo, H.-T. Thai, and T.-K. Nguyen. An analytical method for the vibration and buckling of functionally graded beams under mechanical and thermal loads. *Composites Part B: Engineering*, **100**, (2016), pp. 152–163. https://doi.org/10.1016/j.compositesb.2016.06.067.

[29] T.-K. Nguyen, B.-D. Nguyen, T. P. Vo, and H.-T. Thai. Hygro-thermal effects on vibration and thermal buckling behaviours of functionally graded beams. *Composite Structures*, **176**, (2017), pp. 1050–1060. https://doi.org/10.1016/j.compstruct.2017.06.036.

[30] X. Li, Y. H. Li, and Y. Qin. Free vibration characteristics of a spinning composite thin-walled beam under hygrothermal environment. *International Journal of Mechanical Sciences*, **119**, (2016), pp. 253–265. https://doi.org/10.1016/j.ijmecsci.2016.10.028.

[31] Y. Sun, S.-R. Li, and R. C. Batra. Thermal buckling and post-buckling of FGM Timoshenko beams on nonlinear elastic foundation. *Journal of Thermal Stresses*, **39**, (2016), pp. 11–26. https://doi.org/10.1080/01495739.2015.1120627.

[32] S. K. Simonetti, G. Turkalj, and D. Lanc. Thermal buckling analysis of thin-walled closed section FG beam-type structures. *Thin-Walled Structures*, **181**, (2022). https://doi.org/10.1016/j.tws.2022.110075.

[33] D. Pantousa. Numerical study on thermal buckling of empty thin-walled steel tanks under multiple pool-fire scenarios. *Thin-Walled Structures*, **131**, (2018), pp. 577–594. https://doi.org/10.1016/j.tws.2018.07.025.

[34] N.-D. Nguyen, T.-K. Nguyen, T. P. Vo, T.-N. Nguyen, and S. Lee. Vibration and buckling behaviours of thin-walled composite and functionally graded sandwich I-beams. *Composites Part B: Engineering*, **166**, (2019), pp. 414–427. https://doi.org/10.1016/j.compositesb.2019.02.033.

[35] N.-I. Kim, D. K. Shin, and M.-Y. Kim. Flexural–torsional buckling loads for spatially coupled stability analysis of thin-walled composite columns. *Advances in Engineering Software*, **39**, (2008), pp. 949–961. https://doi.org/10.1016/j.advengsoft.2008.03.001.

Vibration and buckling analysis of porous metal foam thin-walled beams with closed section

Xuan-Bach Bui, Trung-Kien Nguyen, Tien-Tho Do & Thuc P. Vo

Published online: 01 Jul 2024.

Submit your article to this journal ⍐

View related articles ⍐

View Crossmark data ⍐

Taylor & Francis
Taylor & Francis Group

Check for updates

Vibration and buckling analysis of porous metal foam thin-walled beams with closed section

Xuan-Bach Bui[a], Trung-Kien Nguyen[b], Tien-Tho Do[a], and Thuc P. Vo[c]

[a]Faculty of Civil Engineering, Ho Chi Minh City University of Technology and Education, Ho Chi Minh City, Vietnam; [b]CIRTech Institute, HUTECH University, Ho Chi Minh City, Vietnam; [c]School of Computing, Engineering and Mathematical Sciences, La Trobe University, Bundoora, VIC, Australia

ABSTRACT

This paper investigates the vibration and buckling analysis of porous metal foam thin-walled box beams. These beams exhibit a unique structural configuration with symmetrical and asymmetrical porosity distributions along their wall thickness, thereby altering the effective mechanical properties. The first-order shear deformable beam theory is employed and the governing equations are derived using the Hamilton's principle. Numerical results are presented for porous metal foam thin-walled box beams under simply-supported, clamped–clamped and clamped-free boundary conditions. The effects of various porosity parameters, length-to-side and side-to-wall-thickness ratios on the beams' performance are also examined. A comprehensive comparison between the porous metal foam thin-walled box beams and their counterparts in the form of equivalent homogeneous are presented.

1. Introduction

In the past few decades, the advances of technology in the fabrication of materials allows for the development of porous materials. These materials are characterized by a spatially varying porosity and composition, granting them the ability to reduce the self-weight while simultaneously optimize mechanical, thermal, and electrical properties across their volume. This feature enables the material scientists and engineers to fine-tune the structural components made from functionally graded (FG) porous materials to satisfy the demands of the industry applications (Ishizaki, Komarneni, and Nanko 2013; Liu and Chen 2014). In addition, the thin-walled beams are known as an important slender structural element in many engineering field such as aerospace, civil, mechanical and naval engineerings, etc. (Liviu Librescu 2006; Wu, Yang, and Kitipornchai 2020). Although their wall thickness is small in comparison with their cross-sectional dimensions and length, they possess a high efficiency in strength-to-weight ratio. Therefore, the consideration of FG materials with porosity application in the thin-walled beams has been an interesting topic attracted researches in recent years to better understand and predict their behaviors.

Although many theories have been proposed to analyze thin-walled beams with different cross-sections and material properties, only some representative references are herein cited. The classical thin-walled beam theory (CTWBT) was proposed by Vlasov (1959), which neglects the shear effects and requires modifications to predict the thin-walled beam's responses. In practice, due to its simplicity in theoretical formulation and programming, the CTWBT has commonly

used to predict static and dynamic responses of laminated composite and FG thin-walled beams with open and closed sections. Bauld and Lih-Shyng (1984) presented linear and nonlinear theoretical formulations of isotropic and laminated composite thin-walled beams with open sections. By using the CTWBT and finite element method (FEM), Lanc et al. (2015) investigated stability analysis of FG sandwich box beams and Vo and Lee (2007) studied the flexural–torsional behaviors of laminated composite thin-walled box beams under vertical and torsional loads. Kim and Lee (2018) investigated the geometrical nonlinearity of the FG thin-walled box beams with consideration of both single and double cells. Belabed, Tounsi, Bousahla, et al. (2024) proposed an enhanced FEM to predict the forced and free vibration responses of FG beams with non-uniform cross-section. It is noted that due to neglecting the shear effects, the CTWBT is only suitable for slender beams. In order to deal with thick beams, the first-order thin-walled beam theory (FTWBT) is used. Ambrosini, Riera, and Danesi (2000) presented the dynamic analysis of thin-walled beams by considering the effects of shear flexibility, rotatory inertia in the stress resultants. Choi and Kim (2021) proposed a higher-order Vlasov's torsion theory that incorporates extra sectional deformation modes for thin-walled box beams. By using FTWBT, Ziane et al. (2013) investigated the free vibration of FG thin-walled box beam. Kvaternik et al. (2019) compared the FG thin-walled beam's buckling responses between the CTWBT and the refined theory using Carrera Unified Formulation. Librescu, Oh, and Song (2005) proposed the thermoelastic modeling of spining FG thin-walled beams under high thermal load. Nguyen et al. (2019), (2023) studied structural responses of FG sandwich beams with I- and channel-sections using the FTWBT and Ritz method. Bui et al. (2023) investigated the size dependent effects on bending and free vibration of FG sandwich thin-walled beams using the FTWBT, modified couple stress theory and Ritz method. Bui, Nguyen, and Nguyen (2024) employed the FTWBT and polynomial chaos expansion theory for buckling and vibration analysis of FG thin-walled beams. It can be observed that the FTWBT is considered as the simplest theory accounting for the shear effects, however it requires a shear correction factor to correct the traction-free boundary condition on the wall surfaces. Another approach is to use the higher-order shear deformation thin-walled beam theory (HTWBT) in which the shear strains are supposed to be varied in terms of the high-order polynomials in the wall thickness, therefore the shear stresses could be adequately computed by constitutive equations. Chandiramani, Librescu, and Shete (2002) examined free vibration responses of thin-walled composite box beams in which the shear strains were approximated under a third-order polynomial in the wall thickness. Bui et al. (2022), Bui and Nguyen (2023) proposed a unified HTWBT for deterministic and stochastic analysis of laminated composite thin-walled I-beams using the Ritz method in which the shear strains were introduced under general high-order polynomials satisfied the traction-free boundary conditions on the wall surfaces. Bui Manh et al. (2024) proposed a refined shear deformation theory employing hyperbolic sine functions and FEM to study the static responses of rotating FG beams. Meftah et al. (2024) formulated a new beam FEM based on the high-order shear deformation theory which can be used for in-plane loaded masonry walls and other structures. Although this approach required the additional computations, the HTWBT showed that the shear effects are significant for small length-to-depth ratios.

Furthermore, the porous metal foam (PMF) material has many practical applications in multiple industries, thanks to its unique combination of properties such as low density, high specific strength, excellent energy absorption capacity, vibration damping effectiveness, and thermal conductivity (Lefebvre, Banhart, and Dunand 2008). By accurately predicting the vibration and buckling behaviors of the PMF structures, designers apply the simulation results in many notable applications such as crash absorption structures in vehicles (Srinath et al. 2010), seismic dampers in buildings (Ebadi-Jamkhaneh, Rezaei, and Ahmadi 2021), explosive containment in military (Homae et al. 2021), and high-performance sports equipments (Dukhan 2013). Therefore, PMFs have increasingly enticed researchers to explore its characteristics and behaviors for various

structures. Addou, Bousahla, and Alnujaie (2023), Addou et al. (2024) analyzed the impacts of porosity on static behaviors of laminated composite shells and plates based on high-order shear deformation theory. Lakhdar et al. (2024) and Bentrar et al. (2023) studied the free vibration responses of porous FG structures using the p-version FEM. Alsubaie et al. (2023), Belabed, Tounsi, Al-Osta Mohammed, et al. (2024), Hadji et al. (2023) and Khorasani (2023) investigated the combined effects of porosity and foundation conditions on the beam's responses. Chitour et al. (2024) examined the influence of porosity on the stability of imperfect FG sandwich plates using a novel quasi-3D high shear deformation theory. Moreover, Al-Osta et al. (2021) and Bourada et al. (2023) scrutinized the relation between the porosity of FG structures with their hygro-thermal responses by employing intricate computational models. Despite the growing number of recent researches in PMF beams with rectangular sections (Chen, Yang, and Kitipornchai 2016; Derikvand, Farhatnia, and Hodges 2023; Keleshteri and Jelovica 2022; Tang, Li, and Hu 2018), only a few earlier studies have examined the static and dynamic responses of FG thin-walled beams with porosity. By using the FTWBT and Galerkin method, Ziane et al. (2017) analyzed the thermal effects on the stability of FG box beams with porosity using the FTWBT and Galerkin method, while Farsadi (2022) investigated the static and dynamic responses of FG thin-walled rotating blades with porosity. The literature review indicates a notable absence of research on the mechanical responses of PMF thin-walled beams. This paper aims to address this gap by employing a novel analytical model and computational techniques tailored to accurately study their mechanical behaviors. The methods and results presented herein offer critical insights that can be advantageous in designing lightweight yet robust components across the aerospace, automotive, and civil engineering industries. These insights not only fill a crucial gap in the literature, but also contribute to the future analysis and design considerations to enhance the structural integrity and performance optimization of PMF components.

This paper presents the vibration and buckling analysis of the PMF box beam using the FTWBT for the first time. Both symmetric and nonsymmetric porosity distributions *via* the thickness are considered. Governing equations are derived from the Hamilton's principle and are solved using the Ritz-type hybrid series solution. The effects of porosity configurations, boundary conditions, length-to-height ratio, height-to-wall-thickness ratio and cross-section shapes on the vibration and buckling analysis of PMF thin-walled box beams are evaluated.

2. Theoretical formulation

Consider a PMF thin-walled box beam with length L. Three sets of coordinate systems are displayed in Fig. 1: Cartesian coordinate system (x_1, x_2, x_3), local plate coordinate system (n, s, x_3) and contour coordinate s along the profile of the section. θ is an angle of orientation between (n, s, x_3) and (x_1, x_2, x_3) coordinate systems. The pole P with coordinates (x_1^P, x_2^P) is considered as the shear center of the section. For simplicity purpose, the following assumptions are made: the strains are small and the section contour does not deform in its own plane, the shear and warping shear strains are uniform over the section, local buckling and pre-buckling deformation are negligible.

2.1. Kinematics

The vertical and horizontal displacements $u_1(n, s, x_3)$ and $u_2(n, s, x_3)$ at any points in the contour coordinate system under a small rotation ϕ about the pole axis can be expressed in terms of those at the pole $u_1^P(x_3)$ and $u_2^P(x_3)$ in x_1- and x_2- directions, respectively, as follows (Vlasov 1959):

$$u_1(n, s, x_3) = u_1^P(x_3) - \left(X_2 - x_2^P\right)\phi(x_3) \tag{1a}$$
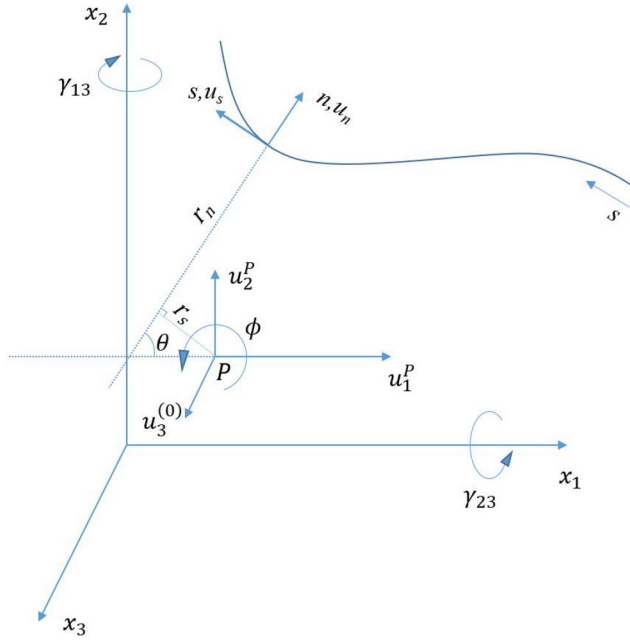
Figure 1. Thin-walled coordinate systems.

$$u_2(n, s, x_3) = u_2^P(x_3) + \left(X_1 - x_1^P\right)\phi(x_3) \tag{1b}$$

where $X_1 = x_1 + nx_{2,s}$, $X_2 = x_2 - nx_{1,s}$. Moreover, the displacements in the contour lines $u_n(n, s, x_3)$, $u_s(n, s, x_3)$ can be derived from those in Eq. (1) as follows:

$$u_n(n, s, x_3) = u_1^P(x_3)X_{2,s} - u_2^P(x_3)X_{1,s} - R_s(n, x_3)\phi(x_3) \tag{2a}$$

$$u_s(n, s, x_3) = u_1^P(x_3)X_{1,s} + u_2^P(x_3)X_{2,s} + R_n(n, x_3)\phi(x_3) \tag{2b}$$

where $R_s(n, s) = r_s(s)$, $R_n(n, s) = r_n(s) + n$ in which $r_s(s), r_n(s)$ are the lengths of the perpendiculars from P to the tangent and normal of the profile line. Furthermore, the shear strains $(\gamma_{s3}, \gamma_{n3})$ in the contour of thin-walled beams can be written in terms of the transverse shear strains $(\gamma_{13}, \gamma_{23})$ and a direct shear strain caused by the change rate of twist angle $\phi_{,3}$ (Megson 2021) as follows:

$$\gamma_{s3}(n, s, x_3) = \gamma_{13}(n, x_3)X_{1,s} + \gamma_{23}(n, x_3)X_{2,s} + 2n\phi_{,3}(x_3) = u_{s,3} + u_{3,s} \tag{3a}$$

$$\gamma_{n3}(n, s, x_3) = \gamma_{13}(n, x_3)X_{2,s} - \gamma_{23}(n, x_3)X_{1,s} = u_{n,3} + u_{3,n} \tag{3b}$$

It is assumed that the transverse shear strains $(\gamma_{13}, \gamma_{23})$ are constant in the wall thickness, i.e., $\gamma_{13}(n, x_3) = \gamma_{13}^{(0)}(x_3)$, $\gamma_{23}(n, x_3) = \gamma_{23}^{(0)}(x_3)$ where $\gamma_{13}^{(0)}, \gamma_{23}^{(0)}$ are mid-surface transverse shear strains. Substituting Eq. (2) into Eq. (3) and then integrating the subsequent results with respect to s and n lead to the expression of the axial displacement as follows:

$$u_3(n, s, x_3) = u_3^{(0)}(x_3) + \theta_2(x_3)X_1(n, s) + \theta_1(x_3)X_2(n, s) - \phi_{,3}(x_3)\bar{F}_\omega(n, s) \tag{4}$$

where $\theta_1(x_3) = \gamma_{23}^{(0)} - v_{p,3}$ and $\theta_2(x_3) = \gamma_{13}^{(0)} - u_{p,3}$ are rotations with respect to x_1- and x_2- axes; $\bar{F}_\omega = F_\omega - nr_s$ where $F_\omega(s)$ is a warping function defined by:

$$F_\omega(s) = \int_{s_0}^{s}\left(r_n - \frac{2\Omega}{\beta}\right)(s)ds \tag{5}$$

where Ω is the area enclosed by the contour line of the beam and β is the cross-section perimeter.

The kinematics of FTWBT at any points of the PMF thin-walled beam with closed sections can be finally expressed as follows:

$$u_1(n, s, x_3) = u_1^P(x_3) - (x_2 - nx_{1,s} - x_2^P)\phi(x_3) \tag{6a}$$

$$u_2(n, s, x_3) = u_2^P(x_3) + (x_1 + nx_{2,s} - x_1^P)\phi(x_3) \tag{6b}$$

$$u_3(n, s, x_3) = u_3^{(0)}(x_3) + \theta_2(x_3)(x_1 + nx_{2,s}) + \theta_1(x_3)(x_2 - nx_{1,s}) - \phi_{,3}(x_3)\bar{F}_\omega \tag{6c}$$

2.2. Strains

The linear nonzero strains related to the displacements in Eq. (6) are given by:

$$\varepsilon_{33}(n, s, x_3) = \varepsilon_{33}^{(0)} + n\varepsilon_{33}^{(1)} \tag{7a}$$

$$\gamma_{s3}(n, s, x_3) = \gamma_{s3}^{(0)} + n\gamma_{s3}^{(1)} \tag{7b}$$

$$\gamma_{n3}(n, s, x_3) = \gamma_{n3}^{(0)} \tag{7c}$$

where

$$\varepsilon_{33}^{(0)}(s, x_3) = u_{3,3}^{(0)} + \theta_{2,3}x_1 + \theta_{1,3}x_2 - \phi_{,33}F_\omega \tag{8a}$$

$$\varepsilon_{33}^{(1)}(s, x_3) = \theta_{2,3}x_{2,s} - \theta_{1,3}x_{1,s} + \phi_{,33}r_s \tag{8b}$$

$$\gamma_{s3}^{(0)}(s, x_3) = \gamma_{13}^{(0)}x_{1,s} + \gamma_{23}^{(0)}x_{2,s} \tag{8c}$$

$$\gamma_{s3}^{(1)}(s, x_3) = 2\phi_{,3} \tag{8d}$$

$$\gamma_{n3}^{(0)}(s, x_3) = \gamma_{13}^{(0)}x_{2,s} - \gamma_{23}^{(0)}x_{1,s} \tag{8e}$$

2.3. Stress

The stress–strain relation of the PMF thin-walled beams whose material properties vary continuously in the thickness can be written as follows:

$$\left\{\begin{array}{c} \sigma_{33} \\ \sigma_{s3} \\ \sigma_{n3} \end{array}\right\} = \left(\begin{array}{ccc} Q_{11} & 0 & 0 \\ 0 & Q_{66} & 0 \\ 0 & 0 & Q_{55} \end{array}\right) \left\{\begin{array}{c} \varepsilon_{33} \\ \gamma_{s3} \\ \gamma_{n3} \end{array}\right\} \tag{9}$$

where $Q_{11} = E(n)$, $Q_{66} = Q_{55} = \frac{E(n)}{2(1+\nu)}$; $E(n)$ is Young's modulus; ν is constant Poisson's ratio. In this study, two porosity patterns (Chen, Yang, and Kitipornchai 2015; Fang et al. 2019; Gao, Li, and Yang 2019) of PMF thin-walled beams are considered as indicated in Fig. 2.

a) Symmetric pore distribution (Type A)

b) Asymmetric pore distribution (Type B)
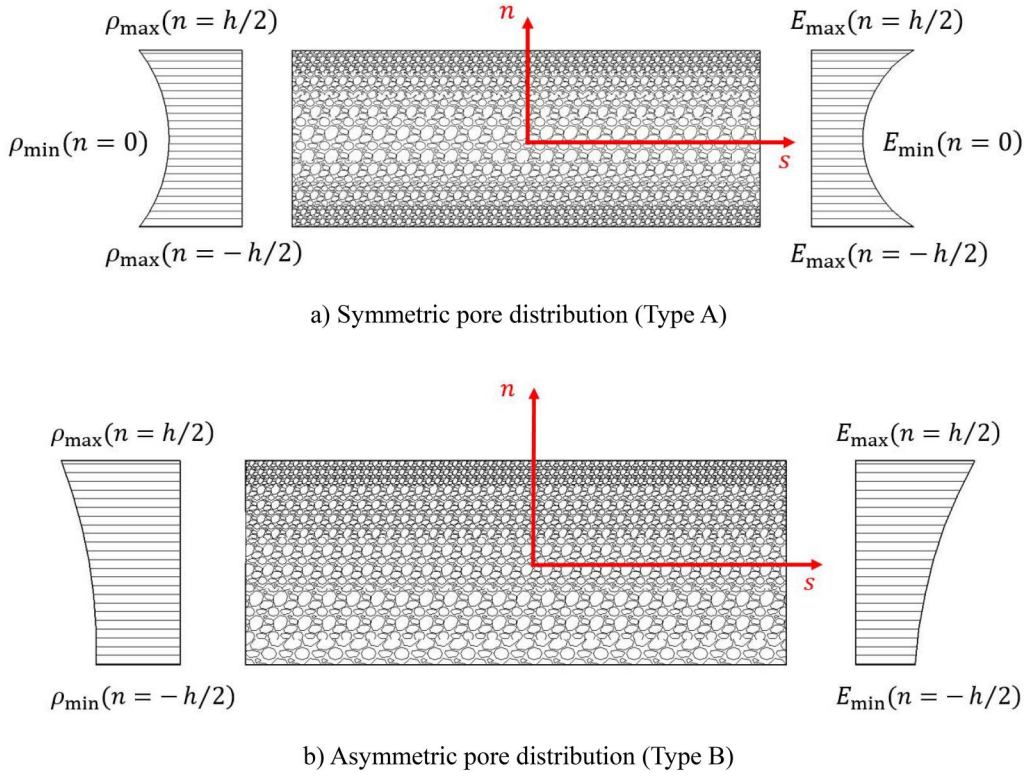
Figure 2. Porous metal foam (PMF) material distribution in the wall thickness.

Symmetric pore distribution (Type A)

$$E(n) = E_{\max}\left(1 - e_0 \cos\left(\frac{\pi n}{h}\right)\right) \tag{10a}$$

$$\rho(n) = \rho_{\max}\left(1 - e_m \cos\left(\frac{\pi n}{h}\right)\right) \tag{10b}$$

Asymmetric pore distribution (Type B)

$$E(n) = E_{\max}\left[1 - e_0 \cos\left(\frac{\pi n}{2h} + \frac{\pi}{4}\right)\right] \tag{11a}$$

$$\rho(n) = \rho_{\max}\left[1 - e_m \cos\left(\frac{\pi n}{2h} + \frac{\pi}{4}\right)\right] \tag{11b}$$

where: $E_{\max}$ and $\rho_{\max}$ are the maximum values of Young's modulus and mass density, respectively; e_0 and $e_m = 1 - \sqrt{1 - e_0}$ are the porosity parameters; $\rho(n)$ is mass density of the PMF thin-walled beams.

2.4. Variational formulation

The characteristic equations of the system can be derived from Hamilton's principle (Goldstein 1980) as follows:

$$\int_{t_1}^{t_2} (\delta\Pi_S + \delta\Pi_W - \delta\Pi_K)dt = 0 \tag{12}$$

where the variation of strain energy $\delta\Pi_S$ of the system is defined by:

$$\delta\Pi_S = \int_V (\sigma_{33}\delta\varepsilon_{33} + \sigma_{s3}\delta\gamma_{s3} + \sigma_{n3}\delta\gamma_{n3})dV \tag{13}$$

where the shear correction coefficient is assumed to be unity. Substituting Eq. (7) into Eq. (13) leads to:

$$\delta\Pi_S = \int_0^L \Big[T_{33}\delta u_{3,3}^{(0)} + M_{22}\delta\theta_{2,3} + M_{11}\delta\theta_{1,3} + M_{\varpi}\delta\phi_{,33} \\ + V_{11}\delta\Big(u_{1,3}^P + \theta_2\Big) + V_{22}\delta\Big(u_{2,3}^P + \theta_1\Big) + M_{33}\delta\phi_{,3}\Big]dx_3 \tag{14}$$

where the stress resultants $(T_{33}, M_{22}, M_{11}, M_{\varpi}, V_{11}, V_{22}, M_{33})$ are defined as follows:

$$(T_{33}, M_{22}, M_{11}, M_{\varpi}) = \int_A (1, X_1, X_2, nr_s - F_{\omega})\sigma_{33}dsdn \tag{15a}$$

$$(V_{11}, V_{22}, M_{33}) = \int_A (\sigma_{s3}x_{1,s} + \sigma_{n3}x_{2,s}, \sigma_{s3}x_{2,s} - \sigma_{n3}x_{1,s}, 2n\sigma_{s3})dsdn \tag{15b}$$

These stress resultants are related to the displacement gradients as follows:

$$\begin{Bmatrix} T_{33} \\ M_{22} \\ M_{11} \\ V_{11} \\ V_{22} \\ M_{33} \\ M_{\varpi} \end{Bmatrix} = \begin{bmatrix} L_{11} & L_{12} & L_{13} & 0 & 0 & 0 & L_{17} \\ L_{12} & L_{22} & L_{23} & 0 & 0 & 0 & L_{27} \\ L_{13} & L_{23} & L_{33} & 0 & 0 & 0 & L_{37} \\ 0 & 0 & 0 & L_{44} & L_{45} & L_{46} & 0 \\ 0 & 0 & 0 & L_{45} & L_{55} & L_{56} & 0 \\ 0 & 0 & 0 & L_{46} & L_{56} & L_{66} & 0 \\ 0 & 0 & 0 & 0 & 0 & 0 & L_{77} \end{bmatrix} \begin{Bmatrix} u_{3,3}^{(0)} \\ \theta_{2,3} \\ \theta_{1,3} \\ u_{1,3}^P + \theta_2 \\ u_{2,3}^P + \theta_1 \\ \phi_{,3} \\ \phi_{,33} \end{Bmatrix} \tag{16}$$

where the stiffness components of the PMF thin-walled beams are defined by:

$$L_{11} = \int_s A_{11}ds, \quad L_{12} = \int_s (A_{11}x_1 + B_{11}x_{2,s})ds, \quad L_{13} = \int_s (A_{11}x_2 - B_{11}x_{1,s})ds$$

$$L_{17} = \int_s (B_{11}r_s - A_{11}F_{\omega})ds, \quad L_{22} = \int_s \Big(A_{11}x_1^2 + 2B_{11}x_1x_{2,s} + D_{11}x_{2,s}^2\Big)ds$$

$$L_{23} = \int_s \Big[A_{11}x_1x_2 + B_{11}(x_2x_{2,s} - x_1x_{1,s}) - D_{11}x_{1,s}x_{2,s}\Big]ds$$

$$L_{27} = \int_s [-A_{11}x_1F_\omega + B_{11}(x_1r_s - x_{2,s}F_\omega) + D_{11}r_sx_{2,s}]ds$$

$$L_{33} = \int_s \left(A_{11}x_2^2 - 2B_{11}x_{1,s}x_2 + D_{11}x_{1,s}^2\right)ds$$

$$L_{37} = \int_s [-A_{11}x_2F_\omega + B_{11}(x_2r_s + x_{1,s}F_\omega) - D_{11}r_sx_{1,s}]ds$$

$$L_{44} = \int_s \left(A_{66}x_{1,s}^2 + A_{55}x_{2,s}^2\right)ds, \; L_{45} = \int_s (A_{66} - A_{55})x_{1,s}x_{2,s}ds, \; L_{46} = \int_s 2B_{66}x_{1,s}ds$$

$$L_{55} = \int_s \left(A_{66}x_{2,s}^2 + A_{55}x_{1,s}^2\right)ds, \; L_{56} = \int_s 2B_{66}x_{2,s}ds, \; L_{66} = \int_s 4D_{66}ds$$

$$L_{77} = \int_s \left(A_{11}F_\omega^2 - 2B_{11}r_sF_\omega + D_{11}r_s^2\right)ds$$

$$(A_{ij}, B_{ij}, D_{ij}) = \int_s (1, n, n^2)Q_{ij}ds \tag{17}$$

The variation of the geometric incremental potential is given by:

$$\delta\Pi_w = N^0 \int_0^L \left[\delta u_{1,3}^P(u_{1,3}^P - J_P\phi_{,3}) + \delta u_{2,3}^P(u_{2,3}^P + I_P\phi_{,3}) + \delta\phi_{,3}(I_Pu_{2,3}^P - J_Pu_{1,3}^P + K_p\phi_{,3})\right]dx_3 \tag{18}$$

where

$$(I_P, J_P, K_p) = \iint_{s\,n} \left[X_1 - x_1^P, X_2 - x_2^P, (X_1 - x_1^P)^2 + (X_2 - x_2^P)^2\right]dsdn \tag{19}$$

The variation of kinetic energy Π_K of the system is given by:

$$\delta\Pi_K = \int_\Omega \rho(n)(\dot{u}_1\delta\dot{u}_1 + \dot{u}_2\delta\dot{u}_2 + \dot{u}_3\delta\dot{u}_3)d\Omega$$

$$= \int_0^L \left\{ \delta\dot{u}_1^P\left(m_1\dot{u}_1^P - m_2\dot{\phi}\right) + \delta\dot{u}_2^P\left(m_1\dot{u}_2^P + m_3\dot{\phi}\right) + \delta\dot{u}_3^{(0)}\left(m_1\dot{u}_3^{(0)} + m_6\dot{\theta}_2 + m_{10}\dot{\theta}_1 - m_{13}\dot{\phi}_{,3}\right) \right.$$

$$+ \delta\dot{\theta}_2\left(m_6\dot{u}_3^{(0)} + m_7\dot{\theta}_2 + m_8\dot{\theta}_1 - m_9\dot{\phi}_{,3}\right) + \delta\dot{\theta}_1\left(m_{10}\dot{u}_3^{(0)} + m_8\dot{\theta}_2 + m_{11}\dot{\theta}_1 - m_{12}\dot{\phi}_{,3}\right)$$

$$\left. + \delta\dot{\phi}\left[-m_2\dot{u}_1^P + m_3\dot{u}_2^P + (m_4 + m_5)\dot{\phi}\right] + \delta\dot{\phi}_{,3}\left[-m_{13}\dot{u}_3^{(0)} - m_9\dot{\theta}_2 - m_{12}\dot{\theta}_1 + m_{14}\dot{\phi}_{,3}\right] \right\}dx_3 \tag{20}$$

Table 1. Shape functions and essential BCs of PMF thin-walled box beams.

BC	$\varphi_j(x_3)$	$x_3 = 0$	$x_3 = L$
S–S	$(x_3 - L)\left(1 - \dfrac{x_3}{L}\right)e^{\frac{-jx_3}{L}}$	$\xi = \eta = \phi = 0$	$\xi = \eta = \phi = 0$
C–F	$\left(\dfrac{x_3}{L}\right)^2 e^{\frac{-jx_3}{L}}$	$\xi = \eta = \phi = 0$ $\xi_{,3} = \eta_{,3} = \phi_{,3} = 0$ $\zeta = \psi_2 = \psi_1 = \psi_\varpi = 0$	
C–C	$\left(\dfrac{x_3}{L}\right)^2\left(1 - \dfrac{x_3}{L}\right)^2 e^{\frac{-jx_3}{L}}$	$\xi = \eta = \phi = 0$ $\xi_{,3} = \eta_{,3} = \phi_{,3} = 0$ $\zeta = \psi_2 = \psi_1 = \psi_\varpi = 0$	$\xi = \eta = \phi = 0$ $\xi_{,3} = \eta_{,3} = \phi_{,3} = 0$ $\zeta = \psi_2 = \psi_1 = \psi_\varpi = 0$

where the terms of mass m_i are given as follows:

$$\{m_1, m_2, m_3, m_4, m_5\} = \int_A \rho\left\{1, X_2 - x_2^P, X_1 - x_1^P, (X_2 - x_2^P)^2, (X_1 - x_1^P)^2\right\}dnds \tag{21a}$$

$$\{m_6, m_7, m_8, m_9\} = \int_A \rho X_1\{1, X_1, X_2, \bar{F}_\omega\}dnds \tag{21b}$$

$$\{m_{10}, m_{11}, m_{12}\} = \int_A \rho X_2\{1, X_2, \bar{F}_\omega\}dnds \tag{21c}$$

$$\{m_{13}, m_{14}\} = \int_A \rho\{\bar{F}_\omega, \bar{F}_\omega^2\}dnds \tag{21d}$$

2.5. Hybrid series solution

The displacement field is approximated *via* Ritz-type series with six unknowns ($u_{1j}^P(t)$, $u_{2j}^P(t)$, $u_{3j}(t)$, $\theta_{2j}(t)$, $\theta_{1j}(t)$ and $\phi_j(t)$) and hybrid shape functions $\psi_j(x_3)$ as follows:

$$\{u_1^P, u_2^P, \phi\}(x_3, t) = \sum_{j=1}^m \psi_j(x_3)\{u_{1j}^P, u_{2j}^P, \phi_j\}(t) \tag{22a}$$

$$\{u_3^{(0)}, \theta_1, \theta_2\}(x_3, t) = \sum_{j=1}^m \psi_{j,3}(x_3)\{u_{3j}, \theta_{1j}, \theta_{2j}\}(t) \tag{22b}$$

In this paper, hybrid shape functions in Table 1 are combined of exponential and admissible functions to satisfy various boundary conditions (BCs).

By substituting Eq. (22) into Eqs. (14) (18) and (20), and then the subsequent results into Eq. (12) lead to the characteristic equations for buckling and vibration analysis of PMF thin-walled box beams as follows:

$$(\mathbf{K}_m + \mathbf{K}_g)\mathbf{d} + \mathbf{M}\ddot{\mathbf{d}} = \mathbf{0} \tag{23}$$

where $\mathbf{K}_m, \mathbf{K}_g$ are the material and geometric stiffness matrix, respectively; $\mathbf{M}$ is the mass matrix; $\mathbf{d} = \begin{bmatrix} \mathbf{u}_1^P & \mathbf{u}_2^P & \mathbf{u}_3 & \boldsymbol{\theta}_2 & \boldsymbol{\theta}_1 & \boldsymbol{\Phi} \end{bmatrix}^T$ is the displacement vector. The material stiffness matrix $\mathbf{K}_m$ is given

as:

$$\mathbf{K}_m = \begin{bmatrix} \mathbf{K}_m^{11} & \mathbf{K}_m^{12} & \mathbf{0} & \mathbf{K}_m^{14} & \mathbf{K}_m^{15} & \mathbf{K}_m^{16} \\ {}^T\mathbf{K}_m^{12} & \mathbf{K}_m^{22} & \mathbf{0} & \mathbf{K}_m^{24} & \mathbf{K}_m^{25} & \mathbf{K}_m^{26} \\ {}^T\mathbf{K}_m^{13} & {}^T\mathbf{K}_m^{23} & \mathbf{K}_m^{33} & \mathbf{K}_m^{34} & \mathbf{K}_m^{35} & \mathbf{K}_m^{36} \\ {}^T\mathbf{K}_m^{14} & {}^T\mathbf{K}_m^{24} & {}^T\mathbf{K}_m^{34} & \mathbf{K}_m^{44} & \mathbf{K}_m^{45} & \mathbf{K}_m^{46} \\ {}^T\mathbf{K}_m^{15} & {}^T\mathbf{K}_m^{25} & {}^T\mathbf{K}_m^{35} & {}^T\mathbf{K}_m^{45} & \mathbf{K}_m^{55} & \mathbf{K}_m^{56} \\ {}^T\mathbf{K}_m^{16} & {}^T\mathbf{K}_m^{26} & {}^T\mathbf{K}_m^{36} & {}^T\mathbf{K}_m^{46} & {}^T\mathbf{K}_m^{56} & \mathbf{K}_m^{66} \end{bmatrix} \tag{24}$$

where

$$K_{mij}^{11} = L_{44}S_{ij}^{11}, K_{mij}^{12} = L_{45}S_{ij}^{11}, K_{mij}^{14} = L_{44}S_{ij}^{11}, K_{mij}^{15} = L_{45}S_{ij}^{11}, K_{mij}^{16} = L_{46}S_{ij}^{11}$$

$$K_{mij}^{22} = L_{55}S_{ij}^{11}, K_{mij}^{24} = L_{45}S_{ij}^{11}, K_{mij}^{25} = L_{55}S_{ij}^{11}, K_{mij}^{26} = L_{56}S_{ij}^{11}$$

$$K_{mij}^{33} = L_{11}S_{ij}^{22}, K_{mij}^{34} = L_{12}S_{ij}^{22}, K_{mij}^{35} = L_{13}S_{ij}^{22}, K_{mij}^{36} = L_{17}S_{ij}^{22}$$

$$K_{mij}^{44} = L_{22}S_{ij}^{22} + L_{44}S_{ij}^{11}, K_{mij}^{45} = L_{23}S_{ij}^{22} + L_{45}S_{ij}^{11}$$

$$K_{mij}^{46} = L_{27}S_{ij}^{22} + L_{46}S_{ij}^{11}, K_{mij}^{55} = L_{33}S_{ij}^{22} + L_{55}S_{ij}^{11}$$

$$K_{mij}^{56} = L_{37}S_{ij}^{22} + L_{56}S_{ij}^{11}, K_{mij}^{66} = L_{77}S_{ij}^{22} + L_{66}S_{ij}^{11}$$

$$S_{ij}^{rs} = \int_0^L \frac{\partial^r \psi_i}{\partial x_3^r} \frac{\partial^s \psi_j}{\partial x_3^s} dx_3 \tag{25}$$

The geometric stiffness matrix $\mathbf{K}_g$ is given by:

$$\mathbf{K}_g = \begin{bmatrix} \mathbf{K}_g^{11} & \mathbf{0} & \mathbf{0} & \mathbf{0} & \mathbf{0} & \mathbf{K}_g^{16} \\ \mathbf{0} & \mathbf{K}_g^{22} & \mathbf{0} & \mathbf{0} & \mathbf{0} & \mathbf{K}_g^{26} \\ \mathbf{0} & \mathbf{0} & \mathbf{0} & \mathbf{0} & \mathbf{0} & \mathbf{0} \\ \mathbf{0} & \mathbf{0} & \mathbf{0} & \mathbf{0} & \mathbf{0} & \mathbf{0} \\ \mathbf{0} & \mathbf{0} & \mathbf{0} & \mathbf{0} & \mathbf{0} & \mathbf{0} \\ {}^T\mathbf{K}_g^{16} & {}^T\mathbf{K}_g^{26} & \mathbf{0} & \mathbf{0} & \mathbf{0} & \mathbf{K}_g^{66} \end{bmatrix}$$

where

$$K_{gij}^{11} = S_{ij}^{11}, K_{gij}^{16} = -J_P S_{ij}^{11}, K_{gij}^{22} = S_{ij}^{11}, K_{gij}^{26} = I_P S_{ij}^{11}, K_{gij}^{66} = K_P S_{ij}^{11}$$

$$(I_P, J_P, K_P) = \int_{n,s} \frac{1}{A} \left[X_1 - x_1^P, X_2 - x_2^P, (X_1 - x_1^P)^2 + (X_2 - x_2^P)^2 \right] dsdn \tag{26}$$
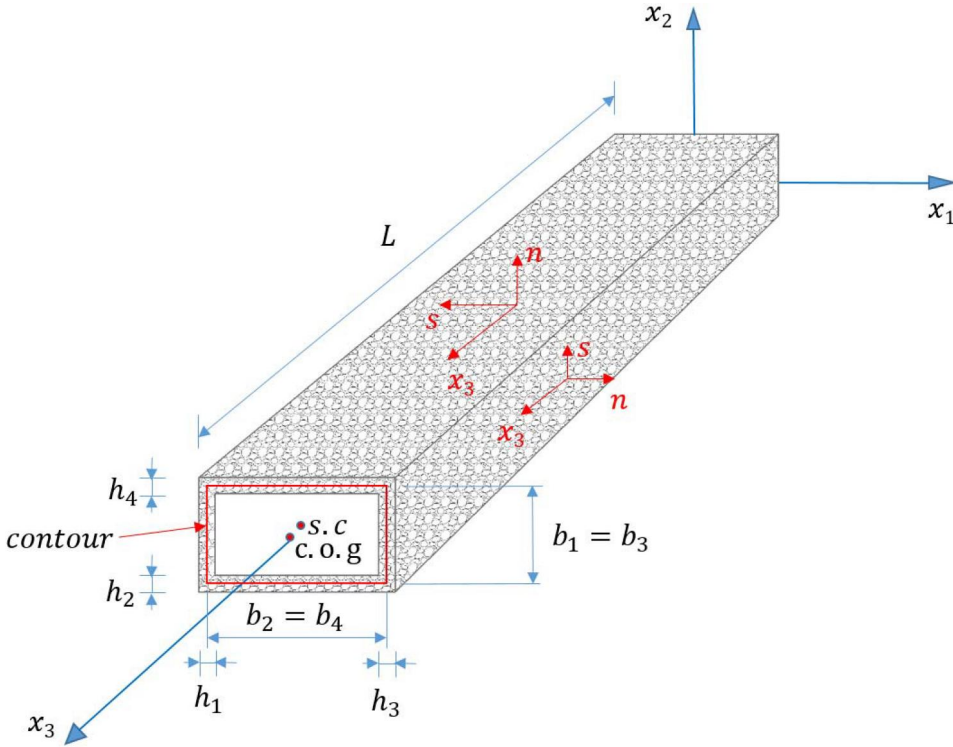
Figure 3. Geometry of PMF thin-walled box beams.

Table 2. Convergence of fundamental frequencies (Hz) and critical buckling load (MN) of the PMF thin-walled box beams.

	m					
BCs	2	4	6	8	10	12
Critical buckling loads (MN)						
S–S	0.24018	0.23473	0.23307	0.23305	0.23305	0.23305
C–C	0.45929	0.45862	0.45851	0.45851	0.45851	0.45851
C–F	0.06162	0.05830	0.05830	0.05830	0.05830	0.05830
Fundamental frequencies (Hz)						
S–S	141.27	139.43	138.90	138.90	138.90	138.90
C–C	203.98	197.32	196.29	196.13	196.12	196.11
C–F	50.22	49.55	49.51	49.51	49.51	49.51

The components of mass matrix $\mathbf{M}$ are given by:

$$\mathbf{M} = \begin{bmatrix} \mathbf{M}^{11} & \mathbf{0} & \mathbf{0} & \mathbf{0} & \mathbf{0} & \mathbf{M}^{16} \\ \mathbf{0} & \mathbf{M}^{22} & \mathbf{0} & \mathbf{0} & \mathbf{0} & \mathbf{M}^{26} \\ \mathbf{0} & \mathbf{0} & {}^{T}\mathbf{M}^{33} & \mathbf{M}^{34} & \mathbf{M}^{35} & \mathbf{M}^{36} \\ \mathbf{0} & \mathbf{0} & {}^{T}\mathbf{M}^{34} & \mathbf{M}^{44} & \mathbf{M}^{45} & \mathbf{M}^{46} \\ \mathbf{0} & \mathbf{0} & {}^{T}\mathbf{M}^{35} & {}^{T}\mathbf{M}^{45} & \mathbf{M}^{55} & \mathbf{M}^{56} \\ {}^{T}\mathbf{M}^{16} & {}^{T}\mathbf{M}^{26} & {}^{T}\mathbf{M}^{36} & {}^{T}\mathbf{M}^{46} & {}^{T}\mathbf{M}^{56} & \mathbf{M}^{66} \end{bmatrix} \tag{27}$$

where

$$M_{ij}^{11} = m_1 S_{ij}^{00}, M_{ij}^{16} = -m_2 S_{ij}^{00}, M_{ij}^{22} = m_1 S_{ij}^{00}, M_{ij}^{26} = m_3 S_{ij}^{00}, M_{ij}^{33} = m_1 S_{ij}^{11}$$

Table 3. Verification of the critical buckling loads ($10^6 N$) of the FG thin-walled box beams.

BC	Mode	References	p							
			0	0.2	0.5	1	2	5	10	1000
$L/b_3 = 80$										
C–F	Y	Present	0.08550	0.07433	0.06305	0.05162	0.04000	0.02809	0.02255	0.01583
	Y	Lanc et al. (2015)	0.08552	0.07435	0.06306	0.05163	0.04001	0.02810	0.02255	0.01583
	X	Present	0.24406	0.21133	0.17849	0.14551	0.11232	0.07886	0.06351	0.04516
	X	Lanc et al. (2015)	0.24420	0.21146	0.17859	0.14559	0.11239	0.07890	0.06355	0.04519
S–S	Y	Present	0.34182	0.29714	0.25204	0.20637	0.15991	0.11231	0.09014	0.06327
	Y	Lanc et al. (2015)	0.34209	0.29740	0.25225	0.20654	0.16004	0.11240	0.09022	0.06332
	X	Present	0.97463	0.84391	0.71277	0.58105	0.44854	0.31490	0.25363	0.18036
	X	Lanc et al. (2015)	0.97683	0.84587	0.71439	0.58237	0.44956	0.31562	0.25421	0.18076
C–C	Y	Present	1.36407	1.18577	1.00578	0.82351	0.63810	0.44815	0.35972	0.25248
	Y	Lanc et al. (2015)	1.36903	1.19017	1.00947	0.82655	0.64047	0.44982	0.36105	0.25340
	X	Present	3.87270	3.35325	2.83210	2.30870	1.78217	1.25117	1.00776	0.71664
	X	Lanc et al. (2015)	3.90921	3.38512	2.85891	2.33061	1.79912	1.26307	1.01732	0.72340
$L/b_3 = 20$										
C–F	Y	Present	1.36407	1.18577	1.00578	0.82351	0.63810	0.44815	0.35972	0.25248
	X	Present	3.87270	3.35325	2.83210	2.30870	1.78217	1.25117	1.00776	0.71664
S–S	Y	Present	5.40583	4.69897	3.98544	3.26299	2.52819	1.77558	1.42530	1.00060
	X	Present	15.09092	13.06604	11.03473	8.99483	6.94309	4.87435	3.92625	2.79256
C–C	Y	Present	20.85207	18.12158	15.36625	12.57769	9.74325	6.84270	5.49386	3.85957
	X	Present	54.71422	47.36360	39.99177	32.59172	25.15278	17.65808	14.22589	10.12471
$L/b_3 = 10$										
C–F	Y	Present	5.40583	4.69897	3.98544	3.26299	2.52818	1.77558	1.42530	1.00059
	X	Present	15.09092	13.06604	11.03473	8.99483	6.94309	4.87435	3.92625	2.79256
S–S	Y	Present	20.85207	18.12159	15.36625	12.57770	9.74325	6.84270	5.49386	3.85957
	X	Present	54.71424	47.36359	39.99177	32.59172	25.15278	17.65808	14.22590	10.12471
C–C	Y	Present	72.99406	63.38984	53.70910	43.92641	34.00344	23.87902	19.18438	13.51007
	X	Present	159.24272	137.77879	116.26984	94.70104	73.04994	51.28126	41.33262	29.46647

Table 4. Verification of the critical buckling loads ($10^6 N$) of the FG thin-walled box beams (1-2-1 skin–core–skin ratio).

BC	Mode	References	p							
			0	0.2	0.5	1	2	5	10	1000
$L/b_3 = 80$										
C–F	Y	Present	0.08550	0.07969	0.07387	0.06805	0.06224	0.05642	0.05378	0.05064
	Y	Lanc et al. (2015)	0.08552	0.07970	0.07388	0.06807	0.06225	0.05643	0.05379	0.05062
	X	Present	0.24406	0.22747	0.21088	0.19428	0.17769	0.16109	0.15355	0.14460
	X	Lanc et al. (2015)	0.24420	0.22760	0.21099	0.19439	0.17779	0.16119	0.15364	0.14458
S–S	Y	Present	0.34182	0.31856	0.29530	0.27205	0.24880	0.22555	0.21499	0.20246
	Y	Lanc et al. (2015)	0.34209	0.31882	0.29554	0.27227	0.24900	0.22574	0.21517	0.20248
	X	Present	0.97463	0.90836	0.84210	0.77583	0.70957	0.64330	0.61319	0.57744
	X	Lanc et al. (2015)	0.97683	0.91042	0.84400	0.77758	0.71117	0.64476	0.61457	0.57835
C–C	Y	Present	1.36407	1.27125	1.17845	1.08565	0.99287	0.90011	0.85795	0.80793
	Y	Lanc et al. (2015)	1.36903	1.27587	1.18273	1.08959	0.99648	0.90338	0.86107	0.81031
	X	Present	3.87270	3.60938	3.34607	3.08276	2.81946	2.55617	2.43650	2.29448
	X	Lanc et al. (2015)	3.90921	3.64341	3.37761	3.11182	2.84604	2.58027	2.45947	2.31451
$L/b_3 = 20$										
C–F	Y	Present	1.36407	1.27125	1.17845	1.08565	0.99287	0.90011	0.85795	0.80793
	X	Present	3.87270	3.60938	3.34607	3.08276	2.81946	2.55617	2.43650	2.29448
S–S	Y	Present	5.40583	5.03800	4.67020	4.30245	3.93476	3.56716	3.40010	3.20186
	X	Present	15.09092	14.06484	13.03878	12.01275	10.98674	9.96077	9.49444	8.94101
C–C	Y	Present	20.85207	19.43327	18.01459	16.59609	15.17782	13.75985	13.11544	12.35078
	X	Present	54.71422	50.99411	47.27403	43.55403	39.83412	36.11434	34.42360	32.41701
$L/b_3 = 10$										
C–F	Y	Present	5.40583	5.03800	4.67020	4.30245	3.93476	3.56716	3.40009	3.20186
	X	Present	15.09092	14.06485	13.03879	12.01275	10.98674	9.96077	9.49444	8.94100
S–S	Y	Present	20.85207	19.43327	18.01459	16.59609	15.17782	13.75985	13.11545	12.35078
	X	Present	54.71424	50.99411	47.27403	43.55404	39.83414	36.11436	34.42361	32.41705
C–C	Y	Present	72.99406	68.02798	63.06231	58.09715	53.13269	48.16917	45.91341	43.23662
	X	Present	159.24272	148.41592	137.58924	126.76267	115.93624	105.11024	100.18945	94.34946

$$M_{ij}^{34} = m_6 S_{ij}^{11}, M_{ij}^{35} = M_{10} S_{ij}^{11}, M_{ij}^{36} = -m_{13} S_{ij}^{11}, M_{ij}^{44} = m_7 S_{ij}^{11}, M_{ij}^{45} = m_8 S_{ij}^{11}$$

$$M_{ij}^{34} = m_6 S_{ij}^{11}, M_{ij}^{35} = M_{10} S_{ij}^{11}, M_{ij}^{36} = -m_{13} S_{ij}^{11}, M_{ij}^{44} = m_7 S_{ij}^{11}, M_{ij}^{45} = m_8 S_{ij}^{11}$$

$$M_{ij}^{46} = -m_9 S_{ij}^{11}, M_{ij}^{55} = m_{11} S_{ij}^{11}, M_{ij}^{56} = -m_{12} S_{ij}^{11}, M_{ij}^{66} = m_{14} S_{ij}^{11} + (m_4 + m_5) S_{ij}^{00} \tag{28}$$

It is noted that the free vibration behaviors are obtained by setting $\mathbf{d}(t) = \mathbf{d} e^{i\omega t}$ where ω is the natural frequency and $i^2 = -1$ is the imaginary unit, and then solving the subsequent result $(\mathbf{K} - \omega^2 \mathbf{M})\mathbf{d} = \mathbf{0}$. The buckling responses are found by solving $\det(\mathbf{K}_m - N_0 \mathbf{K}_g) = \mathbf{0}$.

3. Numerical results

The present FTWBT model for the PMF box beams is compared and computed for different cases in this section. Porous alumina, which is chosen in this study, has been widely used in the industry due to many advantages such as cost, environmental sustainability, and production time. Its material properties are assumed to be $E_{\max} = 380 GPa$, $v = 0.3$, $\rho_{\max} = 3800 kgm^{-3}$. The following subsections investigate the effects of porosity, boundary conditions (BCs) and geometry on the buckling and vibration behaviors of the PMF thin-walled box beams. It is noted that when $e_0 = 0$, the PMF thin-walled box beam is isotropic, homogenous and pore-less.

3.1. Convergence study

By refering to the geometry symbols shown in Fig. 3, the convergence and accuracy of the present solution are studied for the sample thin-walled box beams with the following dimensions:

Buckling analysis: $h = h_1 = h_2 = h_3 = h_4 = 0.005m$, $b_1 = b_3 = 0.1m$, $b_2 = b_4 = 0.2m$, $L = 8m$.

Vibration analysis: $h = h_1 = h_2 = h_3 = h_4 = 0.000762m$, $b_1 = b_3 = 0.0136m - h$, $b_2 = b_4 = 0.0242m - h$, $L = 0.762m$.

Table 2 shows the fundamental frequencies and the critical buckling loads of the PMF thin-walled box beams as the series number m increases. It can be seen that the present solution

Table 5. Verification of vibration analysis (rad/s) of the PMF thin-walled and thick-walled box beams.

BC	References	$p = 0.2$ Mode Y	Mode X	$p = 1$ Mode Y	Mode X	$p = 10$ Mode Y	Mode X
Thin-walled box beam							
C–F	Present	324.84	510.28	285.79	446.86	203.40	317.90
	Ziane et al. (2013)	324.61	509.80	285.57	446.42	203.24	317.61
	Abaqus (Ziane et al. 2013)	321.65	509.00	283.05	447.19	203.16	319.36
S–S	Present	911.37	1430.56	801.81	1252.75	570.65	891.23
	Ziane et al. (2013)	909.98	1427.72	800.50	1250.22	569.72	889.43
	Abaqus (Ziane et al. 2013)	913.20	1433.70	805.30	1261.20	574.16	898.29
C–C	Present	2060.33	3221.20	1812.57	2820.71	1290.01	2006.70
	Ziane et al. (2013)	2044.51	3189.01	1797.73	2791.97	1279.39	1986.23
	Abaqus (Ziane et al. 2013)	1998.40	3180.80	1752.90	2789.90	1256.40	1992.50
Thick-walled box beam							
C–F	Present	243.02	477.86	223.50	422.91	160.59	301.28
	Ziane et al. (2013)	242.87	476.97	223.32	422.08	160.45	300.68
	Abaqus (Ziane et al. 2013)	254.13	492.69	236.17	448.12	171.46	322.42
S–S	Present	681.37	1335.44	626.59	1181.78	450.20	841.90
	Ziane et al. (2013)	680.53	1330.39	625.55	1176.97	449.41	838.44
	Abaqus (Ziane et al. 2013)	709.67	1372.60	659.38	1248.00	478.70	897.87
C–C	Present	1535.21	2958.56	1410.85	2616.54	1013.56	1863.88
	Ziane et al. (2013)	1525.49	2903.00	1398.94	2563.97	1004.50	1826.14
	Abaqus (Ziane et al. 2013)	1584.90	3025.70	1469.40	2744.90	1067.40	1974.80

Table 6. Buckling loads (*MN*) of PMF thin-walled box beams with various values of porosity parameter e_0.

BC	Mode	e_0 0	0.1	0.2	0.3	0.4	0.5	0.6	0.7
Type A, $L/b_3 = 80$									
S–S	x_2	0.34182	0.32006	0.29831	0.27655	0.25480	0.23305	0.21129	0.18954
	x_1	0.97463	0.91259	0.85054	0.78850	0.72646	0.66441	0.60237	0.54033
C–C	Min	0.57432	0.55116	0.52800	0.50483	0.48167	0.45851	0.43534	0.41218
	x_2	1.36407	1.27726	1.19045	1.10363	1.01682	0.93001	0.84319	0.75638
	x_1	3.87270	3.62617	3.37964	3.13311	2.88658	2.64005	2.39351	2.14698
C–F	x_2	0.08550	0.08006	0.07462	0.06918	0.06374	0.05830	0.05285	0.04741
	x_1	0.24406	0.22853	0.21299	0.19745	0.18192	0.16638	0.15084	0.13531
Type B, $L/b_3 = 80$									
S–S	x_2	0.34182	0.32057	0.29931	0.27806	0.25681	0.23556	0.21431	0.19306
	x_1	0.97463	0.91309	0.85155	0.79001	0.72848	0.66694	0.60540	0.54386
C–C	Min	0.57432	0.54047	0.50662	0.47277	0.43892	0.40506	0.37121	0.33735
	x_2	1.36407	1.27926	1.19446	1.10965	1.02484	0.94003	0.85522	0.77041
	x_1	3.87270	3.62816	3.38362	3.13908	2.89454	2.65001	2.40547	2.16093
C–F	x_2	0.08550	0.08019	0.07487	0.06956	0.06424	0.05893	0.05361	0.04829
	x_1	0.24406	0.22865	0.21324	0.19783	0.18242	0.16701	0.15160	0.13619
Type A, $L/b_3 = 10$									
S–S	Min	1.88353	1.77722	1.67091	1.56460	1.45829	1.35198	1.24567	1.13937
	x_2	20.85207	19.52498	18.19788	16.87079	15.54369	14.21660	12.88950	11.56241
	x_1	54.71424	51.23119	47.74813	44.26508	40.78203	37.29898	33.81592	30.33287
C–C	Min	6.07297	5.70060	5.32822	4.95585	4.58348	4.21110	3.83873	3.46636
	x_2	72.99406	68.34831	63.70256	59.05680	54.41105	49.76530	45.11955	40.47379
	x_1	159.24273	149.10537	138.96801	128.83065	118.69329	108.55594	98.41858	88.28122
C–F	Min	0.83616	0.79637	0.75658	0.71679	0.67699	0.63720	0.59741	0.55762
	x_2	5.40580	5.06180	4.71775	4.37371	4.02967	3.68563	3.34158	2.99754
	x_1	15.09090	14.13020	13.16958	12.20891	11.24825	10.28758	9.32691	8.36624

converges at series number $m = 8$ for all boundary conditions. For that reason, this series number is applied in the upcoming examples.

3.2. Verification study

Since there is no previous numerical data for the vibration and buckling analysis of the PMF thin-walled box beams, the present solutions are verified with those of Ziane et al. (2013) for vibration and Lanc et al. (2015) for buckling analysis of FG thin-walled box beams. The material properties are given by: $E_c = 380 GPa, E_m = 70 GPa, \rho_c = 3800 kgm^{-3}, \rho_m = 2707 kgm^{-3}, \nu = 0.3$

Example 1: The buckling loads of the present beam model align exceptionally with those computed by Lanc et al. (2015) as shown in Tables 3 and 4. The solutions are computed with the different BCs (S–S, C–C and C–F), power-law indices p, and types of FG material distribution. It is noted that while Lanc et al. (2015) used the CTWBT, this paper applies the FTWBT. Therefore, the buckling loads computed by the present model are expected to be lower than those of Lanc et al. (2015), which is shown in all cases. Nonetheless, the differences are only noticeable in S–S and C–C beams. This is due to the shear effects being only significant when the length-to-height ratio L/b_3 is low but the current beam's L/b_3 ratio equals 80 which is relatively high. The buckling responses for the FG box beams with $L/b_3 = 10$ and $L/b_3 = 20$ are included in Tables 3 and 4 for future studies.

Example 2: The free vibration of the FG thin-walled and thick-walled box beams is examined. Table 5 shows excellent agreements between the present solutions with those from Ziane et al. (2013) and Abaqus software (Ziane et al. 2013) for all cases of $p = 0.2, 1$ and 10 under various BCs. Even though the FTWBT is used in both studies, the formulation of the stress resultants displayed in Eq. (16) of this paper is different from previous one (Ziane et al. 2013). The natural
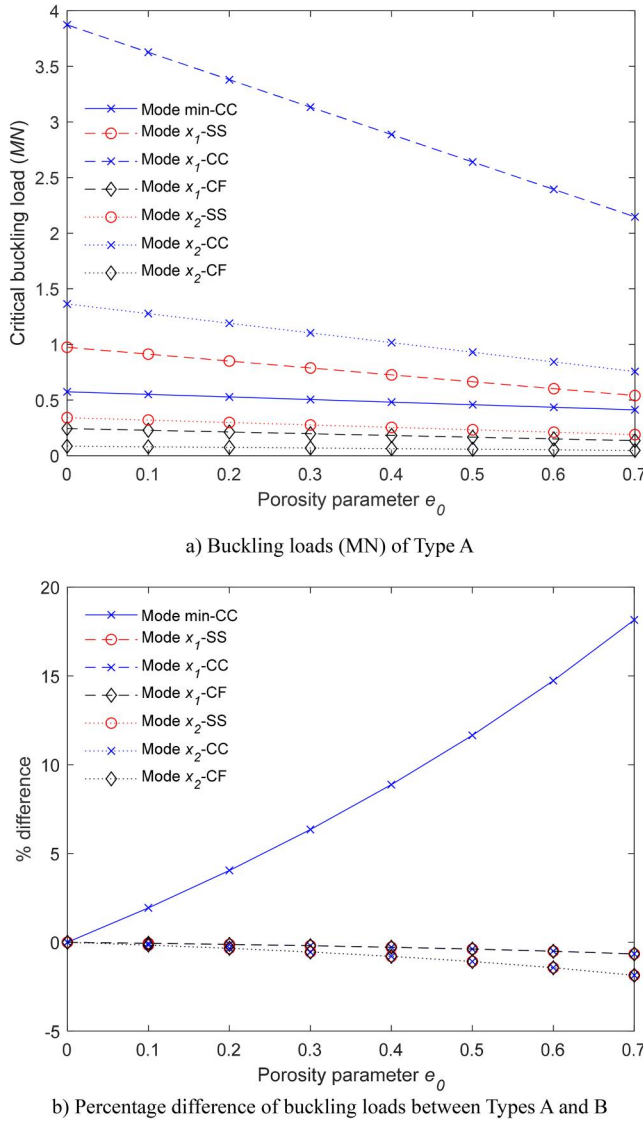
a) Buckling loads (MN) of Type A

b) Percentage difference of buckling loads between Types A and B

Figure 4. Buckling loads (MN) of PMF thin-walled box beams with respect to various values of porosity parameter e_0.

frequencies shown in Ziane et al. (2013) are for the bending modes in X and Y direction which are equivalent to those in x_1- and x_2- directions of this paper.

3.3. Parametric study

This section investigates the effects of porosity distribution (Type A and B), porosity parameters, BCs and geometry on the buckling and vibration responses of PMF thin-walled box beams, which are made from porous alumina with the following properties: $E_{max} = 380 GPa$, $\rho_{max} = 3800 kgm^{-3}$, $\nu = 0.3$. Unless stated otherwise, the geometry of the beam in this parametric study section, as displayed in Fig. 3, is $h = h_1 = h_2 = h_3 = h_4 = 0.005$ m, $b_2 = b_4 = 2b_1 = 2b_3 = 0.2m$. The percentage differences of the beams' responses between the porosity distribution Type A and Type B

Table 7. Natural frequencies (*Hz*) of PMF thin-walled box beams with various values of porosity parameter e_0 ($L/b_3 = 10$).

| BC	Mode	e_0							
		0.0	0.1	0.2	0.3	0.4	0.5	0.6	0.7
Type A									
S–S	Min	203.11	200.60	198.08	195.57	193.11	190.78	188.72	187.20
	x_2	670.41	659.59	648.46	637.05	625.43	613.72	602.23	591.60
	x_1	1072.96	1055.63	1037.81	1019.54	1000.93	982.18	963.77	946.73
C–C	Min	412.80	406.62	400.31	393.89	387.42	381.00	374.85	369.41
	x_2	1398.49	1375.91	1352.70	1328.90	1304.65	1280.23	1256.25	1234.06
	x_1	2014.93	1982.39	1948.93	1914.62	1879.66	1844.45	1809.88	1777.88
C–F	Min	92.39	91.58	90.79	90.04	89.36	88.78	88.40	88.34
	x_2	242.98	239.05	235.02	230.89	226.67	222.43	218.27	214.41
	x_1	399.37	392.92	386.29	379.49	372.56	365.58	358.73	352.39
Type B									
S–S	Min	203.11	199.95	196.70	193.38	190.02	186.65	183.37	180.38
	x_2	670.41	660.08	649.49	638.69	627.76	616.85	606.29	596.77
	x_1	1072.96	1055.88	1038.34	1020.39	1002.13	983.80	965.87	949.41
C–C	Min	412.80	406.14	399.31	392.29	385.15	377.95	370.87	364.30
	x_2	1398.49	1376.78	1354.53	1331.81	1308.78	1285.76	1263.43	1243.21
	x_1	2014.93	1982.72	1949.62	1915.71	1881.21	1846.54	1812.59	1781.34
C–F	Min	92.39	91.02	89.62	88.19	86.75	85.33	83.96	82.75
	x_2	242.98	239.24	235.41	231.50	227.54	223.60	219.78	216.35
	x_1	399.37	393.02	386.50	379.83	373.04	366.23	359.57	353.46
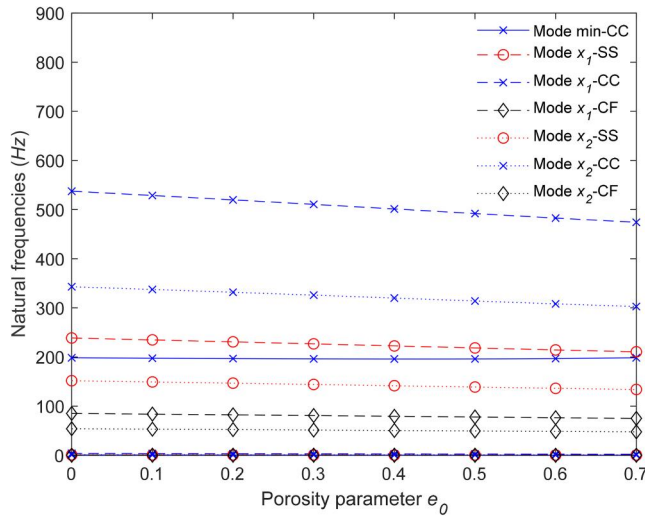
Figure 5. Natural frequencies of Type A PMF thin-walled box beams with respect to various values of porosity parameter e_0.

are computed as:

$$\frac{\text{response}_{\text{typeA}} - \text{response}_{\text{typeB}}}{\text{response}_{\text{typeA}}} \times 100\%.$$

Example 3: This example aims to investigate effects of porosity parameters and BCs on buckling and vibration of PMF thin-walled box beams. The length-to-height ratio L/b_3 is equal to 10 and 80 for the buckling analysis, and equal to 10 for the vibration analysis. Table 6 and Fig. 4 show the critical buckling loads (*MN*) while Table 7 and Fig. 5 show the natural frequencies (*Hz*) of the PMF thin-walled box beams for various e_0 and all three BCs (S–S, C–C, C–F). In Table 6, when $L/b_3 = 80$, the first buckling mode of the S–S and C–F PMF thin-walled box beams is always x_2- mode but that of C–C beams is torsional mode. When $L/b_3 = 10$, the buckling loads

Table 8. Buckling loads (*MN*) of PMF thin-walled box beams with various values of L/b_3 ($e_0 = 0.5$).

BC	Mode	L/b_3									
		10	20	30	40	50	60	70	80	90	100
Type A											
S–S	Min	1.35198	0.63720	0.50483	0.45851	0.43706	0.41405	0.30431	0.23305	0.18417	0.14919
	x_2	14.21660	3.68563	1.64936	0.93001	0.59587	0.41405	0.30431	0.23305	0.18417	0.14919
	x_1	37.29898	10.28758	4.66139	2.64005	1.69502	1.17914	0.86721	0.66441	0.52521	0.42556
C–C	Min	4.21110	1.35198	0.82252	0.63720	0.55143	0.50483	0.47674	0.45851	0.44601	0.43706
	x_2	49.76530	14.21660	6.48998	3.68563	2.36932	1.64935	1.21355	0.93001	0.73530	1.21648
	x_1	108.55587	37.29896	17.81220	10.28758	6.66666	4.66139	3.43892	2.64005	2.08984	1.69502
C–F	Min	0.63720	0.45851	0.41405	0.23305	0.14919	0.10362	0.07614	0.05830	0.04606	0.03731
	x_2	3.68563	0.93001	0.41405	0.23305	0.14919	0.10362	0.07614	0.05830	0.04606	0.03731
	x_1	10.28758	2.64005	1.17914	0.66441	0.42556	0.29566	0.21728	0.16638	0.13148	0.10650
Type B											
S–S	Min	1.29757	0.58356	0.45134	0.40506	0.38364	0.37201	0.30760	0.23556	0.18615	0.15080
	x_2	14.36292	3.72498	1.66709	0.94003	0.60230	0.41852	0.30760	0.23556	0.18615	0.15080
	x_1	37.42319	10.32539	4.67886	2.65001	1.70144	1.18361	0.87051	0.66694	0.52721	0.42718
C–C	Min	4.15358	1.29757	0.76868	0.58356	0.49788	0.45134	0.42328	0.40506	0.39257	0.38364
	x_2	50.21296	14.36292	6.55861	3.72498	2.39473	1.66709	1.22661	0.94003	0.74323	0.60230
	x_1	108.81873	37.42322	17.87596	10.32539	6.69147	4.67886	3.45186	2.65001	2.09774	1.70143
C–F	Min	0.58356	0.40506	0.37201	0.23556	0.15080	0.10474	0.07696	0.05893	0.04656	0.03772
	x_2	3.72498	0.94003	0.41852	0.23556	0.15080	0.10474	0.07696	0.05893	0.04656	0.03772
	x_1	10.32539	2.65001	1.18361	0.66694	0.42718	0.29678	0.21810	0.16701	0.13198	0.10691

Table 9. Natural frequencies (*Hz*) of PMF thin-walled box beams with various values of L/b_3 ($e_0 = 0.5$).

BCs	Mode	L/b_3								
		10	15	20	25	30	35	40	45	50
Type A										
S–S	Min	190.78	99.24	65.52	48.76	38.88	32.39	27.79	24.37	21.71
	x_2	613.72	277.71	157.23	100.94	70.21	51.64	39.56	31.27	25.34
	x_1	982.18	457.05	261.64	168.86	117.81	86.80	66.58	52.67	42.70
C–C	Min	381.00	178.83	107.55	74.11	55.59	44.12	36.44	30.98	26.92
	x_2	1280.23	604.67	348.17	225.35	157.47	116.13	89.14	70.55	57.21
	x_1	1844.45	936.03	557.45	367.28	259.33	192.50	148.39	117.81	95.75
C–F	Min	88.78	50.48	34.68	26.21	20.99	17.47	14.11	11.15	9.03
	x_2	222.43	99.72	56.27	36.06	25.06	18.42	14.11	11.15	9.03
	x_1	365.58	166.35	94.38	60.65	42.21	31.05	23.80	18.81	15.25
Type B										
S–S	Min	186.65	95.80	62.61	46.27	36.71	30.48	26.09	22.83	20.31
	x_2	616.85	279.17	158.07	101.47	70.59	51.91	39.77	31.44	25.47
	x_1	983.80	457.86	262.11	169.17	118.03	86.96	66.71	52.77	42.79
C–C	Min	377.95	176.29	105.29	72.08	53.74	42.43	34.89	29.56	25.61
	x_2	1285.76	607.60	349.94	226.52	158.30	116.75	89.61	70.92	57.52
	x_1	1846.54	937.39	558.35	367.91	259.78	182.06	148.66	118.02	95.93
C–F	Min	85.33	48.09	32.89	24.78	19.80	16.45	14.06	11.21	9.08
	x_2	223.60	100.25	56.57	36.26	25.20	18.52	14.19	11.21	9.08
	x_1	366.23	166.66	94.56	60.76	42.29	31.11	23.84	18.85	15.27

are much higher than when $L/b_3 = 80$, but these loads also decrease as the porosity parameter e_0 rises. Meanwhile, in case of $L/b_3 = 10$, Table 7 shows that the first vibration mode is always torsional mode and the corresponding frequencies are significantly lower than those of bending modes. In Figs. 4 and 5, it can be seen from Eqs. (10) and (11) that the increasing porosity parameter e_0 leads to the decrement of the Young's modulus and the mass of porous beams. Consequently, as the e_0 increases from 0 to 0.7, the critical buckling loads decrease by up to 44%. However, as shown in Fig. 5, there is a less drastic drop in natural frequencies since they are inversely proportional to the square root of mass. The reduction in the beams' stiffness is offset by the lower beams' mass and therefore, when e_0 increases from 0 to 0.7, the natural frequencies
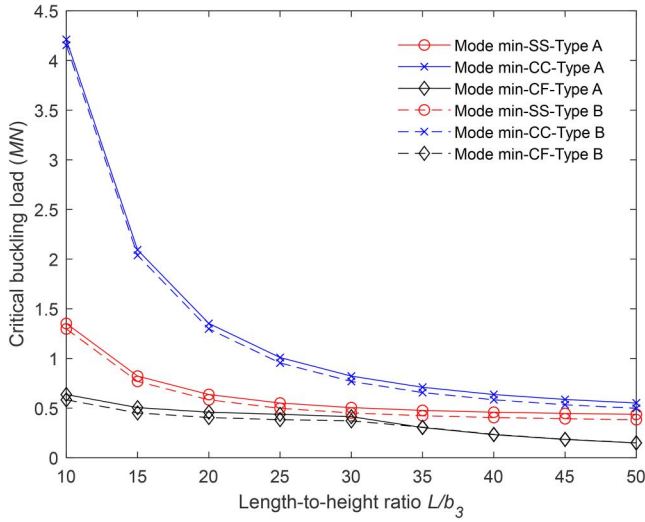
Figure 6. Critical buckling loads (MN) of Types A and B thin-walled box beams with various values of L/b_3 ($e_0 = 0.5$).
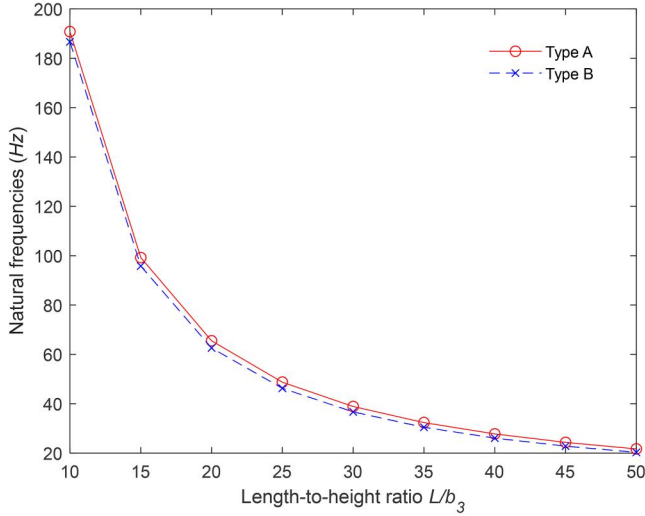

Figure 7. Natural frequencies of PMF thin-walled box S-S beams with respect to L/b_3 ($e_0 = 0.5$).

for all bending modes decrease by 11.7%. When the beam is under C–C boundary condition, the natural frequencies of its lowest mode (torsional) dip slightly as e_0 goes from 0 to 0.4. Nonetheless, when e_0 increases from 0.4 to 0.7, these natural frequencies rise to the value where $e_0 = 0$.

Example 4: The objective of this example is to consider the effect of length-to-height ratio L/b_3 on buckling and free vibration of PMF thin-walled box beams. The PMF thin-walled box beams with the aforementioned dimensions and $e_0 = 0.5$ is examined in this example. The beam's height is kept constant with $b_3 = 0.5, b_2 = 0.1$ m and the wall thickness is $h = h_1 = h_2 = h_3 = h_4 = 0.005$ m. While keeping the beam's height b_3 intact for both the buckling and vibration analysis, the length is varied for multiple L/b_3 ratios ranging from $L/b_3 = 10$ to $L/b_3 = 50$. Tables 8 and 9 show the critical buckling loads (MN) and the natural frequencies (Hz) of the PMF thin-walled beams. It is apparent that the short beams are much stiffer than the long ones which can be seen
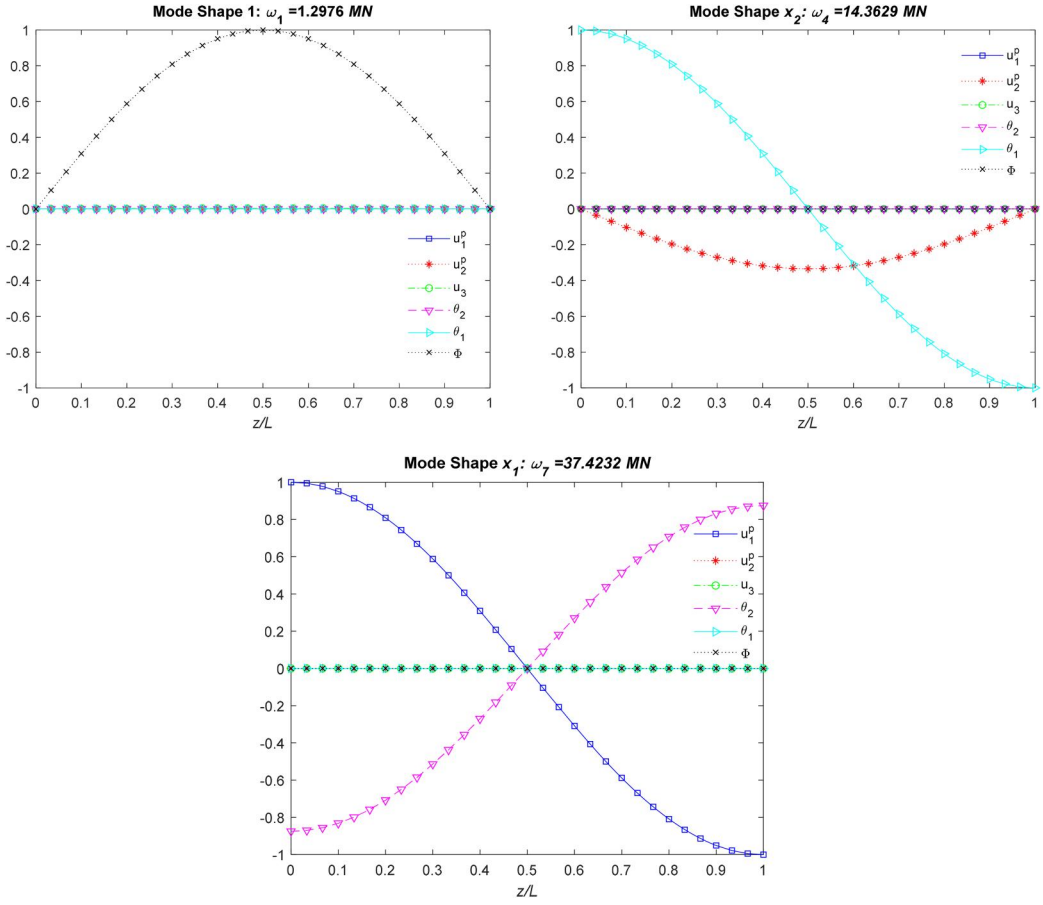
Figure 8. Buckling mode shapes of Type B PMF thin-walled box S–S beams with $e_0 = 0.5$ and $L/b_3 = 10$.

from both tables as well as Figs. 6 and 7. The critical buckling loads and natural frequencies are subjected to exponential decay where the decay constant increases in the order of C–F < S–S < C–C boundary conditions. This relation between the PMF beams' responses and L/b_3 ratios are understandable and well observed in thin-walled beams made of other materials. Comparing the porosity distribution Types A and B, there is a minimal difference of the critical buckling loads and fundamental frequencies across all values of L/b_3. When $L/b_3 > 35$, the critical buckling loads of the C–F PMF box beams are identical. However, as seen in Fig. 6, the critical buckling loads of these cantilevered beams experience a sharper drop compared to when $L/b_3 < 30$. Moreover, Figs. 8 and 9 display the buckling and vibration mode shapes of the Type A PMF box beams when $L/b_3 = 10$. The ascending order of the beams' responses are with reference to the torsional, x_2- and x_1-modes, respectively. For S–S beams (Fig. 8), the mode shapes of the beam's highest displacement variable is a half wave. Nonetheless, for C–F beams in Fig. 9, these shapes are a quarter wave.

Example 5: This example is to examine the effect of height-to-thickness ratio on buckling and vibration responses of PMF thin-walled box beams. In this example, the PMF thin-walled box beams with $L/b_3 = 20$, $e_0 = 0.5$ are considered. The thickness of the beam walls is fixed at $h = h_1 = h_2 = h_3 = h_4 = 0.005m$ for both the buckling analysis and for the vibration analysis.
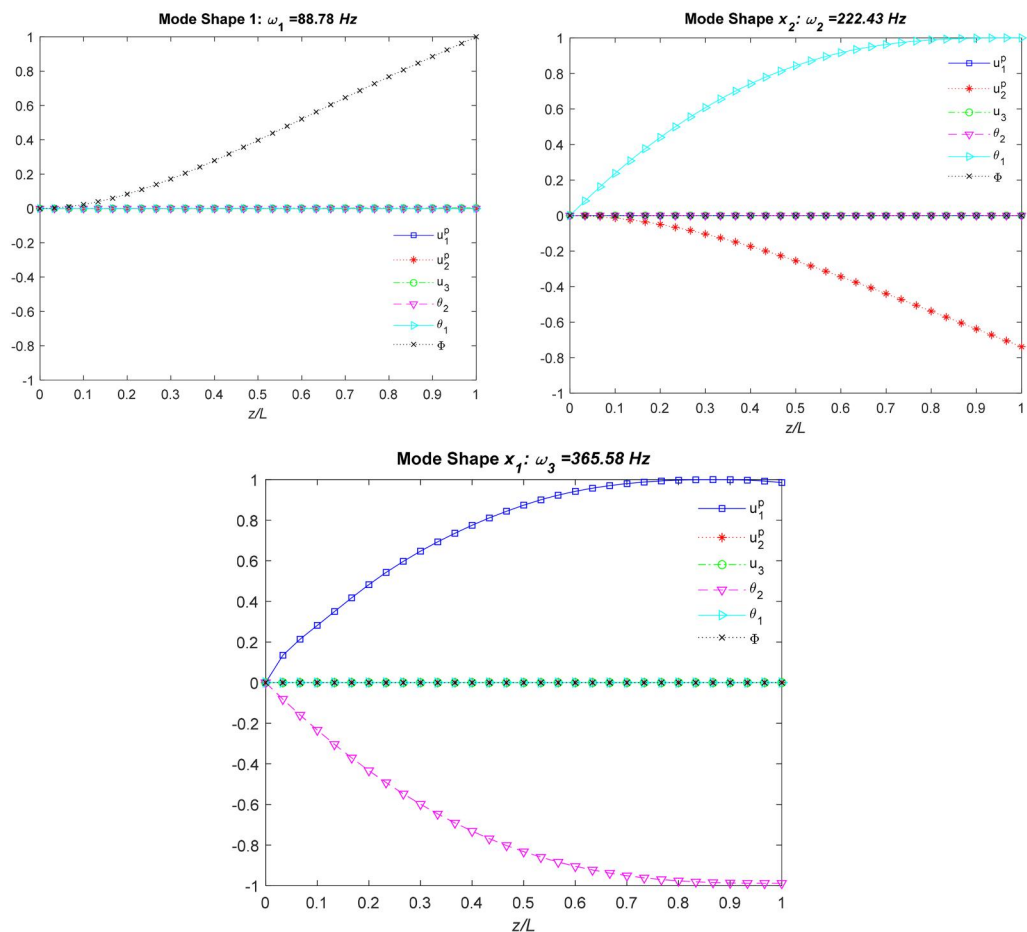
Figure 9. Free vibration mode shapes of Type A PMF thin-walled box beams with $e_0 = 0.5$, C–F boundary condition and $L/b_3 = 10$.

Table 10. Buckling loads (MN) of PMF thin-walled box beams with various values of b_3/h ($L/b_3 = 20$, $e_0 = 0.5$).

BC	Mode	b_3/h									
		5	10	15	20	25	30	35	40	45	50
Type A											
S–S	Min	0.93311	0.91865	0.71140	0.63720	0.61632	0.62211	0.64316	0.67373	0.71066	0.75204
	x_2	0.93311	1.84750	2.76604	3.68563	4.60563	5.52584	6.44617	7.36657	8.28702	9.20751
	x_1	2.57749	5.14603	7.71656	10.28758	12.85881	15.43013	18.00151	20.57293	23.14436	25.71583
C–C	Min	1.85031	1.28293	1.25016	1.35198	1.50773	1.69045	1.88860	2.09639	2.31061	2.52933
	x_2	3.59767	7.12571	10.66922	14.21660	17.76552	21.31522	24.86536	28.41578	31.96638	35.51710
	x_1	9.34312	18.65684	27.97709	37.29896	46.62150	55.94443	65.26741	74.59061	83.91392	93.23708
C–F	Min	0.23548	0.46620	0.57670	0.45851	0.39347	0.35503	0.33180	0.31807	0.31068	0.30772
	x_2	0.23548	0.46620	0.69797	0.93001	1.16215	1.39435	1.62658	1.85882	2.09108	2.32335
	x_1	0.66148	1.32061	1.98026	2.64005	3.29988	3.95974	4.61962	5.27950	5.93939	6.59929
Type B											
S–S	Min	0.97118	0.81146	0.63989	0.58356	0.57341	0.58635	0.61250	0.64691	0.68682	0.73058
	x_2	0.97118	1.88642	2.80525	3.72498	4.64507	5.56533	6.48570	7.40614	8.32661	9.24712
	x_1	2.61468	5.18363	7.75430	10.32539	12.89666	15.46801	18.03941	20.61084	23.18229	25.75376
C–C	Min	1.63355	1.17419	1.17763	1.29757	1.46419	1.65417	1.85750	2.06918	2.28642	2.50756
	x_2	3.73895	7.27037	10.81499	14.36292	17.91217	21.46209	25.01239	28.56292	32.11361	35.66442
	x_1	9.46513	18.78033	28.10105	37.42322	46.74589	56.06880	65.39195	74.71513	84.03843	93.36171
C–F	Min	0.24519	0.47611	0.50546	0.40506	0.35071	0.31940	0.30125	0.29134	0.28692	0.28634
	x_2	0.24519	0.47611	0.70796	0.94003	1.17220	1.40441	1.63665	1.86890	2.10116	2.33344
	x_1	0.67129	1.33052	1.99021	2.65001	3.30985	3.96972	4.62960	5.28949	5.94938	6.60928

Table 11. Natural frequencies (*Hz*) of PMF thin-walled box beams with various values of b_3/h ($L/b_3 = 20$, $e_0 = 0.5$).

BC	Mode	b_3/h									
		5	10	15	20	25	30	35	40	45	50
Type A											
S–S	Min	632.89	222.50	106.58	65.52	46.11	35.24	28.43	23.82	20.50	18.01
	x_2	632.89	314.86	209.71	157.23	125.77	104.80	89.82	78.59	69.86	62.87
	x_1	1047.67	523.38	348.87	261.64	209.30	174.42	149.50	130.81	116.28	104.65
C–C	Min	969.31	292.53	158.61	107.55	81.43	65.66	55.11	47.55	41.85	37.39
	x_2	1401.05	697.18	464.37	348.17	278.50	232.06	198.90	174.03	154.69	139.22
	x_1	2231.92	1115.11	743.30	557.45	445.95	371.62	318.53	278.71	247.74	222.97
C–F	Min	226.50	112.68	57.41	34.68	23.71	17.53	13.67	11.09	9.27	7.93
	x_2	226.50	112.68	75.05	56.27	45.01	37.50	32.14	28.12	25.00	22.50
	x_1	377.94	188.80	125.85	94.38	75.50	62.92	53.93	47.19	41.94	37.75
Type B											
S–S	Min	645.64	208.55	100.90	62.61	44.42	34.18	27.73	23.32	20.14	17.74
	x_2	645.64	318.15	211.19	158.07	126.30	105.17	90.10	78.80	70.02	63.01
	x_1	1055.15	525.28	349.71	262.11	209.61	174.63	149.66	130.93	116.37	104.72
C–C	Min	908.45	279.63	153.83	105.29	80.19	64.92	54.63	47.22	41.61	37.22
	x_2	1427.96	704.13	467.49	349.94	279.63	232.85	199.48	174.48	155.04	139.51
	x_1	2246.02	1118.69	744.90	558.35	446.53	372.02	318.82	278.94	247.92	223.11
C–F	Min	231.10	112.43	54.21	32.89	22.57	16.74	13.10	10.67	8.94	7.68
	x_2	231.10	113.87	75.58	56.57	45.20	37.64	32.24	28.20	25.06	22.55
	x_1	380.70	189.50	126.16	94.56	75.62	63.00	53.99	47.23	41.98	37.78
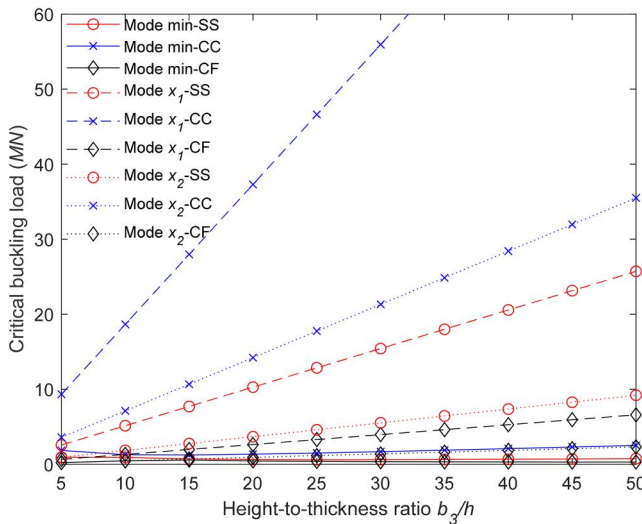
Figure 10. Buckling loads (*MN*) of Type A PMF thin-walled box beams with respect to various values of b_3/h.

Tables 10 and 11 and Figs. 10 and 11 demonstrate the variation of the critical buckling loads and natural frequencies as the beams' height b_3 increases by the factor of $b_3/h = 5$ to 50. The buckling loads in bending mode x_1 and x_2 become larger as the b_3/h ratio increases in all boundary conditions. However, the lowest critical buckling loads dip slightly from $b_3/h = 5$ to 25 before rising slowly up until $b_3/h = 50$ in the S–S and C–C beams. This trend is opposite to that of the C–F case where the lowest critical buckling loads increase from $b_3/h = 5$ to 15 but gradually drop afterwards. On the other hand, the natural frequencies experience an exponential decay as the height-to-thickness ratio rises. Comparing the responses of beams with Types A and B porosity distributions, Fig. 11b shows little discrepancy when the beams are in mode x_1 and x_2.
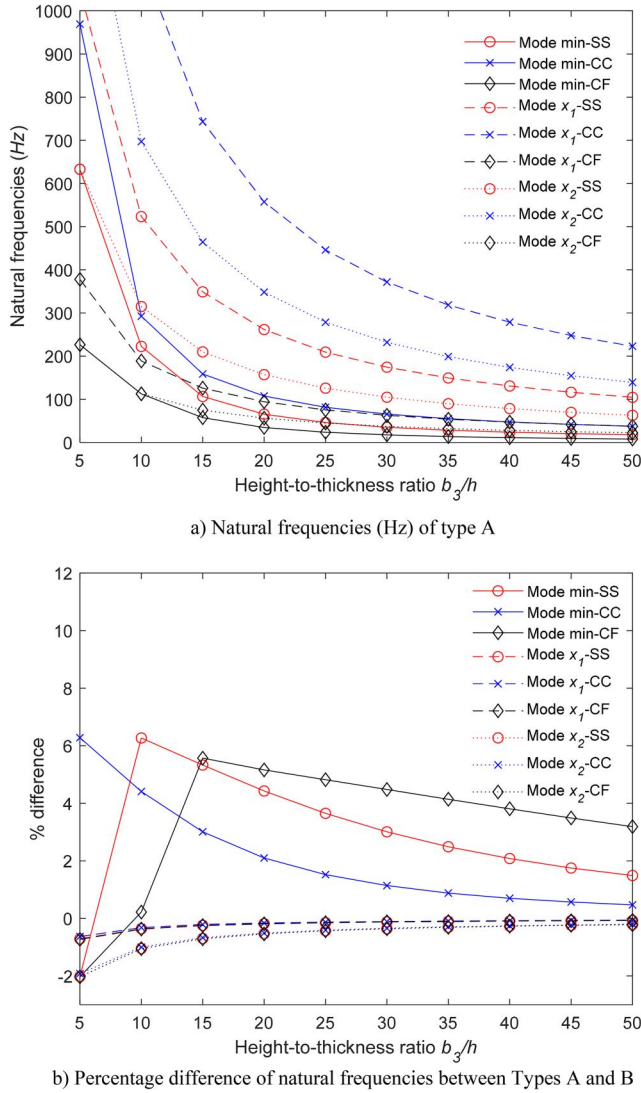
a) Natural frequencies (Hz) of type A

b) Percentage difference of natural frequencies between Types A and B

Figure 11. Natural frequencies (*Hz*) of PMF thin-walled box beams with respect to various values of b_3/h.

The differences are only significant in the cases of the lowest mode. Under the C–C boundary condition, the beam's lowest mode is torsional mode for all b_3/h ratios and the highest percentage difference is 6%. The sudden change of the "mode min" plots for S–S and C–F boundary condition at $b_3/h = 10$ and $b_3/h = 15$, respectively, are due to the fact that at these thresholds, the Type A PMF beams' lowest mode transitions from x_2-bending mode to torsion mode, while the Type B PMF beams' lowest mode remains torsional.

4. Conclusions

This paper proposed a first-order shear-deformable thin-walled box beam model for analyzing the buckling and vibration of porous metal foam thin-walled box beams, focusing on both symmetric (Type A) and nonsymmetric (Type B) porosity distributions. Using Hamilton's principles and a hybrid series solution, the responses of the beams are determined. The convergence and

accuracy of the present model have been demonstrated for the FG thin-walled box beams. Additionally, the beams are analyzed with varying parameters such as boundary conditions, porosity parameter, length-to-height ratio, height-to-thickness ratio, and width-to-height ratio. The analysis leads to the following conclusions:

- The effects of porosity distribution: An increasing porosity parameter e_0 decreases both the critical buckling loads and natural frequencies of porous beams, with the effects being more pronounced in buckling responses. Reduction in critical buckling loads is particularly significant for bending modes, with the most extreme case for C–C beams, being 45% decrease as e_0 goes from 0 to 0.7. The difference between Type A and B porous beams with respect to e_0 is only noticeable in the lowest mode in C–C boundary condition.
- The effects of geometric ratios: The increasing length-to-height ratio L/b_3 drastically reduces the critical buckling loads and natural frequencies especially when the L/b_3 goes from 10 to 30. When $L/b_3 \geq 60$, the lowest mode of the PMF thin-walled box beam changes from the torsional mode to the bending mode under S–S and C–F boundary conditions. The increasing height-to-thickness ratio b_3/h raises the critical buckling loads in bending mode significantly but does not quite affect the lowest mode. The increasing height-to-thickness ratio b_3/h lowers the natural frequencies of all modes in the way of a negative exponential relationship.

Disclosure statement

Funding

References

Addou, Bourada, Meradjah Bousahla, and Tounsi Ghazwani Alnujaie. 2023. "Impact of Porosity Distribution on Static Behavior of Functionally Graded Plates Using a Simple Quasi-3D HSDT." *Computers and Concretes* 32 (1): 87–97. https://doi.org/10.12989/cac.2023.32.1.087

Addou, F. Y., F. Bourada, A. Tounsi, A. A. Bousahla, A. Tounsi, K. H. Benrahou, and H. Albalawi. 2024. "Effect of Porosity Distribution on Flexural and Free Vibrational Behaviors of Laminated Composite Shell Using a Novel Sinusoidal HSDT." *Archives of Civil and Mechanical Engineering* 24 (2): 102. https://doi.org/10.1007/s43452-024-00894-w

Al-Osta, M., H. Saidi, A. Tounsi, and S. U. Al-Dulaijan. 2021. "Influence of Porosity on the Hygro-Thermo-Mechanical Bending Response of an AFG Ceramic–Metal Plates Using an Integral Plate Model." *Smart Structures and Systems* 28 (4): 499–513. https://doi.org/10.12989/sss.2021.28.4.499

Alsubaie, A. M., M. Al-Osta, A. Tounsi, A. Chikh, I. M. Mudhaffar and S. Tahir. 2023. "Porosity-Dependent Vibration Investigation of Functionally Graded Carbon Nanotube-Reinforced Composite Beam." *Comp. Concrete* 32 (1): 75–85. https://doi.org/10.12989/cac.2023.32.1.075

Ambrosini, R. D., J. D. Riera, and R. F. Danesi. 2000. "A Modified Vlasov Theory for Dynamic Analysis of Thin-Walled and Variable Open Section Beams." *Engineering Structures* 22 (8): 890–900. https://doi.org/10.1016/S0141-0296(99)00043-7

Bauld, N. R., and T. Lih-Shyng. 1984. "A Vlasov Theory for Fiber-Reinforced Beams with Thin-Walled Open Cross Sections." *International Journal of Solids and Structures* 20 (3): 277–297. https://doi.org/10.1016/0020-7683(84)90039-8

Belabed, Z., A. Tounsi, A. Al-Osta Mohammed, A. Tounsi, and H.-L. Minh. 2024. "On the Elastic Stability and Free Vibration Responses of Functionally Graded Porous Beams Resting on Winkler-Pasternak Foundations via Finite Element Computation." *Geomechanics and Engineering* 36 (2): 183–204. https://doi.org/10.12989/GAE.2024.36.2.183

Belabed, Z., A. Tounsi, A. A. Bousahla, A. Tounsi, and M. Yaylacı. 2024. "Accurate Free and Forced Vibration Behavior Prediction of Functionally Graded Sandwich Beams with Variable Cross-Section: A Finite Element Assessment." *Mechanics Based Design of Structures and Machines* 1–34. https://doi.org/10.1080/15397734.2024.2337914

Bentrar, H., M. Chorfi Sidi, A. Belalia Sid, A. Tounsi, H. Ghazwani Mofareh, and A. Alnujaie. 2023. "Effect of Porosity Distribution on Free Vibration of Functionally Graded Sandwich Plate Using the P-Version of the Finite Element Method." *Structural Engineering and Mechanics* 88 (6): 551–567. https://doi.org/10.12989/SEM.2023.88.6.551

Bourada, Bousahla, Tounsi Tounsi, O. Al Tahir, and V. Do. 2023. "An Integral Quasi-3D Computational Model for the Hygro-Thermal Wave Propagation of Imperfect FGM Sandwich Plates." *Computers and Concretes* 32 (1): 61–74. https://doi.org/10.12989/cac.2023.32.1.061

Bui Manh, C., T. Abdelouahed, T. Do Van, V. Nguyen Thi Hai, and M. Phung Van. 2024. "Finite Element Modelling for the Static Bending Response of Rotating FG-GPLRC Beams with Geometrical Imperfections in Thermal Mediums." *Computers and Concretes* 33 (1): 91–102. https://doi.org/10.12989/CAC.2024.33.1.091

Bui, X.-B., and T.-K. Nguyen. 2023. "Deterministic and Stochastic Flexural Behaviors of Laminated Composite Thin-Walled I-Beams Using a Sinusoidal Higher-Order Shear Deformation Theory." *Mechanics Based Design of Structures and Machines* 1–30. https://doi.org/10.1080/15397734.2023.2297840

Bui, X.-B., T.-K. Nguyen, A. Karamanli, and T. P. Vo. 2023. "Size-Dependent Behaviours of Functionally Graded Sandwich Thin-Walled Beams Based on the Modified Couple Stress Theory." *Aerospace Science and Technology* 142: 108664. https://doi.org/10.1016/j.ast.2023.108664

Bui, X.-B., T.-K. Nguyen, N.-D. Nguyen, and T. P. Vo. 2022. "A General Higher-Order Shear Deformation Theory for Buckling and Free Vibration Analysis of Laminated Thin-Walled Composite I-Beams." *Composite Structures* 295: 115775. https://doi.org/10.1016/j.compstruct.2022.115775

Bui, X.-B., T.-K. Nguyen, and P. T. T. Nguyen. 2024. "Stochastic Vibration and Buckling Analysis of Functionally Graded Sandwich Thin-Walled Beams." *Mechanics Based Design of Structures and Machines* 52 (4): 2017–2039. https://doi.org/10.1080/15397734.2023.2165101

Chandiramani, N. K., L. Librescu, and C. D. Shete. 2002. "On the Free-Vibration of Rotating Composite Beams Using a Higher-Order Shear Formulation." *Aerospace Science and Technology* 6 (8): 545–561. https://doi.org/10.1016/S1270-9638(02)01195-1

Chen, D., J. Yang, and S. Kitipornchai. 2015. "Elastic Buckling and Static Bending of Shear Deformable Functionally Graded Porous Beam." *Composite Structures* 133: 54–61. https://doi.org/10.1016/j.compstruct.2015.07.052

Chen, D., J. Yang, and S. Kitipornchai. 2016. "Free and Forced Vibrations of Shear Deformable Functionally Graded Porous Beams." *International Journal of Mechanical Sciences* 108–109: 14–22. https://doi.org/10.1016/j.ijmecsci.2016.01.025

Chitour, M., A. Bouhadra, F. Bourada, B. Mamen, A. A. Bousahla, A. Tounsi, A. Tounsi, M. A. Salem, and K. M. Khedher. 2024. "Stability Analysis of Imperfect FG Sandwich Plates Containing Metallic Foam Cores Under Various Boundary Conditions." *Structures* 61: 106021. https://doi.org/10.1016/j.istruc.2024.106021

Choi, S., and Y. Y. Kim. 2021. "Higher-Order Vlasov Torsion Theory for Thin-Walled Box Beams." *International Journal of Mechanical Sciences* 195: 106231. https://doi.org/10.1016/j.ijmecsci.2020.106231

Derikvand, M., F. Farhatnia, and D. H. Hodges. 2023. "Functionally Graded Thick Sandwich Beams with Porous Core: Buckling Analysis via Differential Transform Method." *Mechanics Based Design of Structures and Machines* 51 (7): 3650–3677. https://doi.org/10.1080/15397734.2021.1931309

Dukhan, N. 2013. *Metal Foams: Fundamentals and Applications*. Japan: DEStech Publications, Inc.

Ebadi-Jamkhaneh, M., M. Rezaei, and M. Ahmadi. 2021. "Seismic Behavior of Steel Braced Frames Equipped with Metal Foam." *International Journal of Steel Structures* 21 (4): 1420–1430. https://doi.org/10.1007/s13296-021-00513-x

Fang, Weihua, Tiantang Yu, Le Van Lich, and Tinh Quoc Bui. 2019. "Analysis of Thick Porous Beams by a Quasi-3D Theory and Isogeometric Analysis." *Composite Structures* 221: 110890. https://doi.org/10.1016/j.compstruct.2019.04.062

Farsadi, T. 2022. "Variable Thickness Thin-Walled Rotating Blades Made of Functionally Graded Porous Materials." *Proceedings of the Institution of Mechanical Engineers, Part C: Journal of Mechanical Engineering Science* 236 (14): 7674–7689. https://doi.org/10.1177/09544062221080654

Gao, K., R. Li, and J. Yang. 2019. "Dynamic Characteristics of Functionally Graded Porous Beams with Interval Material Properties." *Engineering Structures* 197: 109441. https://doi.org/10.1016/j.engstruct.2019.109441

Goldstein, H. 1980. *Classical Mechanics*. Boston: Addison-Wesley Publishing Company.

Hadji, B., M. Abderahmane, A. Abdelmoumen, B. Bourada, and B. Tounsi 2023. "Combined Influence of Porosity and Elastic Foundation Parameters on the Bending Behavior of Advanced Sandwich Structures." *Steel Composites and Structures* 46 (1): 1–13. https://doi.org/10.12989/scs.2023.46.1.001

Homae, T., Y. Sugiyama, T. Matsumura, and K. Wakabayashi. 2021. "Blast Wave Mitigation from a Straight Tube Using Metal Foam Floor Plate." *Science and Technology of Energetic Materials* 82 (3): 83–87. https://doi.org/10.34571/stem.82.3_83

Ishizaki, K., S. Komarneni, and M. Nanko. 2013. *Porous Materials: Process Technology and Applications*. US: Springer.

Keleshteri, M. M., and J. Jelovica. 2022. "Nonlinear Vibration Analysis of Bidirectional Porous Beams." *Engineering with Computers* 38 (6): 5033–5049. https://doi.org/10.1007/s00366-021-01553-x

Khorasani, Lampani Tounsi. 2023. "A Refined Vibrational Analysis of the FGM Porous Type Beams Resting on the Silica Aerogel Substrate." *Steel Composites and Structures* 47 (5): 633–644. https://doi.org/10.12989/scs.2023.47.5.633

Kim, N.-I., and J. Lee. 2018. "Geometrically Nonlinear Coupled Analysis of Thin-Walled $\Hbox{Al/Al}_{2}\Hbox{O}_{3}$FG Sandwich Box Beams with Single and Double Cells." *Acta Mechanica* 229 (11): 4677–4699. https://doi.org/10.1007/s00707-018-2238-8

Kvaternik, S., M. Filippi, D. Lanc, G. Turkalj, and E. Carrera. 2019. "Comparison of Classical and Refined Beam Models Applied on Isotropic and FG Thin-Walled Beams in Nonlinear Buckling Response." *Composite Structures* 229: 111490. https://doi.org/10.1016/j.compstruct.2019.111490

Lakhdar, Z., S. M. Chorfi, S. A. Belalia, K. M. Khedher, A. E. Alluqmani, A. Tounsi, and M. Yaylacı. 2024. "Free Vibration and Bending Analysis of Porous Bi-Directional FGM Sandwich Shell Using a TSDT p-Version Finite Element Method." *Acta Mechanica* 235 (6): 3657–3686. https://doi.org/10.1007/s00707-024-03909-y

Lanc, D., T. P. Vo, G. Turkalj, and J. Lee. 2015. "Buckling Analysis of Thin-Walled Functionally Graded Sandwich Box Beams." *Thin-Walled Structures* 86: 148–156. https://doi.org/10.1016/j.tws.2014.10.006

Lefebvre, L. P., J. Banhart, and D. C. Dunand. 2008. "Porous Metals and Metallic Foams: Current Status and Recent Developments." *Advanced Engineering Materials* 10 (9): 775–787. https://doi.org/10.1002/adem.200800241

Librescu, L., S.-Y. Oh, and O. Song. 2005. "Thin-Walled Beams Made of Functionally Graded Materials and Operating in a High Temperature Environment: Vibration and Stability." *Journal of Thermal Stresses* 28 (6–7): 649–712. https://doi.org/10.1080/01495730590934038

Liu, P., and G.-F. Chen. 2014. *Porous Materials: Processing and Applications*. Amsterdam: Elsevier.

Liviu Librescu, O. S. 2006. *Thin-Walled Composite Beams: Theory and Application, Solid Mechanics and its Applications*. Dordrecht: Springer.

Meftah, S. A., S. M. Aldosari, A. Tounsi, T. Cuong-Le, K. M. Khedher, and A. E. Alluqmani. 2024. "Simplified Homogenization Technique for Nonlinear Finite Element Analysis of In-Plane Loaded Masonry Walls." *Engineering Structures* 306: 117822. https://doi.org/10.1016/j.engstruct.2024.117822

Megson, T. H. G. 2021. *Aircraft Structures for Engineering Students*. 7th ed. United Kingdom: Butterworth-Heinemann.

Nguyen, N.-D., T.-K. Nguyen, T. P. Vo, and L. B. Nguyen. 2023. "Bending, Buckling and Free Vibration Behaviors of Thin-Walled Functionally Graded Sandwich and Composite Channel-Section Beams." *Mechanics Based Design of Structures and Machines* 51 (2): 932–960. https://doi.org/10.1080/15397734.2020.1859385

Nguyen, N.-D., T.-K. Nguyen, T. P. Vo, T.-N. Nguyen, and S. Lee. 2019. "Vibration and Buckling Behaviours of Thin-Walled Composite and Functionally Graded Sandwich I-Beams." *Composites Part B: Engineering* 166: 414–427. https://doi.org/10.1016/j.compositesb.2019.02.033

Srinath, G., A. Vadiraj, G. Balachandran, S. N. Sahu, and A. A. Gokhale. 2010. "Characteristics of Aluminium Metal Foam for Automotive Applications." *Transactions of the Indian Institute of Metals* 63 (5): 765–772. https://doi.org/10.1007/s12666-010-0117-7

Tang, Haishan, Li Li, and Yujin Hu. 2018. "Buckling Analysis of Two-Directionally Porous Beam." *Aerospace Science and Technology* 78: 471–479. https://doi.org/10.1016/j.ast.2018.04.045

Vlasov, V. Z. 1959. "Thin-Walled Elastic Beams." *PST Catalogue* 428.

Vo, T. P., and J. Lee. 2007. "Flexural–Torsional Behavior of Thin-Walled Closed-Section Composite Box Beams." *Engineering Structures* 29 (8): 1774–1782. https://doi.org/10.1016/j.engstruct.2006.10.002

Wu, H., J. Yang, and S. Kitipornchai. 2020. "Mechanical Analysis of Functionally Graded Porous Structures: A Review." *International Journal of Structural Stability and Dynamics* 20 (13): 2041015. https://doi.org/10.1142/S0219455420410151

Ziane, N., S. A. Meftah, H. A. Belhadj, A. Tounsi, and E. A. A. Bedia. 2013. "Free Vibration Analysis of Thin and Thick-Walled FGM Box Beams." *International Journal of Mechanical Sciences* 66: 273–282. https://doi.org/10.1016/j.ijmecsci.2012.12.001

Ziane, N., S. A. Meftah, G. Ruta, and A. Tounsi. 2017. "Thermal Effects on the Instabilities of Porous FGM Box Beams." *Engineering Structures* 134: 150–158. https://doi.org/10.1016/j.engstruct.2016.12.039